

Advances in Civil Engineering

# Advances in Seismic Performance Assessment and Improvement of Structures

Lead Guest Editor: Tadeh Zirakian

Guest Editors: David M. Boyajian, Vistasp M. Karbhari, and Mikayel G. Melkumyan





---

# **Advances in Seismic Performance Assessment and Improvement of Structures**

Advances in Civil Engineering

---

## **Advances in Seismic Performance Assessment and Improvement of Structures**

Lead Guest Editor: Tadeh Zirakian

Guest Editors: David M. Boyajian, Vistasp M. Karbhari,  
and Mikayel G. Melkumyan



---

Copyright © 2019 Hindawi. All rights reserved.

This is a special issue published in “Advances in Civil Engineering.” All articles are open access articles distributed under the Creative Commons Attribution License, which permits unrestricted use, distribution, and reproduction in any medium, provided the original work is properly cited.

## Editorial Board

- Khalid Abdel-Rahman, Germany  
José Aguiar, Portugal  
Reza Akhavian, USA  
Maria Cruz Alonso, Spain  
Serji N. Amirkhanian, USA  
P. Ch. Anastasopoulos, USA  
Venu G. M. Annamdas, Singapore  
Mehrdad Arashpour, Australia  
Pedro Arias-Sánchez, Spain  
Farhad Aslani, Australia  
Daniele Baraldi, Italy  
Emilio Bastidas-Arteaga, France  
Chiara Bedon, Italy  
Rafik Belarbi, France  
Giovanni Biondi, Italy  
Hugo C. Biscaia, Portugal  
Giosuè Boscato, Italy  
Melina Bosco, Italy  
Jorge Branco, Portugal  
Emanuele Brunesi, Italy  
Alberto Campisano, Italy  
Francesco Canestrari, Italy  
Giulio Castori, Italy  
Robert Černý, Czech Republic  
Constantin Chalioris, Greece  
Noel Challamel, France  
Daniel W.M. Chan, Hong Kong  
Edwin H W Chan, Hong Kong  
Carlos Chastre, Portugal  
Ghassan Chehab, Lebanon  
Wensu Chen, Australia  
Nicholas Chileshe, Australia  
Heap-Yih (John) Chong, Australia  
Francesco Colangelo, Italy  
Ottavia Corbi, Italy  
Marco Corradi, Italy  
Mario D'Aniello, Italy  
Jorge de Brito, Portugal  
Gianmarco de Felice, Italy  
Stefano de Miranda, Italy  
Tayfun Dede, Turkey  
Angelo Di Egidio, Italy  
Luigi Di Sarno, Italy  
Giulio Dondi, Italy  
Mohamed ElGawady, USA  
Ahmed Elghazouli, UK  
Behzad Esmaeili, USA  
Flora Faleschini, Italy  
Harry Far, Australia  
Antonio Formisano, Italy  
Giovanni Garcea, Italy  
Emilio García-Taengua, UK  
Elhem Ghorbel, France  
Agathoklis Giaralis, UK  
Rodrigo Gonçalves, Portugal  
Arturo Gonzalez, Ireland  
Belén González-Fonteboa, Spain  
Salvatore Grasso, Italy  
Fan Gu, UK  
Kirk Hatfield, USA  
Khandaker Hossain, Canada  
Zahid Hossain, USA  
Mohammad R. Hosseini, Australia  
Bon-Gang Hwang, Singapore  
Dong-Sheng Jeng, Australia  
Jian Ji, China  
Andreas Lampropoulos, UK  
Raffaele Landolfo, Italy  
Eul-Bum Lee, Republic of Korea  
Chun-Qing Li, Australia  
Dongsheng Li, China  
Li Li, Canada  
Xuemei Liu, Australia  
Zaobao Liu, China  
Davide Lo Presti, UK  
Sui Pheng Low, Singapore  
Lyan-Ywan Lu, Taiwan  
Eric Lui, USA  
Zhongguo John Ma, USA  
Lorenzo Macorini, UK  
Yann Malecot, France  
John Mander, USA  
Giuseppe Carlo Marano, Italy  
Fabio Mazza, Italy  
Claudio Mazzotti, Italy  
Ahmed Mebarki, France  
Shazim A. Memon, Kazakhstan  
Giovanni Minafò, Italy  
Hossein Moayedi, Iran  
Abbas Mohajerani, Australia  
Fabrizio Mollaioli, Italy  
Rosario Montuori, Italy  
Ayman S. Mosallam, USA  
Roberto Nascimbene, Italy  
Luís C. Neves, UK  
Trung Ngo, Australia  
Sanjay Nimbalkar, Australia  
Giuseppe Oliveto, Italy  
Alejandro Orfila, Spain  
Togay Ozbakkaloglu, Australia  
Hayri Baytan Ozmen, Turkey  
Alessandro Palmeri, UK  
Fabrizio Paolacci, Italy  
Fulvio Parisi, Italy  
Ignacio Paya-Zaforteza, Spain  
Arnaud Perrot, France  
Christophe Petit, France  
Giuseppe Piccardo, Italy  
Prodromos Psarropoulos, Greece  
Giuseppe Quaranta, Italy  
Carlo Rainieri, Italy  
Damien Rangedard, France  
Dimitris Rizos, USA  
Geoffrey W. Rodgers, New Zealand  
Hugo Rodrigues, Portugal  
Hamid Reza Ronagh, Australia  
Pier Paolo Rossi, Italy  
Lukasz Sadowski, Poland  
Anna Saetta, Italy  
Timo Saksala, Finland  
Evangelos J. Sapountzakis, Greece  
Vasilis Sarhosis, UK  
Halil Sezen, USA  
M. Shahria Alam, Canada  
Faiz U.A. Shaikh, Australia  
Mostafa Sharifzadeh, Australia  
Sanjay Kumar Shukla, Australia  
Amir Si Larbi, France  
Stefano Sorace, Italy  
Flavio Stochino, Italy  
Claudio Tamagnini, Italy  
Yaya Tan, China



---

Patrick W.C. Tang, Australia  
Yinshan Tang, UK  
Tai Thai, Australia  
Filippo Ubertini, Italy  
Humberto Varum, Portugal  
Castorina S. Vieira, Portugal  
C. Vipulanandan, USA  
Claudia Vitone, Italy  
Hao Wang, USA  
Lei Wang, USA

Linbing Wang, USA  
Wayne Yu Wang, UK  
Roman Wan-Wendner, Austria  
Bo Xia, Australia  
Wei-Chau Xie, Canada  
Michael Yam, Hong Kong  
Libo Yan, Germany  
Jian Yang, China  
Xu Yang, Australia  
Hui Yao, China

Victor Yepes, Spain  
Qingliang Yu, Netherlands  
Mariano Angelo Zanini, Italy  
Xiong Zhang, USA  
Yuqing Zhang, UK  
Dong Zhao, USA  
Xianbo Zhao, Australia  
Annan Zhou, Australia  
Abdul Aziz bin Abdul Samad, Malaysia

# Contents

## **Advances in Seismic Performance Assessment and Improvement of Structures**

Tadeh Zirakian , David M. Boyajian, Vistasp M. Karbhari, and Mikayel G. Melkumyan   
Editorial (2 pages), Article ID 9078428, Volume 2019 (2019)

## **Assessment of the Dynamic Behavior of Beam-to-Column Connections in Steel Pallet Racks under Cyclic Load: Numerical Investigation**

Zhi-Jun Lyu , Meng Wu, YuXin Huang , YiMing Song , and Xiong Cui  
Research Article (12 pages), Article ID 9243216, Volume 2018 (2019)

## **Seismic Vulnerability Assessment of Liquid Storage Tanks Isolated by Sliding-Based Systems**

Alexandros Tsipianitis and Yiannis Tsompanakis   
Research Article (14 pages), Article ID 5304245, Volume 2018 (2019)

## **Tests of Inclined Concrete-Filled Steel Tubular Stub Columns under Vertical Cyclic Loading**

Chayanon Hansapinyo , Chinnapat Buachart, and Preeda Chaimahawan  
Research Article (9 pages), Article ID 5426731, Volume 2018 (2019)

## **Comparative Study of Nonlinear Static and Time-History Analyses of Typical Korean STS Container Cranes**

Quang Huy Tran , Jungwon Huh , Van Bac Nguyen, Achintya Halder, Choonghyun Kang, and Kyeong Min Hwang  
Research Article (13 pages), Article ID 2176894, Volume 2018 (2019)

## **Earthquake Response Control of Double-Layer Truss Walls by means of Innovative Fuse Connections**

Koichiro Ishikawa   
Research Article (9 pages), Article ID 1425672, Volume 2018 (2019)

## **An Investigation of Damage Mechanism Induced by Earthquake in a Plate Girder Bridge Based on Seismic Response Analysis: Case Study of Tawarayama Bridge under the 2016 Kumamoto Earthquake**

Mya Nan Aye, Akira Kasai, and Mitsuhiro Shigeishi   
Research Article (19 pages), Article ID 9293623, Volume 2018 (2019)

## **Experimental Study of the Low-Cycle Fatigue in Double-Walled Hollow Pipe Members**

Lu Zhaohong , Zunce Wang , Yan Xu , Gao Shanshan, and Han Lianfu  
Research Article (10 pages), Article ID 7041851, Volume 2018 (2019)

## **Comparative Study of CFRP-Confined CFST Stub Columns under Axial Compression**

Ying Guo and Yufen Zhang   
Research Article (8 pages), Article ID 7109061, Volume 2018 (2019)

## Editorial

# Advances in Seismic Performance Assessment and Improvement of Structures

**Tadeh Zirakian** <sup>1</sup>, **David M. Boyajian**,<sup>1</sup> **Vistasp M. Karbhari**,<sup>2</sup>  
**and Mikayel G. Melkumyan** <sup>3</sup>

<sup>1</sup>California State University, Northridge, CA, USA

<sup>2</sup>The University of Texas at Arlington, Arlington, TX, USA

<sup>3</sup>Armenian Association for Earthquake Engineering, Yerevan, Armenia

Correspondence should be addressed to Tadeh Zirakian; [tadeh.zirakian@csun.edu](mailto:tadeh.zirakian@csun.edu)

Received 15 November 2018; Accepted 15 November 2018; Published 8 January 2019

Copyright © 2019 Tadeh Zirakian et al. This is an open access article distributed under the Creative Commons Attribution License, which permits unrestricted use, distribution, and reproduction in any medium, provided the original work is properly cited.

This special issue provided a forum for presentation and discussion of the latest findings and developments in the area of earthquake engineering. It is well known that earthquakes are catastrophic events inducing major human and economic losses. Structural failure may be avoided if preventive measures, such as the enhancement of various earthquake-resistant measures, are properly implemented. Assessment and enhancement of the seismic performance of buildings and structures is therefore of paramount importance.

This special issue contains a collection of eight original research papers covering concrete-filled steel tubular as well as CFRP-confined CFST stub columns, beam-to-column connections, double-layered truss walls, STS container cranes, liquid storage tanks, double-walled hollow pipe members, and a case study of a plate girder bridge.

A paper by C. Hansapinyo et al. presents an experimental study on the cyclic behavior of inclined concrete-filled steel tubular columns. The effect of inclination angle, concrete strength, and wall thickness on the loading capacity, ductility, and energy dissipation is investigated. A paper by Z.-J. Lyu et al. presents numerical results based on cyclic tests on different types of industrial rack joints. The geometrical factors in beam-to-column connections affecting the dynamic behavior of the braced racks are investigated with the aim of enhancing the seismic performance of the connections. A paper by Y. Guo and Y. Zhang presents a comparative study on the structural

behaviors of concrete-filled steel tubular stub columns having both inner and outer confinements using CFRPs for seismic performance improvement of structures. A paper by Ishikawa studies partial cylindrical truss walls equipped with damper connections subjected to horizontal earthquake motions with the objective of enhancing the seismic performance of the structure. A paper by Q. H. Tran et al. investigates the suitability of two nonlinear static analysis procedures, i.e., capacity spectrum method and equivalent linearization method, for studying the seismic behavior of ship-to-shore container gantry cranes. A paper by A. Tsipianitis and Y. Tsompanakis focuses on the fragility analysis of tanks isolated by sliding bearings of various pendulum types by considering the isolators' displacements due to near-fault earthquakes. A paper by M. N. Aye et al. surveys the damages sustained by some bridges affected by the 2016 Kumamoto Earthquake and evaluates the seismic response of the Tawarayama Bridge via numerical modeling and analysis. A paper by L. Zhaohong et al. reports an experimental study on double-walled hollow pipe specimens subjected to low-cycle loading tests in order to investigate their energy dissipation and antiseismic performance.

It is the hope of the Editorial Team that this special issue will contribute in advancing the state-of-the-art towards seismic performance evaluation and improvement of future structures.

**Conflicts of Interest**

The editors declare that there are no conflicts of interest regarding the publication of this special issue.

*Tadeh Zirakian  
David M. Boyajian  
Vistasp M. Karbhari  
Mikayel G. Melkumyan*

## Research Article

# Assessment of the Dynamic Behavior of Beam-to-Column Connections in Steel Pallet Racks under Cyclic Load: Numerical Investigation

Zhi-Jun Lyu <sup>1,2</sup>, Meng Wu,<sup>1,2</sup> YuXin Huang <sup>1,2</sup>, YiMing Song <sup>1,2</sup> and Xiong Cui<sup>3,2</sup>

<sup>1</sup>College of Mechanical Engineering, Donghua University, Shanghai 201620, China

<sup>2</sup>Shanghai Engineering Research Centre of Storage & Logistics Equipment, Shanghai 201611, China

<sup>3</sup>Shanghai Jingxing Storage Equipment Engineering Co., Ltd., Shanghai 201611, China

Correspondence should be addressed to Zhi-Jun Lyu; lvzj@dhu.edu.cn

Received 1 June 2018; Accepted 30 August 2018; Published 11 November 2018

Academic Editor: Tadeh Zirakian

Copyright © 2018 Zhi-Jun Lyu et al. This is an open access article distributed under the Creative Commons Attribution License, which permits unrestricted use, distribution, and reproduction in any medium, provided the original work is properly cited.

Steel pallet racks (SPRs) are characterized by boltless beam-column connections (BCCs). The role of BCCs becomes more significant during hazardous conditions such as earthquakes. Due to the great number of beam-end connector types and member geometries, the accurate evaluation of their structural behavior, especially under seismic loads, seems to be very difficult to perform so far. In this paper, the authors present results of simulation based on cyclic tests on different types of industrial rack joints by the finite element (FE) modeling of connections. This paper mainly investigates the BCC geometrical factors affecting the dynamic behavior of braced racks. Design indications are consequently provided in order to guarantee a globally homogenous ductility among different BCC configurations under seismic actions.

## 1. Introduction

Opposite of what happens for traditional civil engineering structures, the material of steel member for high-rise steel pallet racks (SPR) is thin and lightweight, and storage pallet racking systems can usually carry live load many times larger than the dead load with an extraordinary height [1]. However, this well-recognized advantage is counterbalanced by a structural response that is too complex to predict, especially under earthquakes. Main reason maybe that dynamic behavior of pallet racks is affected by not only the particular geometry of their structural members made by high slender thin-walled, open-section profiles (hence leading to local, global and even distortional buckling problems) but also beam-to-column connections representing a strong nonlinear behavior. It is generally considered that the beam-end connector is the most critical part of the assembly which determines the dynamic stability of SPR in the down-aisle direction [2].

In view of its importance, the most recent design codes, such as that of the RMI [3], EN15512 [4], and AS4084 [5], suggest individual experimental testing and define testing protocols with a marginal difference to predict the moment-rotation ( $M-\theta$ ) behavior of beam-to-column connections. Bajoria and Talikoti [6] adopted a double cantilever test method and compared with the single side cantilever beam test method. After that, the finite element simulation model was established based on the test. The superiority of the double cantilever test method and the feasibility of the finite element simulation were verified. Monotonic experimental tests were conducted in [7] to investigate the flexural behavior of connections under hogging loading in a single cantilever test setup. Several groups of beam-upright connections with different constructional details, such as the upright's profile, the thickness, and the number of tabs in the beam-end connector, were investigated. These tests highlighted that the failure mode of connections mainly depends on the relative thickness between the upright and the beam-end connector. Bernuzzi and Castiglioni [8] performed

a series of 11 monotonic and 11 cyclic tests on two different types of beam-to-upright connections used in Europe. The experimental results obtained from the monotonic tests indicated that the connections were characterized by significant ductile behavior. Federico Gusella et al. [9] presented results of monotonic and cyclic tests on four different types of industrial rack joints to illustrate the influence of the welding layout of beam-end connectors on the structural response and failure mode of joints. In addition, as one of the universal methods for evaluating seismic performance of connections, Tang and Chouw [10] describe a series of full-scale shake table tests performed to extend the understanding of the uplift behavior of interlocking columns. It is no doubt that experimental investigations are expensive and difficult to repeat. Therefore, a suitable solution is to derive a particular uniform  $M-\theta$  relationship for each connection type in terms of geometric parameters through finite element (FE) modeling. The structural behavior of rack connections has been also investigated by finite element numerical models. In [11], results of experimental tests on rack beam-end connections using both a cantilever and a double cantilever test setup were compared with those obtained through nonlinear finite element analyses, which were found to match well with the full-scale frame tests. The influence of the modeling of beam-column joints on the overall structural response of pallet racks was investigated in the numerical studies developed in [12], where frame models with semirigid joints were suggested, and in [13], where the importance of taking into account the cyclic behavior of connections to perform more reliable dynamic nonlinear analyses was underlined. Markazi et al. [2] conducted tests on the four different types of commercially available beam-end connectors to determine the parameters governing an efficient beam-end connector. Carlos [14] presented experimental findings about the beam-column connection under static and cyclic loads. The similarity of the static and cyclic failure modes indicate that the failure was controlled entirely by the connecting elements. Yin et al. [15] adopted some indexes such as the energy dissipation capability and the displacement ductility factor to explore the bearing capacity and energy dissipation of several variations of speed-lock connections of cold-formed steel storage racks. Mashaly et al. [16] presented a simple and accurate three-dimensional (3D) finite element model (FE) capable of predicting the actual behavior of beam-to-column joints in steel frames subjected to lateral loads. In this paper, the surface-to-surface element was used instead of node-to-node element to enhance the model. The FE results showed good correlation with the experimental one. However, reports about relationship between the structure features of SPR BCCs and its dynamic behavior have not been seen so far.

Based on the cyclic behavior of SPR BCC's test, this paper presents the results of simulation performed on the specimens of different BCC configurations using FE software ABAQUS. In terms of hysteretic loop and backbone curve, this paper discusses the structure geometrical factors affecting the dynamic behavior of braced racks. Moreover, the

authors quantify the global ductility and stiffness deterioration of specimens in comparison with the design standard values. Finally, the paper highlights the vulnerability of braced racks to connection failures and provides design indications for a more ductile rack design with good BCC configurations.

## 2. Cyclic Experiment Investigation

*2.1. Connection Types and Specimen Details.* In this study, two tests were carried out in order to declare the accuracy of the results obtained by the finite element models established using FE software ABAQUS. All the test specimens including columns, beams, and beam-end connectors were manufactured from cold-formed steel. The material properties of them are given in Table 1.

In steel pallet racks, the rivet connection is commonly used because of its flexible installation, as shown in Figure 1. Therefore, in this study, the rivet connection was adopted to identify the effects of various parameters which may affect the overall seismic performance of beam-to-column connections. Details of the rivet connection are shown in Figure 2. These specimens were distinguished by two different columns and beam depths. Each specimen consists of a 400 mm long column and a 750 mm long beam, which was manufactured in accordance with the FEM 10.2.08 [17]. M100 and M120 columns and B80 and B100 beams were selected according to the actual situation of enterprise. Both beam-end connectors have three rivets. Detailed specimen parameters are given in Table 2.

*2.2. Test Setup and Instrumentation.* In this study, the cantilever test method was adopted to obtain the hysteresis curve of the beam-to-column connections. The test setup consists of a testing frame, a loading device, and displacement transducers, as illustrated in Figure 3. The column was fixed on the column welding plate, and the beam was connected to the column by the connector. In the test, the measuring plate used to reflect the rotation angle  $\theta$  was installed on the beam, and two displacement transducers were installed on the plate for collecting the variation of deflection  $\delta$ . The loading point had been applied at a distance of 400 mm from the surface of the upright. During the test, the loading device imposed a preload on the beam in advance, which is 10% of the expected failure load and then unloaded. The load was gradually increased till the connector failed. During the test, the data measured by the displacement transducers and pressure sensors were recorded by the data acquisition card, and then  $M-\theta$  curves were generated by processing the data.

*2.3. Cyclic Loading Protocol.* The cyclic loading protocol was based on the variable amplitude load control mode. Before yielding, the load was increased by 1000N for each level, and the load was repeated twice. After yielding, the load was still increased 1000N every step but repeated once. The cyclic loading protocol is illustrated in Figure 4. When the force was downward, the direction was seen as positive, the angle  $\theta$

TABLE 1: Material properties of specimens.

Young's modulus, $E$ (GPa)	Poisson's ratio, $\mu$	Yield strength, $f_y$ (MPa)	Ultimate strength, $f_u$ (MPa)
210	0.3	235	390

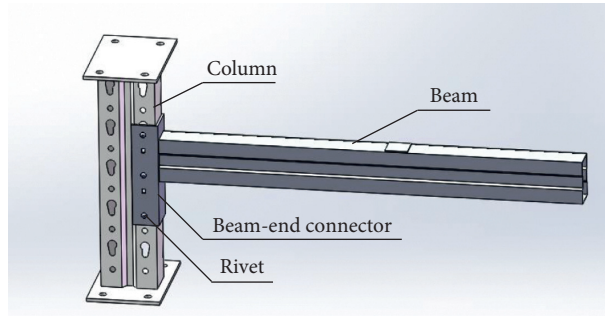


FIGURE 1: The rivet connection.

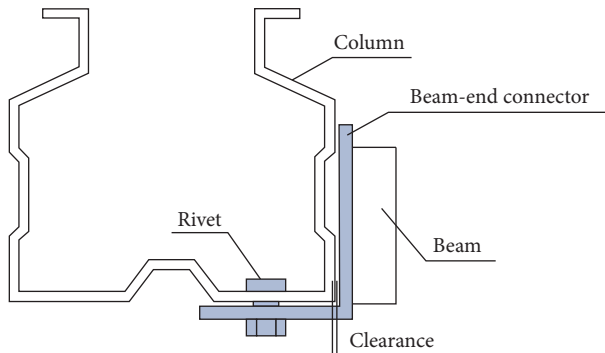


FIGURE 2: Details of the rivet connection.

TABLE 2: Detailed specimen parameters.

	Column	Column thickness (mm)	Beam	Number of rivets	Beam-end connector thickness (mm)
Test 1	M120	2.5	B100	3	4
Test 2	M100	2.5	B80	3	4

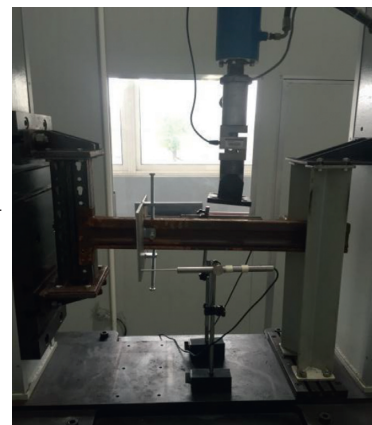
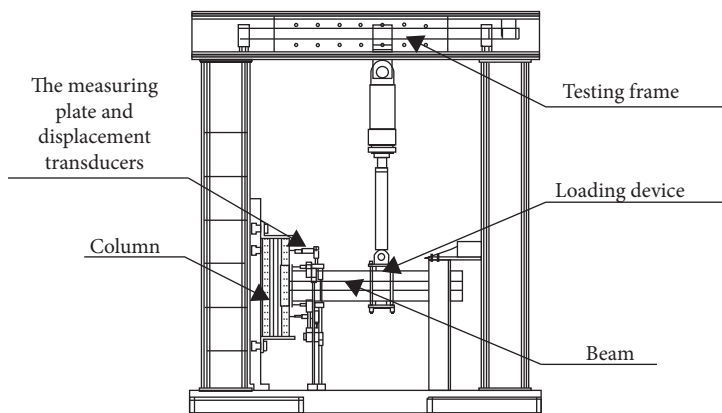


FIGURE 3: The test setup.

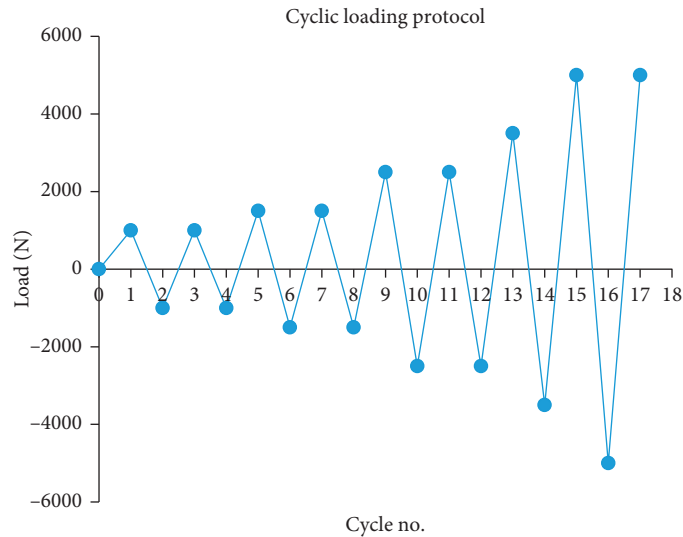


FIGURE 4: The cyclic loading protocol.

was negative, the load was negative, and vice versa. When the sample's connector, welding spot, or column holes appeared obviously damaged, the test stopped.

### 3. Finite Element Simulation

In this study, the three-dimensional model of different combinations of beam-to-column connections was developed to evaluate the effect of different parameters. In this paper, six parameters that might affect the seismic performance of the beam-to-column connections were selected, such as column thickness, beam depth, thickness of the beam-end connector, and the welding position of beam to the beam-end connector. Details of specimens are listed in Table 3. Specimens A only made changes to the beam depth to analyze the influence of beam depth on the seismic performance of beam-to-column connections. Similarly, specimens B, C, D, E, and F were used to analyze the influence of column thickness, thickness of the beam-end connector, the welding position of the beam, number of rivets, and clearance between column and beam-end connector, respectively. To ensure the accuracy, the details such as the flange's opening, the stiffener, and the fillet were reserved. Then, a finite element model was established using the commercial FE software ABAQUS.

**3.1. Material Properties and Element Types.** Different combinations of beam, column, and beam-end connector assemblies were modeled. The material properties of all the three components listed in Table 1 were used for FE modeling (FEM). Element C3D10 (a 10-node quadratic tetrahedron) was used for all the three parts of an assembly.

**3.2. Connection Modeling and Surface Interaction.** Contact nonlinearity was incorporated into the FE model by defining the interactions among column, beam-end

connectors, and rivets. The surface-to-surface interactions (front and side) between the column and the beam-end connector were defined through tangential frictionless behavior, as shown in Figure 5(a). Similarly, the surface-to-surface interactions between the column and rivets were defined in two ways: (i) normal hard contact, as shown in Figure 5(b), and (ii) tangential frictionless contact, as shown in Figure 5(c). The former was defined to avoid the relative movement between the surfaces of the column and the rivet, whereas the latter was defined to restrain the sideways movement (normal to longitudinal axes) of the column.

**3.3. Loading and Boundary Conditions.** Loading and boundary conditions were consistent with the test setup. In the experimental setup, both column ends were clamped and the column moves only up and down as a rigid body. Therefore, similar boundary conditions were applied to end of beams and the column. Upper and lower column ends are pinned support, that is, three degrees of freedom of X, Y, and Z were constrained, and freedom in Z direction was constrained for the beam. The concentrated force has been applied at a distance of 400 mm from the column's face. Similar loading procedure was adopted for FE analysis.

### 3.4. Simulation Results

**3.4.1. Failure Mode.** Comparing experimental results with simulation results, failure modes of the FE model exhibited close agreement with the experimental results. Under the cyclic load, holes were gradually deformed due to tension and compression of rivets and swinging of beams. After test, column holes appeared as gaps and rivets and the beam-end connector underwent obvious deformation. A comparison of failure modes in both experimental and FE analysis is presented in Figure 6. Deformation of the abovementioned components together resulted in failure of the beam-column connection.

TABLE 3: Details of specimens.

ID	Column	Column thickness (mm)	Thickness of beam-end connector (mm)	Beam depth	Beam position	Number of rivets	Clearance	
A	A-1	M120	2.5	4	B80	Upper	3	1
	A-2	M120	2.5	4	B100	Upper	3	1
	(standard)	M120	2.5	4	B120	Upper	3	1
B	B-1	M120	2	4	B100	Upper	3	1
	B-2	M120	2.5	4	B100	Upper	3	1
	(standard)	M120	2.5	4	B100	Upper	3	1
C	C-1	M120	3	4	B100	Upper	3	1
	C-2	M120	2.5	4	B100	Upper	3	1
	(standard)	M120	2.5	4	B100	Upper	4	1
D	D-1	M120	2.5	4	B100	Upper	3	1
	D-2	M120	2.5	4	B100	Middle	3	1
	(standard)	M120	2.5	4	B100	Lower	3	1
E	E-1	M120	2.5	4	B100	Upper	3	1
	E-2	M120	2.5	5	B100	Upper	3	1
	(standard)	M120	2.5	6	B100	Upper	3	1
F	F-1	M120	2.5	4	B100	Upper	3	1
	F-2	M120	2.5	4	B100	Upper	3	2
	(standard)	M120	2.5	4	B100	Upper	3	3

3.4.2. *Hysteretic Loop and Backbone Curve.* Based on experimental data, the nondimensional moment-rotation curves are drawn in Figure 7. The hysteresis loops show a z-shape during loading. Along with the increase of force, the slope of hysteretic loop keeps changing and decreasing and strength and stiffness decreasing. The maximum bending moment in the first cycle of each group is greater than in subsequent two cycles because of the deterioration undergone by the connector device.

Backbone curve analysis is one of the methods to analyze seismic performance. For each connection, the backbone curve is a line that connects peak points of the cyclic moment-rotation curve. The backbone curves from hysteretic moment-rotation responses are shown in Figure 8. By comparison, it can be found that experimental results are in close agreement with the backbone curves of simulation results, but there are greater errors in individual points and mainly appeared in the latter part of cyclic load. On the other hand, to achieve the same rotation of the backbone curves, the bending moment required by the finite element model is slightly larger than that of the test. The main reason for the error is that the finite element model does not consider geometric errors and initial defects, which will cause backbone curve difference.

3.4.3. *Rotation Ductility Factor.* Ductility is an important index to evaluate seismic performance of structure [15]. The ductility factor  $\mu$  is usually defined by the following equation:

$$\mu = \frac{\theta_u}{\theta_y}, \quad (1)$$

where  $\theta_u$  is the limit state (e.g., ultimate) rotation and  $\theta_y$  is the yielding rotation.

In this study, because there is no definite yielding point in Figure 8, to figure out the yielding rotation, a revised general yielding moment method (GYMM) [18] is employed. A schematic sketch of the method is shown in Figure 9. Based on a backbone curve of moment-rotation relation in Figure 9, OH is a line that represents the elastic theory value and intersects with the horizontal line of the ultimate load C at H. Then, a vertical line passing H intersects with backbone curve at A. Point H' is the intersection point of line OA and line CH. Then, a vertical line passing H' intersects with the backbone curve at B, which is the yielding point. The horizontal axis value of point B is identified as the yielding rotation  $\theta_y$ . Limit state rotation  $\theta_u$  is the value that corresponds with the limit state (or ultimate) moment  $M_u$  [15]. Then, the ductility factors of all connections for both positive and negative loading are calculated and provided in Table 4.

3.4.4. *Stiffness Deterioration Index.* For cyclic loading, displacement increases gradually to the limit state rotation  $\theta_u$  while stiffness reduces with cycles. This stiffness deterioration can be calculated from the hysteresis loops. The relationship of stiffness  $K$  and rotation  $\theta$  can be analyzed based on the data. As shown in Figure 10, polyline C'-B'-A'-O-A-B-C is a simplified "trifold" backbone curve after dimensionless processing. The slope  $K_1$  of DE is positive unloading stiffness. In order to calculate the stiffness deterioration index, relative stiffness  $K_1/K_0$  and relative

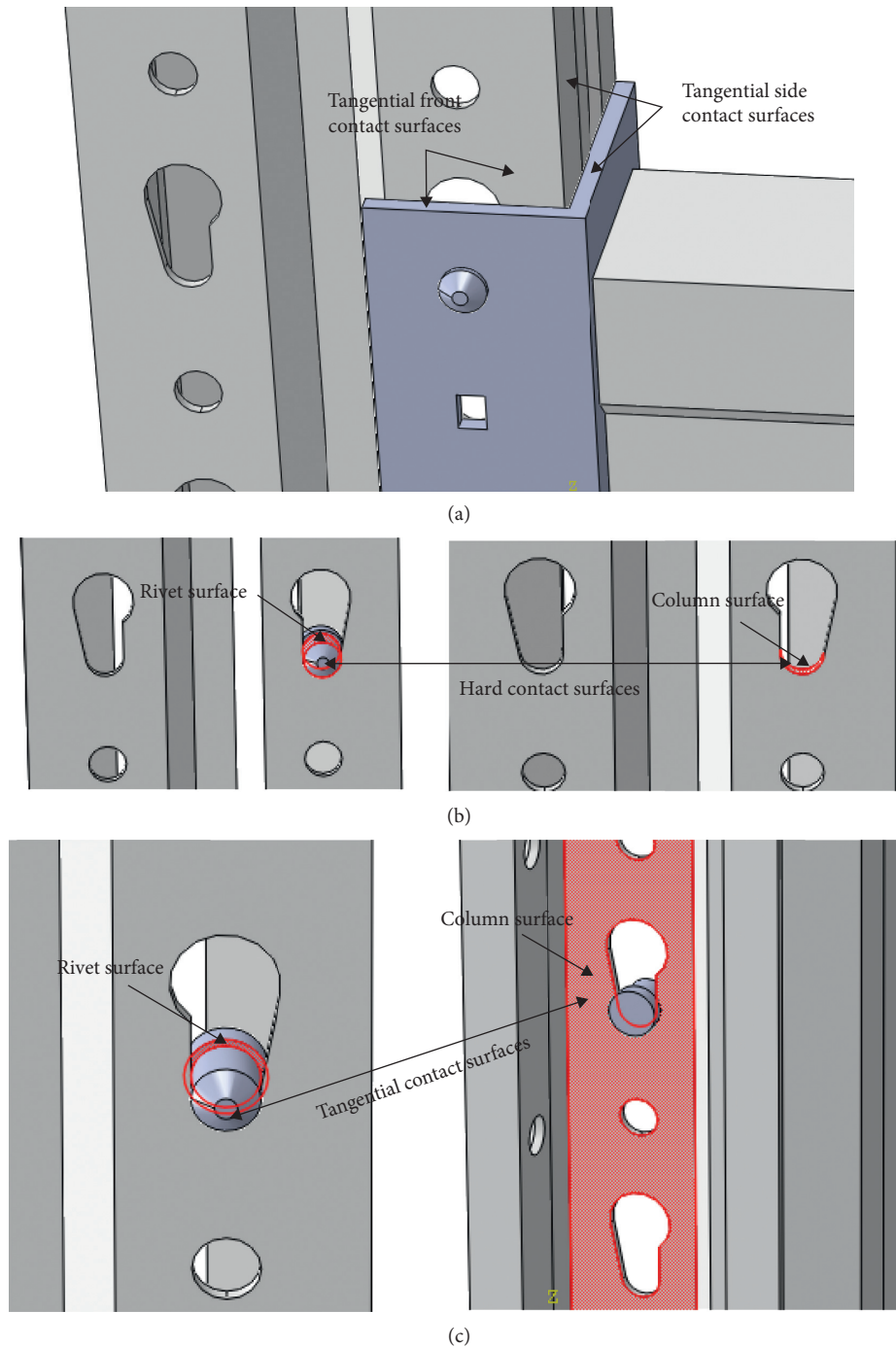


FIGURE 5: Surface-to-surface interaction among components. (a) Interactions between column and the beam-end connector. (b) Normal hard contact between column and rivets. (c) Tangential frictionless contact between column and rivets.

rotation  $\Delta_1/\Delta_u^+$  need to be calculated, where  $\Delta_1$  is the rotation corresponding to the unloading point of each hysteresis loop,  $K_0$  is initial stiffness, and  $\Delta_u^+$  is the rotation corresponding to the positive yield point. Similarly,  $K_2$ ,  $K_3$ , and  $K_4$  are negative loading stiffness, negative unloading stiffness, and positive loading stiffness, respectively.  $K_2/K_0$ ,

$\Delta_2/\Delta_u^+$ ;  $K_3/K_0$ ,  $\Delta_3/\Delta_u^-$ ; and  $K_4/K_0$ ,  $\Delta_4/\Delta_u^-$  are calculated, respectively.

In the study, taking M120 column as an example, the stiffness degeneration curve is fitted using MATLAB lsqcurvefit function, and the fitted curves are shown in Figure 11. Calculate the stiffness deterioration as follows:

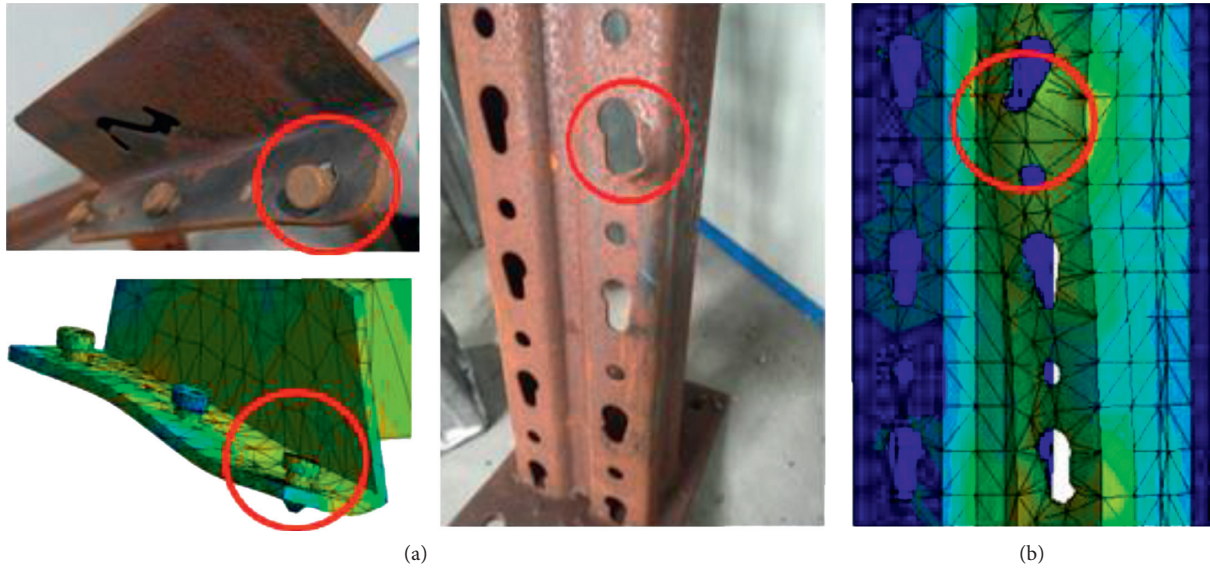


FIGURE 6: Comparison of simulation and experimental deformation. (a) Deformation of rivets and beam-end connector and (b) gap of holes.

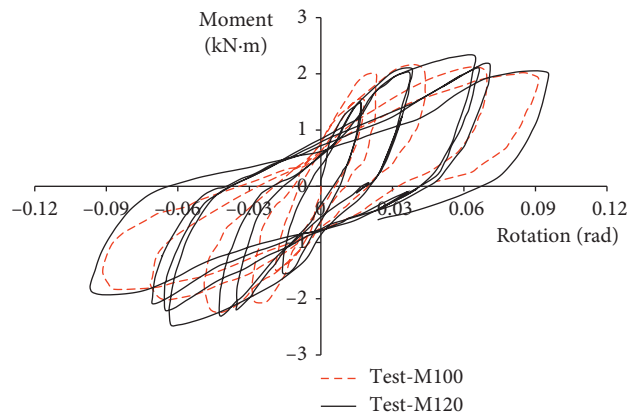


FIGURE 7: The hysteresis loops.

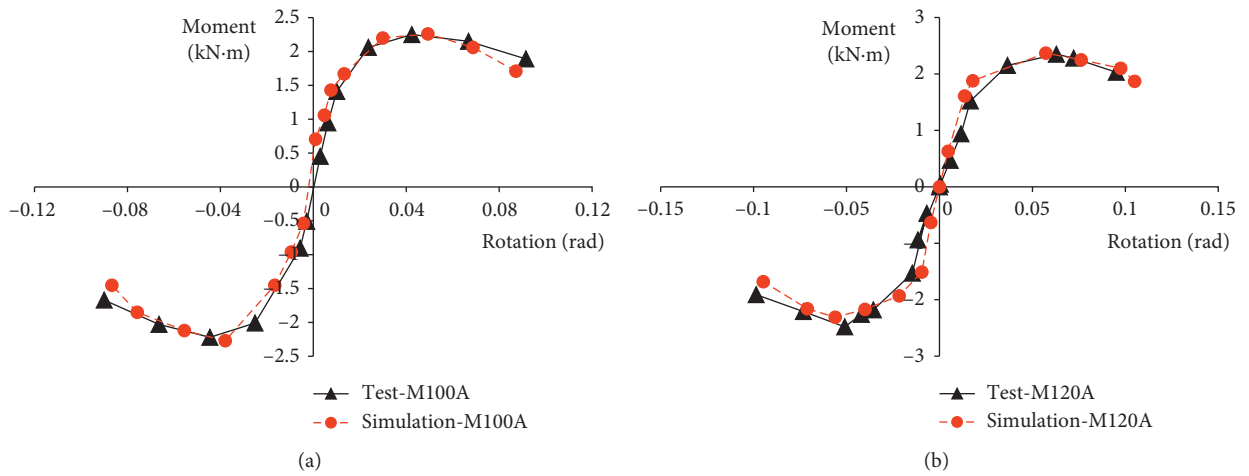


FIGURE 8: Comparison of experimental and simulation backbone curves. (a) M100 and (b) M120.

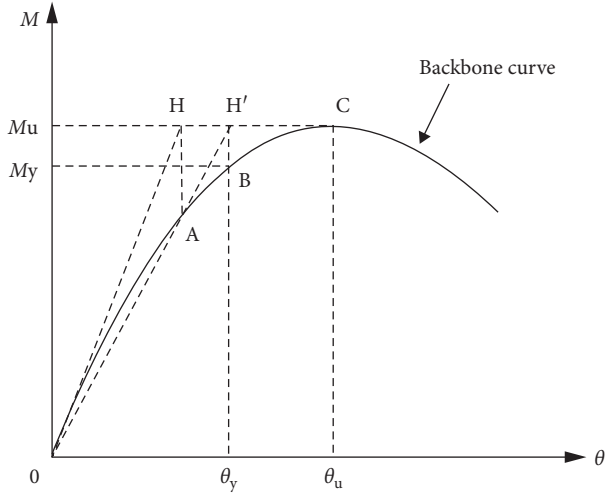


FIGURE 9: Schematic illustration of the general yielding moment method.

TABLE 4: Ductility factors of different connections.

ID	Ductility factor	Absolute difference rate (%)
A-1	1.764	7.45
A-2 (standard)	1.906	/
A-3	2.035	6.77
B-1	1.795	5.82
B-2 (standard)	1.906	/
B-3	2.009	5.40
C-1 (standard)	1.906	/
C-2	2.175	14.11
D-1 (standard)	1.906	/
D-2	1.985	4.14
D-3	1.912	<1%
E-1 (standard)	1.906	/
E-2	2.053	7.71
E-3	2.095	9.92
F-1 (standard)	1.906	/
F-2	1.875	2.46
F-3	1.718	9.86

$$\text{positive unloading stiffness: } \frac{K_1}{K_0} = -2.427 \ln\left(\frac{\Delta_1}{\Delta_u^+}\right) + 3.153,$$

$$\text{negative loading stiffness: } \frac{K_2}{K_0} = 3.447e^{-1.281(\Delta_2/\Delta_u^+)},$$

$$\text{negative unloading stiffness: } \frac{K_3}{K_0} = 3.102e^{-1.198(\Delta_3/\Delta_u^-)},$$

$$\text{positive loading stiffness: } \frac{K_4}{K_0} = -1.825 \ln\left(\frac{\Delta_4}{\Delta_u^-}\right) + 1.257.$$

(2)

Similarly, stiffness deterioration rules of other groups were also calculated. It was found that the fitting formulas and degeneracy rules were basically the same. With cyclic

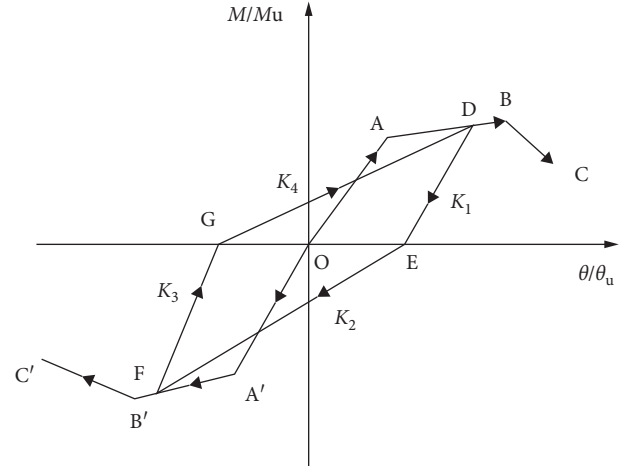


FIGURE 10: Stiffness deterioration calculation diagram.

loading and unloading, stiffness of structures showed obvious deterioration.

After comparing forms of the stiffness deterioration curve fitting formula, it was found that the fitting formulas of the positive unloading and loading stiffness degeneration curves were in the forms of formulas (3) and (4) respectively, while the negative loading and unloading stiffness deterioration curves were in the forms of formulas (5) and (6), respectively. Therefore, the stiffness deterioration can be compared by comparing the values of “a” and “h” in the positive stiffness degeneration. For negative stiffness degeneration, the variation of “d” and “g” is small. Therefore, only the “c” and “f” values need to be compared to evaluate the deterioration rate of negative stiffness. According to calculation results of the positive and negative stiffness degeneration of various beam-column connections, the values of a, h, c, and f were extracted, respectively, for analysis of the stiffness deterioration, and the results are shown in Table 5. The absolute difference rate in the table is obtained by taking the standard specimen as the denominator, and the difference is the increase or decrease relative to the previous result. The comparison of the absolute difference is shown in Figure 12.

$$\frac{K_1}{K_0} = -a \ln\left(\frac{\Delta_1}{\Delta_u^+}\right) + b, \quad (a > 0, b > 0), \quad (3)$$

$$\frac{K_4}{K_0} = -h \ln\left(\frac{\Delta_4}{\Delta_u^-}\right) + i, \quad (h > 0, i > 0), \quad (4)$$

$$\frac{K_2}{K_0} = ce^{-d(\Delta_2/\Delta_u^+)}, \quad (c > 0, d > 0), \quad (5)$$

$$\frac{K_3}{K_0} = fe^{-g(\Delta_3/\Delta_u^-)}, \quad (f > 0, g > 0). \quad (6)$$

#### 4. Parametric Analysis and Assessment

The FE model that was developed to validate the experimental testing was further extended for parametric analysis.

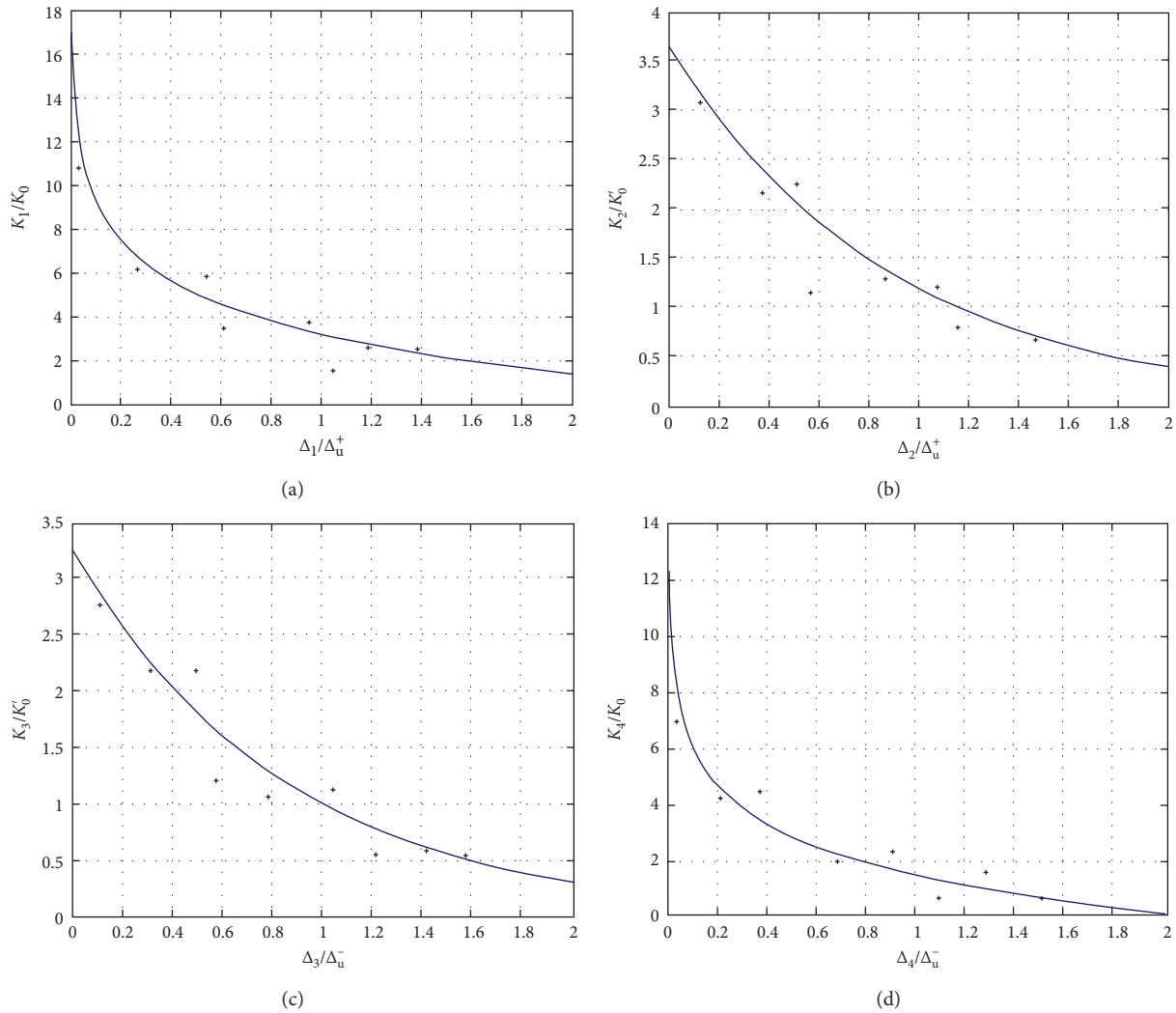


FIGURE 11: The stiffness deterioration of BCC under the cyclic loading protocol. (a) Positive unloading stiffness. (b) Negative loading stiffness. (c) Negative unloading stiffness. (d) Positive loading stiffness.

The analyzed parameters are as follows: variation in beam depth, column thickness, and number of rivets in the beam-end connector, variation in the thickness of the beam-end connector, variation in the welding position of beams to the beam-end connector, and variation in the clearance between the column and the beam-end connector. Different sizes of specimens were chosen for parametric analysis to observe the connection response.

By comparing ductility factors in Table 4 and stiffness deterioration rules in Table 5 of different combinations, except for the number of rivets, the effect of the thickness of the beam-end connector and clearance on the stiffness deterioration and ductility is slightly greater than the other three factors. The impact of different parameters on the seismic performance of beam-to-column connections was analyzed as follows.

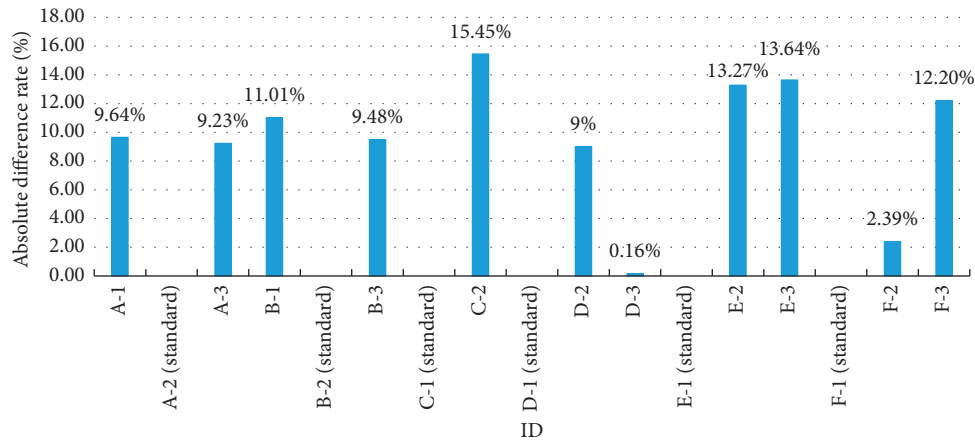
**4.1. Effect of Varying Beam Depth, Column Thickness, and Number of Rivets in the Beam-End Connector.** With specimens A, the FEM results can be further utilized to assess the

effect of beam depth. Compared with B100 beam, the ductility factor of the B80 beam was decreased by 7.45%, while for B120 beam, the ductility factor showed an increase of 6.77%. The positive unloading stiffness deterioration was increased by 9.64%, and the B120 beam was decreased by about 9.23%. Other stiffness deteriorations showed the same rule, which is compared to the B100 beam, the stiffness deterioration of the B80 beam decreased more rapidly, and the B120 decreased slowly. To figure out the effect of column thickness and number of rivets in the beam-end connector, specimens B and C showed that increasing the column thickness (2 mm, 2.5 mm, and 3 mm) and number of rivets (from three to four), the ductility increased, and the stiffness deterioration slowed down.

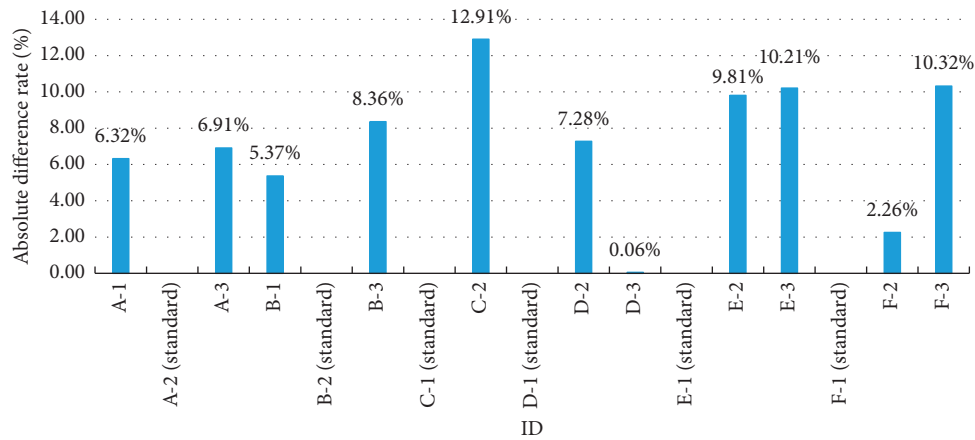
**4.2. Effect of Welding Position of Beam to the Beam-End Connector.** Parametric analysis was performed on specimens D in order to assess the effect of welding position of beam to the beam-end connector. The FE analysis of specimens D was performed to assess the effect of the

TABLE 5: Deterioration comparison of positive and negative stiffness.

ID	Positive unloading stiffness		Negative loading stiffness		Negative unloading stiffness		Positive loading stiffness		
	<i>a</i>	Absolute difference rate (%)	<i>c</i>	Absolute difference rate (%)	<i>f</i>	Absolute difference rate (%)	<i>h</i>	Absolute difference rate (%)	
A	A-1	2.661	9.64	3.665	6.32	3.271	5.45	1.973	8.11
	A-2 (standard)	2.427	/	3.447	/	3.102	/	1.825	/
	A-3	2.203	9.23	3.209	6.91	2.827	8.87	1.613	11.62
B	B-1	2.694	11.01	3.632	5.37	3.347	7.32	2.017	10.52
	B-2 (standard)	2.427	/	3.447	/	3.102	/	1.825	/
	B-3	2.197	9.48	3.159	8.36	2.808	9.47	1.593	12.71
C	C-1 (standard)	2.427	/	3.447	/	3.102	/	1.825	/
	C-2	2.052	15.45	3.002	12.91	2.765	10.86	1.405	23.01
D	D-1 (standard)	2.427	/	3.447	/	3.102	/	1.825	/
	D-2	2.209	9.00	3.196	7.28	2.904	6.38	1.618	11.34
	D-3	2.431	0.16	3.426	0.06	3.098	0.12	1.834	0.49
E	E-1 (standard)	2.427	/	3.447	/	3.102	/	1.825	/
	E-2	2.105	13.27	3.109	9.81	2.822	9.03	1.466	19.67
	E-3	2.096	13.64	2.757	10.21	2.519	9.49	1.423	22.03
F	F-1 (standard)	2.427	/	3.447	/	3.102	/	1.825	/
	F-2	2.485	2.39	3.525	2.26	3.158	1.81	1.913	4.82
	F-3	2.723	12.20	3.803	10.32	3.601	16.09	2.258	23.73



(a)



(b)

FIGURE 12: Continued.

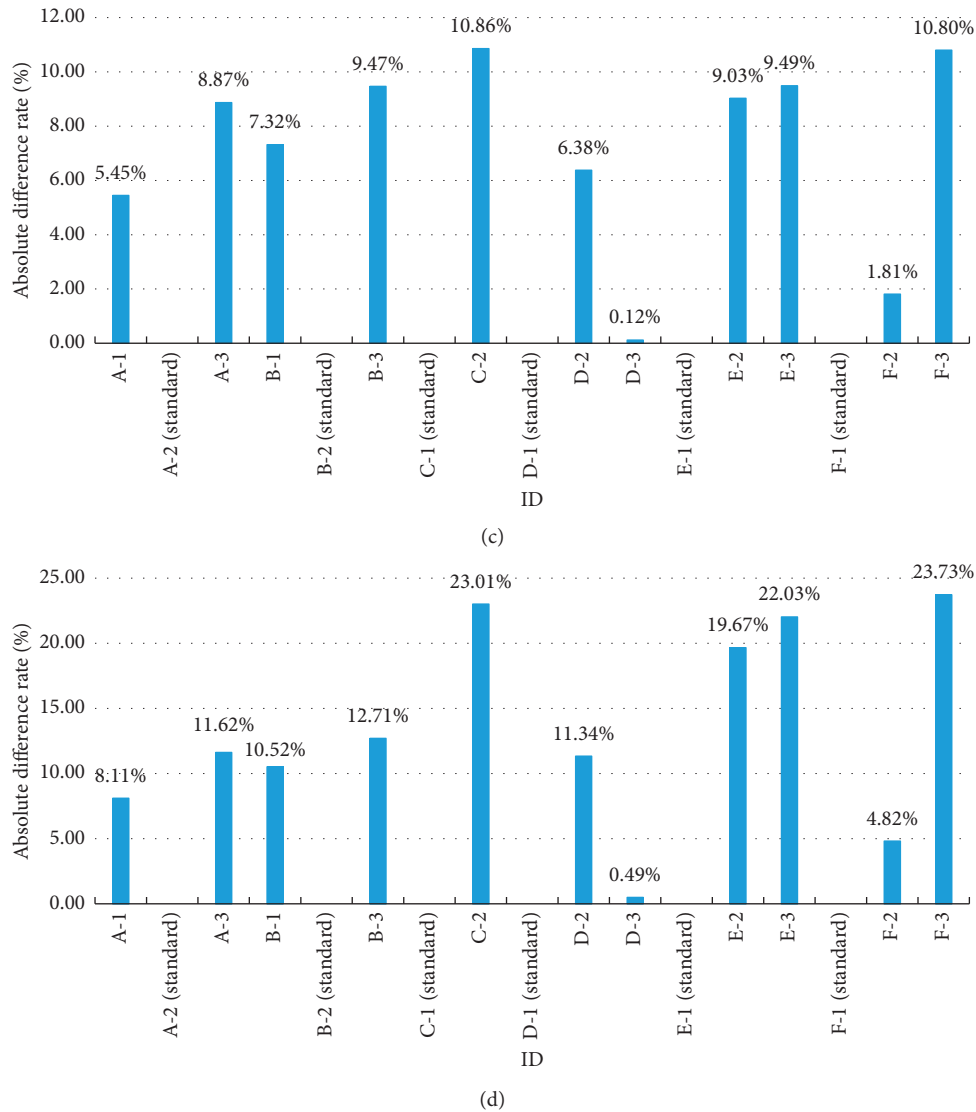


FIGURE 12: The comparison of stiffness deterioration. (a) Positive unloading stiffness. (b) Negative loading stiffness. (c) Negative unloading stiffness. (d) Positive loading stiffness.

welding position of beam to the beam-end connector. Judging from the analysis results, when the beam was middle-welded, the seismic performance was the best, when the beam was up-welded and down-welded, the seismic performance was basically the same.

**4.3. Effect of Variation in the Thickness of the Beam-End Connector.** Parametric analysis was performed on specimens E in order to assess the effect of the thickness of the beam-end connector. In specimens E, 4 mm, 5 mm, and 6 mm thick beam-end connectors were used. Increasing the thickness of the beam-end connector from 4 mm to 5 mm and 6 mm (specimen E) significantly affected the ductility (increased by 7.71% and 9.92%) and the stiffness deterioration of the connection. Taking the positive unloading stiffness as a base, the 5 mm and 6 mm thickness were

decreased by 13.27% and 13.64%, respectively. In general, the stiffness appeared a greater deterioration.

**4.4. Effect of Variation in the Clearance between Column and the Beam-End Connector.** Clearance between the column and the beam-end connector was 1 mm, 2 mm, and 3 mm in the FE analysis of specimens F. Increasing clearance from 1 mm to 2 mm, the ductility factor showed a smaller increase (2.46%) and slight stiffness deterioration appeared ( $\leq 5\%$ ). When increasing clearance from 1 mm to 3 mm, significant decrease in the ductility factor was observed (9.86%). At the same time, stiffness had a greater deterioration.

**5. Conclusion**

In this paper, the cyclic responses of different combinations of beam-to-column connections were investigated in order

to study the influence of different parameters on the dynamic behavior of the beam-to-column connections. These parameters included column thickness, beam depth, thickness of the beam-end connector, and the welding position of beam to the beam-end connector. Utilizing the cantilever test method, cyclic loading tests were conducted to explore their dynamic behaviors. By comparison with ductility factors and stiffness deterioration index, based on different configurations of beam-to-column connections except for the number of rivets, the effect of the thickness of the beam-end connector and clearance on the stiffness deterioration and ductility was slightly greater than the other three factors. Increasing beam-end connector thickness from 4 mm to 5 mm and 6 mm significantly improved the ductility and the stiffness had a slighter deterioration. When increasing clearance from 1 mm to 2 mm, the ductility factor showed a smaller increase, and slight stiffness deterioration appeared. But when increasing clearance from 1 mm to 3 mm, the ductility factor showed significant decrease and stiffness had a greater deterioration. In summary, increasing thickness of the beam-end connector can significantly improve the seismic performance of connections. Although increasing the clearance between the column and the beam-end connector is better for the assembling of steel pallet rack, it needs to be elaborately selected because it greatly reduced the performance of connections. The results in our paper seem to be preliminary; however, it has been observed that the dynamic behavior of SPR BCCs relies on geometrical parameters. The increasing demand of cold-formed thin-walled steel in high-rise rack needs to explore reliable and simple methods of accurate prediction of the behavior of storage racks and contents, which should be in a close coordination and interaction with the experimental test.

### Data Availability

The data used to support the findings of this study are all included in the article.

### Conflicts of Interest

The authors declare that they have no conflicts of interest.

### Acknowledgments

This paper has been funded by the National Key R&D Program of China (2017YFB1304000), technology innovation program of Shanghai Municipal Science and Technology Commission (17DZ2283800), and Minhang Science and Technology Foundation (2017mH205).

### References

- [1] C. Bernuzzi and M. Simoncelli, "An advanced design procedure for the safe use of steel storage pallet racks in seismic zones," *Thin-Walled Structures*, vol. 109, pp. 73–87, 2016.
- [2] F. D. Markazi, R. G. Beale, and M. H. R. Godley, "Experimental analysis of semi-rigid boltless connectors," *Thin-Walled Structures*, vol. 28, no. 1, pp. 57–87, 1997.
- [3] Rack Manufacturers Institute (RMI), *Specification for the Design, Testing and Utilization of Industrial Steel Storage Rack*, Material Handling Industry, MH16.1 2012, Charlotte, NC, USA, 2012.
- [4] EN15512, *Steel Static Storage Systems—Adjustable Pallet Racking Systems—Principles for Structural Design*, European Committee for Standardization, Brussels, Belgium, 2009.
- [5] Standards Australia, *Steel Storage Racking, AS4084*, Standards Australia, Sydney, Australia, 2012.
- [6] K. M. Bajoria and R. S. Talikoti, "Determination of flexibility of beam-to-column connectors used in thin walled cold-formed steel pallet racking systems," *Thin-Walled Structures*, vol. 44, no. 3, pp. 372–380, 2006.
- [7] X. Zhao, T. Wang, Y. Chen, and K. S. Sivakumaran, "Flexural behavior of steel storage rack beam to-upright connections," *Journal of Constructional Steel Research*, vol. 99, pp. 161–175, 2014.
- [8] C. Bernuzzi and C. A. Castiglioni, "Experimental analysis on the cyclic behaviour of beam-to-column joints in steel storage pallet racks," *Thin-Walled Structures*, vol. 39, no. 10, pp. 841–859, 2001.
- [9] F. Gusella, G. Lavacchini, and M. Orlando, "Monotonic and cyclic tests on beam-column joints of industrial pallet racks," *Journal of Constructional Steel Research*, vol. 140, pp. 92–107, 2018.
- [10] Z. Tang and N. Chouw, "Experimental investigation on uplift behaviour of mortar-free interlocking columns," in *Proceedings of New Zealand Society for Earthquake Engineering (NZSEE)*, Auckland, New Zealand, March 2014.
- [11] S. N. R. Shah, N. H. Ramli Sulong, R. Khan, M. Z. Jumaat, and M. Shariati, "Behavior of industrial steel rack connections," *Mechanical Systems and Signal Processing*, vol. 70–71, pp. 725–740, 2016.
- [12] N. Baldassino and C. Bernuzzi, "Analysis and behaviour of steel storage pallet racks," *Thin-Walled Structures*, vol. 37, no. 4, pp. 277–304, 2000.
- [13] F. Gusella, M. Orlando, and A. Vignoli, "Effects of pinching in the hysteresis loop of rack connections," in *Proceedings of the XVII Convegno ANIDIS*, Pistoia, Italy, September 2017.
- [14] A. Carlos, "Structural properties of connections for rack structures," in *Connections in Steel Structures V*, Federico Santa Maria University, Valparaiso, Chile, June 2004.
- [15] L. Yin, G. Tang, M. Zhang, B. Wang, and B. Feng, "Monotonic and cyclic response of speed-lock connections with bolts in storage racks," *Engineering Structures*, vol. 116, pp. 40–55, 2016.
- [16] E. Mashaly, M. El-Heweity, H. Abou-Elfath, and M. Osman, "Finite element analysis of beam-to-column joints in steel frames under cyclic loading," *Alexandria Engineering Journal*, vol. 50, no. 1, pp. 91–104, 2011.
- [17] FEM 10.2.08, *The Design of Static Steel Pallet Racking in Seismic Conditions*, FEM Racking & Shelving Product Group, West Bromwich, UK, 2011.
- [18] B. Zhu, *Seismic Test of Structure*, Earthquake Express, Beijing, China, 1989, in Chinese.

## Research Article

# Seismic Vulnerability Assessment of Liquid Storage Tanks Isolated by Sliding-Based Systems

Alexandros Tsipianitis and Yiannis Tsompanakis 

*School of Environmental Engineering, Technical University of Crete, 73100 Chania, Greece*

Correspondence should be addressed to Yiannis Tsompanakis; jt@science.tuc.gr

Received 28 February 2018; Revised 1 August 2018; Accepted 15 August 2018; Published 3 October 2018

Academic Editor: Tadeh Zirakian

Copyright © 2018 Alexandros Tsipianitis and Yiannis Tsompanakis. This is an open access article distributed under the Creative Commons Attribution License, which permits unrestricted use, distribution, and reproduction in any medium, provided the original work is properly cited.

Liquid-filled tanks are effective storage infrastructure for water, oil, and liquefied natural gas (LNG). Many such large-scale tanks are located in regions with high seismicity. Therefore, very frequently base isolation technology has to be adopted to reduce the dynamic distress of storage tanks, preventing the structure from typical modes of failure, such as elephant-foot buckling, diamond-shaped buckling, and roof damage caused by liquid sloshing. The cost-effective seismic design of base-isolated liquid storage tanks can be achieved by adopting performance-based design (PBD) principles. In this work, the focus is given on sliding-based systems, namely, single friction pendulum bearings (SFPBs), triple friction pendulum bearings (TFPBs), and mainly on the recently developed quintuple friction pendulum bearings (QFPBs). More specifically, the study is focused on the fragility analysis of tanks isolated by sliding-bearings, emphasizing on isolators' displacements due to near-fault earthquakes. In addition, a surrogate model has been developed for simulating the dynamic response of the superstructure (tank and liquid content) to achieve an optimal balance between computational efficiency and accuracy.

## 1. Introduction

The safe functioning of liquid storage tanks is of paramount importance, especially in seismic prone regions, since this severe natural hazard can lead to large-scale technological disasters, the so-called NATECH events. In general, cylindrical liquid storage tanks are structures that are widely used to store water, petrochemicals, and liquefied natural gas (LNG). Many such tanks are located in areas subjected to strong ground motions, and the seismic risk is higher compared to conventional structures due to devastating consequences. Failures of storage tanks due to earthquakes can cause leakages and explosions, as shown in many cases in the past earthquakes (Northridge (1994); Kobe (1995); Chi-Chi (1999)). In any case, a robust performance-based seismic design is required, as significant socioeconomical losses and environmental problems may result from even a minor failure.

Compared to ordinary structures (such as buildings and bridges), liquid storage tanks present different dynamic behavior due to liquid-tank interaction, since they are

subjected to inertial earthquake loads and hydrodynamic pressures. The mechanical model of Housner [1] represents this behavior in a realistic manner. More specifically, the hydrodynamic response of the tank-liquid system is divided in two uncoupled components: the impulsive component (i.e., the lower part of the liquid that moves horizontally and follows the tank wall movements) and the convective component (i.e., the upper part of the liquid that generates the sloshing motion). Many studies [2–4] have shown the dominance of impulsive liquid component on the global tank seismic response. In contrast, the convective component can be neglected since it is associated to long periods (which is  $>6$  sec for the examined tanks), that are substantially higher compared to the fundamental period of the tank-liquid system (approximately 2 sec for the examined isolated tanks, while it is  $<0.2$  sec for fixed-base conditions). Thus, typical forms of storage tank failures in past earthquakes (e.g., “elephant foot” and “diamond shape” buckling types) are mostly related to the impulsive component and less caused by liquid sloshing [5].

Base-isolation technology is considered as an efficient approach to reduce the seismic vulnerability of liquid storage tanks. The fundamental concept of base-isolation is the “decoupling” of structure from ground motions by installing isolators, i.e., devices with low horizontal and high vertical stiffness to accommodate the vertical loads of the structure. Therefore, the stresses and accelerations imposed on the tank are notably reduced, even if the displacements are quite high due to the increased deformability of the flexible bearings [6, 7]. Some large-scale liquid storage tanks isolated by friction isolators are presented in EPS [8]. Firstly, two LNG tanks of Revithoussa, Greece, each having a capacity of 65,000 m<sup>3</sup>, are equipped with totally 424 SFPB isolators. Secondly, two large LNG tanks located in Melchorita facility in Peru [9] are isolated by TFPBs, where earthquakes with magnitude >8 of Richter scale may occur.

Many studies have been devoted to the seismic analysis and vulnerability assessment of liquid storage tanks base-isolated with friction isolators. Firstly, Wang et al. [10] studied the effectiveness of SFPBs installed at the base of cylindrical tanks using a hybrid structure-hydrodynamic numerical model. Parameters such as tank aspect ratio, friction coefficient of SFPBs and earthquake intensity were examined. It was concluded that the impulsive pressures can be significantly reduced due to seismic isolation, while the convective pressures were slightly changed. Jadhav and Jangid [11] compared the seismic response of liquid storage tanks isolated by elastomeric bearings and sliding systems, while the continuous liquid mass of the tank was modeled as lumped masses, namely, sloshing mass, impulsive mass, and rigid mass. Using a similar simplified model of the masses, Panchal and Jangid [12] investigated the seismic response of liquid storage tanks isolated with variable friction pendulum system (VFPS). Based on the assumption of the concentrated masses, the kinematic equations for the VFPS and the storage tank were formed and solved. It was concluded that using VFPS as base-isolation system for liquid storage tanks, their seismic response could be controlled within desirable limits.

The work of Abali and Uckan [13] reported the efficiency of SFPBs in controlling the earthquake response of slender tanks compared to squat tanks. More specifically, a parametric analysis was conducted taking into account isolation period, tank aspect ratio and coefficient of friction. It was derived that base shear was reduced for both squat and slender tanks. Conversely, sloshing displacements of squat tanks were not significantly changed. The double variable frequency pendulum system (DVFPS) that isolated the liquid storage tank was included in the numerical model of Soni et al. [14]. The examined DVFPS was analyzed for different geometry and friction coefficient values. The main conclusions derived from this study were that DVFPS with higher initial stiffness from top sliding surface to bottom presented better behavior for slender tank, while the isolator having the same initial stiffness and coefficient of friction performed better for the squat tank.

Seleemah and El-Sharkawy [15] investigated the dynamic response of elevated squat and slender liquid storage tanks isolated by elastomeric and sliding bearings (SFPB).

In addition, the behavior of the storage tanks was compared for the cases where the isolators were placed at the bottom or at the top of the supporting structure. It was reported that base isolation affected in a beneficial manner the slender tanks and less the corresponding squat tanks. Furthermore, when an elevated tank was isolated with SFPBs, it presented better seismic performance than with elastomeric bearings. In addition, the examined tank presented better seismic behavior when isolators were placed at the top of the shaft support.

Panchal and Jangid [16] examined the seismic behavior of liquid storage tanks equipped with variable curvature friction pendulum system (VCFPS) under near-fault ground motions. The most important parameters for this investigation were the fundamental period, the friction coefficient, and the tank aspect ratio. It was found that the VCFPS is a quite effective seismic isolation device in controlling base shear, sloshing displacement, and the impulsive displacement of liquid storage tanks.

Moeindarbari et al. [17] investigated the efficiency of SFPB and TFPB installed at elevated liquid storage tanks subjected to multihazard level excitations. TFPB is capable of performing multiple level analysis at different hazard scenarios, such as Service Level Earthquake (SLE), Design Basis Earthquake (DBE), and Maximum Credible Earthquake (MCE). Hence, the results revealed that TFPB outperformed the SFPB, since the adaptive performance of TFPB played an important role in decreasing the seismic demand on the liquid storage tanks. Similarly, the effectiveness of two isolation systems of elevated storage tanks was studied by Paolacci [18]. Records from the Kocaeli Earthquake (1999) were used for the dynamic analysis of high damping rubber bearing (HDRB) and SFPB installed at the elevated tanks located in Habas pharmaceuticals plant in Turkey. It was concluded that elevated tanks isolated both by HDRB and SFPB presented major reductions in base shear as well as stress levels in the tank's wall. Due to the limitation of maximum bearing displacement and the higher value of sloshing displacement for the HDRB, the SFPB was considered as the superior isolation scheme for this specific case study.

Bagheri and Farajian [19] investigated the impact of PGA level and special characteristics of near-fault impulses on the earthquake performance of liquid storage tanks isolated by SFPBs. A mechanical model that accurately estimated the seismic response of the liquid storage tank was adopted. The results indicated that SFPB is an effective isolation system, capable of reducing critical parameters, such as impulsive displacement, overturning moment, and base shear, while the sloshing displacement did not present significant changes. Phan et al. [20] conducted a seismic fragility analysis of elevated liquid storage tanks isolated by concave sliding bearings (CSB). For this purpose, a lumped-mass simplified model was used for the examined tank. The cloud method was applied for the seismic fragility assessment, where nonlinear dynamic analysis through a linear regression-based probabilistic model was implemented. CSB scheme was found to be an effective isolation system for the reduction of the seismic demand on the tank.

In the majority of the aforementioned studies, the seismic response and/or vulnerability assessment of liquid storage tanks base-isolated by SFPBs or TFPBs was investigated. The influence of many critical parameters (i.e., base shear, aspect ratio, isolation period, etc.) on the results was examined, and it was proven that single-stage (SFPBs) and multistage (such as TFPBs) friction bearings were effective in reducing the seismic response, even when strong near-fault excitations were imposed. On the other hand, the newly appeared QFPB is a state-of-the-art seismic isolation device capable of accommodating very large displacements and performing complex multistage behavior [21]. It consists of six spherical sliding surfaces with five effective pendula. To the best of the authors' knowledge, seismic vulnerability assessment of liquid storage tanks isolated by QFPBs has not been reported in the literature.

Accordingly, in this study, which is an extension of a recent conference paper of the authors [22], the seismic vulnerability assessment of liquid-filled tanks isolated by different types of friction isolators is examined, following performance-based design (PBD) principles. More specifically, the study is focused on the response of single-surface isolators SFPBs, and the corresponding multiple-surface isolators: TFPBs and QFPBs. Utilizing peak ground acceleration (PGA) as the intensity measure (IM) and isolator displacement as the damage index (DI) for three earthquake hazard levels, fragility analysis is performed for each of these three sliding bearing configurations. Surrogate numerical models, based on the work of Bakalis et al. [23], have been developed for modeling both squat and slender liquid storage tanks. Compared to detailed finite element simulations, such models combine the minimization of computational cost with adequate accuracy of the dynamic response calculations. They consist of a concentrated impulsive mass that is attached to a vertical beam element supported by rigid beam spokes. Moreover, they can be implemented utilizing any general-purpose structural analysis software and can be used for either static or dynamic analysis.

## 2. Friction-Based Isolation Devices

**2.1. Single Friction Pendulum Bearings.** Figure 1(a) depicts a typical SFPB, which is a device that uses its special geometrical setting to provide seismic isolation [24]. The pendulum motion is represented by the spherical bearing surface, while the period of the isolator depends on the radius of curvature of the concave sliding surface. Additionally, another critical feature of SFPB is that the center of resistance coincides with the center of mass. Thus, the torsion response of the superstructure is limited. Therefore, parameters such as structural response, ductility, and energy dissipation can be controlled, and damage to building structural and nonstructural members and contents can be minimized or even avoided.

**2.2. Triple Friction Pendulum Bearings.** TFPB is an adaptive sliding isolation system that can exhibit different stiffness and damping properties during its operation [25] and

represents the new generation of friction isolators. It utilizes multiple spherical concave sliding surfaces, thus, both low transmissibility of vibration to the superstructure and zero residual displacements at the sliding structure after an earthquake are provided [26]. Hence, its operation is different from the conventional sliding bearings that exhibit constant stiffness and energy dissipation. In TFPBs, different combinations of curvature and friction of sliding interfaces can be selected. Moreover, these parameters can be adjusted depending on the imposed excitation levels. Therefore, multiple performance objectives can be achieved, which is ideal from a PBD perspective.

A TFPB consists of three friction pendulum mechanisms, which are activated at different stages as the seismic demand is amplified. As illustrated in Figure 1(b), these mechanisms are created via four concave surfaces in a single bearing. According to Constantinou et al. [27], the two inner surfaces share the same values for their friction coefficients ( $\mu_2 = \mu_3$ ) and radius of curvature ( $R_2 = R_3$ ). Analogously, it is also common that the outer concave surfaces have the same values ( $\mu_1 = \mu_4$ ) and ( $R_1 = R_4$ ). In a typical TFPB functioning, sliding occurs in different surfaces as the displacement demand increases. When TFPB approaches its maximum displacement capacity, the surfaces change again due to the fact that the displacement restraints of the sliders are reached, causing incremental hardening behavior [28].

The calculated values of the force-displacement curve for the TFPB configuration that has been used in the current investigation are shown in Figure 2(a). As it can be easily noticed, it is divided into several parts, depending on the selection of geometrical and frictional parameters. The horizontal force of TFPB is a combination of the friction force and the restoring force due to the curvature of the spherical surfaces. Normalized horizontal force,  $F/W$ , is conveniently used, since the resultant force,  $F$ , is proportional to the vertical force,  $W$ . Evidently, TFPB is ideal for PBD, since by selecting appropriate values for friction coefficients and radii of curvature for each surface, different behavior under service level earthquake (SLE), where sliding occurs on surfaces 2 and 3; design basis earthquake (DBE), where motion stops on surface 2 and sliding occurs on surfaces 1 and 3; and maximum considered earthquake (MCE), where sliding occurs on surfaces 1 and 4 can be achieved [8, 17].

**2.3. Quintuple Friction Pendulum Bearings.** According to Lee and Constantinou [21], the newly developed QFPB is an extended version of TFPB. In particular, it consists of six spherical sliding surfaces, five effective pendula, and nine operation regimes (Figure 1(c)) in a single bearing. The computed force-displacement curve of the examined QFPB is depicted in Figure 2(b). The adaptability of isolator behavior is increased due to the increased number of pendula and sliding patterns. Thus, although the functioning is similar, it is capable of a more complex and multistage performance compared to TFPB. Additionally, QFPB is ideal for high displacement demands due to severe earthquake excitations.

Similar to TFPBs, QFPBs can also be implemented within a PBD framework. Although the number of sliding

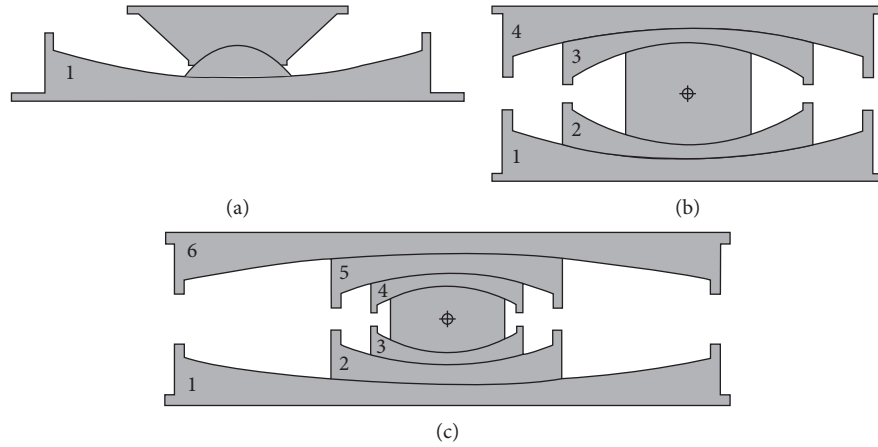


FIGURE 1: (a) Section view of SFPBs, (b) TFPBs, and (c) QFPBs, where numbers correspond to different sliding surfaces (adopted from [21]).

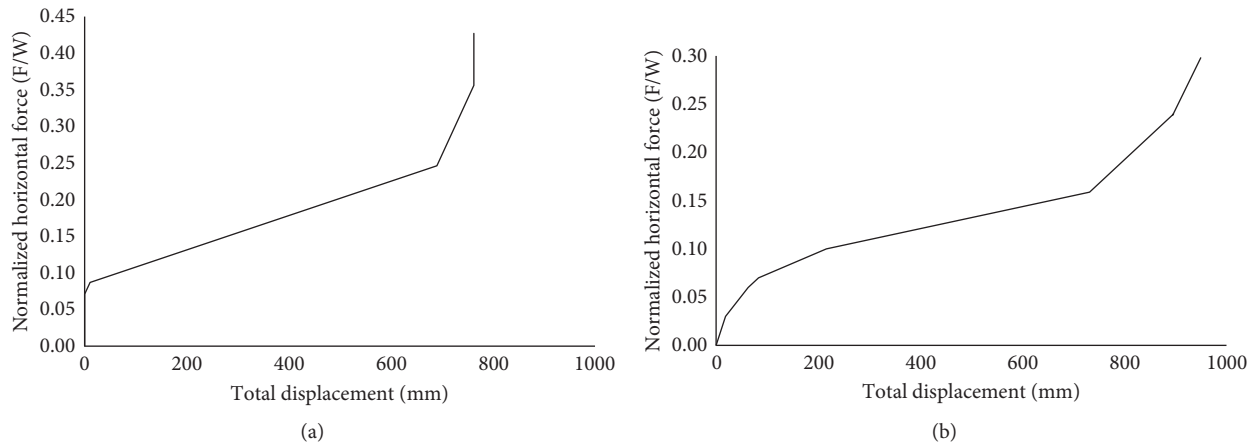


FIGURE 2: (a) Computed force-displacement curves for the examined bearing configurations: (a) TFPBs and (b) QFPBs.

surfaces is increased (six for QFPBs vs. four in the case of TFPBs as shown in Figures 2(a) and 2(b), respectively), the performance levels remain the same in this investigation, in particular, service level earthquake (SLE), where sliding occurs on surfaces 3 and 4; design basis earthquake (DBE), where motion stops on surface 6 and sliding occurs on surfaces 2 and 5; and maximum considered earthquake (MCE), where sliding occurs on surface 1.

**2.3.1. Model Validation.** In this section, the analytical and experimental validation of QFPBs utilizing finite element software SAP2000 [29] is presented, following the recommendations of Lee and Constantinou [21]. The isolator is simulated in the software as a series model, combining one triple friction pendulum (FP) element with one double FP element. The double FP isolator is actually a “condensed” triple FP element. This is achieved by specifying arbitrary values of the radius of curvature and friction coefficient that lead to motion initiation of the inner sliding surfaces. In this manner, the double FP isolator operation is performed utilizing SAP2000 (Figure 3(a)). The configuration examined has friction coefficient values:  $\mu_3 = \mu_4 < \mu_5 \leq \mu_2 < \mu_6 \leq \mu_1$ .

Figures 4 and 5, respectively, illustrate the force-displacement curves taken from a recent study [21] for the experimental (tested in the experimental setup at the University at Buffalo [30]) and the analytical QFPB models, which are compared to the numerical results of the same configurations obtained herein utilizing SAP2000 software. Firstly, the experimental model of one QFPB (Table 1) based on the multistage experimental setup of the isolator tested at the University at Buffalo [30] is validated numerically via SAP2000 software. A harmonic excitation with frequency equal to 0.005 Hz was imposed to the tested QFPB, together with a constant vertical load of  $W = 88964.4 \text{ N}$ . The displacement amplitude of the imposed harmonic motion was equal to 127 mm, since this was the displacement capacity of the testing device. Figure 4 illustrates the validation of QFPB with respect to the experimental model. As it can be noticed in this plot, there is an excellent matching of the force-displacement curves of the experimental model and the corresponding isolator model developed in SAP2000.

The second validation is performed by comparing the obtained numerical results with the corresponding ones of the analytical QFPB model for another case study [21]. In this example, a sinusoidal harmonic excitation is imposed to

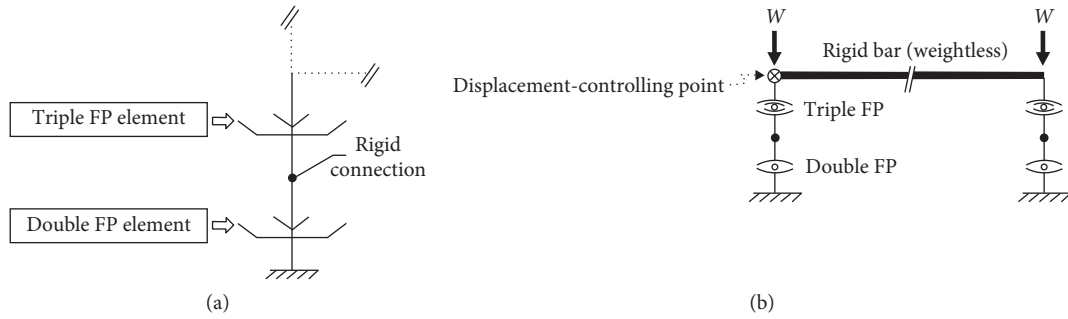


FIGURE 3: (a) Series model of QFPB with a pair of double and triple FP elements and (b) model equipped with QFPBs as implemented in SAP2000 (adopted from [21]).

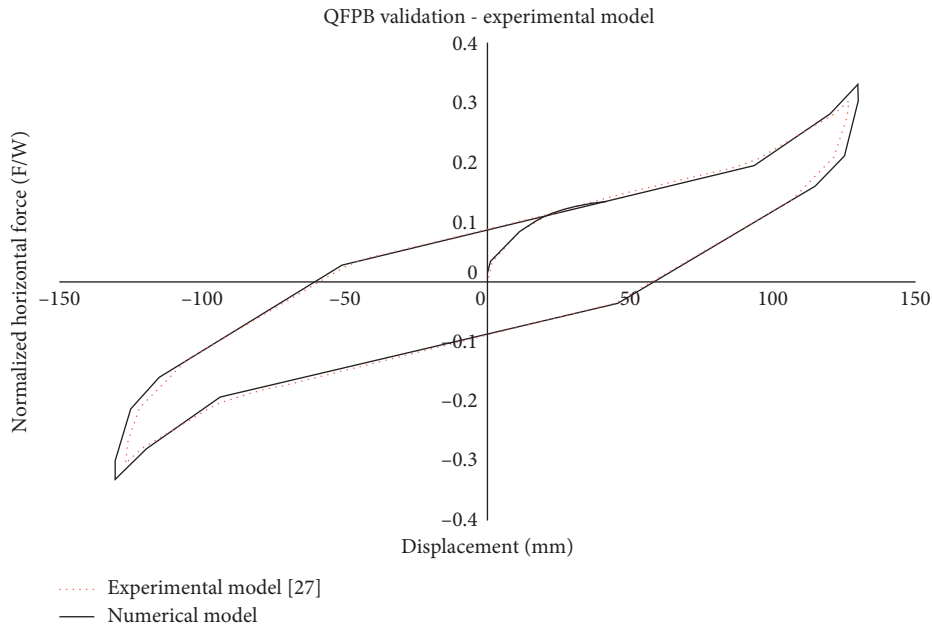


FIGURE 4: Comparison of current numerical QFPB model with experimental results derived from Lee and Constantinou [21].

the isolator, having an amplitude of approximately 1 m, equal to the displacement limit of the analytical model. Further information considering the force-displacement expressions used for the current validation can be found in the detailed study of [21]. By observing Figure 5, it can be noticed that the numerical isolator model developed utilizing SAP2000 captures exactly the behavior of the analytical model. Hence, the QFPB configuration presented in Figure 5 has been considered suitable for the fragility analysis of the examined liquid storage tanks. Consequently, after the successful validation of the present numerical implementation of the examined isolators, a detailed parametric study has been performed regarding their implementation for the seismic isolation of liquid storage tanks, as it will be presented in the sequence.

### 3. Multistep Dynamic Analysis

For such critical infrastructures as liquid storage tanks, a wide range of ground motion records should be taken into account for the reliable implementation of performance-based design.

Consequently, a huge number of nonlinear dynamic analyses need to be executed in an incremental manner. Incremental dynamic analysis (IDA) and multiple-stripe dynamic analysis (MSDA) are the most frequently applied methods [31]. Such methods are widely used in earthquake engineering for seismic performance assessment of various types of structures. They are based on the simple concept of scaling each ground motion until it leads to the collapse of the examined structure. MSDA is ideal for performance-based evaluation of structures using a set of ground motion records at multiple performance levels. Many sets of analyses are performed for multiple peak ground acceleration (PGA) levels, where at each analysis (stripe) a number of structural analyses are performed for a group of ground motion records, which are scaled every time to a specific PGA value. In this way, a set of intensity measure and damage index values is produced.

Therefore, obtaining the relation between the seismic intensity level and the corresponding maximum response quantity of the base isolation system is the main objective of these multistep procedures. A suitable intensity measure (IM) and an engineering demand parameter (EDP) describe

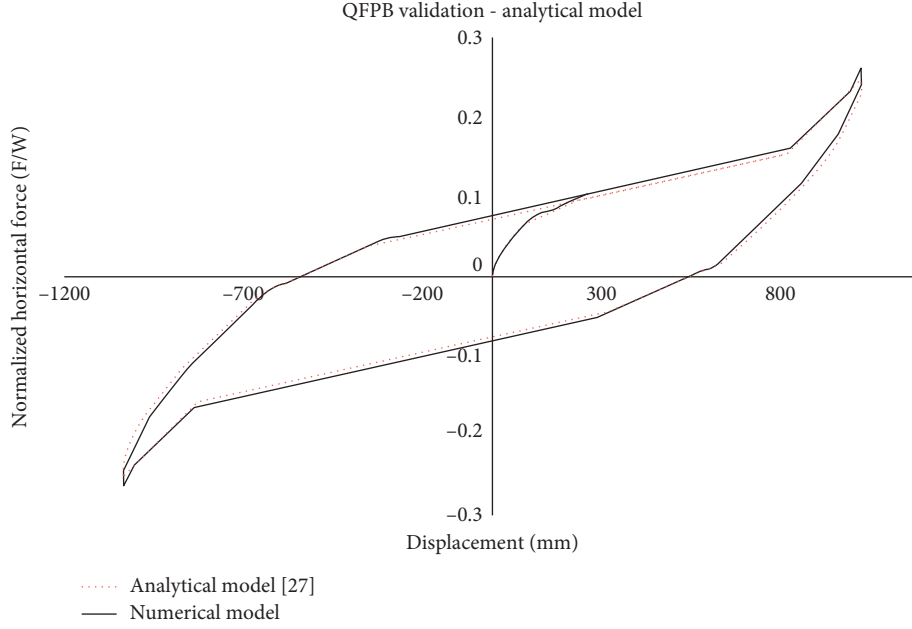


FIGURE 5: Comparison of current numerical QFPB model with analytical results derived from Lee and Constantinou [21].

TABLE 1: Parameters of the QFPB model (taken from [21]).

Radius (m)	Height (m)	Coefficient of friction	Displacement capacity (m)
$R_1 = 0.4572$	$h_1 = 0.03556$	$\mu_1 = 0.12$	$d_1 = 0.0381$
$R_2 = 0.2032$	$h_2 = 0.03048$	$\mu_2 = 0.085$	$d_2 = 0.03302$
$R_3 = 0.0508$	$h_3 = 0.02286$	$\mu_3 = 0.015$	$d_3 = 0.01397$
$R_4 = 0.0508$	$h_4 = 0.02286$	$\mu_4 = 0.015$	$d_4 = 0.01397$
$R_5 = 0.2032$	$h_5 = 0.03048$	$\mu_5 = 0.035$	$d_5 = 0.03302$
$R_6 = 0.4572$	$h_6 = 0.03556$	$\mu_6 = 0.11$	$d_6 = 0.0381$

the seismic intensity level and the friction isolators response, respectively. Generally, the following steps are implemented for both MSDA and IDA procedures: (a) create an efficient nonlinear finite element model for performing repeated nonlinear dynamic analyses, (b) select an appropriate group of natural or artificial accelerograms, (c) choose proper IM and EDP, and (d) select scaling factors in order to run the analyses and obtain the IM-EDP curves.

#### 4. Fragility Function Evaluation

Seismic fragility is associated to the probability of exceedance of a limit state for a given seismic intensity level. Typically, a fragility function is defined by a lognormal cumulative distribution function (CDF) [32]:

$$P(C|IM = x) = \Phi\left(\frac{\ln(x/\theta)}{\beta}\right), \quad (1)$$

where  $P(C|IM = x)$  is the probability that a ground motion with  $IM = x$  will lead to structural collapse,  $\Phi$  denotes the standard normal CDF,  $\theta$  is the median of the fragility function and  $\beta$  is the standard deviation of  $\ln\theta$ . Regarding

the selection of  $IM$ , the PGA is a valid choice for liquid storage tanks due to the impulsive load pattern [20, 33, 34].

In the current study, fragility curves related to SFPBs, TFPBs, and QFPBs displacements are calculated for different performance levels, namely, 50% probability of exceedance in 50 years (i.e., SLE), 10% probability of exceedance in 50 years (i.e., DBE), and 2% probability of exceedance in 50 years (i.e., MCE). In the present investigation, the methodology for fragility function fitting proposed by Baker [32] has been adopted, in which by performing repeated dynamic analyses for all ground motions and for each IM level a number of failures (i.e., in terms of isolators' displacement) is determined. The probability of  $z_j$  failures being observed out of  $n_j$  ground motions having  $IM = x_j$  is represented by the following binomial distribution [32]:

$$P(z_j \text{ collapses in } n_j \text{ ground motions}) = \binom{n_j}{z_j} p_j^{z_j} \cdot (1 - p_j)^{n_j - z_j}, \quad (2)$$

in which  $p_j$  is the probability that a ground motion with  $IM = x_j$  will cause failure of the structure.

When analysis data are obtained at multiple IM levels, the product of the binomial probabilities at each level provides the likelihood for the entire data set:

$$\text{likelihood} = \prod_{j=1}^m \binom{n_j}{z_j} p_j^{z_j} (1 - p_j)^{n_j - z_j}, \quad (3)$$

where  $m$  is the number of IM levels and  $\Pi$  is a product over all levels. Substituting Equation (1) for  $p_j$ , the fragility parameters are explicitly included in the likelihood function:

$$\text{likelihood} = \prod_{j=1}^m \binom{n_j}{z_j} \Phi \left( \frac{\ln(x_j/\theta)}{\beta} \right)^{z_j} \cdot \left( 1 - \Phi \left( \frac{\ln(x_j/\theta)}{\beta} \right) \right)^{n_j - z_j} \quad (4)$$

While the maximization of the likelihood function produces the estimates of the fragility function parameters as follows:

$$\{\hat{\theta}, \hat{\beta}\} = \arg_{\theta, \beta} \max \sum_{j=1}^m \left\{ \ln \binom{n_j}{z_j} + z_j \ln \Phi \left( \frac{\ln(x_j/\theta)}{\beta} \right) + (n_j - z_j) \ln \left( 1 - \Phi \left( \frac{\ln(x_j/\theta)}{\beta} \right) \right) \right\} \quad (5)$$

## 5. Base-Isolated Liquid Storage Tanks

**5.1. General Details.** The storage tank models presented by Haroun [35] (Tank B and T types) are used in this work. More specifically, Tank B (Figure 6(a)) is a squat cylindrical tank with height to radius ratio  $H/R = 0.67$ . The radius of the first tank is  $R = 18.29$  m, the height of liquid surface is  $H = 12.192$  m, the tank wall thickness is  $t = 0.0254$  m, and the total weight of the liquid content is  $W = 126273.45$  kN. The second model (Figure 6(b)) is a slender cylindrical tank with height to radius ratio  $H/R = 3$ . Tank T has radius  $R = 7.32$  m, height  $H = 21.96$  m, width  $t = 0.0254$  m, and the liquid weight is  $W = 36245.4$  kN. The fundamental periods of the two tank-liquid systems are  $T_{f-B} = 0.162$  sec and  $T_{f-T} = 0.188$  sec, for Tanks B and T, respectively.

**5.2. Surrogate Models.** Modeling of liquid storage tanks is not an easy task due to the hydrodynamic response of the tank-liquid system [13, 19, 23]. In general, detailed finite-element models are computationally demanding [36]. To reduce the computational load and model complexity, one common approach is to develop valid simplified models to effectively replace the complicated three-dimensional (3D) models [37]. Therefore, a simplified representation of the liquid storage tank is adopted herein, based on the so-called "Joystick model" of fixed-base tanks [23]. The developed Joystick model consists of a vertical beam element carrying the impulsive mass that is supported by fully rigid beam-spokes, which in turn are supported by the sliding bearings (Figure 6). The two examined models are validated by accurate matching of the impulsive fundamental period ( $T_i$ ) provided by Eurocode 8-Part 4 [38] recommendations for liquid storage tanks.

As aforementioned, the hydrodynamic response is mainly affected by the impulsive liquid component. The convective liquid mass is neglected since several studies [18, 39, 40] have proven that although the impulsive pressure is reduced due to seismic isolation, the convective pressure remains practically unchanged. Moreover, the effects of the

convective part of liquid content can be separately estimated [23]. In the developed surrogate model, the weight of the water is represented as lumped masses at the base beam-spokes of the tank (Figure 6). Therefore, the vertical load is directly applied to the friction isolation devices. The self-weight of the tank can be omitted as it is only 5% of the total tank mass [12, 16, 29, 34].

**5.3. Design of Isolation Bearings.** Generally, the design of structural isolation systems is an iterative process, since the bearing properties are influenced by the structural properties. Firstly, the maximum bearing displacement has to be evaluated, which is mostly affected by the target period of the isolated system, the weight of the superstructure, and the intensity level of the imposed seismic excitation.

In this study, the equivalent linear force (ELF) procedure according to Eurocode 8 (Soil A,  $\gamma_i = 1.4$ ,  $a_g = 0.36$  g) is applied for the preliminary design of tank isolation system [41]. The selected SFPB has friction coefficient  $\mu = 0.08$ , radius of curvature  $R = 1.88$  m, theoretical period of 2.75 sec, and displacement limit of 0.305 m. The TFPB properties are listed in Table 2 and the total displacement limit for MCE level is 0.762 m, which is the sum of all partial displacement limits. Finally, a QFPB with the properties is shown in Table 3, while the total displacement limit of 1.04 m (i.e., the sum of all displacements in Table 3) for MCE level is computed following the methodology developed by Lee and Constantinou [21]. The vertical load on the bearings is equal to 2.9 MN for the squat tank and 2.7 MN for the slender tank, respectively.

**5.4. Numerical Modeling and Earthquake Selection.** As previously mentioned, each Joystick tank model, which is supported either on SFPBs, TFPBs, or QFPBs, is simulated utilizing the finite element software SAP2000 [29]. This simplified tank model consists of a vertical beam element carrying the impulsive mass and is supported by fully rigid beam-spokes that represent the tank base. The properties of the vertical beam were determined using simple structural analysis calculations following the recommendations of Eurocode 8-Part 4 [38]. In order to test the isolators under strong excitations, the near-fault earthquake ground motion set produced within the FEMA/SAC Project [42] is used in this investigation ([www.nisee.berkeley.edu/elibrary/files/documents/data/strong\\_motion/sacsteel/motions/nearfault.htm](http://www.nisee.berkeley.edu/elibrary/files/documents/data/strong_motion/sacsteel/motions/nearfault.htm)). Time-histories derived from natural and simulated records are included in this suite of accelerograms. The use of a sufficient number of properly selected excitations (i.e., exhibiting certain characteristics to avoid using an excessive number of records and maintaining an optimal balance among computational cost and accuracy) in conjunction with a huge number of MSDA/IDA analyses is imperative in order to achieve reliable fragility analysis results. The specific suite of acceleration time-histories consists such a case, since it is a well-established set of impulsive ground motions, with epicentral distances less than 10 km and very high PGA recorded values ranging from 0.45 g to 1.07 g, which is usually used in fragility analysis studies [43].

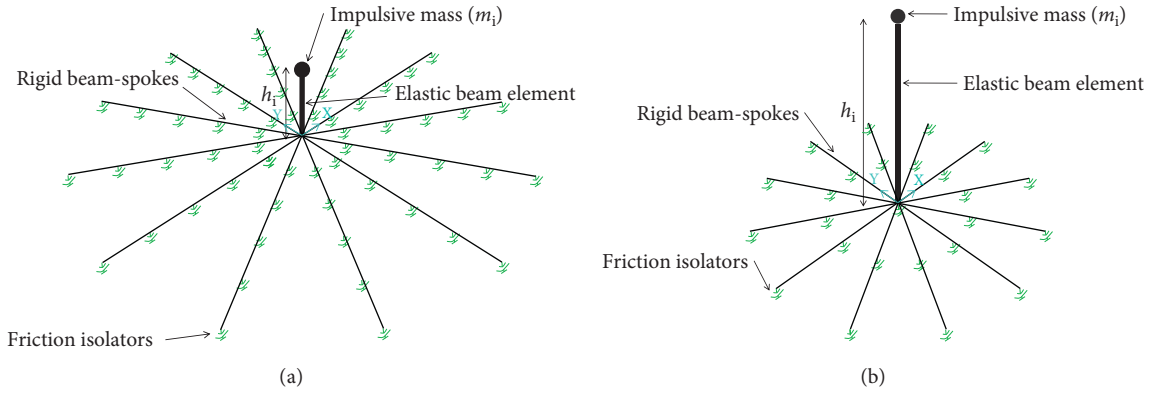


FIGURE 6: Joystick models for a squat (a) and a slender tank (b).

TABLE 2: Design parameters for the TFPB isolated squat tank.

Friction coefficient	Radii of curvature (m)	Height (m)	Effective radii (m)	Displacement limit (m)
$\mu_{1,\text{slow}} = \mu_{4,\text{slow}} = 0.09$	$R_1 = R_4 = 2.235$	$h_1 = h_4 = 0.102$	$R_{1,\text{eff}} = R_{4,\text{eff}} = 2.133$	$d_1^* = d_4^* = 0.34$
$\mu_{2,\text{slow}} = \mu_{3,\text{slow}} = 0.071$	$R_2 = R_3 = 0.406$	$h_2 = h_3 = 0.076$	$R_{2,\text{eff}} = R_{3,\text{eff}} = 0.33$	$d_2^* = d_3^* = 0.041$

TABLE 3: Design parameters for the QFPB isolated squat tank.

Sliding surface	Effective radius of curvature (m)	Coefficient of friction	Displacement limit (m)
Surface 1	$R_{1,\text{eff}} = 5.84$	$\mu_1 = 0.1$	$d_1^* = 0.344$
Surface 2	$R_{2,\text{eff}} = 1.12$	$\mu_2 = 0.06$	$d_2^* = 0.134$
Surface 3	$R_{3,\text{eff}} = 0.508$	$\mu_3 = 0.01$	$d_3^* = 0.047$
Surface 4	$R_{4,\text{eff}} = 0.508$	$\mu_4 = 0.01$	$d_4^* = 0.047$
Surface 5	$R_{5,\text{eff}} = 1.12$	$\mu_5 = 0.03$	$d_5^* = 0.134$
Surface 6	$R_{6,\text{eff}} = 3.76$	$\mu_6 = 0.07$	$d_6^* = 0.337$

More specifically, for each of the three performance levels, the selected twenty earthquake records are suitably scaled and then they are imposed at the isolated Joystick models until displacement limits are reached. Regarding the numerical analyses, the fast nonlinear analysis (FNA) is ideal for structural systems in which the nonlinear response is concentrated at the base isolation system, while the superstructure remains elastic [29]. FNA is a computationally efficient approach and is often preferred than direct-integration schemes. The damping for the structural system is taken equal to 5% and for the impulsive liquid component equal to 2% [44, 45].

## 6. Numerical Results

**6.1. Fragility Curves.** As aforementioned, maximum displacement of the different TFPBs and QFPBs sliding schemes is associated to three hazard levels. Accordingly, using the data listed in Tables 2 and 3 and the isolator configurations previously described, the values presented in Table 4 were computed. For instance, for the TFPB and DBE level, the resulting displacement is derived by adding  $d_2^*$  to  $d_6^*$ , which gives a displacement limit equal to 0.699 m. Figure 7 illustrates the adopted performance-based approach for the three examined isolator schemes. More specifically for the examined three hazard levels: dotted blue

TABLE 4: PBD levels of friction pendulum isolators.

Isolator type	SLE	DBE	MCE
SFPB	-	-	0.305 m
TFPB	0.084 m	0.423 m	0.762 m
QFPB	0.095 m	0.699 m	1.04 m

curves represent SLE, continuous red curves denote DBE, and dashed black curves correspond to MCE. A similar correlation of isolators' performance with respect to the three hazard levels has been adopted by Moeindarbari et al. [17] for TFPBs.

Firstly, SLE level with 50% in 50 years probability of exceedance (resulting to displacement limits equal to 0.084 m for TFPBs and 0.095 m for QFPBs) is represented by the inner pendulum mechanism of the bearings; secondly, DBE level with 10% in 50 years probability of exceedance, which results to displacement limits of 0.423 m for TFPBs and 0.699 m for QFPBs; and lastly, MCE level with 2% in 50 years probability of exceedance of the maximum allowable displacement, which are equal to 0.762 m for TFPBs and 1.04 m for QFPBs. Additionally, the simple SFPB scheme is compared with the two multistage isolators, which is designed only for MCE level (with corresponding displacement limit of 0.305 m) with 2% in 50 years probability of exceedance [8].

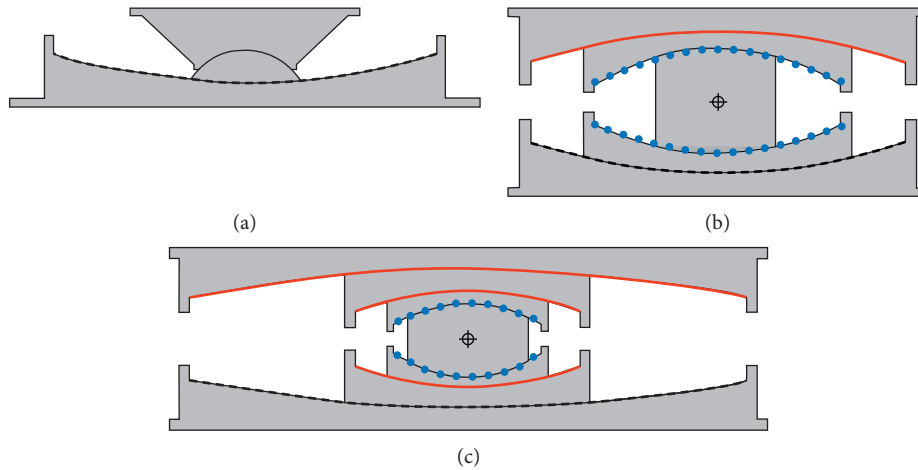


FIGURE 7: PBD levels in terms of isolator displacements for (a) SFPB, (b) TFPB, and (c) QFPB isolation schemes.

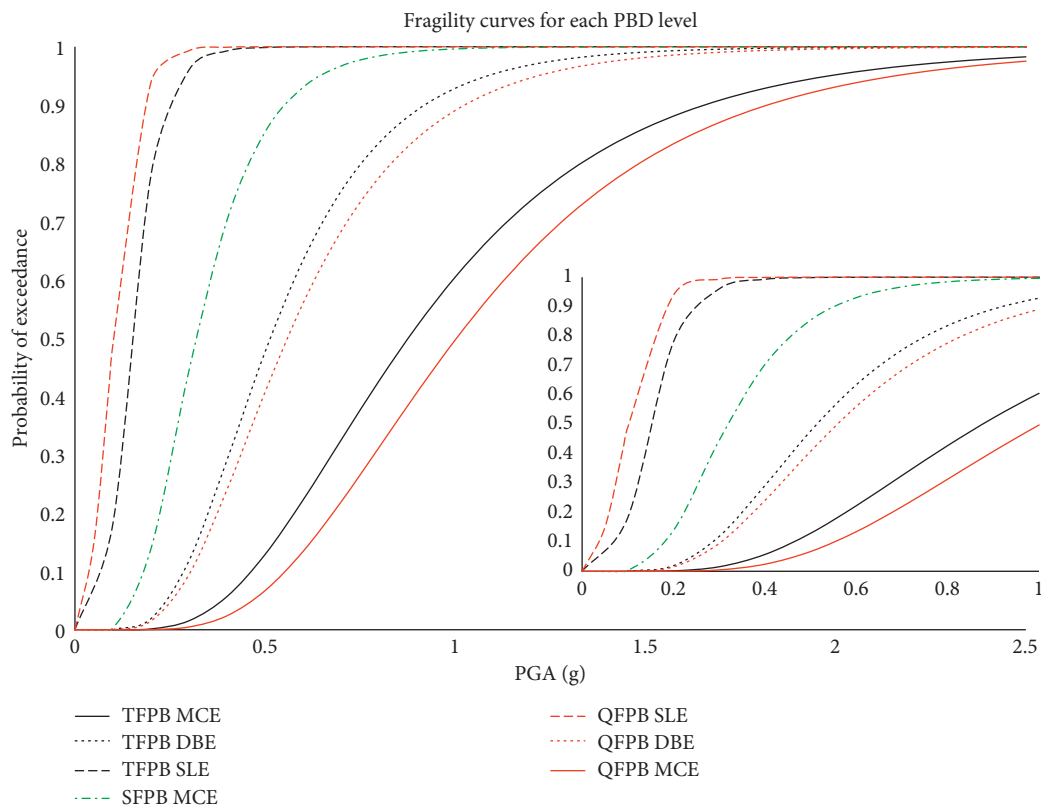


FIGURE 8: PBD fragility curves for SFPB, TFPB, and QFPB isolation schemes.

Accordingly, the probability of collapse considering the isolators' displacements for TFPBs and QFPBs different sliding mechanisms (depending on the hazard level) and SFPBs, is displayed in the fragility curves presented in Figure 8. Extreme PGA values are used to demonstrate the high capabilities of modern multistage isolators, while for fixed-base tanks the maximum PGA is much less (i.e., usually up to 1 g) [20, 34]. The embedded plot in Figure 8 shows the performance of all isolators within the range of more realistic expected PGA values, where the differences among the "truncated" fragility curves, especially for the

lower PGA levels is more evident. It can be seen that for the case of the minor earthquake hazard scenario of SLE (where sliding occurs at the inner sliding surfaces), TFPBs presents better results than QFPBs. This is attributed to the values of friction coefficients, since TFPBs have higher values ( $\mu_2 = 0.06$ ,  $\mu_3 = 0.071$ ) compared to QFPB ( $\mu_3 = \mu_4 = 0.01$ ). Thus, it is reasonable that sliding surfaces with lower values of friction coefficients will reach the displacement limit earlier than corresponding surfaces with higher values. On the other hand, for the more severe seismic scenarios of DBE and, especially, in MCE, it is evident that the QFPBs

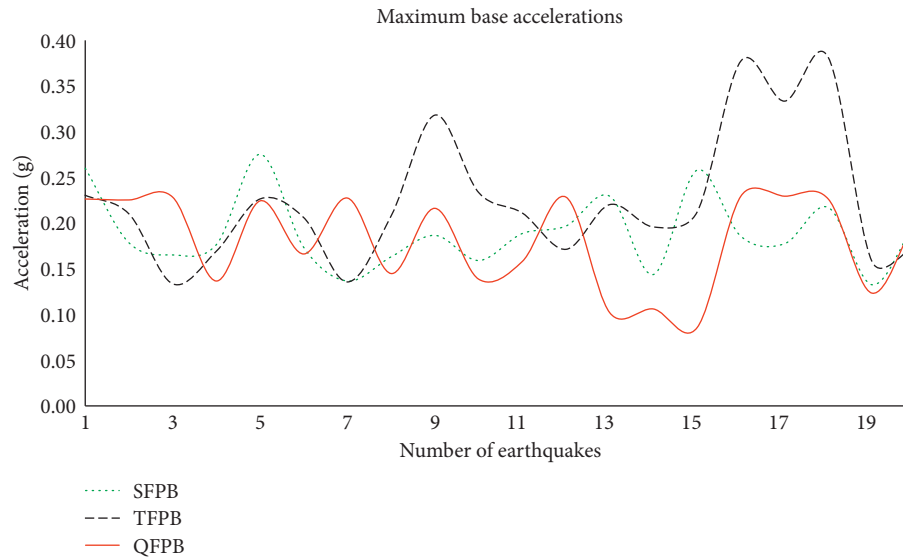


FIGURE 9: Base accelerations of storage tanks equipped with SFPB, TFPB, and QFPB isolators.

present significantly better results with respect to the obtained fragility estimates.

Hence, both TFPBs and QFPBs can withstand high displacement amplitudes, achieving thus lower failure probabilities even at higher seismic levels. It can be noticed that the multistage bearings of TFPBs and especially QFPBs play an important role, since they assist liquid storage tanks to maintain their structural integrity and functioning. It is also evident that these devices provide much better protection to the superstructure under severe seismic excitations compared to simple SFPBs.

**6.2. Comparison of Tank Accelerations.** When a fixed-base liquid storage tank is considered, then its probability of failure presents high values even for medium intensity levels (as expressed in terms of PGA values), which is not the case for base-isolated tanks [20, 34]. Base-isolation reduces the acceleration levels transmitted to the superstructure, and it can be assumed that due to isolation the tank behaves linearly even for quite high seismic intensity levels; thus, damages are avoided in the superstructure for the usually expected range of PGAs. Consequently, the emphasis related to failure of the whole system is given in the present investigation on the isolator displacements; thus, the probability of failure actually refers to the exceedance of the allowable isolators' displacement limits for various performance levels.

Nonetheless, when the imposed PGA reaches extreme values as examined herein, the transmitted acceleration, i. e., the acceleration that is measured at tank's base above the isolators, can also reach significant values, depending on the special characteristics of the excitation. This is indicatively illustrated in Figure 9, which depicts the maximum accelerations values (i.e., maximum value of the reduced acceleration transmitted to the superstructure) at the tank base level above the isolators for each of the twenty near-fault records. As it can be easily noticed, the storage tank equipped with TFPBs presents the highest values of

base accelerations, especially for three records (9, 16, and 18). The superstructure isolated with SFPBs presents lower values, but as shown in the fragility analysis (Figure 8), these isolators exhibit higher collapse probabilities. In most cases, the base accelerations of storage tanks isolated with QFPBs are lower compared to those obtained by TFPBs and close to the ones corresponding to SFPBs. Therefore, it is derived that overall QFPBs present better results compared to TFPBs and SFPBs, since it is an effective isolator configuration that combines lower probabilities of collapse in terms of sliding displacements and low values of base accelerations transmitted to the superstructure.

**6.3. Influence of Tank Slenderness Ratio.** The plots in Figure 10 illustrate the influence of tank slenderness ratio ( $H/R$ ) in the fragility curves. It is reminded that three bearing types were examined, the single-stage SFPBs and the multistage TFPBs and QFPBs. As it can be seen in this plot, due to the presence of the isolators, the fragility curves are not influenced by slenderness ratio, since there is not any significant difference among squat and slender tanks. In contrast to this finding, unanchored slender tanks are more susceptible to uplifting phenomena than the corresponding squat tanks [46]. Regarding TFPBs, for DBE and MCE levels, squat tanks are slightly less vulnerable compared to slender tanks at low to medium PGA values. For increased seismic intensity and higher probability of collapse, the fragility curves are almost identical. For SLE level, there is not any observable difference. In the case of SFPBs and for MCE scenario, squat tanks are slightly less vulnerable than slender tanks for PGA values between 0.5 g and 1.0 g. For the case of QFPBs, SLE and DBE levels do not present any difference, while for the MCE level, the slender tanks are marginally less vulnerable compared to squat tanks at low PGA values.

**6.4. Influence of  $\lambda_{max}$  Factor.** A fragility analysis considering performance deterioration due to aging, contamination, etc.

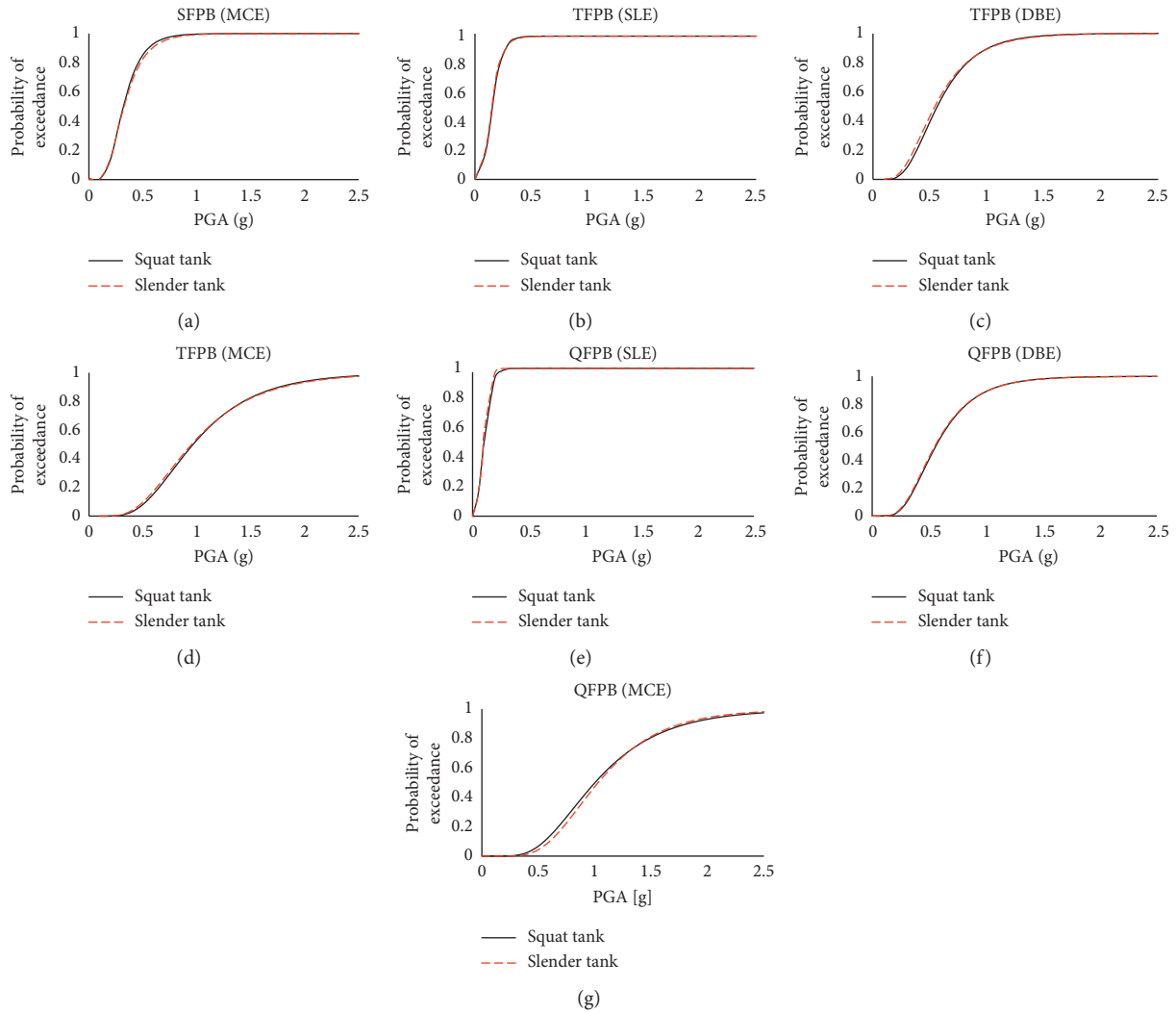


FIGURE 10: PBD fragility curves of squat and slender tanks using SFPBs, TFPBs, and QFPBs isolators.

of isolators is performed for the squat tank, by incorporating  $\lambda_{max}$  factor in the design of TFPBs friction isolators. This parameter is directly applied to the nominal value of the coefficient of friction to forecast aging and deterioration phenomena that will affect the performance of friction isolation bearings [47]. According to the recommendations of Constantinou et al. [27], the value of 1.1 is selected for aging and 1.05 for contamination, and  $\lambda_{max}$  factor is calculated as the product of these two values.

As it can be noticed from Figure 11, the incorporation of  $\lambda_{max}$  in the design of friction isolators for the squat tank affects the results for the more severe hazard levels. Especially for the higher seismicity intensity levels (DBE), the TFPBs designed with the factor  $\lambda_{max}$  present better performance, while for the low seismicity intensity level (SLE), there are only marginal differences.

## 7. Conclusions

In this paper, the seismic vulnerability of liquid storage tanks isolated with three types of sliding bearings, namely,

SFPBs and the multistage TFPBs and QFPBs were investigated. More specifically, the displacement capacity of SFPBs and of the different pendulum mechanisms of TFPBs and QFPBs were associated to three PBD levels (SLE, DBE, and MCE) by performing repeated dynamic nonlinear analyses. A high displacement capacity is a very crucial parameter for the isolators used to protect such critical infrastructures, especially against severe near-fault earthquakes. Additionally, the resulting base accelerations transmitted at the storage tanks isolated with the aforementioned devices were compared. In order to achieve optimal balance between computational efficiency and accuracy, simplified models were developed for the realistic representation of the hydrodynamic response of liquid storage tanks.

The following conclusions can be derived from the present investigation:

- (a) Friction isolation bearings with multistage and adaptive behavior (TFPBs and mostly QFPBs) present superior seismic performance compared to

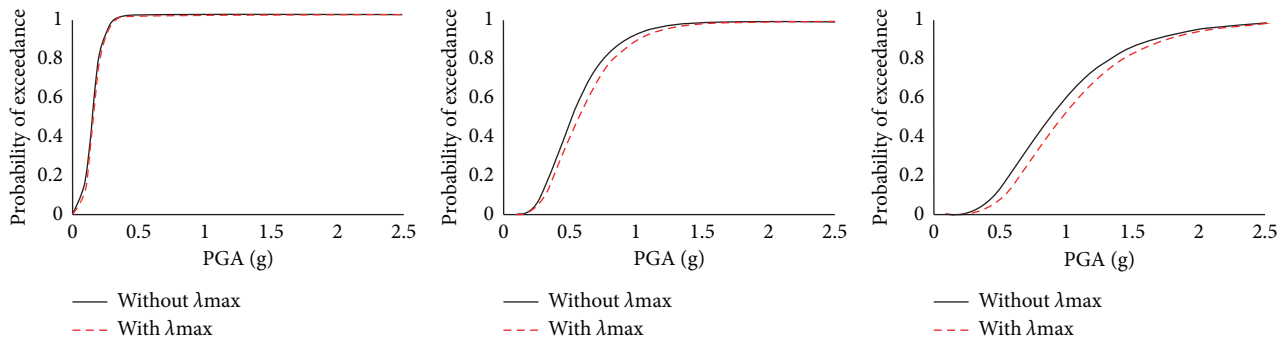


FIGURE 11: Comparison of  $\lambda_{max}$  factor influence on TFPBs friction bearings' performance for the squat tank. (a) SLE. (b) DBE. (c) MCE.

single bearings (SFPBs). Thus, they have the ability of accommodating much larger displacements (i.e., higher PGA demand levels).

- (b) In general, as expected, the QFPB is the superior isolator device due to its ability to withstand higher displacements at different PBD levels.
- (c) Regarding the base accelerations of storage tanks isolated with different friction bearings, the best results are derived from the superstructure equipped with QFPBs. A QFPB is an efficient base-isolation scheme that can combine the accommodation of large displacement amplitudes of near-fault excitations with low base acceleration values. Thus, it can protect the structural integrity of such critical infrastructure even at high seismic demand levels.
- (d) The slenderness ratio of the cylindrical base-isolated storage tanks via SFPBs, TFPBs, and QFPBs do not significantly affect the fragility estimations when maximum isolator displacements are considered.
- (e) The future performance deterioration in the design of sliding bearings, represented by the factor  $\lambda_{max}$ , can influence the fragility analysis results. More specifically, when this factor is incorporated in the analysis, the base-isolated liquid storage tanks present a slightly less vulnerable performance for the higher seismic demand levels.

## Abbreviations

3D:	Three-dimensional
CDF:	Cumulative Distribution Function
CSB:	Concave Sliding Bearing
DBE:	Design Basis Earthquake
DI:	Damage Index
DVFPS:	Double Variable Frequency Pendulum System
EDP:	Engineering Demand Parameter
ELF:	Equivalent Linear Force
EPS:	Earthquake Protection Systems
FNA:	Fast Nonlinear Analysis
FP:	Friction Pendulum
HDRB:	High Damping Rubber Bearing
IDA:	Incremental Dynamic Analysis
IM:	Intensity Measure
LNG:	Liquefied Natural Gas

MCE:	Maximum Credible Earthquake
MFPS:	Multiple Friction Pendulum System
MSDA:	Multistriple Dynamic Analysis
NATECH:	Natural and Technological disasters
PBD:	Performance-Based Design
PGA:	Peak Ground Acceleration
QFPB:	Quintuple Friction Pendulum System
SFPB:	Single Friction Pendulum Bearing
SLE:	Service Level Earthquake
TFPB:	Triple Friction Pendulum Bearing
VCFPS:	Variable Curvature Friction Pendulum System
VFPS:	Variable Friction Pendulum System.

## Data Availability

The data supporting the results reported in the article are quite huge. Nevertheless, interested readers may access these data of the study by directly asking authors to provide them.

## Disclosure

An earlier version of this work was presented as a poster at the Second Young Researchers Workshop of Hellenic Society of Earthquake Engineering, 3/11/2017, Athens, Greece.

## Conflicts of Interest

The authors declare that there are no conflicts of interest regarding the publication of this paper.

## Acknowledgments

This research has been generously supported by Bakopouleio Foundation, Greece, via a Ph.D. scholarship for the first author, which is gratefully acknowledged. The authors would also like to thank Mr. Donghun Lee for providing useful insight regarding the QFPB analytical model.

## References

- [1] G. Housner, "The dynamic behavior of water tanks," *Bulleting of the Seismological Society of America*, vol. 53, no. 2, pp. 381–387, 1963.
- [2] T. Larkin, "Seismic response of liquid storage tanks incorporating soil structure interaction," *ASCE Journal of*

- Geotechnical and Geoenvironmental Engineering*, vol. 134, no. 12, pp. 1804–1814, 2008.
- [3] P. K. Malhotra, “Seismic response of soil-supported unanchored-liquid storage tanks,” *ASCE Journal of Structural Engineering*, vol. 123, no. 4, pp. 440–450, 1997.
  - [4] A. S. Veletsos, Y. Tang, and H. T. Tang, “Dynamic response of flexibly supported liquid-storage tanks,” *ASCE Journal of Structural Engineering*, vol. 118, no. 1, pp. 264–289, 1992.
  - [5] K. Bakalis, D. Vamvatsikos, and M. Fragiadakis, “Seismic risk assessment of liquid storage tanks via a nonlinear surrogate model,” *Earthquake Engineering and Structural Dynamics*, vol. 46, no. 15, pp. 2851–2868, 2017.
  - [6] T. Kelly, *Base Isolation of Structures-Design Guidelines*, Holmes Consulting Group Ltd., Auckland, New Zealand, 2001.
  - [7] M. R. Shekari, N. Khaji, and M. T. Ahmadi, “On the seismic behavior of cylindrical base-isolated liquid storage tanks excited by long-period ground motions,” *Soil Dynamics and Earthquake Engineering*, vol. 30, no. 10, pp. 968–980, 2010.
  - [8] EPS, *Earthquake Protection Systems*, 2011, <http://www.earthquakeprotection.com>.
  - [9] V. R. Panchal and D. P. Soni, “Seismic behavior of isolated fluid storage tanks: a-state-of-the-art review,” *KSCSE Journal of Civil Engineering*, vol. 18, no. 4, pp. 1097–1104, 2014.
  - [10] Y. P. Wang, M. C. Teng, and K. W. Chung, “Seismic isolation of rigid cylindrical tanks using friction pendulum bearings,” *Earthquake Engineering and Structural Dynamics*, vol. 30, no. 7, pp. 1083–1099, 2001.
  - [11] M. B. Jadhav and R. S. Jangid, “Response of base-isolated liquid storage tanks,” *Shock and Vibration*, vol. 11, no. 1, pp. 33–45, 2004.
  - [12] V. R. Panchal and R. S. Jangid, “Variable friction pendulum system for seismic isolation of liquid storage tanks,” *Nuclear Engineering and Design*, vol. 238, no. 6, pp. 1304–1315, 2008.
  - [13] E. Abali and E. Uckan, “Parametric analysis of liquid storage tanks base isolated by curved surface sliding bearings,” *Soil Dynamics and Earthquake Engineering*, vol. 30, pp. 21–31, 2010.
  - [14] D. P. Soni, P. P. Mistry, R. S. Jangid, and V. R. Panchal, “Seismic response of the double variable frequency pendulum isolator,” *Structural Control and Health Monitoring*, vol. 18, no. 4, pp. 450–470, 2011.
  - [15] A. A. Seleemah and M. El-Sharkawy, “Seismic analysis and modeling of isolated elevated liquid storage tanks,” *Earthquakes and Structures*, vol. 2, no. 4, pp. 397–412, 2011.
  - [16] V. R. Panchal and R. S. Jangid, “Behaviour of liquid storage tanks with VCFPS under near-fault ground motions,” *Structure and Infrastructure Engineering*, vol. 8, no. 1, pp. 71–88, 2012.
  - [17] H. Moeindarbari, M. Malekzadeh, and T. Taghikhany, “Probabilistic analysis of seismically isolated elevated liquid storage tank using multi-phase friction bearing,” *Earthquakes and Structures*, vol. 6, no. 1, pp. 111–125, 2014.
  - [18] F. Paolacci, “On the effectiveness of two isolation systems for the seismic protection of elevated tanks,” *Journal of Pressure Vessels Technology*, vol. 137, no. 3, article 031801, 2015.
  - [19] S. Bagheri and M. Farajian, “The effects of input earthquake characteristics on the nonlinear dynamic behavior of FPS isolated liquid storage tanks,” *Journal of Vibration and Control*, vol. 24, no. 7, pp. 1264–1282, 2016.
  - [20] H. N. Phan, F. Paolacci, D. Corritore, B. Akbas, E. Uckan, and J. J. Shen, “Seismic vulnerability mitigation of liquefied gas tanks using concave sliding bearings,” *Bulletin of Earthquake Engineering*, vol. 14, no. 11, pp. 3283–3299, 2016.
  - [21] D. Lee and M. C. Constantinou, “Quintuple friction pendulum isolator: behavior, modeling and validation,” *Earthquake Spectra*, vol. 32, no. 3, pp. 1607–1626, 2016.
  - [22] A. Tsipianitis and Y. Tsompanakis, “Seismic vulnerability assessment of base-isolated liquid fuels tanks,” in *Proceedings of 12th International Conference on Structural Safety and Reliability (ICOSSAR)*, Vienna, Austria, August 2017.
  - [23] K. Bakalis, M. Fragiadakis, and D. Vamvatsikos, “Surrogate modeling for the seismic performance assessment of liquid storage tanks,” *Journal of Structural Engineering*, vol. 143, no. 4, article 04016199, 2016.
  - [24] V. A. Zayas, S. S. Low, and S. A. Mahin, “The FPS earthquake resisting system-experimental report,” Report No. UCB/EERC-8701, Earthquake Engineering Research Center, College of Engineering, University of California, Berkeley, CA, USA, 1987.
  - [25] D. M. Fenz and M. C. Constantinou, “Spherical sliding isolation bearings with adaptive behavior: theory,” *Earthquake Engineering and Structural Dynamics*, vol. 37, no. 2, pp. 163–183, 2008.
  - [26] T. A. Morgan, *The use of innovative base isolation systems to achieve complex seismic performance objectives*, Ph.D. Dissertation, Department of Civil and Environmental Engineering, University of California, Berkeley, CA, USA, 2007.
  - [27] M. C. Constantinou, I. Kalpakidis, A. Filiatrault, and R. A. E. Lay, “LRFD-based analysis and design procedures for bridge bearings and seismic isolators,” Report No. MCEER-11-0004, Multidisciplinary Center for Earthquake Engineering Research, University of Buffalo, New York, NY, USA, 2011.
  - [28] N. D. Dao, K. L. Ryan, E. Sato, and T. Sasaki, “Predicting the displacement of triple pendulum bearing in a full-scale shaking experiment using a three-dimensional element,” *Earthquake Engineering and Structural Dynamics*, vol. 42, no. 11, pp. 1677–1695, 2013.
  - [29] CSI, *SAP 2000 Version 18, Integrated Software for Structural Analysis and Design, Analysis Reference Manual*, Computer & Structures Inc., Berkeley, CA, USA, 2016.
  - [30] A. Kasalanati and M. C. Constantinou, “Experimental study of bridge elastomeric and other isolation and energy dissipation systems with emphasis on uplift prevention and high velocity near source seismic excitation,” Technical Report, MCEER-99-0004, Multidisciplinary Center for Earthquake Engineering Research, University at Buffalo, Buffalo, NY, USA, 1999.
  - [31] D. Vamvatsikos and C. A. Cornell, “Incremental dynamic analysis,” *Earthquake Engineering and Structural Dynamics*, vol. 31, no. 3, pp. 491–514, 2002.
  - [32] J. W. Baker, “Efficient analytical fragility function fitting using dynamic structural analysis,” *Earthquake Spectra*, vol. 31, no. 1, pp. 579–599, 2015.
  - [33] K. Bakalis, D. Vamvatsikos, and M. Fragiadakis, “Seismic fragility assessment of steel liquid storage tanks,” in *Proceedings of the ASME 2015 Pressure Vessels and Piping Conference*, Boston, Massachusetts, USA, 2015.
  - [34] S. K. Saha, V. A. Matsagar, and A. K. Jain, “Seismic fragility of base-isolated water storage tanks under non-stationary earthquakes,” *Bulletin of Earthquake Engineering*, vol. 14, no. 4, pp. 1153–1175, 2016.
  - [35] M. A. Haroun, “Vibration studies and tests of liquid storage tanks,” *Earthquake Engineering and Structural Dynamics*, vol. 11, no. 2, pp. 179–206, 1983.
  - [36] S. Kilic and Z. Ozdemir, “Simulation of sloshing effects in cylindrical containers under seismic loading,” in *Proceedings*

- of the 6th LS-DYNA Anwenderforum DYNAmore, Dresden, Germany, 2007.
- [37] A. Di Carluccio and G. Fabbrocino, "Some remarks on the seismic demand estimation in the context of vulnerability assessment of large steel storage tank facilities," *ISRN Civil Engineering*, vol. 2012, Article ID 271414, 12 pages, 2012.
  - [38] CEN, *Eurocode 8: Design of structures for earthquake resistance-Part 4: Silos, Tanks and Pipelines*, European Committee for Standardization, Brussels, Belgium, 2006.
  - [39] I. P. Christovasilis and A. S. Whittaker, "Seismic analysis of conventional and isolated LNG tanks using mechanical analogs," *Earthquake Spectra*, vol. 24, no. 3, pp. 599–616, 2008.
  - [40] R. A. Ibrahim, "Recent advances in nonlinear passive vibration isolators," *Journal of Sound and Vibration*, vol. 314, no. 3–5, pp. 371–452, 2008.
  - [41] Y. Bouassida, E. Bouchon, P. Crespo et al., *Bridge Design to Eurocodes-Worked Examples*, JRC Scientific and Technical Reports, EUR 25193 EN-2012, 2012.
  - [42] P. Sommerville, N. Smith, S. Punyamurthula, and J. Sun, "Development of ground motion time histories for phase 2 of the FEMA/SAC Steel Project," NISEE Report: SAC/BD-97-04, SAC Joint Venture, Sacramento, CA, USA, 1997.
  - [43] A. H. M. M. Billah and M. S. Alam, "Seismic fragility assessment of concrete bridge pier reinforced with superelastic shape memory alloy," *Earthquake Spectra*, vol. 31, no. 3, pp. 1515–1541, 2015.
  - [44] M. A. Haroun and G. W. Housner, "Seismic design of liquid storage tanks," *Journal of the Technical Councils of ASCE*, vol. 107, pp. 191–207, 1981.
  - [45] P. K. Malhotra, T. Wenk, and M. Wieland, "Simple procedure for seismic analysis of liquid-storage tanks," *Structural Engineering International*, vol. 10, no. 3, pp. 197–201, 2000.
  - [46] P. K. Malhotra and A. S. Veletsos, "Uplifting response of unanchored liquid-storage tanks," *ASCE Journal of Structural Engineering*, vol. 120, no. 12, pp. 3525–3547, 1994.
  - [47] M. C. Constantinou, A. S. Whittaker, Y. Kalpakidis, D. M. Fenz, and G. P. Warn, *Performance of seismic isolation hardware under service and seismic loading*, Report No. MCEER-07-0012, Multidisciplinary Center for Earthquake Engineering Research, University of Buffalo, New York, NY, USA, 2007.

## Research Article

# Tests of Inclined Concrete-Filled Steel Tubular Stub Columns under Vertical Cyclic Loading

Chayanon Hansapinyo <sup>1</sup>, Chinnapat Buachart,<sup>1</sup> and Preeda Chaimahawan<sup>2</sup>

<sup>1</sup>Excellence Center in Infrastructure Technology and Transportation Engineering (ExCITE), Chiang Mai University, Chiang Mai, Thailand

<sup>2</sup>School of Engineering, University of Phayao, Phayao, Thailand

Correspondence should be addressed to Chayanon Hansapinyo; [chayanon@eng.cmu.ac.th](mailto:chayanon@eng.cmu.ac.th)

Received 30 June 2018; Accepted 26 July 2018; Published 2 September 2018

Academic Editor: Tadeh Zirakian

Copyright © 2018 Chayanon Hansapinyo et al. This is an open access article distributed under the Creative Commons Attribution License, which permits unrestricted use, distribution, and reproduction in any medium, provided the original work is properly cited.

This paper presents an experimental study on the cyclic behavior of fifteen concrete-filled steel tubular columns subjected to vertical cyclic loading. All test samples' cross-sectional area is  $75 \times 75 \text{ mm}^2$  square, and they are 500 mm long. The main variables in the test are the thickness of the steel tube (1.8 and 3.0 mm with the width-to-thickness ratios ( $b/t$ ) of 41.7 and 25), the strength of the infilled concrete (no-fill, 23 MPa, and 42 MPa), and the inclined angle (0, 4, and 9 degrees). The results show that all samples failed due to local buckling in compression followed by tearing of the steel tube in tension. The inclination angles of 4 and 9 degrees decreased the vertical compressive capacity of the 1.8 mm vertical hollowed steel column by 34 and 39 percent, respectively. However, the infilled concrete and thicker tube (3.0 mm) could substantially reduce the adverse effect of the inclination angle. The compressive ductility of the hollowed column with the thinner tube was significantly enhanced by the infilled concrete as well.

## 1. Introduction

A number of buildings and structures have been constructed not only to achieve the functional purpose but also to acquire an aesthetic purpose. Hence, for an architectural reason, buildings with irregularity have been frequently designed such as dome, arch, slender, and inclined columns. For the construction of such structures, steel becomes popular as the high ratio in strength-to-weight characteristic minimizes the negative effect of the mass in the irregular buildings. In addition, its reliable material properties, easy construction procedure, and time efficiency have made the steel more widely adopted. In general, steel performs well under tensile force and gives a ductile manner which is desirable for the seismic resistance design. However, it performs quite poor under compression load with the increase of slenderness. Especially for thin-wall steel member, the local buckling is possibly formed and eventually failed before it reaches the yield point. This undesirable mechanism causes the strength reduction in steel structures.

To enhance the compressive loading capacity, sectional stiffeners with additional lips are included for the thin-wall

steel open sections [1]. For the hollow section, filling of the concrete inside is the most popular solution. It is well recognized that the concrete-filled steel tube column (hereinafter, CFST column) provides an outstanding behavior not only loading capacity but also an admirable durability. The steel hollow section performs as casting form and reinforcement. Furthermore, the CFST column also helps reduce construction time due to its construction simplicity. With the benefits of the CFST columns, using of the columns becomes widely adopted for multistorey building construction [2] and bridge piers [3]. In addition, the CFST columns also offer the advantage of preventing progressive collapse of buildings under blast loading [4]. However, there are some complications in the calculation of its capacity. Estimation of loading capacity of the CFST column is not just a direct superposition of the individual capacity of the infilled concrete and the hollow steel. The combination of the materials results to confinement of the infilled concrete and buckling prevention of the thin-wall steel. Hence, many previous researches focused on determination of parameters affecting the interaction. Schneider [5] conducted an experimental and analytical

study on the behavior of short, concrete-filled steel tube columns concentrically loaded in compression to failure. The effect of thickness, length, and section dimension of the CFST column on the concrete confinement, bearing capacity, and ductility was addressed. With the advancement in materials, the effect of high material strength was investigated by Liu et al. [6] and Zhou et al. [7]. Using of carbon fiber reinforced polymer (CFRP) to confine the CFST columns was investigated by Guo and Zhang [8]. The study indicated the increase of confinement using the outer CFRP especially for the square column. The effect of heat on the CFRP-confined CFST column was investigated by Chen et al. [9].

For loading capacity prediction and code comparisons, Han et al. [10] proposed a mechanic model based on a series of CFST column tests considering the composite action. The predicted load-deflection relationship conformed with the test results. A nonlinear finite element numerical model was adopted by Abed et al. [11] to predict compressive behavior of CFST columns. The study indicated the effect of diameter-to-thickness ratio ( $D/t$ ) as the main variable governing the compressive behavior. The underestimation of the axial capacity calculated by design codes, for example, AISC, ACI318, AS, and EC4, reduces as the  $D/t$  ratio increases. Liu et al. [6] found that unequal widths of the two sides of concrete-filled rectangular hollow section led to poor performance in bearing capacity and ductility. Hence, square section was suitable for the CFST column. Regarding the comparison of loading capacity with design codes, EC4 gave a close prediction with 6% difference. For other codes, AISC and ACI codes underestimated the ultimate load by 16% and 14%, respectively.

Most of the studies focused on stub columns. Buckling of slender CFST columns was investigated by Ruoquan [12], Vrclj and Uy [13], and Goode et al. [14]. The study indicated the accuracy of the bearing capacity using methods presented by EC4. The benefit of using the CFST columns in seismic is also appreciated. Under seismic loading, the CFST performed very well as confirmed by cyclic load tests and analyses conducted by Hansapinyo [15], Abdalla et al. [16], Mao and Xiao [17], and Buachart et al. [18]. Due to the buckling restraint, ductility and energy dissipation capacity are increased.

The more complicated behavior can be seen when the CFST is subjected to combined axial and bending loading or when the loading is not aligned with the member axis. These situations can be easily found for an irregular structural arrangement in a building. Figure 1 shows schematic view of inclined CFST column application in buildings. Opened view, long span, and unique style building can be achieved. However, only a few researches discussed about the loading capacity of the inclined CFST column. Han et al. [19] experimentally investigated the influence of the angle of inclination and tapered CFST columns under compressive loading. It was found that the increase of the inclined angle tended to reduce the bearing capacity of the column. Failure patterns of hollow steel section were both inward and outward buckling. In the CFST columns, only outward buckling could be observed as a result of the constraining effect provided by the infilled concrete.

Although many researches have been conducted in the field of CFST columns, there have been only a few studies on the behavior of inclined CFST columns under cyclic loading. Therefore, this study was aimed to analyse the behavior of inclined CFST columns when subjected to cyclic loading. Fifteen CFST columns were tested under vertical cyclic load until they reach the state of failure. The effect of inclination angle, concrete strength, and wall thickness on the loading capacity, ductility, and energy dissipation is discussed.

## 2. Experimental Works

**2.1. Samples and Experimental Setup.** A total of 15 samples were experimentally examined in this study. For all samples, the cross-sectional depth ( $b$ ) is  $75 \times 75 \text{ mm}^2$  and the length ( $l$ ) is 500 mm. The length-to-depth ratio ( $l/b$ ) is 6.67, enabling the prevention of overall column buckling. The variables in this test are the infilled concrete strength, thickness of the steel tube, and the inclination angle, as shown in Table 1. The sample nomenclature is defined to identify three investigated parameters. The initial letter "T" stands for the thickness of the steel tube. The second letter "C" stands for the designed cylindrical compressive strength of the infilled concrete, and the last letter "A" stands for the inclination angle of the tested samples. For example, the sample with label of T1.8C20A4 indicates the sample with the thickness of steel tube of 1.8 mm, filled with designed 20 MPa concrete, and the inclination angle is 4 degrees. It is noted that the compressive strength was tested for 28-day compressive strength which were 23 and 42 MPa, respectively, for the targeted 20 and 40 MPa concretes. A coupon tensile test was made to determine the yielding and the ultimate tensile strength of the steel tubes. The yield strength was 264 and 382 MPa for T1.8 and T3.0, respectively. The ultimate strength was 305 and 441 MPa for T1.8 and T3.0, respectively. Based on EC4 [20], for the local buckling resistance design, the maximum limit of the width-to-thickness ratios ( $b/t$ ) is calculated using (1). For samples with 1.8 mm and 3 mm thick steel tube, the ratios are about 41.7 and 25, which are, respectively, below the limits of 49.1 and 40.9. For a CFST member, the potential of local buckling is estimated using a width-to-thickness ratio parameter  $R$  [21] as shown in (2). In the equations,  $f_y$ ,  $E$ , and  $\nu$  are yield strength, elastic modulus, and Poisson's ratio of steel, and  $k$  is the buckling coefficient,  $k = 4n^2$ , where  $n = 1$  and 2 for unstiffened section and stiffened section with one stiffener on each wall. For the composite column with the thickness of 1.8 and 3.0 mm, the parameter  $R$  is 0.80 and 0.58, respectively, which is lower than the limit of 0.9 [21].

$$\frac{b}{t} = 52 \sqrt{\frac{235}{f_y}} \quad (1)$$

$$R = \frac{b}{t} \sqrt{\frac{12(1-\nu^2)}{\pi^2 k}} \sqrt{\frac{f_y}{E}} \quad (2)$$

Other important factors for the composite column design are the steel contribution ratio ( $\delta$ ) and confinement factor ( $\xi$ ), which are expressed in (3) and (4), respectively.

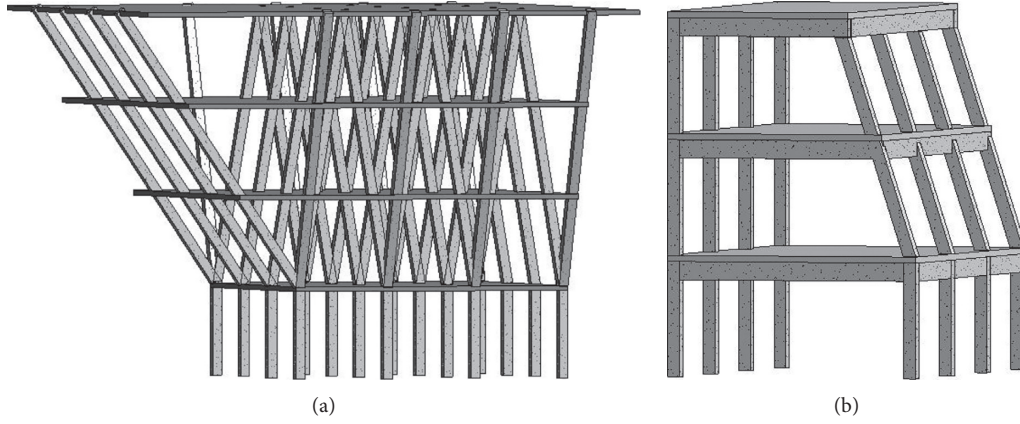


FIGURE 1: Example of application of inclined column.

TABLE 1: Samples.

Number	Sample	$B$ (mm)	$T$ (mm)	$\theta$ (deg)	$b/t$	$R$	$f'_c$ (MPa)	$\delta$	$\xi$	$N_{cu}$ (kN)	$SI_c$	$N_{tu}$ (kN)	$SI_t$
1	T1.8C0A0	75	1.8	0	41.7	—	—	1	—	150.0	1.00	150.7	1.00
2	T1.8C0A4	75	1.8	4	41.7	—	—	1	—	99.0	0.66	150.6	1.00
3	T1.8C0A9	75	1.8	9	41.7	—	—	1	—	91.1	0.61	150.5	1.00
4	T1.8C20A0	75	1.8	0	41.7	0.80	23	0.56	1.30	268.2	1.00	162.4	1.00
5	T1.8C20A4	75	1.8	4	41.7	0.80	23	0.56	1.30	260.0	0.97	163.4	1.01
6	T1.8C20A9	75	1.8	9	41.7	0.80	23	0.56	1.30	253.3	0.94	162.2	1.00
7	T1.8C40A0	75	1.8	0	41.7	0.80	42	0.42	0.71	413.8	1.00	152.8	1.00
8	T1.8C40A4	75	1.8	4	41.7	0.80	42	0.42	0.71	334.5	0.81	192.5	1.26
9	T1.8C40A9	75	1.8	9	41.7	0.80	42	0.42	0.71	327.8	0.79	164.5	1.08
10	T3.0C0A0	75	3.0	0	25.0	—	—	1	—	340	1.00	345	1.00
11	T3.0C0A4	75	3.0	4	25.0	—	—	1	—	330	0.97	342.4	0.99
12	T3.0C0A9	75	3.0	9	25.0	—	—	1	—	325.9	0.96	309.1	0.90
13	T3.0C20A0	75	3.0	0	25.0	0.57	23	0.76	3.13	436.5	1.00	350.2	1.00
14	T3.0C20A4	75	3.0	4	25.0	0.57	23	0.76	3.13	427.9	0.98	342.4	0.98
15	T3.0C20A9	75	3.0	9	25.0	0.57	23	0.76	3.13	343.7	0.79	326	0.93

Note.  $N_{cu}$  and  $N_{tu}$  are, respectively, the ultimate loading capacity under compression and tension.  $SI_c$  and  $SI_t$  are, respectively, the strength index under compression and tension (6).

The simplified design of the composite column, according to EC4 [20] and ACI318 [22], assumes the plastic resistance of the column composite section under compressive load ( $N_0$ ) by the sum of the resistances of the concrete and steel. With the assumption, the steel contribution ratio ( $\delta$ ) is limited between 0.2 and 0.9. The ratios of the test composite samples are ranged from 0.42 to 0.76 as shown in Table 1. Hence, they meet the requirement.

$$\delta = \frac{f_y A_s}{N_0} = \frac{f_y A_s}{0.85 f'_c A_c + f_y A_s}, \quad (3)$$

$$\xi = \frac{f_y A_s}{0.85 f'_c A_c}. \quad (4)$$

In preparation of the CFST columns, fresh concrete was filled into the steel tubular section. During the casting, fresh concrete was vibrated. Then, the CFST columns were kept in the curing process for at least 28 days. Thereafter, the CFST samples were welded to end plates and stiffeners at both ends as illustrated in Figure 2. The end plates were holed in the position for bolting to the loading machine. Two stiffeners were welded

to the column ends along the inclined center line to increase the joint welding strength under tension and control the in-plane bending. Consequently, the sample was put into a universal testing machine (200 tons) and all testing conditions were set, including strain gauges and transducers in 2 horizontal directions and 1 vertical direction as shown in Figure 2.

**2.2. Cyclic Load Test.** The test column was arranged in the loading machine as an inclined column in nonsway structure, and the boundary conditions are specified as illustrated in Figure 3. At both ends, samples were restrained in horizontal ( $x, y$ ), vertical ( $z$ ), and rotation ( $r$ ) movement. The inclination generates more complex acting force compared to the concentric axial loading. It can be seen that all forces, including bending, shearing, and compressive or tensile forces, are at both ends of the column. Larger inclination angle introduces higher eccentricity leading to high eccentric bending moment. In a condition when a member is inclined appreciably, shear is found to be predominant and shear capacity demand should be strictly considered. The cyclic vertical load was applied on the top of the samples. As

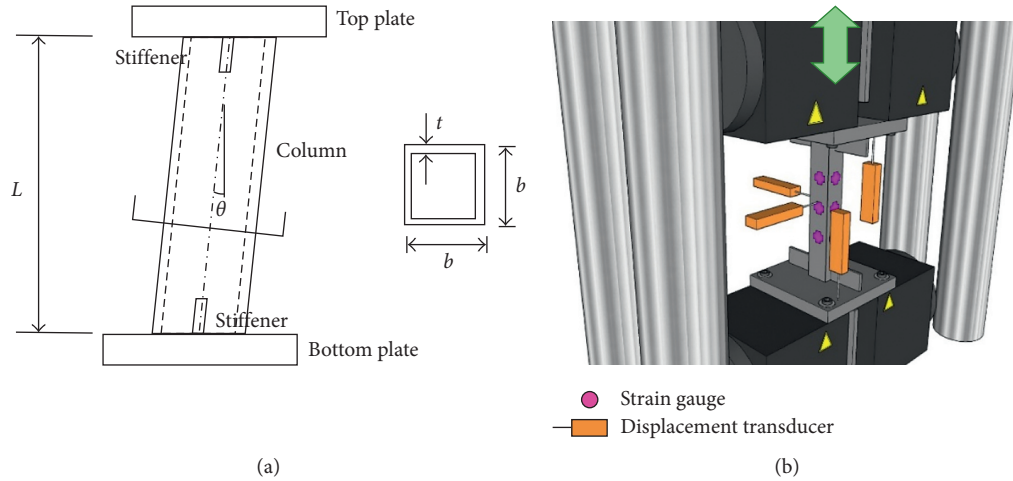


FIGURE 2: CFST column sample and instrumental setup.

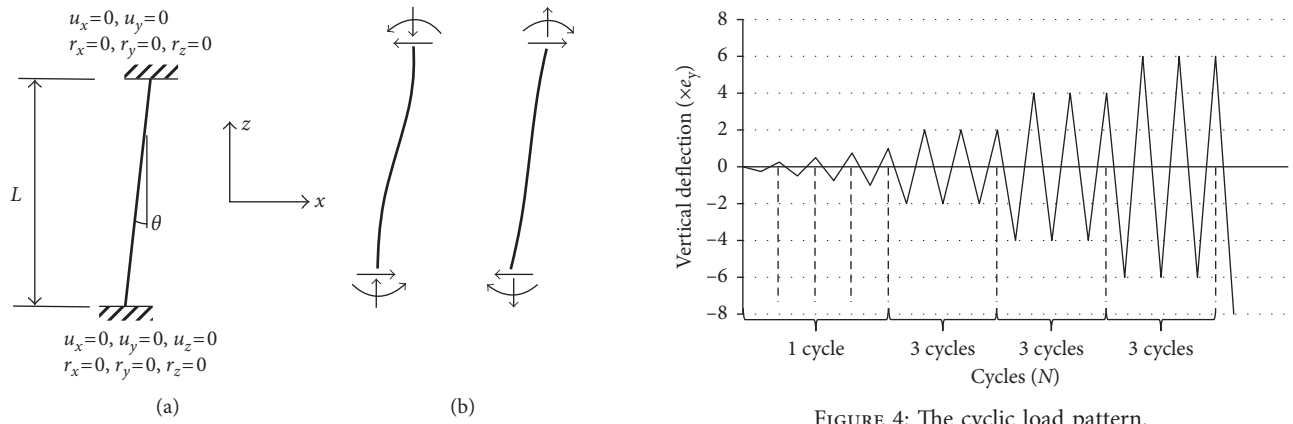


FIGURE 3: Boundary conditions and induced column forces.

as a result, the samples were subjected to both elongation and contraction. The magnitude of each cycle was specified using the percentage of the estimated deformation at yield point ( $e_y$ ) as shown in the following equation:

$$e_y = \frac{f_y}{E} \times L, \quad (5)$$

where  $e_y$  is the estimated vertical deformation at yield point,  $f_y$  is the yield strength (MPa),  $E$  is the modulus of elasticity of the steel tube (MPa), and  $L$  is the total length of the sample (mm). The cyclic load pattern can be divided into 2 parts. At initial step before the expected yielding, a series of single-cycle load of  $0.25e_y$ ,  $0.50e_y$ ,  $0.75e_y$ , and  $1.00e_y$  was applied. Thereafter, a series of three-cycle load of  $2.0e_y$ ,  $4.0e_y$ ,  $6.0e_y$ , and  $8.0e_y$  continued to be applied (Figure 4). The samples were tested until they reached the failure state.

### 3. Experimental Results

**3.1. Failure Mode and Axial Load Capacity.** Under the incremental increase of the cyclic load as shown in Figure 4, all the samples behaved linearly at the early loading stage. With

the larger applied cyclic deformation, local buckling appeared under compressive loading, followed by tension yielding and tearing of the steel tube at the same column section. The yielding and steel tearing led to the complete loss of load bearing capacity. The samples without the infilled concrete were first damaged due to local buckling under the compressive loading, leading to drastic decrease of compressive capacity. With the increase of displacement loading, tension yielding at the local buckling section was generated, but the tension capacity was maintained until the tearing of the tube. However, for the CFST column (with the infilled concrete), major buckling of the steel tube occurred after the tensile yielding. The inclination angle decreases the vertical cyclic compressive loading capacity of the hollowed steel column with thinner wall ( $t = 1.8 \text{ mm}$ ;  $b/t = 41.7$ ). The strength index under compressive loading ( $SI_c$ ) indicating the effect of the inclination angle as calculated by (6) is 0.66 and 0.61, respectively, for the 4-degree and 9-degree inclined columns, as shown in Table 1 and Figure 5. However, the inclination angles of 4 and 9 degrees insignificantly reduced the vertical loading capacity of the hollowed columns with thicker wall ( $t = 3.0 \text{ mm}$ ;  $b/t = 25$ ). The strength index of the two columns is 0.97 and 0.96, respectively. Hence, it can be said that the local buckling capacity of the slender wall

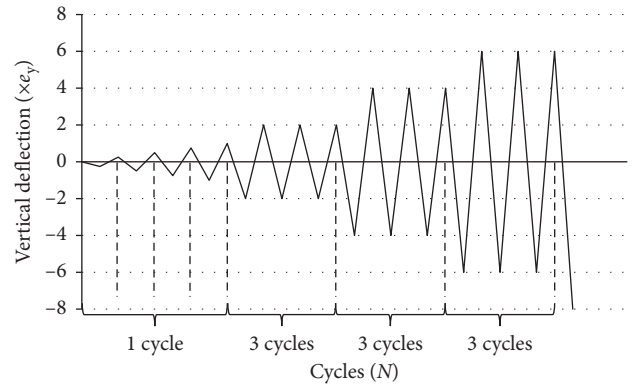


FIGURE 4: The cyclic load pattern.

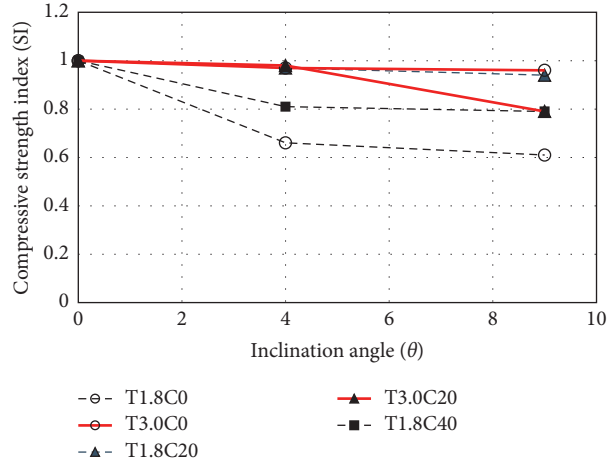


FIGURE 5: Compressive strength index due to inclination angle.

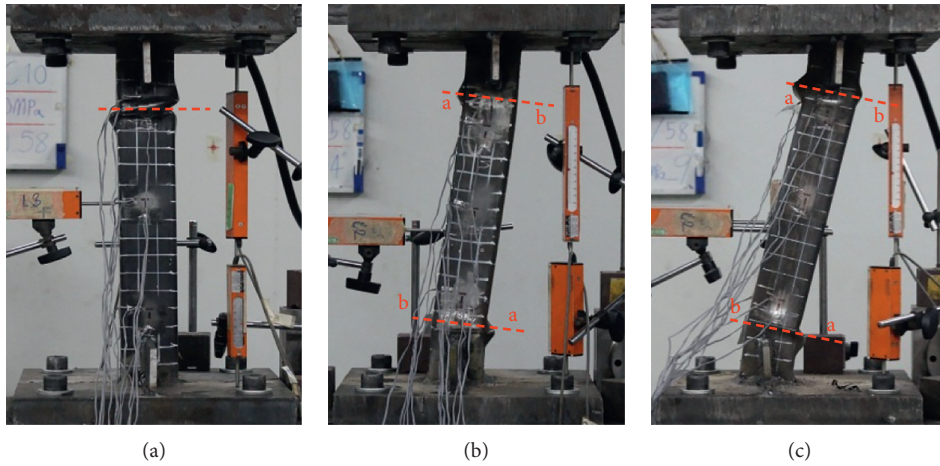


FIGURE 6: Failure pattern of T3.0C20 series samples. (a) T3.0C20A0. (b) T3.0C20A4. (c) T3.0C20A9.

hollowed steel column is significantly affected by the inclination angle. For the CFST columns, local compressive buckling was restrained, and hence, they experienced only outward local buckling. Hence, the CFST columns could carry more compressive loads after local buckling. Infilled concrete reduced negative effect of inclination angle is shown in Figure 5. The ultimate compressive loading capacity of the column was obtained when the confined steel walls suffered large tensile strain and torn. At this loading stage, concrete core confinement was decreased and concrete crushing was observed. As an example, Figure 6 shows the failure of T3.0C20 series samples. It can be seen that the local buckling plane shown as the broken line was formed in a direction perpendicular to the longitudinal direction. The inclination leading to end eccentricity results to nonuniform longitudinal compressive stress. As shown in Figure 6 for the T3.0C20 series samples, buckling was more severe on the face with higher compression (face “a”) compared with the opposite face (face “b”).

$$SI = \frac{N_{u,inc}}{N_{u,ver}}, \quad (6)$$

where SI is the strength index.  $N_{u,inc}$  and  $N_{u,ver}$  are the ultimate strength of inclined and vertical samples, respectively.

**3.2. Cyclic Behaviors and Hysteretic Loop.** The hysteretic loops of all samples are shown in Figure 7. The hysteretic loops illustrate that the columns performed in the elastic manner at the initial stage of the test. The tensile loading capacity was maintained after the peak for all samples. In the cases of hollow steel columns, the compressive strength was much lower than those in CFST columns and the strength dropped drastically after the compressive peak load. Under the tension side, the infilled concrete and the inclination insignificantly influenced the tension-resisting behavior.

From Figure 7, the hysteretic loop of the infilled concrete columns under compression is more stable compared with those of the unfilled columns. The compressive capacity gradually decreased after the peak compressive load. This desirable behavior leads to higher ductility which will be explained in Section 3.3. The inclination angle delays the sudden drop of the compressive strength after the peak

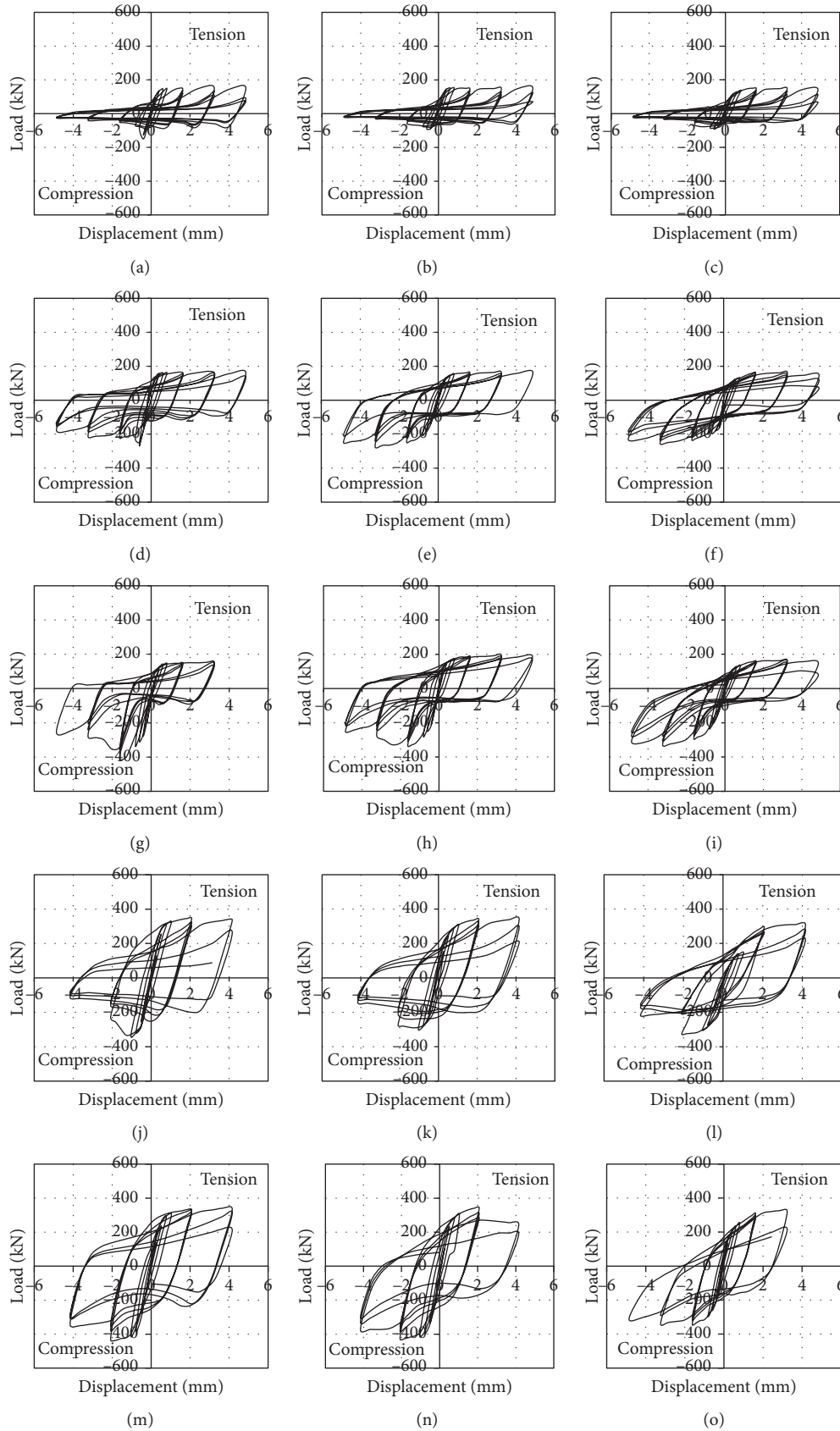


FIGURE 7: Hysteretic loop. (a) T1.8C0A0. (b) T1.8C0A4. (c) T1.8C0A9. (d) T1.8C20A0. (e) T1.8C20A4. (f) T1.8C20A9. (g) T1.8C40A0. (h) T1.8C40A4. (i) T1.8C40A9. (j) T3.0C0A0. (k) T3.0C0A4. (l) T3.0C0A9. (m) T3.0C20A0. (n) T3.0C20A4. (o) T3.0C20A9.

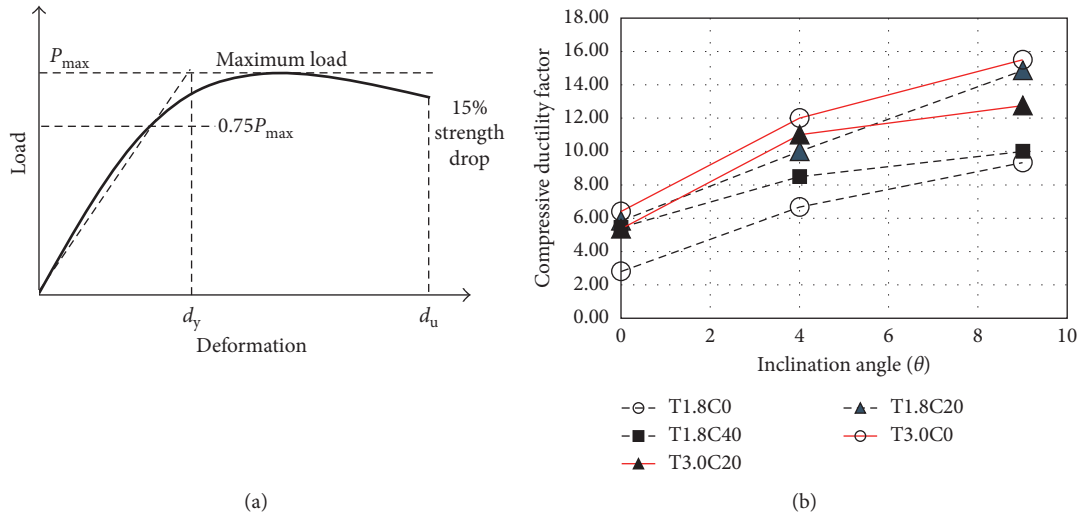


FIGURE 8: Ductility factor. (a) Determination of the ductility factor. (b) Compressive ductility factor of the samples.

TABLE 2: Ductility factor and equivalent viscous damping.

Number	Sample	Ductility in compression			Ductility in tension			Equivalent viscous damping ratio	
		$d_y$ (mm)	$d_u$ (mm)	$\mu$ (deg)	$d_y$ (mm)	$d_u$ (mm)	$\mu$ (deg)	Elastic	Inelastic
1	T1.8C0A0	0.25	0.70	2.80	0.30	5.10	17.00	6.5	25.1
2	T1.8C0A4	0.15	1.00	6.67	0.25	4.75	19.00	7.3	23.2
3	T1.8C0A9	0.15	1.40	9.33	0.25	4.90	19.60	4.5	22.2
4	T1.8C20A0	0.6	3.5	5.83	0.2	4.5	22.50	6.9	26.0
5	T1.8C20A4	0.5	5.0	10.00	0.15	5	33.33	5.2	23.1
6	T1.8C20A9	0.35	5.2	14.86	0.15	4.85	32.33	5.9	24.7
7	T1.8C40A0	0.45	2.45	5.44	0.35	2.75	7.86	5.2	14.4
8	T1.8C40A4	0.5	4.25	8.50	0.3	4.6	15.33	5.2	23.6
9	T1.8C40A9	0.5	5.0	10.00	0.3	4.85	16.17	5.7	15.7
10	T3.0C0A0	0.25	1.60	6.40	0.30	4.20	14.00	3.5	24.4
11	T3.0C0A4	0.10	2.4	12.00	0.15	4.15	27.67	3.3	26.3
12	T3.0C0A9	0.20	3.1	15.50	0.15	4.10	27.33	4.1	25.2
13	T3.0C20A0	0.7	3.75	5.36	0.4	4.1	10.25	6.2	28.7
14	T3.0C20A4	0.4	4.4	11.00	0.5	3.5	7.00	4.8	25.5
15	T3.0C20A9	0.4	5.1	12.75	0.4	2.95	7.38	2.3	22.7

because the inclination angle decreases the ultimate compressive loading capacity and results to higher ductility.

**3.3. Ductility and Equivalent Viscous Damping Ratio.** The ductility determines the ability of a structure to maintain the load carrying capacity after the commencement of yielding to the ultimate displacement. Park [23] proposed the definition of ductility factor ( $\mu$ ) as the ratio of the equivalent yield displacement ( $d_y$ ) to the ultimate displacement ( $d_u$ ). As shown in Figure 8(a), the backbone curves of all samples are drawn, and the ductility factor can be determined. The results are shown in Table 2 and Figure 8(b) which indicates that the inclination angle increases the ductility under compression loading. The smallest compressive ductility factor of 2.8 is from T1.8C0A0, the unfilled thin steel tube

column with zero inclination angle. Filling of lower strength concrete (23 MPa) in the thin hollow steel column can enhance the ductility factor from 2.80 to 5.83. However, the thinner section filled with higher concrete compressive strength may result in the substantial increase of strength but less efficient in ductility enhancement.

The equivalent viscous damping ratio ( $\zeta_{eq}$ ) indicates energy dissipation capacity during inelastic response. The estimation of the ratio expressed by Chopra [24] was implemented in this study, as shown in (7). In the elastic range, the equivalent viscous damping ratios of all of the samples are in the range of 2.3–7.3%. The values are between 14.4 and 28.7 in the inelastic range. The inclination angle seems to have no effect on the ratio, as shown in Figure 9(b). The infilled high strength concrete (42 MPa) tends to decrease the damping ratio of the thinner CFST columns.

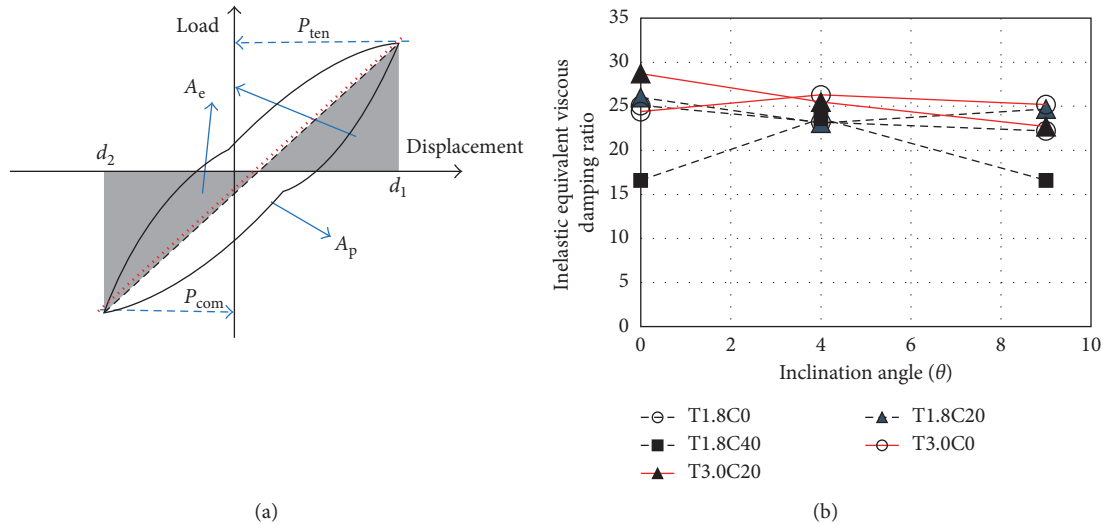


FIGURE 9: Equivalent viscous damping ratio. (a) Determination of the equivalent viscous damping ratio. (b) Equivalent viscous damping ratio of the samples.

$$\zeta_{eq} = \frac{1}{2\pi} \frac{A_p}{A_e} \times 100. \quad (7)$$

#### 4. Conclusions

In this paper, CFST inclined columns were tested under vertical cyclic load. From the test results, the following conclusions can be drawn:

- (1) The local buckling capacity of the slender wall hollowed steel column is significantly affected by the inclination angle. The strength index (SI) under compressive loading of T1.8C0 samples is 0.66 and 0.61, respectively, for the 4-degree and 9-degree inclined columns. However, the inclination angles of 4 and 9 degrees insignificantly reduced the vertical loading capacity of the hollowed columns with thicker wall ( $t = 3.0$  mm,  $D/t = 25$ ). The strength index of the columns is 0.97 and 0.96, respectively.
- (2) The infilled concrete enhanced the compressive cyclic behavior of the steel hollow section. For the ductility, filling of lower strength concrete (23 MPa) in the thin hollow steel column can enhance the ductility factor from 2.80 (T1.8C0A0 sample) to 5.83 (T1.8C20A0 sample). However, the thinner section filled with higher concrete compressive strength may result to the substantial increase of strength but less efficient in ductility enhancement. The inclination angle decreases the ultimate compressive loading capacity and results to the higher ductility.
- (3) For the equivalent viscous damping ratio, the values of all samples are between 14.4 and 28.7 in the inelastic range. The inclination angle seems to have no effect on the ratio. The infilled high strength concrete (42 MPa) tends to decrease the damping ratio of the thinner CFST columns.

#### Data Availability

The data used to support the findings of this study are included within the article.

#### Conflicts of Interest

The authors declare that there are no conflicts of interest regarding the publication of this paper.

#### Acknowledgments

The authors would like to acknowledge the supports provided by Chiang Mai University.

#### References

- [1] C. Hansapinyo, "Buckling performance of irregular section cold-formed steel columns under axially concentric loading," *International Journal of Civil, Structural, Construction and Architectural Engineering*, vol. 9, no. 5, pp. 542–548, 2015.
- [2] J. Y. R. Liew and D. X. Xiong, "Ultra-high strength concrete filled composite columns for multi-storey building construction," *Advances in Structural Engineering*, vol. 15, no. 9, pp. 1487–1503, 2012.
- [3] R. Yadav, B. Chen, H. Yuan, and Z. Lian, "Analytical behavior of CFST bridge piers under cyclic loading," *Procedia Engineering*, vol. 173, pp. 1731–1738, 2017.
- [4] J. Zhang, S. Jiang, B. Chen, C. Li, and H. Qin, "Numerical study of damage modes and damage assessment of CFST columns under blast loading," *Shock and Vibration*, vol. 2016, Article ID 3972791, 12 pages, 2016.
- [5] S. P. Schneider, "Axially loaded concrete-filled steel tubes," *Journal of Structural Engineering*, vol. 124, no. 10, pp. 1125–1138, 1998.
- [6] D. Liu, W. M. Gho, and J. Yuan, "Ultimate capacity of high-strength rectangular concrete-filled steel hollow section stub columns," *Journal of Constructional Steel Research*, vol. 59, no. 12, pp. 1499–1515, 2003.
- [7] X. Zhou, T. Mou, H. Tang, and B. Fan, "Experimental study on ultrahigh strength concrete filled steel tube short columns

- under axial load,” *Advances in Materials Science and Engineering*, vol. 2017, Article ID 8410895, 9 pages, 2017.
- [8] Y. Guo and Y. Zhang, “Comparative study of CFRP-confined CFST stub columns under axial compression,” *Advance in Civil Engineering*, vol. 2018, Article ID 7109061, 8 pages, 2018.
- [9] Y. Chen, K. Wang, K. He, J. Wei, and J. Wan, “Compressive behavior of CFRP-confined post heated square CFST stub columns,” *Thin-Walled Structures*, vol. 127, no. 6, pp. 434–445, 2018.
- [10] L. H. Han, X. L. Zhao, and Z. Tao, “Tests and mechanics model of concrete-filled SHS stub columns, columns and beam-columns, steel and composite structures,” *Steel and Composite Structures*, vol. 1, no. 1, pp. 51–74, 2001.
- [11] F. Abed, M. Alhamaydeh, and S. Abdalla, “Experimental and numerical investigations of the compressive behavior of concrete filled steel tubes (CFSTs),” *Journal of Constructional Steel Research*, vol. 80, no. 1, pp. 429–439, 2013.
- [12] H. Ruoquan, “Behaviour of long concrete filled steel columns, composite construction in steel and concrete II,” in *Proceedings of Engineering Foundation Conference*, pp. 728–737, Santa Barbara, CA, USA, June 1992.
- [13] Z. Vrcelj and B. Uy, “Strength of slender concrete-filled steel box columns incorporating local buckling,” *Journal of Constructional Steel Research*, vol. 58, no. 2, pp. 275–300, 2002.
- [14] C. D. Goode, A. Kuranovas, and A. K. Kvedaras, “Buckling of slender composite concrete-filled steel columns,” *Journal of Civil Engineering and Management*, vol. 16, no. 2, pp. 230–237, 2010.
- [15] C. Hansapinyo, “Responses of concrete-filled cold-formed square hollow and double-C steel stub columns under cyclic and repeated loadings,” *Advanced Materials Research*, vol. 255–260, pp. 198–203, 2011.
- [16] S. Abdalla, F. Abed, and M. Alhamaydeh, “Behavior of CFSTs and CCFSTs under quasi-static axial compression,” *Journal of Constructional Steel Research*, vol. 90, no. 11, pp. 235–244, 2013.
- [17] X. Y. Mao and Y. Xiao, “Seismic behaviour of confined square CFT columns,” *Engineering Structures*, vol. 63, no. 3, pp. 317–325, 2007.
- [18] C. Buachart, C. Hansapinyo, and N. Ueatrongchitt, “Analysis of square concrete-filled cold-formed steel tubular columns under axial cyclic loading,” *International Journal of GEO-MATE*, vol. 15, no. 47, pp. 74–80, 2018.
- [19] L. H. Han, Q. X. Ren, and W. Li, “Test on inclined, tapered and STS concrete-filled steel tubular (CFST) stub columns,” *Journal of Constructional Steel Research*, vol. 66, no. 10, pp. 1186–1195, 2010.
- [20] Eurocode 4, *Design of Composite Steel and Concrete Structures, Part 1.1, General Rules and Rules for Building*, BS EN1994-1-1: 2004, British Standards Institution, London, UK, 2004.
- [21] H. B. Ge and T. Usami, “Strength analysis of concrete-filled thin-walled steel box columns,” *Journal of Constructional Steel Research*, vol. 30, no. 3, pp. 259–281, 1994.
- [22] ACI 318, *Building Code Requirements for Structural Concrete and Commentary*, American Concrete Institute, Farmington Hills, MI, USA, 2014.
- [23] R. Park, “Evaluation of ductility of structures and structural assemblages from laboratory testing,” *Bulletin of the New Zealand National Society for Earthquake Engineering*, vol. 22, no. 3, pp. 155–166, 1989.
- [24] A. K. Chopra, *Dynamic of Structures-Theory and Applications to Earthquake Engineering*, Prentice-Hall, Inc., Englewood Cliffs, NJ, USA, 2011.

## Research Article

# Comparative Study of Nonlinear Static and Time-History Analyses of Typical Korean STS Container Cranes

Quang Huy Tran <sup>1</sup>, Jungwon Huh <sup>1</sup>, Van Bac Nguyen,<sup>1</sup> Achintya Haldar,<sup>2</sup> Choonghyun Kang,<sup>1</sup> and Kyeong Min Hwang<sup>3</sup>

<sup>1</sup>Department of Civil and Environmental Engineering, Chonnam National University, Yeosu 59626, Republic of Korea

<sup>2</sup>Department of Civil Engineering and Engineering Mechanics, University of Arizona, Tucson, AZ 85721, USA

<sup>3</sup>Korea Electric Power Corporation Research Institute, Yuseong-Gu, Republic of Korea

Correspondence should be addressed to Jungwon Huh; [jwonhuh@chonnam.ac.kr](mailto:jwonhuh@chonnam.ac.kr)

Received 28 March 2018; Accepted 18 July 2018; Published 16 August 2018

Academic Editor: Tadeh Zirakian

Copyright © 2018 Quang Huy Tran et al. This is an open access article distributed under the Creative Commons Attribution License, which permits unrestricted use, distribution, and reproduction in any medium, provided the original work is properly cited.

Ship-to-shore (STS) container gantry cranes, used at terminals for loading and unloading containers from a ship, are an important part of harbor structures. The size and weight of modern STS container cranes are increasing to satisfy the demand for bigger ships. This is expected to result in more lateral load when excited by seismic motions. The existing Korean STS container cranes did not behave properly during several recent moderate earthquakes in South Korea. Typical Korean STS container cranes must be checked for the earthquake-resistant capacity. In this research, two nonlinear static analyses procedures, also known as pushover analyses, commonly used for seismic design of buildings, namely, capacity spectrum method and equivalent linearization method, are comprehensively studied to check their suitability for studying seismic behavior of STS cranes. Results obtained by these two nonlinear static analysis methods are then compared with the results obtained by nonlinear time-history analyses of the STS cranes by exciting them with nine recorded earthquake time histories around worldwide. The behaviors of the cranes are analyzed in terms of the total base shear, drift, and base uplift. The comparisons indicate that the nonlinear static methods can be appropriate for estimating the total base shear and drift of the portal frame of a container crane. The pushover analyses also provide information on performance levels as defined in ASCE/SEI 41-13, of a typical Korean STS container crane. Furthermore, it is observed that the uplift response of the crane is strongly influenced by the duration of an earthquake.

## 1. Introduction

Nonlinear static analysis (NSA), also known as pushover analysis (PA), is an effective tool for performance assessment of a structure under a seismic event. It requires less calculation than nonlinear dynamic analysis and avoids using a set of ground motion time histories [1]. As expected, NSA takes a shorter time but is less accurate than the time-history analysis (THA) method since it uses static analysis to capture dynamic effects. The overall steps of the NSA method include the selection of load patterns, nonlinear analysis of the structure to obtain the capacity curve, calculation of displacement demand using a response spectrum, and the assessment of the performance of the structure [1]. There are several NSA methods with the same basic overall schemes,

but the detailed steps required to implement them are different. Some of the concepts officially incorporated in design guidelines include capacity spectrum method (CSM) and displacement coefficient method (DCM) as adopted in ATC-40 [2] and ASCE-41 [3], N2 method as proposed in Eurocode 8 [4], and equivalent linearization method (ELM) and displacement modification method (DMM) as presented in FEMA 440 [5]. In addition, several researchers proposed other procedures. They include the adaptive capacity spectrum method (ACSM) by Casarotti and Pinho [6]; the improved capacity spectrum method (ICSM) by Fajfar [7], Lin and Chang [8], and Mingkui et al. [9]; modal pushover analysis (MPA) by Chopra and Goel [10], Freeman [11], Sucuoglu, and Gunay [12]; adaptive modal combinations (AMC) by Kalkan and Kunnath [13]; and the iterative

displacement coefficient method (IDCM) by Ćosić and Brčić [14]. These methods generally give different results. The definition of the performance point/displacement target and the selection of lateral load patterns used in these methods are the two major reasons for the different results [15]. It is important to note that most of these studies were developed for buildings.

For a special steel structure such as a ship-to-shore (STS) container crane, very different from buildings, as shown in Figure 1, the use of NSA for seismic analyses are expected to be different, with their unique support conditions. In this study, two NSA methods, conventional CSM of ATC-40 and the ELM of FEMA 440, are selected for further consideration. They are selected because they provide a graphical relationship between the capacity of a structure and the seismic demand, and it is relatively easy for engineers to estimate the maximum displacement by using them. In addition, these methods are recommended in many design guidelines and standards worldwide.

The seismic behavior assessment of a typical STS container crane used in South Korea is specifically addressed in this paper. A three-dimensional (3D) finite element (FE) model generated by SAP2000 is analyzed first by CSM and ELM. The results of these NSA methods are then verified by exciting the crane by nine scaled recorded ground motion time histories. The results obtained by CSM and ELM were then compared with the more comprehensive and accurate nonlinear THA. The primary objective of this study is to investigate whether commonly used NSA methods developed for the seismic design of buildings can also be used for a STS container crane. For a comprehensive comparison, the uplift response, base shear, and drift are specifically addressed and compared in this study.

## 2. Nonlinear Static and Dynamic Analyses

**2.1. Capacity Spectrum Method (CSM) Procedure.** CSM was first proposed by Freeman et al. in 1975 [16] and later introduced in ATC-40 in 1996 [2] and FEMA 274 in 1997 [17]. It is a graphical procedure. This method provides a special treatment for reduction of the seismic demand to intersect the capacity curve in spectral coordinates to find a performance point [2]. An interesting study related to CSM was the AutoCSM method proposed by Guyader and Iwan [18]. AutoCSM is an automated Excel sheet, in which the improved effective linear periods are used to replace the secant period used in the conventional CSM. Essentially, the seismic demand is reshaped by a modification factor. In addition, to improve the accuracy of CSM, Chopra and Goel [19] proposed the use of the constant-ductility inelastic design spectra instead of the elastic damped spectra of the conventional CSM, commonly denoted as ICSM. The procedure is controlled by the ductility factor. Lin and Chang [8] improved ICSM by using the real absolute acceleration response spectrum instead of the pseudoacceleration response spectrum, especially for them system with equivalent viscous damping ratio  $\beta_{eq} > 10\%$  and period  $T > 0.15$  s. Later, Mingkui et al. in 2006 [9] proposed two improvements for the conventional CSM. They considered inelastic demand spectra by using yield strength factor as an

elastoplastic index. They also defined and formulated the design acceleration response spectra from the China design building code. Based on the energy equivalent criterion, the equivalent single degree of freedom (SDOF) system was estimated instead of bilinear modeling of pushover curves under the assumption of area equivalence. In 2007, Casarotti and Pinho [6] proposed another procedure, especially for bridge applications, known as ACSM. They constructed an equivalent single-mode capacity curve by combining multimodal pushover response curves. It can be used to study multiple degree of freedom (MDOF) continuous span bridges, considering both flexible and rigid superstructures. Gencturk and Elnashai in 2008 [20] proposed a method for seismic evaluation of wood-frame structures. The results showed a significant improvement in the accuracy of CSM as updating the bilinear idealization of the structural system based on the selected trial performance point on the capacity diagram. Recent studies also compared and verified methods proposed by Causevic and Mitrovic [21] and Ferraioli et al. [22]. As discussed previously, the use of NSA for the design of STS crane is very limited. The question remains whether the conventional CSM as suggested in ATC-40 for the design of buildings can also be used for the design of STS containers.

The conventional CSM procedure consists of the following steps as illustrated in Figure 2 [10]:

- (1) Construct the pushover curve, which represents the relationship between the base shear  $V_b$  and the roof displacement  $\Delta_{roof}$ .
- (2) Convert the pushover curve to a capacity diagram by transforming  $V_b$  to the spectral acceleration  $S_a$  and  $\Delta_{roof}$  to the spectral displacement  $S_d$  by using the following equations:

$$S_{ai} = \left( \frac{1}{\alpha_1 W} \right) V_{bi}, \quad (1)$$

$$S_{di} = \left( \frac{1}{\Gamma_1 \phi_{roof1}} \right) \Delta_{roof},$$

where  $W$  is the total dead load of the structure and applicable portions of other loads (i.e., service live loads),  $\phi_{roof1}$  is the amplitude of mode 1 at the roof level, and  $\Gamma_1$  and  $\alpha_1$  are the modal participation factor and the modal mass coefficient for the first natural mode, respectively. They can be calculated as follows:

$$\Gamma_1 = \frac{\sum_{i=1}^N (w_i \phi_{i1}) / g}{\sum_{i=1}^N (w_i \phi_{i1}^2) / g}, \quad (2)$$

$$\alpha_1 = \frac{\left( \sum_{i=1}^N (w_i \phi_{i1}) / g \right)^2}{\left( \sum_{i=1}^N w_i / g \right) \left( \sum_{i=1}^N (w_i \phi_{i1}^2) / g \right)}.$$

- (3) Convert the elastic response spectrum ( $S_a$  versus  $T$  diagram) to the acceleration—deformation response spectrum format ( $S_a$  versus  $S_d$  format or “ADRS”) using the following equation:

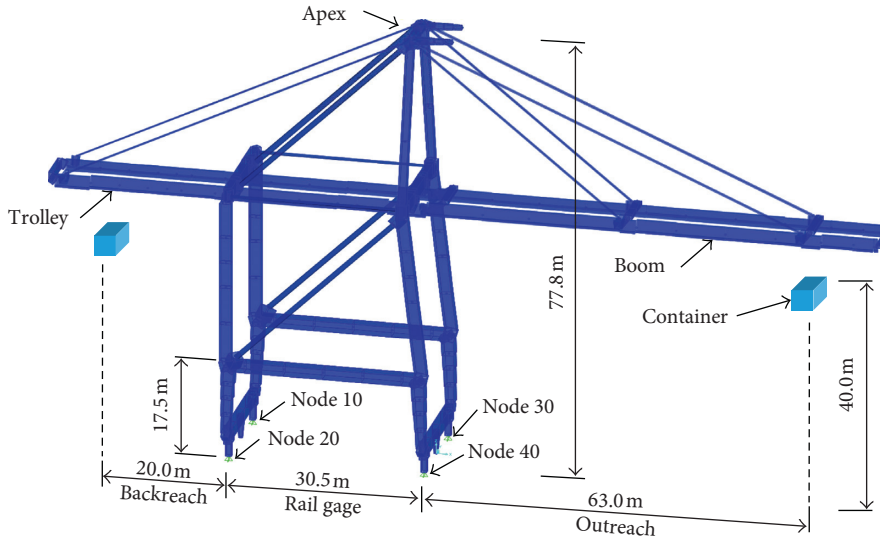


FIGURE 1: 3D numerical FE model of Korea STS container crane.

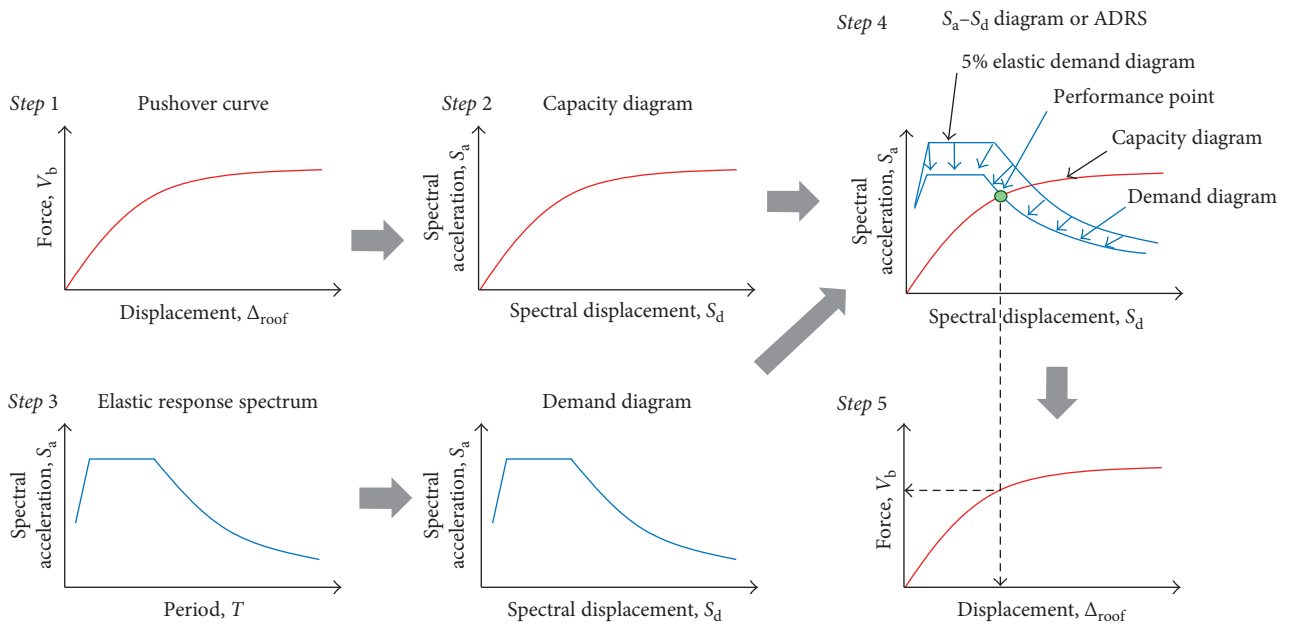


FIGURE 2: Conventional CSM procedure.

$$S_{di} = \frac{T^2}{4\pi^2} S_{ai} g, \quad (3)$$

where  $T$  is the natural period of the system vibrating within linearly elastic range ( $u \leq u_y$ ).

- (4) Plot the demand and capacity diagrams on the top of each other. Instead of dynamic analyses, a sequence of equivalent linear systems with successively updated values of the natural period of the structure,  $T_{eq}$ , and total equivalent viscous damping,  $\hat{\beta}_{eq}$ , provide a basis for estimating the deformation of the inelastic system [10]. The total viscous damping  $\hat{\beta}_{eq}$  of the equivalent linear system is defined as follows:

$$\hat{\beta}_{eq} = \beta_0 + \kappa \beta_{eq}, \quad (4)$$

where  $\beta_0$  is the viscous damping ratio of a bilinear system for vibrations in linear range ( $u \leq u_y$ ),  $\kappa$  is the adjustment factor depending on structural behavior, and  $\beta_{eq}$  is the equivalent viscous damping ratio as defined in (5). It can also be expressed in detail in (6) for bilinear systems based on Figure 3.

$$\beta_{eq} = \frac{1}{4\pi} \frac{E_D}{E_S}, \quad (5)$$

$$\beta_{eq} = \frac{2}{\pi} \frac{(\mu - 1)(1 - \alpha)}{\mu(1 + \alpha\mu - \alpha)}, \quad (6)$$

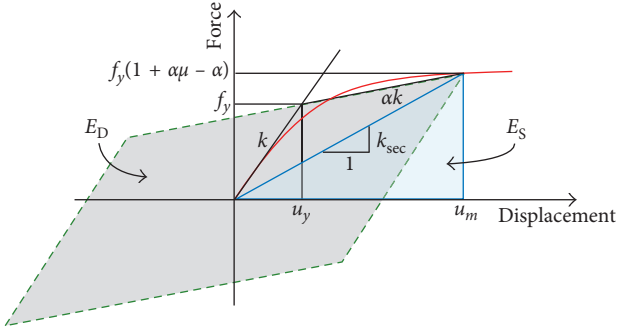


FIGURE 3: SDOF nonlinear system and equivalent viscous damping due to hysteretic energy dissipation.

where  $E_D$  and  $E_S$  are the energy dissipated in the nonlinear system (area of enclosed by hysteresis loop) and linear system (area of triangle), respectively,  $\mu = u_m/u_y$  is the ductility factor,  $\alpha$  is the post-yield stiffness ratio, and  $k_{sec}$  is the secant stiffness. The natural vibration period of the equivalent linear system can be calculated as follows:

$$T_{eq} = T \sqrt{\frac{\mu}{1 + \alpha\mu - \alpha}} \quad (7)$$

- (5) Convert  $S_d$  from step 4 to  $\Delta_{roof}$  or an individual component deformation and then compare them with the limiting values for the specified performance goals [10, 19].

$$\Delta_{roof} = S_{di} \phi_{roof1} \Gamma_1, \quad (8)$$

$$V_b = \alpha_1 S_a W, \quad (9)$$

where all the parameters in (8) and (9) are already explained in (1) and (2).

**2.2. Equivalent Linearization Method (ELM) Procedure.** Similar to CSM, ELM requires a response spectrum family and uses estimates of ductility to obtain effective period and effective damping. In both procedures, the global deformation demand (including elastic and inelastic) on the structure is computed from the response of an equivalent SDOF system. The difference is in the technique used to obtain the maximum displacement demand [5]. In conventional CSM, the equivalent stiffness of inelastic system is assumed to be the secant stiffness and the equivalent damping is related to the area under the capacity curve as illustrated in Figure 3. In ELM, however, the equivalent stiffness is estimated from effective period  $T_{eff}$  and effective damping  $\beta_{eff}$  derived from statistical analyses, expressed as functions of ductility  $\mu$  [5].  $T_{eff}$  and  $\beta_{eff}$  optimized for application to any capacity curve can be estimated as follows:

For  $1.0 < \mu < 4.0$ ,

$$\begin{aligned} \beta_{eff} &= 4.9(\mu - 1)^2 - 1.1(\mu - 1)^3 + \beta_0, \\ T_{eff} &= [0.2(\mu - 1)^2 - 0.038(\mu - 1)^3 + 1]T. \end{aligned} \quad (10)$$

For  $4.0 \leq \mu \leq 6.5$ ,

$$\begin{aligned} \beta_{eff} &= 14 + 0.32(\mu - 1) + \beta_0, \\ T_{eff} &= [0.28 + 0.13(\mu - 1) + 1]T. \end{aligned} \quad (11)$$

For  $\mu > 6.5$ ,

$$\begin{aligned} \beta_{eff} &= 19 \left[ \frac{0.64(\mu - 1) - 1}{[0.64(\mu - 1)]^2} \right] \left( \frac{T_{eff}}{T} \right)^2 + \beta_0, \\ T_{eff} &= \left[ 0.89 \left( \sqrt{\frac{\mu - 1}{1 + 0.05(\mu - 2)}} - 1 \right) + 1 \right] T. \end{aligned} \quad (12)$$

The above expressions are limited for the initial period of vibration  $T$  from 0.2 to 2.0 s [5]. The effective acceleration  $a_{eff}$  must lie on the capacity curve and coincide with the maximum displacement  $d_{max}$ . Thus, the modification factor  $M$ , defined by (13), is used to adjust the demand spectrum. The modified ADRS (MADRS) procedure is described and depicted in Figure 4 [5].

$$M = \frac{a_{max}}{a_{eff}} \quad (13)$$

**2.3. Nonlinear Modal Time-History Analysis.** To verify the NSA methods, nonlinear modal THA is used in this study. It is also known as fast nonlinear analysis (FNA) in SAP2000. The fundamental equilibrium equation of FNA can be expressed as [23, 24]

$$\mathbf{M}\ddot{\mathbf{u}}(\mathbf{t}) + \mathbf{C}\dot{\mathbf{u}}(\mathbf{t}) + \mathbf{K}\mathbf{u}(\mathbf{t}) + \mathbf{R}_{NL}(\mathbf{t}) = \mathbf{R}(\mathbf{t}), \quad (14)$$

where  $\mathbf{M}$ ,  $\mathbf{C}$ , and  $\mathbf{K}$  are the mass, proportional viscous damping, and stiffness matrices, respectively, the  $\mathbf{R}_{NL}(\mathbf{t})$  is the nonlinear object force vector from the sum of the forces in the nonlinear elements, and  $\mathbf{R}(\mathbf{t})$  is the applied load. At each point of time, the uncoupled modal equations are solved exactly within the elastic structural system, whereas forces within the predefined nonlinear DOF (indexed within  $\mathbf{R}_{NL}(\mathbf{t})$ ) are solved through an iterative process which converges to satisfy equilibrium. In (14), the nonlinear forces are treated as external loads and a set of load-dependent ritz (LDR) vectors,  $\Phi$ , is generated to accurately capture the effects of those forces.

The input earthquake time histories used in this study consist of nine horizontal ground motions with magnitude ranging from 6.53 to 7.6. All the data were obtained from Pacific Earthquake Engineering Research Center (PEER) [25]. Table 1 shows seven near-fault ground motions (simply assumed with a rupture distance <15 km) and 2 far-fault ground motions.

### 3. A Case Study of Numerical Modeling for a Typical Korean STS Container Crane

**3.1. Numerical Simulations.** The STS container crane considered in this study is located at a seaport in South Korea. Most of the structural components were made of stiffened hollow box sections, except for diagonal braces, which were tubes, and forestays and backstays, which were wide-flange

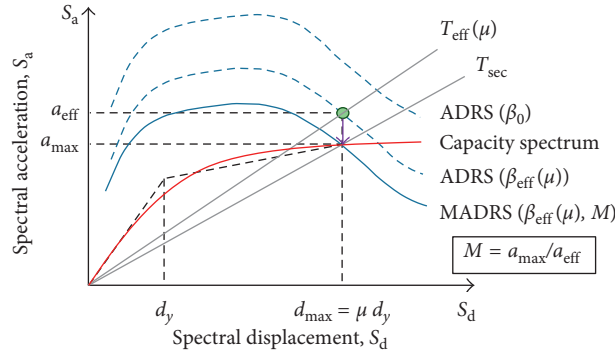


FIGURE 4: Modified acceleration-displacement response spectrum (MADRS).

TABLE 1: Unscaled ground motions recorded during several earthquakes.

Number (GM)	Earthquake name	Year	Station	Mag.	Mechanism	$R_{RUP}$ (km)	PGA (g)
1	Imperial Valley-02	1940	El Centro array #09	6.95	Strike slip	6.1	0.28
2	Imperial Valley-06	1979	El Centro array #06	6.53	Strike slip	1.4	0.45
3	Landers	1992	Barstow	7.28	Strike slip	35	0.13
4	Landers	1992	Yermo Fire station	7.28	Strike slip	24	0.24
5	Loma Prieta	1989	Gilroy-Gavilan Coll.	6.93	Rev. oblique	10	0.36
6	Northridge-01	1994	Newhall-Fire Sta.	6.69	Reverse	5.9	0.58
7	Northridge-01	1994	Sylmar-Converter Sta.	6.69	Reverse	5.4	0.62
8	Kobe, Japan	1995	KJMA	6.90	Strike slip	1.0	0.83
9	Chi-Chi, Taiwan	1999	TCU065	7.62	Rev. oblique	0.6	0.79

Note.  $R_{RUP}$  is the closest distance to the rupture plane (rupture distance).

shapes. The properties of materials comply with the Japanese industrial standards (JIS) JIS-SM490Y and JIS-STK490. The general dimensions of the crane, that is, outreach, crane gage/span, backreach, and height, are illustrated in Figure 1. A 3D FE model of the container was developed by the SAP2000 software package, as discussed earlier. In the FE representation, the total number of elements is 9916: 9912 frame elements and 4 gap elements. The forestays, backstays, and diagonal braces were assigned end releases; hence, these elements worked as truss elements. All nonstructural loads, that is, stairs, drive trucks, stowed pins, machinery house, 1/2 festoon, snag device, and boom hoist rope, were applied as concentrated or distributed loads. The modal shapes, natural periods, and frequencies of the first and third mode analyzed by the Ritz vectors method are shown in Figure 5.

**3.2. Selection of Seismic Demand.** Several boreholes were driven in the area of the seaport to consider the site soil conditions. The soil investigation report showed that the shear wave velocity for the top 30 m of ground for the five boreholes of the S-PS logging test were from 247 m/s to 447 m/s, as shown in Table 2. As a result, the soil profile types ranged from  $S_C$  to  $S_D$  according to Korean Building Code [26], as shown in Table 3. In this study, the soil type  $S_D$  was selected. For the crane's site, seismic zone *I* was considered to be appropriate, and a seismic zone factor  $S = 0.22$  g was assigned for the maximum considered earthquake (MCE), with a return period of 2400 years. The design acceleration response spectrum of soil type  $S_D$  was then developed

corresponding to site coefficients  $F_a$  (for short period) and  $F_v$  (for 1 s period), of 1.36 and 1.96, respectively. From the 5% damping elastic response spectrum of soil type  $S_D$ , as shown in Figure 6 (the red curve), the  $S_a$  at the fundamental period (mode 3 with  $T = 1.35$  s) is 0.21 g. To verify the results of nonlinear static analyses, the response spectra of nine recorded ground motions, as shown in Table 1, were then scaled to a spectral acceleration  $S_a$  of 0.21 g at the fundamental period. The scaled response spectra of the recorded ground motions and design response spectrum according to KBC 2016 are shown in Figure 6.

**3.3. Nonlinear Static Analysis and Damage Criteria.** The plastic hinges were assigned to the portal frame as illustrated in Figure 7 assuming that they develop at the end of the frames using concentrated plasticity model [23, 27]. The properties of plastic hinges are suggested in ASCE/SEI 41-13 [3]. For portal beams, the moment-curvature ( $M-\phi$ ) relationship is sufficient to model the hinges assuming no axial force is acting in them. Although interaction relationship of the axial force ( $P$ ) and the moments ( $M$ ) in both axes is required for portal columns of a 3D model, a pinned support is used for the pushover analysis to generate large portal deformations during autoincrement static pushing. The limit state obtained by pushover analyses can be applied to THA for a FE model using gap elements because the structural capacity is independent of the loading [28]. According to the structural performance levels and damage defined in ASCE/SEI 41-13 for buildings, the expected performance

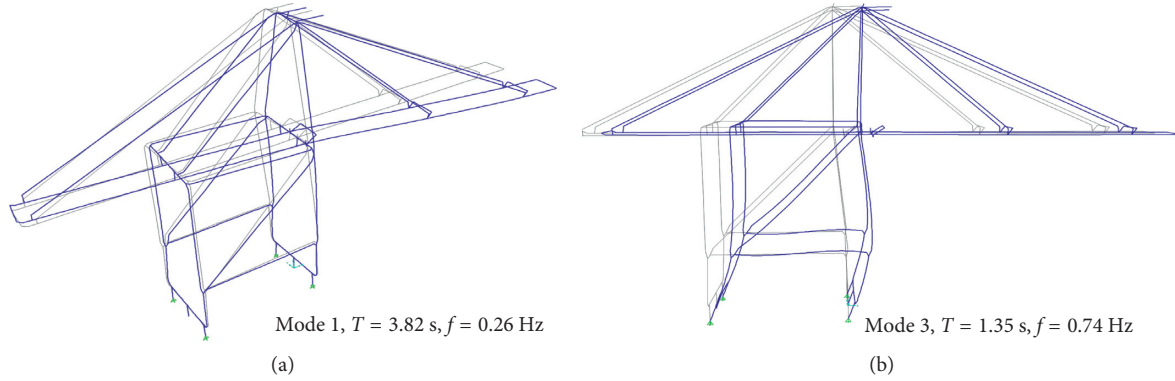


FIGURE 5: Numerical fundamental periods and modal shapes: (a) boom torsion and (b) portal sway.

TABLE 2: Soil investigation at a seaport in South Korea.

Boreholes	Shear wave velocity GL. -30 m, $v_s$ (m/s)	Soil types
BH-1	406	$S_C$
BH-2	252	$S_D$
BH-3	447	$S_C$
BH-4	247	$S_D$
BH-5	337	$S_D$

levels for steel container cranes (considering as steel moment frame, SMF) are shown in Table 4. In previous studies, derailment, defined as the reduction of the axial reaction of at least one leg base to be zero due to sufficient lateral loads, was considered as a damage state [28]. However, it is reported that a crane was repaired by repositioning it on the rails by jacking systems and mobile crane when it was derailed without any damage to the upper structure, that is, the repair of a Krupp crane at the Port of Oakland in the past in this way [29]. Hence, derailment is assumed to be the only form of the crane's movement without damage of the structure, and the portal frame is still considered to be elastic. Consideration of slight derailment is not considered as a damage state in this study. The damage state considered in this study focuses only on the structural behavior of the portal frame. Several other damage criteria for STS container cranes were suggested in previous studies [28, 30], as briefly summarized in Tables 5 and 6, based on observations of damages of container cranes subjected to past earthquakes, testing of scaled models on shaking table, and analyses of FE models.

For the NSA procedures, a concentrated force was applied at the boom level, as illustrated in Figure 7, under displacement-controlled analyses. The results of pushover analyses indicate that both columns reach the limit states at the same portal drift level even when the concentrated force is applied in the seaward or landward direction. In addition, since the cross sections of the waterside and landside legs are slightly different, they are expected to have similar stiffness and strength. As a result, Figure 7 indicates that both columns reach the immediate occupancy (IO), life safety (LS), and collapse prevention (CP) levels at a portal drift of approximately 1.6%, 1.8%, and 2.2%, respectively. In this study,

the complex stiffened box sections of the portal columns have been converted into unstiffened box section for simplicity. The section of the top of the portal columns is illustrated in Figure 8. The  $x$ -axis and  $y$ -axis are the trolley-travel direction and gantry-travel direction (along the rails), respectively. It is noted that the hollow box sections at the top of the portal columns of the Korean crane are smaller than those of crane J100, as mentioned in Table 6. Even the overall height of the Korean crane is greater than that of the J100. Past records indicate that there were few moderate to large earthquakes in Korea. Thus, an optimization of the general stiffness of the whole structure of a crane with less emphasis on the seismic effect can reduce the initial cost for the owner.

The ADRS diagrams consisting of both capacity and seismic demand are shown in Figure 9. The CSM and ELM were performed under the seismic demand of KBC 2016 with a selected damping ratio of 1.5% as suggested by Kosbab for a jumbo container crane [28, 31]. The results from both pushover methods are similar. The performance point of CSM indicates that the total base shear and maximum horizontal displacement at the top of the portal frame are 1691.82 kN and 10.6 cm, respectively. The total base shear and maximum displacement obtained from ELM are 1691.86 kN and 10.6 cm, respectively, with a ductility ratio  $\mu = 1.0$  and the modification factor  $M = 1$ .

**3.4. Dynamic Analyses.** For the input ground motions, the effect of vertical excitation is high when the spectral acceleration  $S_a$  of the crane (with a natural period of 0.3 s) is greater than 0.5 g, as observed in the experimental study by Kosbab. For lower  $S_a$ , the effect of vertical excitation on the portal drift is around 0.1% [28]. In this study, the vertical ground motions are neglected with the assumption that their amplitudes are attenuated by the effect of quay wall and local site.

The nonlinear modal THA was considered incorporating the  $P$ - $\Delta$  effect. The Rayleigh damping,  $\beta$ , which relates to the mass and stiffness matrix, was calculated by (15) and (16), considering mode 1 (boom torsion) and mode 3 (portal sway) as shown in Figure 5.

$$\beta = a_0 \frac{1}{2\omega_n} + a_1 \frac{\omega_n}{2}. \quad (15)$$

TABLE 3: Site classification of KBC 2016.

Soil types	Soil profile name	Average properties on the upper 30 m of the site profile		
		Shear wave velocity, $v_s$ (m/s)	Standard penetration resistance, $\bar{N}$ (blows/30 cm)	Soil undrained shear strength, $\bar{s}_u$ ( $\times 10^{-3}$ MPa)
$S_A$	Hard rock	>1500	—	—
$S_B$	Rock	760 to 1500	—	—
$S_C$	Very dense soil and soft rock	360 to 760	>50	>100
$S_D$	Stiff soil	180 to 360	15 to 50	50 to 100
$S_E$	Soft soil	<180	<15	<50

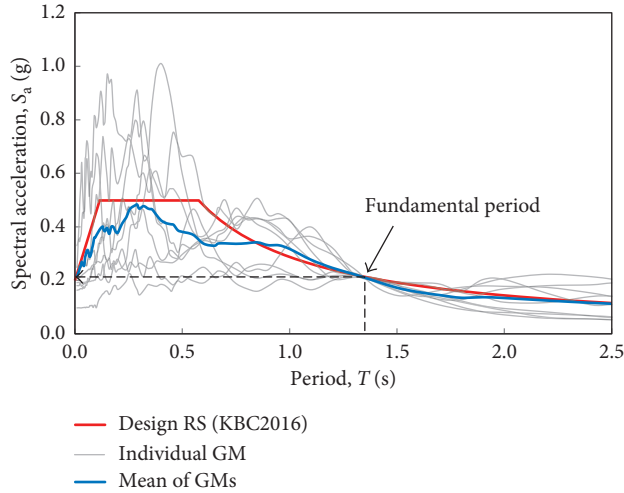


FIGURE 6: Scaled response spectra at the fundamental period.

Assuming that the frequencies of the two modes are  $\omega_i$  and  $\omega_j$ , having an equal damping ratio of 1.5%, the coefficients  $a_0$  and  $a_1$  can be obtained as follows:

$$a_0 = \beta \frac{2\omega_i\omega_j}{\omega_i + \omega_j}, \quad (16)$$

$$a_1 = \beta \frac{2}{\omega_i + \omega_j}.$$

During the operation, the crane is not fixed to rails or quay wall. For nonlinear THA, therefore, a gap link element is used to simulate the contact between trucks and rails. The gap element is activated when structures come closer and deactivated when they go far away [23]. The axial force will be set to zero when the portal leg is uplifted. The gap element does not disengage in the horizontal direction during uplifting. It is also the limit of this support boundary as discussed in detail by Kosbab [28]. However, a gap element (or a similar type called no tension element) was proven to be suitable to assess the uplift response as proposed by Chaudhuri et al. [32]. The results of the THA together with the NSA methods are discussed in detail in Section 4.

## 4. Results and Discussions

**4.1. Drift Response.** In contrast to the global drift analysis of a building at the roof level, most of the plastic hinges were

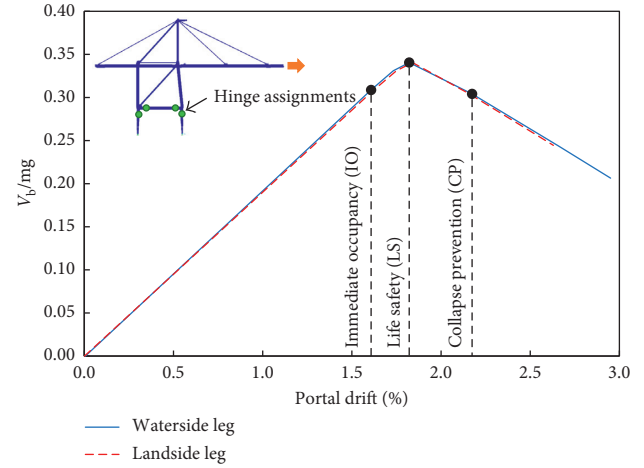


FIGURE 7: Pushover curve and limit states for typical Korean container crane.

observed to be developed in the portal frame of the crane during past earthquakes. Furthermore, the portal frame is the main structure to support the whole upper structures. Thus, the horizontal displacement or drift at the top of the portal frame is commonly considered [33, 34], as shown in Figure 10. The drift at the top of the portal frame (denoted as portal drift) of a container crane provides information on how much of the horizontal deformation occurs at the fundamental mode in the trolley travel direction. Besides measuring the portal drift, the drift at the top of upper legs and apex is monitored along with the corresponding height, as shown in Figure 10. The average drift of the portal frame, top of upper leg, and apex are estimated to be 0.61%, 0.26%, and 0.18%, corresponding to heights of 16.6 m, 47.1 m, and 76.6 m, respectively, in the trolley travel direction from THA under nine ground motions with scaled PGA ranging from 0.10 g to 0.32 g. The results of both pushover analyses using CSM and ELM, shown in Figure 9, are in good agreement with that of THA. In particular, the average portal drift of 0.64% is 0.03% larger than that of THA. On the other hand, by using the deformation of the fundamental mode, the displacements of the apex obtained from pushover analyses are significantly larger compared to the time-history analyses, with an error of over 16%. The portal drifts obtained from time-history and pushover analyses indicate that the crane behaviors are in the elastic state under seismic excitations, based on the performance levels in Figure 7. According to other performance levels and damage criteria

TABLE 4: Structural performance levels and damage based on ASCE/SEI 41-13 [3].

Elements	Immediate occupancy (IO)	Life safety (LS)	Collapse prevention (CP)
For vertical elements of SMFs (i.e., portal columns of the crane)	Minor local yielding at a few places. No fractures. Minor buckling or observable permanent distortion of members.	Hinges form. Local buckling of some beam elements. Severe joint distortion but shear connections remain intact. A few elements may experience partial fracture.	Extensive distortion of beams and column panels. Many fractures at moment connections, but shear connections remain intact.
Overall damage	Light	Moderate	Severe

TABLE 5: Damage criteria for cranes according to PIANC [30].

Level of damage	Degree I	Degree II	Degree III	Degree IV
Displacement	Without derailment	With derailment	Without overturning	Overturning
<i>Peak response stresses/strains</i>				
(i) Upper structures	Elastic	Elastic	Plastic ( $< \mu/\epsilon_{max}$ for upper structure)	Plastic ( $\geq \mu/\epsilon_{max}$ for upper structure)
(ii) Portal frame	Elastic	Plastic ( $< \mu/\epsilon_{max}$ for portal frame)	Without collapse	Collapse
(iii) Toe	Elastic	Damage to toe (including pull-out of vehicle, fracture of anchor/brakes)		

Note.  $\mu$  and  $\epsilon_{max}$  are the ductility factor and strain limit for the structure, respectively.

TABLE 6: Performance levels and limit states proposed by Kosbab [28].

Level of damage/elements	Derailment (DR)	Immediate use (IU)	Structural damage (SD)	Complete collapse (CC)
Whole structures	Derailed without any damage to the structure	Minor structural damage (not significantly impacts its operational capacity). Derailment may or may not have occurred	Extensive damage and will not be suitable for use without major repairs, but not collapse	Local buckling near the portal joints can quickly lead to global instability and eventual collapse
Portal frame	Elastic	Lower limit: elastic. High limit: some minor buckling of hollow sections (within the portal frame or not)	A portal deformation $<$ deformation at max. load capacity up to the point of ultimate ductility	Portal deformation surpasses the estimated point of max. ductility
Overall damage	Derailed	Minor damage	Major damage	Collapse
<i>Limit state in terms of portal drift (for reference)</i>				
(i) Crane J100	1.3%	2.0%	3.0%	4.5%
(ii) Crane LD100	—	1.5%	2.0%	3.0%
(iii) Crane LD50	1.5%	1.9%	2.5%	3.5%

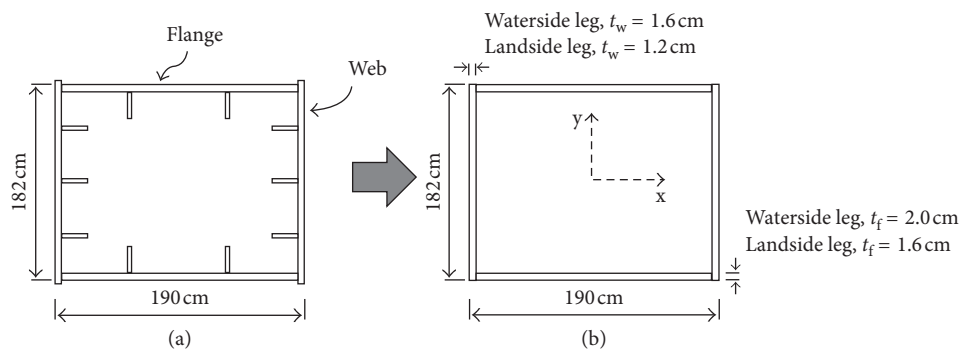


FIGURE 8: Hollow box elements: (a) original stiffened section and (b) simplified unstiffened section.

as summarized in Tables 5 and 6, the crane might work in the damage degree I as defined by PIANC and between DR and IU levels according to Kosbab’s proposal.

4.2. Total Base Shear. The total base shears obtained from CSM and ELM analyses are plotted in Figure 11. The total base shear is observed to be almost unrelated to the scaled

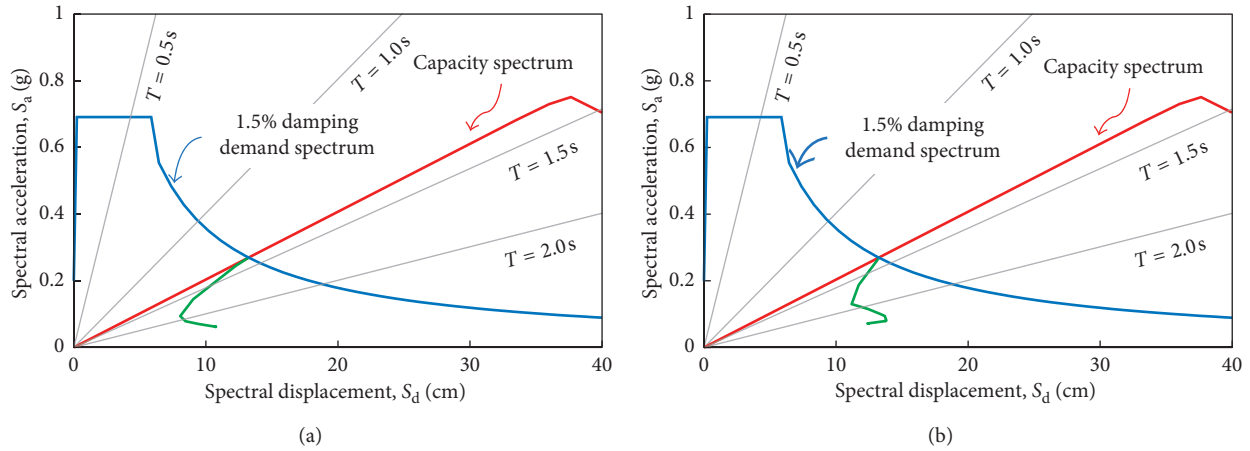


FIGURE 9: Pushover analyses: (a) CSM of ATC-40 and (b) ELM of FEMA 440.

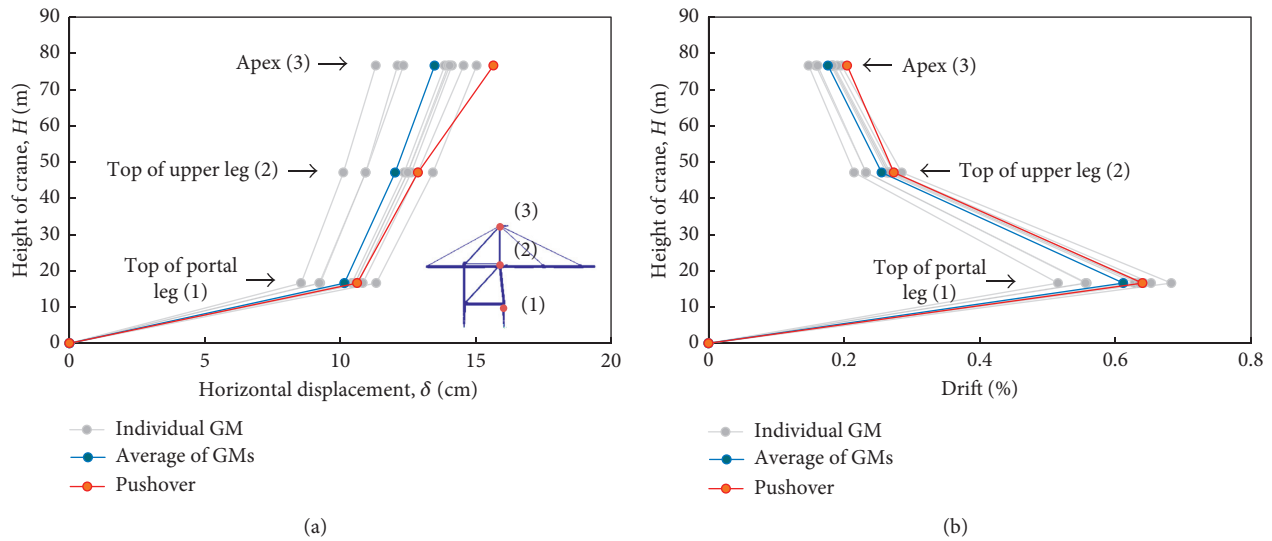


FIGURE 10: Height of crane versus (a) horizontal displacement and (b) drift.

PGA, magnitude, and rupture distance. For an example, the maximum total base shear is obtained from a minimum PGA ground motion, which is the Landers earthquake at Yermo Fire station in 1992 (GM-4) with a PGA of 0.1 g, or the earthquake with a relatively high PGA value of around 0.24 g (GM-2) at a short rupture distance (1.4 km), generates a lower structural response of 1415.73 kN, compared with the average value of 1674.93 kN for the nine ground motion excitations. The total base shears obtained from pushover methods show higher values than the average obtained from THA. In particular, the results for CSM and ELM are 1691.82 kN and 1691.86 kN, respectively, as mentioned in the previous section. From this observation, it can be concluded that the pushover methods are suitable for seismic analysis of a STS container crane.

**4.3. Uplift Behavior.** The uplifting of a crane will result in the redistribution of the load and will change the horizontal

displacement of the whole structure. The uplift is defined by two conditions: (1) the vertical displacement of the uplifted leg should be a positive value or zero (a negative value means the gap element is still “close”), and (2) the vertical reaction of the uplifted leg is zero. In this study, four portal legs, two landside legs (node 10 and 20) and two waterside legs (node 30 and 40) as shown in Figure 1, are considered to study uplift responses. Figure 12 shows the potential uplift (in terms of vertical response/displacement) and the time of occurrence of the landside leg (node 20) and waterside leg (node 30). It is noted that the term “potential uplift” is used because the full uplift was not occurred under the earthquake demand as discussed in Section 3.2, just a slight uplift might happen in this study. The full uplift of a crane leg is considered when a leg totally wins against the initial gravity load, which meets both conditions as mentioned above. It can be observed that the potential uplift of landside leg will occur sooner than that of the waterside leg, except for GM-3, GM-8, and GM-9. The reason could be that the center of total

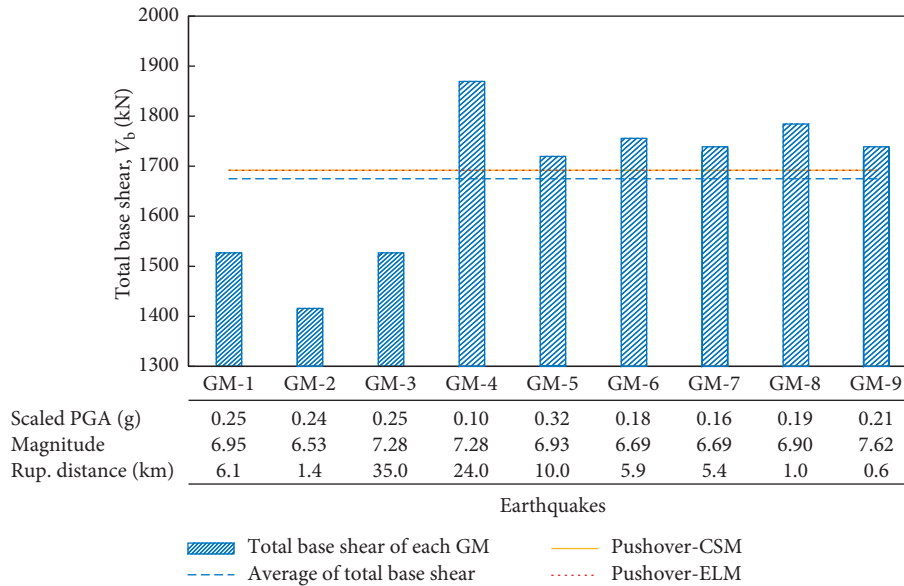


FIGURE 11: Total base shear versus earthquakes.

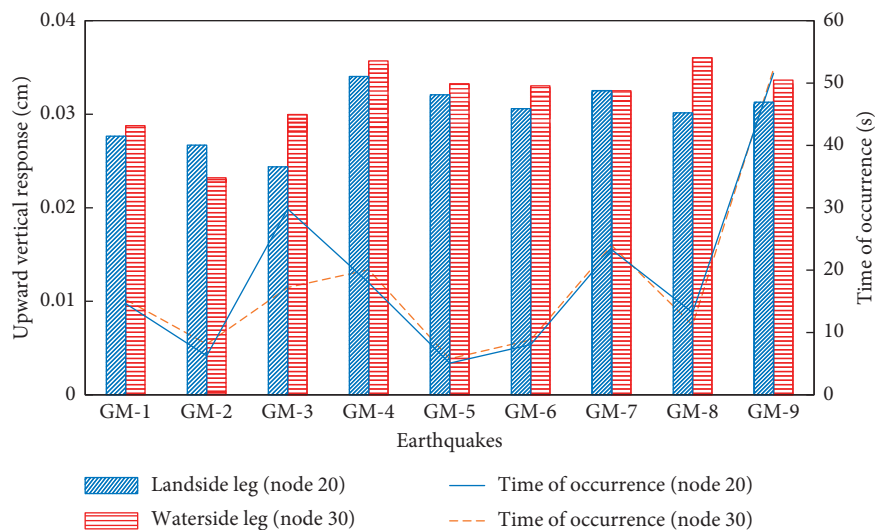


FIGURE 12: Upward vertical responses/displacements of the landside and waterside legs versus time of occurrence due to dynamic analysis (gravity analysis not included).

mass is not at the center of the two portal legs. The total mass concentrates closer to the waterside legs than the landside legs. Thus, the first uplift will occur at the landside legs. When a leg is uplifted, the axial force of the opposite leg will increase significantly. In particular, in this study, it is observed that the maximum axial compressive force increases up to 1204.96 kN on the landside leg (node 10) due to the upward vertical response/displacement of the waterside leg when excited by the Landers earthquake (GM-4) at Yermo Fire station. It is interesting to note that the increase of the axial force of node 10 is approximately 49.5% compared with the initial gravity force of that node of around 2434.86 kN.

On the other hand, the vertical response of crane leg is observed to be strongly influenced by the ground motions' characteristics. Figure 13 indicates that the amplitude of

vertical response/displacement decays significantly with time after reaching the peak value when subjected to short-duration earthquakes such as GM-2, GM-5, GM-6, and GM-8. However, the vertical response maintains large amplitude for a long time when excited by long-duration earthquakes even when the acceleration amplitude is not as high as in GM-4, GM-7, and GM-9. It can be stated that a long-duration earthquake may generate uplift and for a long period of time even when the input ground motion is of low amplitude. Assessment of the uplift behavior is an important issue that should be considered in the seismic design of a container crane to predict the overloading on the portal legs. It is noted that a positive value of the vertical response shown in Figure 13 means that the crane's leg moves upward, whereas a negative value indicates a compression (downward

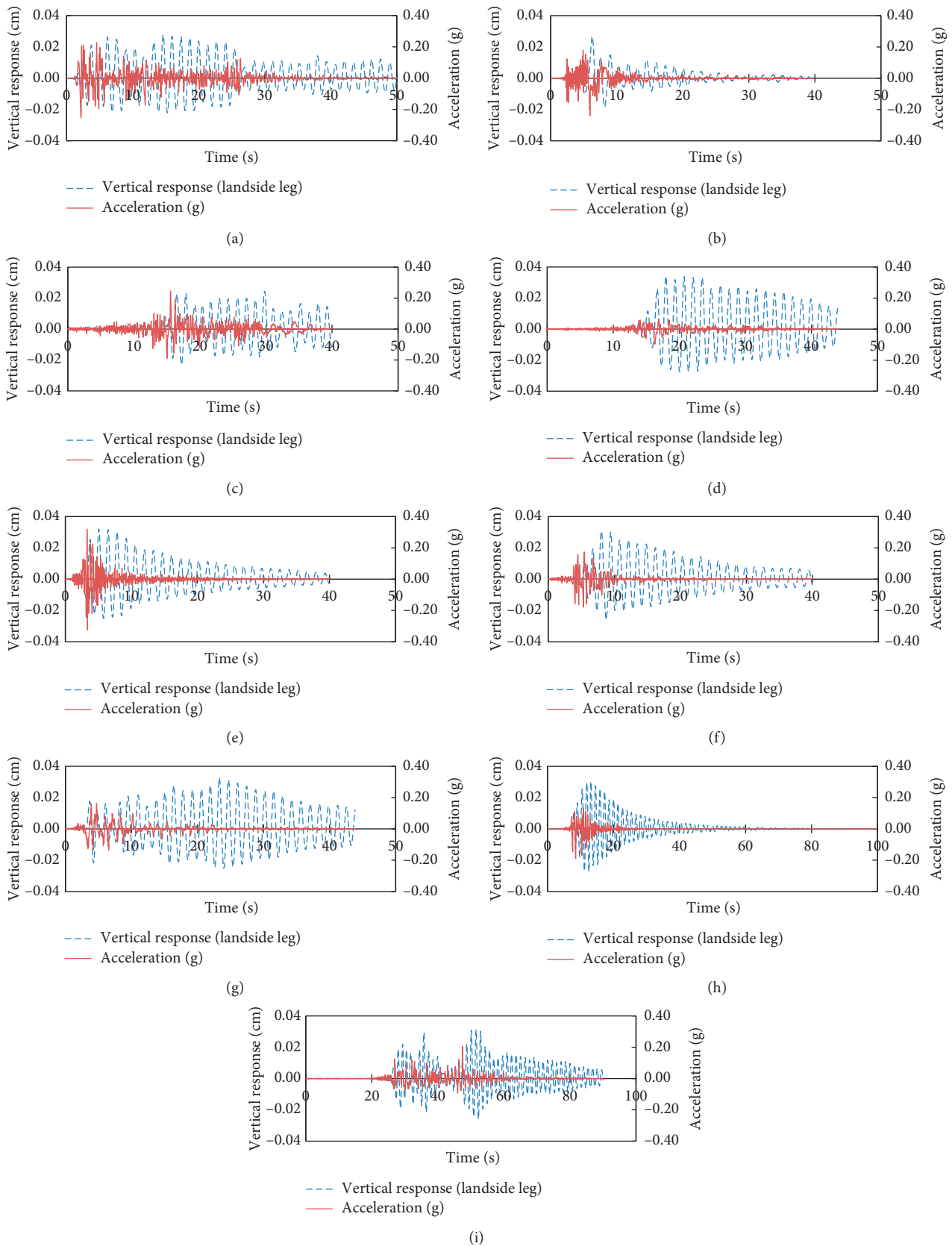


FIGURE 13: Time-history vertical response of the landside leg (node 20). (a) Imperial Valley-02 (GM-1). (b) Imperial Valley-06 (GM-2). (c) Landers, Barstow (GM-3). (d) Landers, Yermo Fire Station (GM-4). (e) Loma Prieta (GM-5). (f) Northridge-01, Newhall (GM-6). (g) Northridge-01, Sylmar (GM-7). (h) Kobe, Japan (GM-8). (i) Chi-Chi, Taiwan (GM-9).

movement), comparing with the state after analyzing gravity load. When taking into account both static analysis (gravity load analysis) and dynamic analysis, the value of vertical displacement is still negative in all cases, indicating no full uplift occurrence. For example, under subjected by the earthquake GM-4 (Landers at Yermo fire station), the landside leg (node 20) results in a positive value of 0.034 cm for dynamic analysis and a negative value of  $-0.058$  cm for gravity load analysis; thus, the value considering both cases of analysis is approximately  $-0.024$  cm by summation. This means that the crane might be slightly uplifted and will be fully uplifted if the value of displacement reaches zero, and the vertical reaction of the crane leg is zero as well.

## 5. Conclusions

This study represents a preliminary investigation for the seismic behavior of a typical Korean STS container crane. The complex seismic response of the crane is estimated by representing it by a 3D FE model. Nonlinear time-history analysis and both CSM and ELM pushover analyses methods are used to analyze the crane and compare the results. Several key observations can be made based on the results obtained from this study. They are as follows.

The conventional CSM and ELM are found to be sufficient to analyze a STS container crane. In particular, the relative errors of the portal drift and total base shear obtained from pushover methods are 4.6% and 1.0%, respectively, comparing with those using the nonlinear time-history analyses. However, the horizontal displacements of the apex of the crane obtained from CSM and ELM appear to be overestimated because these methods consider only the fundamental mode, whereas the nonlinear time-history analysis uses the superposition principle of multiple modes.

Assessment of uplift response is an important issue that should be considered in the seismic analysis of a container crane. It is clearly seen in this study that the axial force of the landside legs increases nearly 50% of the initial gravity force, as the waterside legs are slightly uplifted. Thus, a gap element, which is integrated into most of the commercial software, is appropriate for modeling base support to study the uplift behavior. On the other hand, the uplift response is strongly influenced by the characteristics of the ground motions. The potential uplift can have large amplitude for a long time when excited by long-duration earthquakes even when the acceleration amplitude may not be high.

The portal drifts of the typical Korean STS container crane corresponding to performance levels of IO, LS, and CP, as defined in ASCE/SEI 41-13, are 1.6%, 1.8%, and 2.2%, respectively. These values can be used as damage limits for the fragility analysis.

## Data Availability

The data used to support the findings of this study are available from the corresponding author upon request.

## Conflicts of Interest

The authors declare no conflict of interest.

## Acknowledgments

This research was supported by Basic Science Research Program through the National Research Foundation of Korea (NRF) funded by the Ministry of Education (2017R1D1A3B03032854) and by Ministry of public Administration and Security as Disaster Prevention Safety Human resource development Project and was also a part of the project titled "Development of performance-based seismic design technologies for advancement in design codes for port structures," funded by the Ministry of Oceans and Fisheries, Korea.

## References

- [1] G. H. Powell, *Static Pushover Methods-Explanation, Comparison and Implementation*, 2013, <https://wiki.csiamerica.com/display/perform/Static+pushover+methods+-+explanation+%2C+comparison+and+implementation>.
- [2] ATC 40, *Seismic Evaluation and Retrofit of Concrete Buildings*, Applied Technology Council, Redwood, CA, USA, 1996.
- [3] ASCE/SEI 41, *Seismic Evaluation and Retrofit of Existing Buildings*, American Society of Civil Engineers, Reston, VA, USA, 2013.
- [4] Eurocode 8, *Design of Structures for Earthquake Resistance Part 1: General Rules, Seismic Actions and Rules for Buildings EN 1998*, European Committee for Standardization (CEN), Brussels, Belgium, 2004.
- [5] FEMA 440, *Improvement of Nonlinear Static Seismic Analysis Procedures*, Applied Technology Council (ATC-55 Project), Federal Emergency Management Agency, Washington, DC, USA, 2006.
- [6] C. Casarotti and R. Pinho, "An adaptive capacity spectrum method for assessment of bridges subjected to earthquake action," *Bulletin of Earthquake Engineering*, vol. 5, no. 4, pp. 377–390, 2007.
- [7] P. Fajfar, "Capacity spectrum method based on inelastic demand spectra," *Earthquake Engineering and Structural Dynamics*, vol. 28, no. 9, pp. 979–993, 1999.
- [8] Y.-Y. Lin and K. Chang, "An improved capacity spectrum method for ATC 40," *Earthquake Engineering and Structural Dynamics*, vol. 32, no. 13, pp. 2013–2025, 2003.
- [9] X. Mingkui, D. Yinfeng, L. Gang, and C. Guangjun, "An improved capacity spectrum method based on inelastic demand spectra," in *Proceedings of 4th International Conference on Earthquake Engineering*, Taipei, Taiwan, October 2006.
- [10] A. Chopra and R. Goel, "Evaluation of NSP to estimate seismic deformation: SDF systems," *Journal of Structural Engineering*, vol. 126, no. 4, pp. 482–490, 2000.
- [11] S. Freeman, "Development and use of capacity spectrum method," in *Proceedings of 6th U.S. NCEE Conference on Earthquake Engineering*, pp. 1–12, Seattle, WA, USA, June 1998.
- [12] H. Sucuoglu and M. S. Gunay, "Generalized force vectors for multi-mode pushover analysis," *Earthquake Engineering and Structural Dynamics*, vol. 40, no. 1, pp. 55–74, 2011.
- [13] E. Kalkan and S. K. Kunnath, "Adaptive modal combination procedure for nonlinear static analysis of building structures," *Journal of Structural Engineering*, vol. 132, no. 11, pp. 1721–1731, 2006.
- [14] M. Ćosić and S. Brčić, "Iterative displacement coefficient method: mathematical formulation and numerical analyses," *Grđevinar*, vol. 65, no. 3, pp. 199–211, 2013.

- [15] S. Taghavi-pour, T. Majid, and T. Lau, "Assessment of non-linear static (pushover) procedures using time-history direct integration analysis," *Australian Journal of Basic and Applied Sciences*, vol. 7, no. 8, pp. 468–479, 2013.
- [16] S. Freeman, J. Nicoletti, and J. Tyrell, "Evaluations of existing buildings for seismic risk—a case study of Puget Sound Naval Shipyard, Bremerton, Washington," in *Proceedings of the 1st US National Conference on Earthquake Engineering*, Oakland, CA, USA, June 1975.
- [17] FEMA 274, *NEHRP Commentary on the Guidelines for the Seismic Rehabilitation of Buildings*, Federal Emergency Management Agency, Washington, DC, USA, 1997.
- [18] A. Guyader and W. Iwan, *Automated Capacity Spectrum Method of Analysis*, California Institute of Technology, Pasadena, CA, USA, 2004.
- [19] A. K. Chopra and R. K. Goel, "Capacity-demand-diagram methods based on inelastic design spectrum," *Earthquake Spectra*, vol. 15, no. 4, pp. 637–656, 1999.
- [20] B. Gencturk and A. S. Elnashai, "Development and application of an advanced capacity spectrum method," *Engineering Structures*, vol. 30, no. 11, pp. 3345–3354, 2008.
- [21] M. Causevic and S. Mitrovic, "Comparison between non-linear dynamic and static seismic analysis of structures according to European and US provisions," *Bulletin of Earthquake Engineering*, vol. 9, no. 2, pp. 467–489, 2011.
- [22] M. Ferraioli, A. Lavino, and A. Mandara, "An adaptive capacity spectrum method for estimating seismic response of steel moment-resisting frames," *International Journal of Earthquake Engineering*, Anno XXXIII, Speciale CTA 2015, no. 1-2, pp. 47–60, 2015, <http://ingegneriasismica.org/wp-content/uploads/2016/09/Ferraioli-Nuova-impaginazione.pdf>.
- [23] SAP2000, *Linear and Nonlinear Static and Dynamic Analysis and Design of 3D Structures: Basic Analysis Reference Manual*, CSI, Berkeley, CA, USA, 2006.
- [24] E. Wilson, *Three-Dimensional Static and Dynamic Analysis of Structures: A Physical Approach with Emphasis on Earthquake Engineering*, CSI, Berkeley, CA, USA, 2002.
- [25] J. Huh, A. Haldar, and S. Yim, "Effect of uncertainty in frequency content and strong motion duration on structural seismic risks," *International Journal of Ocean System Engineering*, vol. 2, no. 1, pp. 25–37, 2012.
- [26] Architectural Institute of Korea, *Korean Building Code*, Architectural Institute of Korea, Seoul, Republic of Korea, 2016.
- [27] J. Huh, Q. H. Tran, A. Haldar, I. Park, and J.-H. Ahn, "Seismic vulnerability assessment of a shallow two-story underground RC box structure," *Applied Sciences*, vol. 7, no. 7, p. 735, 2017.
- [28] B. D. Kosbab, *Seismic Performance Evaluation of Port Container Cranes Allowed to Uplift*, Georgia Institute of Technology, Atlanta, GA, USA, 2010.
- [29] Liftech, *On the Mend*, Liftech Consultants Inc., Oakland, CA, USA, 2008.
- [30] PIANC, *Seismic Design Guidelines for Port Structures*, A.A. Balkema, Leiden, The Netherlands, 2001.
- [31] L. Jacobs, B. Kosbab, R. Leon, and R. DesRoches, "Seismic behavior of a jumbo container crane including uplift," *Earthquake Spectra*, vol. 27, no. 3, pp. 745–773, 2011.
- [32] S. Chaudhuri, D. Karmakar, U. Na, and M. Shinozuka, "Seismic performance evaluation of container cranes," in *Proceedings of ATC & SEI 2009 Conference on Improving the Seismic Performance of Existing Buildings and Other Structures*, San Francisco, CA, USA, December 2009.
- [33] L. Jacobs, *Shake Table Experiments for the Determination of the Seismic Response of Jumbo Container Cranes*, Georgia Institute of Technology, Atlanta, GA, USA, 2010.
- [34] T. Kanayama and A. Kashiwazaki, "An evaluation of uplifting behavior of container cranes under strong earthquakes," *Transactions of the Japan Society of Mechanical Engineers*, vol. 64, no. 618, pp. 100–106, 1998, in Japanese.

## Research Article

# Earthquake Response Control of Double-Layer Truss Walls by means of Innovative Fuse Connections

Koichiro Ishikawa 

University of Fukui, Fukui-shi, Japan

Correspondence should be addressed to Koichiro Ishikawa; [ishikawa@u-fukui.ac.jp](mailto:ishikawa@u-fukui.ac.jp)

Received 8 May 2018; Accepted 8 July 2018; Published 15 August 2018

Academic Editor: David M. Boyajian

Copyright © 2018 Koichiro Ishikawa. This is an open access article distributed under the Creative Commons Attribution License, which permits unrestricted use, distribution, and reproduction in any medium, provided the original work is properly cited.

This study deals with partial cylindrical truss walls equipped with damper connections due to horizontal earthquake motions. The damper connection consists of an aluminum ball joint, an aluminum hub, and a steel bolt. A ductile elongation of the steel bolt due to a tensile stress is expected by avoiding the brittle collapse. The study proposes a fuse-type connection by means of yield of the steel bolt due to tension stress realized by the ductile failure collapse mechanism of the wall-type spatial structure. The proposed truss wall with the fuse-type connection can realize a deformation of nodes within the restriction for avoiding a nonstructural member damage. It is confirmed in the dynamic elastoplastic analysis that the control of the dynamic collapse mechanism such as the steel bolt elongation can avoid a brittle collapse mechanism such as a chain of member buckling. The evaluation method is also proposed by means of the limit displacement considering a ductility factor of the steel bolt within 2.0.

## 1. Introduction

This study deals with the dynamic elastoplastic analysis considering a member buckling, and the fuse-type connection consists of an aluminum ball joint, an aluminum hub, and a steel bolt. A ductile elongation of the steel bolt due to a tensile stress is expected by avoiding the brittle collapse in our previous paper [1–3]. The study proposes a fuse-type connection by means of yield of the steel bolt due to tension stress realized by the ductile failure collapse mechanism of the wall-type spatial structure.

The seismic response characteristics of spatial structures such as roof and wall types depend on their form and support conditions, and several reviews [4, 5] and guidelines [6–13] quoting many studies have been published depending on the performance of building structures. Several performance prediction methods have been developed for this purpose; however, the earthquake resistance capacity of spatial structures requires the variation of the form and the support condition, and it is very difficult to apply them to wall-type spatial structures. For the performance design, several prediction methods such as a pushover analysis and an adaptive capacity spectrum method have been developed for structures such as buildings and bridges [14–18].

The control of the dynamic collapse mechanism is also proposed to improve the earthquake resistance capacity by a damper connection such as the steel bolt elongation.

Effect of the member buckling and yield elongation of the steel bolt on the seismic response out of the plane is shown in comparison with the response of the wall structure subjected to the horizontal earthquake motions. The earthquake evaluation method is also proposed considering the dynamic collapse mechanism. A validity of the proposed method is shown by means of the accuracy between the analysis and the estimation.

## 2. Examples of Aluminum Truss Structures

Since earthquake resistance standards in Japan were improved, buildings which were designed on the basis of old seismic standards before 1981 need to be reinforced quickly on the basis of the exiting new ones.

The aluminum braces are useful for seismic retrofitting of existing buildings because they achieve good workability in the erection site and reduce the seismic loading and additional loads on the foundations due to their lightweight and aluminum alloy members owing to their long-term corrosion resistance.

Figure 1 shows double-layer latticed walls and roofs made of an aluminum alloy truss system, and the walls

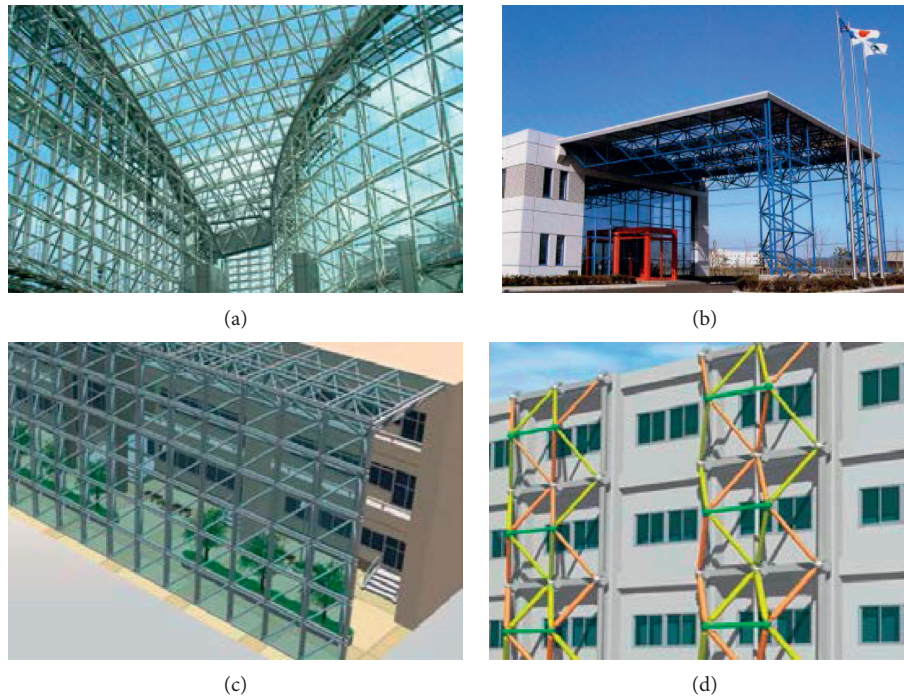


FIGURE 1: Aluminum truss walls and retrofit.

resist in-plane shearing load in an earthquake. Figures 1(a) and 1(b) show the entrance canopy of the office and the atrium at the entrance of the railroad station, and they are L-shaped application of an aluminum truss wall. The truss walls achieve structural rigidity and strength on seismic loading, and the slender members with cladding prevent daylight. Figures 1(c) and 1(d) are CG images of seismic retrofit of RC school buildings using the aluminum truss walls.

### 3. Connection Design of an Aluminum Truss Wall

We propose two types of connection systems: an aluminum ball-jointed truss wall and aluminum pin-connected braces. As described in more detail below, both systems have improved in their plastic deformability to resist excessive seismic loads. In our previous paper [1], the brittle collapse mechanism of the truss wall structure to resist lateral loads has been investigated to evaluate the earthquake resistance capacity.

Figure 2 illustrates the aluminum alloy ball-jointed truss connection used to retrofit; this nodal connection consists of aluminum parts and a steel bolt. All aluminum parts are extruded, and in heat-treated aluminum alloy 6061-T6, the end plug is welded at its edge to the strut by using a friction welding method. Friction welding, which is one of the various welding processes, is known for high joint efficiency and high reliability in comparison with MIG or TIG welding. The collar transfers the compression stress, and the steel bolt

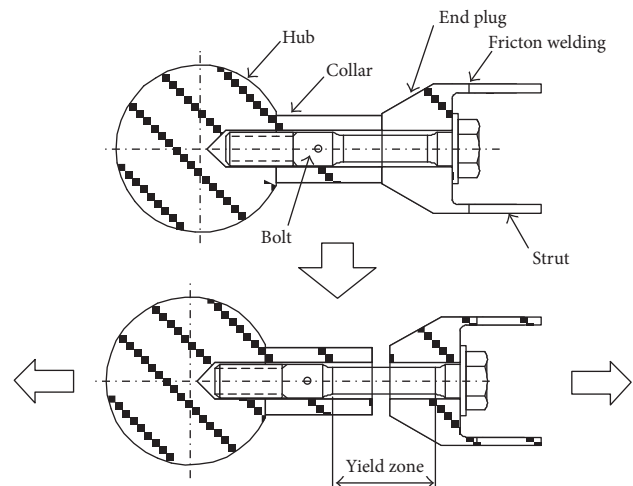


FIGURE 2: Yielding bolt mechanism.

transfers the tension stress. The bolt is made of high-strength steel; the figure of the bolt is slimmed in the axle of the bolt as shown in Figure 2.

The connection of the truss wall is designed by means of the condition such as  $N_{cr} > N_u$ , where  $N_{cr}$  is a member buckling or an ultimate strength of the welded joint and  $N_u$  is an ultimate strength of the bolt. The bolts are able to extend by excessive tensile loading in a major earthquake; therefore, the truss wall structure achieves a good hysteretic curve as described in Figure 3. In our previous paper [2], it is investigated that the fuse-type connection realizes the tension yield of the steel bolt before the member buckling occurs.

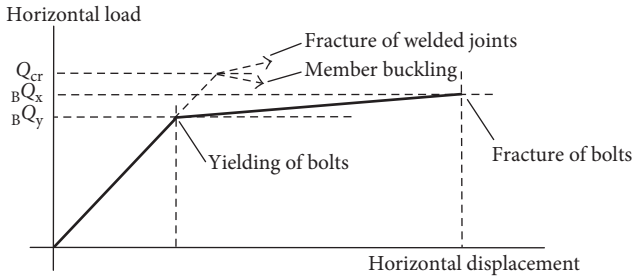


FIGURE 3: Hysteretic curve of the truss wall used to retrofit.

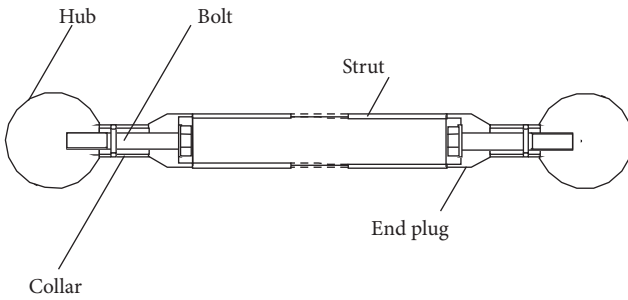


FIGURE 4: Truss system.

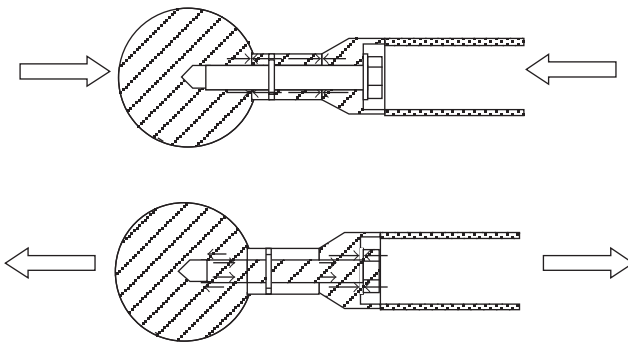


FIGURE 5: Mechanism of stress transfer.

#### 4. Truss Members including Joints and Modeling

The fuse connection consists of two hubs, two collars, two bolts, and a strut, as shown in Figure 4. The steel bolt resists against the tension axial stress, and the collar resists against the compression axial stress, as far as the resistance mechanism of the axial stress between the hub and strut is concerned. Figures 5–7 show the numerical analysis model in this study.

#### 5. Hysteresis Models of the Truss Member

The present analysis adopts an assumption that struts buckle due to compression and yield under tension. Figure 8 shows the hysteresis curves used for the slenderness ratio of a member. The maximum compressive stress  $\sigma_{cr}$  is determined using (1) which considers member crookedness

and the residual stresses existing in the strut. Figure 9 shows the hysteresis curves of the steel bolt which yields under tension and slips under compression. The hub resists against the compression instead of the yielding bolt. The yield stress  $\sigma_y$  and Young’s modulus  $E$  are taken to be 210 MPa and 70 GPa, respectively. The maximum compressive stress  $\sigma_{cr}$  is calculated by (1), and the maximum tension stress of the weld fracture is taken to be  $0.71\sigma_y$  due to a tension axial stress. The initial tension stress is not introduced in the steel bolt:

$$\frac{\lambda}{\Lambda} \leq 1.0 : \sigma_{cr} = \frac{F}{\{1 - 0.5(\lambda/\Lambda)^2\}},$$

$$\frac{\lambda}{\Lambda} > 1.0 : \sigma_{cr} = \frac{F}{\{2(\lambda/\Lambda)^2\}}, \quad (1)$$

$$\Lambda = \sqrt{\frac{\pi^2 E}{0.5F}} = \frac{37.17}{\sqrt{F}} = 81.1.$$

#### 6. Time-History Analysis of the Truss Wall

Geometric and material nonlinearity is considered in the time-history analysis of the truss walls subjected to the horizontal earthquake motion of El Centro NS (PGA: 5.61 m/sec<sup>2</sup>). The Rayleigh damping matrix is used in this analysis. The damping factor  $h = 0.02$  is used for first and second vibration modes in the damping matrix. The numerical integration method uses the Newmark method.  $\beta = 1/4$  is used in this study because  $\beta = 1/4$  will be unconditionally stable for the seismic response analysis.

6.1. Analysis Model of the Double-Layer Partial Cylindrical Truss Wall. The truss wall has a configuration as shown in Figure 10. The length is 14 m with 7 grids, and the height is 7.2 m with 4 grids. The bottom nodes are constrained for all directions. The top nodes are free for the horizontal plane ( $X$  direction). They are restrained for the vertical direction ( $Y$  direction) and out of the plane ( $Z$  direction).

An aluminum alloy A6061-T6 is used in the strut, and a high tensile strength steel SCM435 with the yield strength of 649 N/mm<sup>2</sup> is used in the connection steel bolt. A truss model is used in the analysis. The model is a lightweight structure made of an aluminum alloy. The structure can bear the dead load, which is confirmed as the static design.

Table 1 shows the member length  $L$  (mm), the slenderness ratio  $\lambda$ , the cross-sectional secondary radius  $i$  (mm), and the sectional area  $A$  (mm<sup>2</sup>). The member is determined by the earthquake-proof design using the base shear coefficient of 1.0. And the strength of pullout of the bolt such as the yield axial force is also shown in Table 1.

6.2. Vibration Characteristics and Seismic Responses of the Truss Wall. The natural period and the vibration mode of

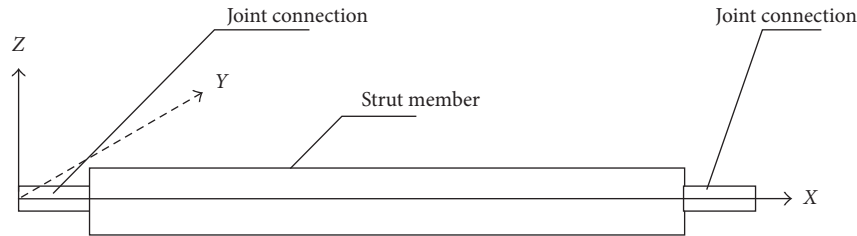


FIGURE 6: Components of the member.



FIGURE 7: Truss model of each element for analysis.

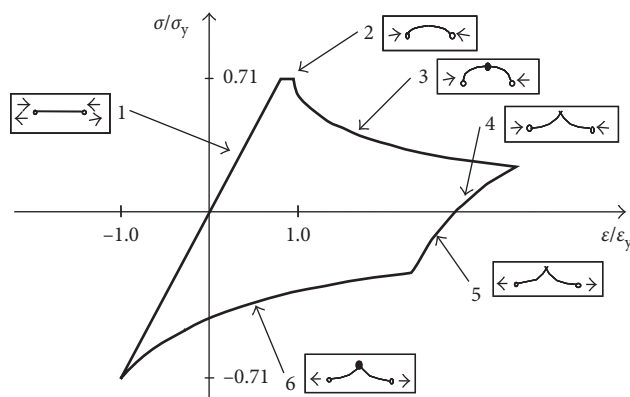


FIGURE 8: Hysteresis model of the aluminum strut.

the two walls with the 1 m and 0.4 m wall depths are obtained by means of the eigenvalue analysis, respectively. The first and third natural periods  $T_1$  and  $T_3$  are shown in Figure 11. The corresponding vibration modes are also shown in Figure 11, respectively. It is seen that the shear deformation mode of a wall appears in the first vibration mode of the two walls and the third mode of the wall with the 1 m depth. The out-of-plane shape in the third mode of the wall with the 0.4 m depth also appears due to the lower bending rigidity than in the wall with the 1 m depth. The study focuses on the out-of-plane deformation of the thin depth wall subjected to earthquake motions.

**6.3. Dynamic Response Behavior of the Truss Walls Subjected to Earthquake Motions.** In the present study, the earthquake resistance capacity of the dome is evaluated by investigating the maximum horizontal displacement  $\delta_{max}$  at the top of the wall subjected to horizontal earthquake motions with the peak ground acceleration (PGA) multiplied by the PGA amplification factor  $\lambda_E$ . The damage limit artificial earthquake motion with a phase characteristic of the El Centro NS wave is used in the seismic response analysis. The PGA is taken to be  $1.12 \text{ m/sec}^2$ . The relationship between  $\lambda_E$  and  $\delta_{max}$  of the two walls with different wall depths is shown in Figures 12 and 13. The

location of the steel bolt yield is shown in Figure 14 at the beginning of the bolt yield and the member buckling, respectively. It is seen in the results that the bolt yield precedes the member buckling and the linear relationship between  $\lambda_E$  and  $\delta_{max}$  is kept within the plastic region from the beginning of the bolt yield to the beginning of the member buckling. This means that the response control can be feasible by means of the fuse-type connection such as the steel bolt yielding elongation.

The time-history energy response of the restoring force of the member and the damping of the structure to the in-plane (X) and out-of-plane (Z) directions is shown in Figures 15 and 16, respectively. It is seen in the wall with depths that the structural damping almost absorbs the input energy due to the seismic response just before the member buckling occurs. The member buckling induces the absorbed energy in the case of the wall with 1 m depth subjected to earthquake motions with  $\lambda_E = 9.4$ . The out-of-plane also consumes energy greater due to member buckling as seen in Table 2. On the contrary, a sudden dynamic collapse of the wall with the 0.4 m depth occurs just after the member buckling because of the bending rigidity out of the plane with the less wall depth.

The maximum strains of the steel connection bolt in both depths are 2 times less than the first yield strain as shown in Figure 17. It is confirmed in the study that all members in both walls are also 2 times less than the first yield strain.

## 7. Evaluation Method of the Response Estimation by means of the Limit Displacement

The comparison between the PGA amplification factor  $\lambda_E$  of the input earthquake motion and the maximum displacement  $\delta_{max}$  to the horizontal in-plane (X) direction at the top of the wall with the 1 m and 0.4 m wall depths is shown in Figure 18 by means of the dynamic analysis. And the proposed estimation method uses the limit displacement. The limit displacement  $\delta_{ud}$  is defined in the study as  $1.2\delta_{y1}$  in the red line in Figure 18. The structural yield displacement  $\delta_{y1}$  is the horizontal in-plane displacement  $\delta$  at the top of the wall just on the first occurrence of the steel bolt yield. It is also noticed that a ductility factor of the steel bolt is taken to be within 2.0 at the limit displacement  $\delta_{ud}$ . This is the reason that the limit displacement  $\delta_{ud}$  is taken to be  $1.2\delta_{y1}$ . The structural buckling displacement

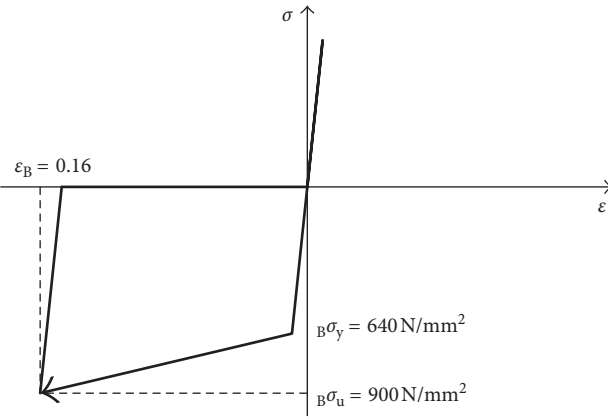


FIGURE 9: Hysteresis model of the steel bolt.

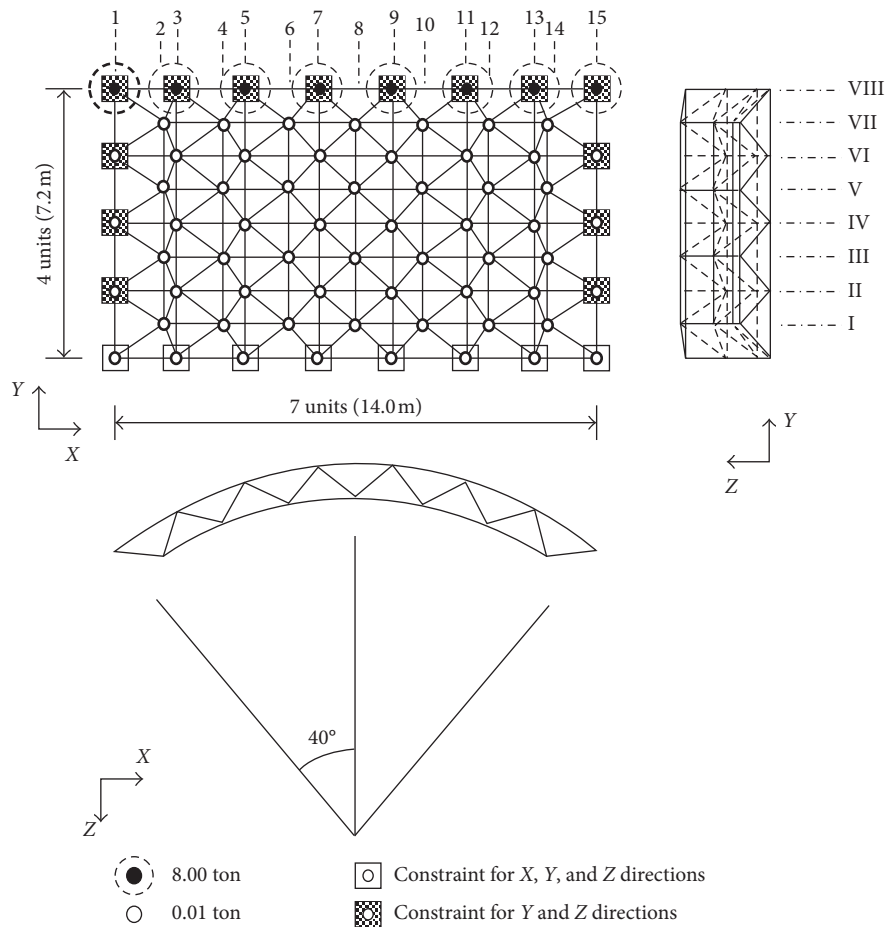


FIGURE 10: Analysis model of the double-layer partial cylindrical truss wall.

$\delta_{y2}$  is the horizontal in-plane displacement  $\delta$  at the top of the wall just on the first occurrence of the strut member buckling.

The evaluation method of the response estimation by means of the limit displacement is the first to calculate the  $\delta_{max}$  using the linear relationship between  $\lambda_E$  and  $\delta_{max}$ . It can be evaluated for engineers that the dynamic collapse occurs in the case of  $\delta_{max}$  larger than  $\delta_{ud}$ . The estimation value  $\lambda_{EU}$  is practically calculated by the proposed method using the

response analysis. The proposed method can be applied to the wall with an aspect ratio of the shear-dominant deformation type.

### 8. Conclusions

This study deals with the partial cylindrical truss wall with the damper joint connection due to horizontal earthquake motions. It is confirmed in the dynamic elastoplastic analysis

TABLE 1: Member characteristics of the truss wall.

Wall depth: 1.0 m					
	Strut (mm)	Sectional area (mm <sup>2</sup> )	Cross-sectional secondary radius (mm)	Member length (mm)	Slenderness ratio/limit slenderness ratio
Chord member of X direction	$\phi 180 \times t21$	10489.8	56.7	1705	0.367
Chord member of Y direction	$\phi 180 \times t21$	10489.8	56.7	1400	0.305
Web member	$\phi 150 \times t12$	5202.5	49.0	1162	0.240
	Bolt (mm)	Sectional area (mm <sup>2</sup> )	Member length (mm)	Minimum elongation (%)	Yield axial force (kN)
Chord member of X direction	$\phi 30.0$	706.9	200	16	452.3
Chord member of Y direction	$\phi 30.0$	706.9	200	16	452.3
Web member	$\phi 15.0$	254.5	267	16	162.9
Wall depth: 0.4 m					
	Strut (mm)	Sectional area (mm <sup>2</sup> )	Cross-sectional secondary radius (mm)	Member length (mm)	Slenderness ratio/limit slenderness ratio
Chord member of X direction	$\phi 180 \times t21$	10189.8	56.7	1705	0.367
Chord member of Y direction	$\phi 180 \times t21$	10189.8	56.7	1400	0.305
Web member	$\phi 150 \times t12$	5202.5	49.0	994	0.240
	Bolt (mm)	Sectional area (mm <sup>2</sup> )	Member length (mm)	Minimum elongation (%)	Yield axial force (kN)
Chord member of X direction	$\phi 30.0$	706.9	200	16	452.3
Chord member of Y direction	$\phi 30.0$	706.9	200	16	452.3
Web member	$\phi 15.0$	254.5	228	16	162.9

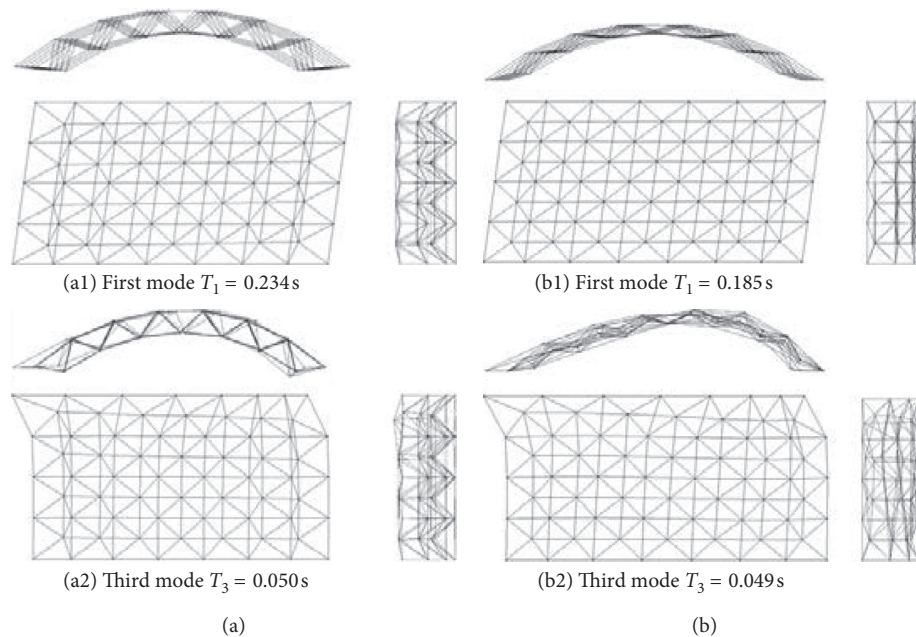


FIGURE 11: The first and third vibration modes and natural periods. (a) Wall depth: 1.0 m. (b) Wall depth: 0.4 m.

that the control of the dynamic collapse mechanism such as the steel bolt elongation can avoid a brittle collapse mechanism such as a chain of member buckling. Effect of the member buckling and yield elongation of the steel bolt on the seismic response out of the plane is also shown in

comparison with the response of the wall structure subjected to the horizontal earthquake motions.

The evaluation method is also proposed by means of the limit displacement considering a ductility factor of the steel bolt within 2.0. This means that the response control can be

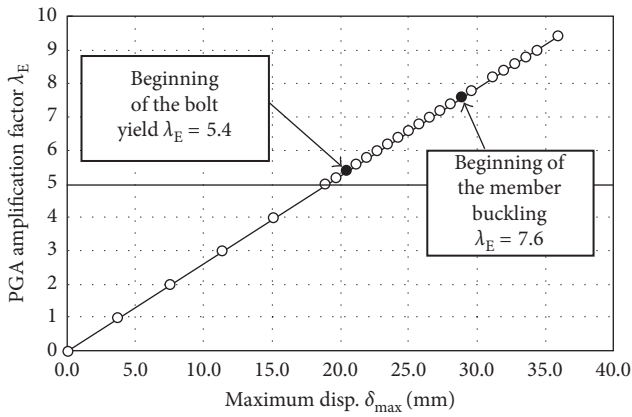


FIGURE 12:  $\lambda_E$  and  $\delta_{max}$  of the wall depth with 1 m.

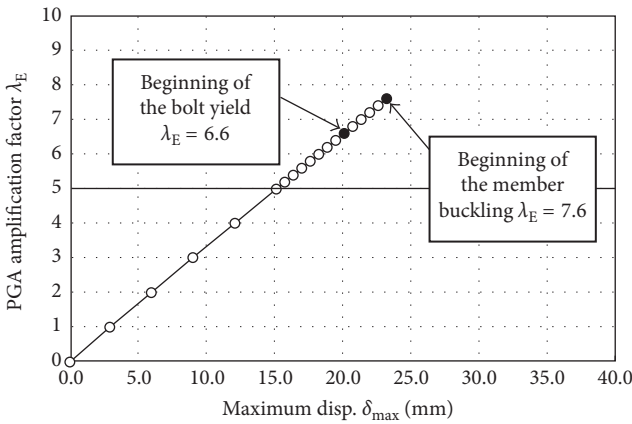


FIGURE 13:  $\lambda_E$  and  $\delta_{max}$  of the wall depth with 0.4 m.

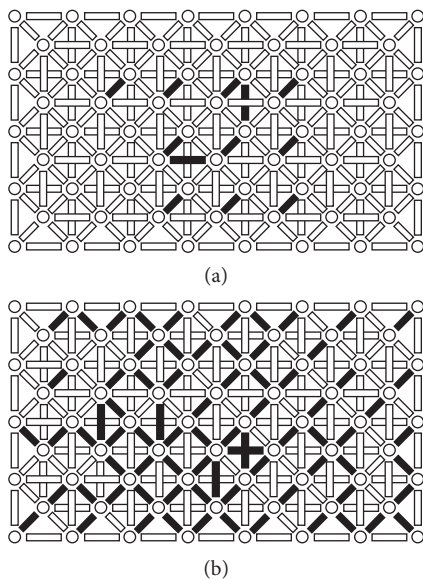


FIGURE 14: Continued.

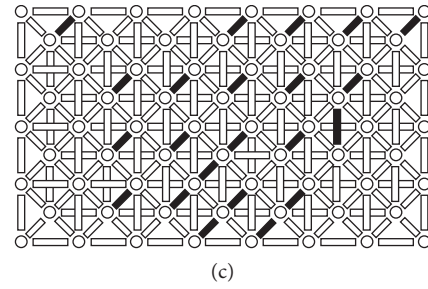


FIGURE 14: Location of the bolt yield of the wall depth with 1 m and 0.4 m. (a) Case of  $\lambda_E = 7.4$  (1 m depth). (b) Case of  $\lambda_E = 9.4$  (1 m depth). (c) Case of  $\lambda_E = 7.6$  (0.4 m depth).

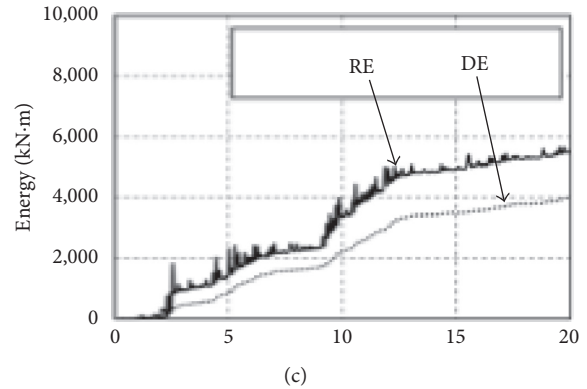
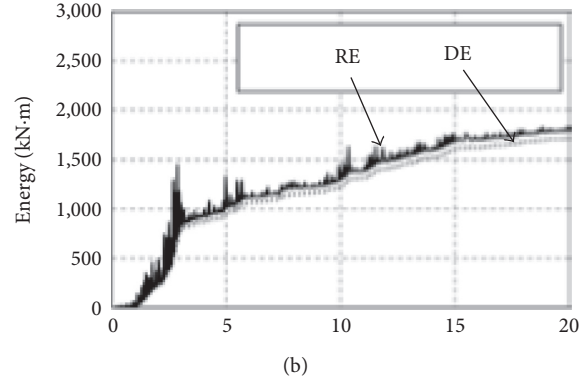
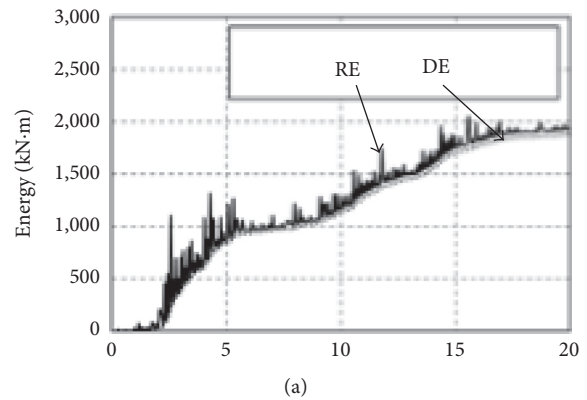


FIGURE 15: Time-history energy response of the restoring force of the member and the damping of the structure to the in-plane (X) direction component. (a) 1 m wall depth ( $\lambda_E = 7.4$ ). (b) 0.4 m wall depth ( $\lambda_E = 7.6$ ). (c) 1 m wall depth ( $\lambda_E = 9.4$ ). RE = restoring force energy; DE = damping energy.

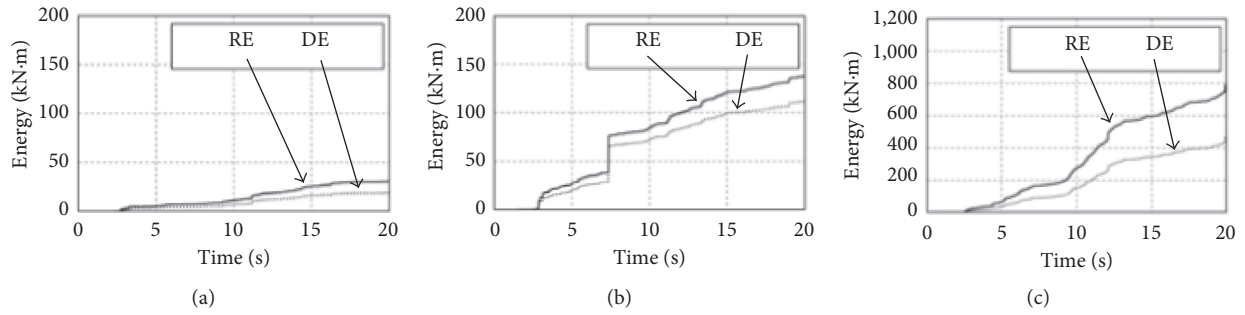


FIGURE 16: Time-history energy response to the out-of-plane (Z) direction component. (a) 1 m wall depth ( $\lambda_E = 7.4$ ). (b) 0.4 m wall depth ( $\lambda_E = 7.6$ ). (c) 1 m wall depth ( $\lambda_E = 9.4$ ). RE = restoring force energy; DE = damping energy.

TABLE 2: Ratio of the total energy in the out-of-plane (Z) direction to that in the in-plane (X) direction.

Failure type	Wall depth (m)	$\lambda_E$	Consumption energy in the in-plane direction $E_i$ (kN·m)	Consumption energy in the out-of-plane direction $E_o$ (kN·m)	$E_o/(E_i + E_o)$ (%)
Steel bolt yield	1.0	7.4	1937.8	30.33	1.54
	0.4	7.6	1814.7	137.83	7.06
Member buckling	1.0	9.4	5588.6	790.69	12.39

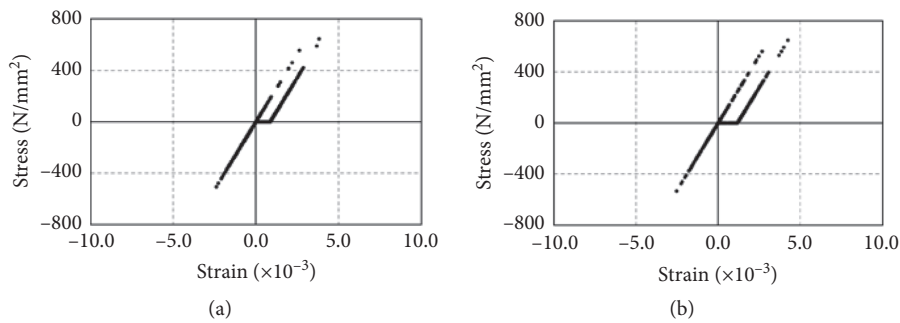


FIGURE 17: Relationship between stress and strain of the web member. (a) 1 m wall depth before the member buckling ( $\lambda_E = 7.4$ ). (b) 0.4 m wall depth before the collapse ( $\lambda_E = 7.6$ ).

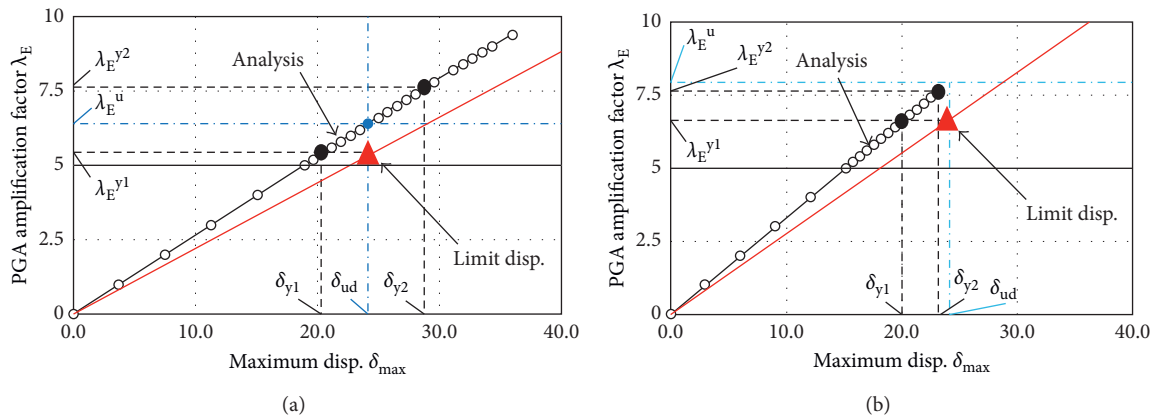


FIGURE 18: Comparison between the limit displacement and the analysis. (a) 1 m wall depth. (b) 0.4 m wall depth.

feasible by the damper connection such as the steel bolt elongation due to tension stress.

### Data Availability

The data used to support the findings of this study are available from the corresponding author upon request.

### Conflicts of Interest

The author declares that there are no conflicts of interest.

### Acknowledgments

This work was supported by JSPS KAKENHI (Grant no. 18K04427).

### References

- [1] K. Ishikawa, S. Okubo, Y. Hiyama, and S. Kato, "Evaluation method for predicting dynamic collapse of double layer latticed space truss structures due to earthquake motion," *International Journal of Space Structures*, vol. 15, no. 3, pp. 249–257, 2000.
- [2] S. Okubo, Y. Hiyama, K. Ishikawa, R. Wendel, and L. Fischer, "Load capacity and plastic deformable ability of aluminum alloy double layer latticed wall subjected to plane load," in *Proceedings of the IASS Symposium*, Nagoya, Japan, 2001.
- [3] K. Ishikawa and S. Kato, "Elastic-plastic buckling analysis of reticular dome subjected to earthquake motion," *International Journal of Space Structures*, vol. 12, no. 3-4, pp. 205–215, 1997.
- [4] Y. Taniguchi, P. L. Gould, and M. Kurano, "Earthquake input energy at dynamic collapse for double-layer cylindrical lattice roofs," *Journal of the International Association for Shell and Spatial Structures*, vol. 49, no. 2, 2008.
- [5] F. Fan, S. Z. Shen, and G. A. R. Parke, "Theoretical and experimental study of vibration reduction in braced domes using a viscous damper system," *International Journal of Space Structures*, vol. 19, no. 4, pp. 195–202, 2004.
- [6] M. Midorikawa, "Performance-based seismic design provisions for buildings in Japan," in *Proceedings of the IASS 2005*, vol. 1, pp. 307–316, Bucharest, Romania, September 2005.
- [7] G. C. Giuliani, "Overview on the dynamic control of structures," in *Proceedings of the IASS, 2002*, pp. 561–567, Warsaw, Poland, 2002.
- [8] Z. P. Zeng, "Structural analysis and design of the latticed shell for Fujian Gymnasium," *Journal of Spatial Structures*, vol. 13, no. 2, pp. 44–48, 2007.
- [9] L. Ilzarbe, M. J. Álvarez, E. Viles, and M. Tanco, "Practical applications of design of experiments in the field of engineering: a bibliographical review," *Quality and Reliability Engineering International*, vol. 24, no. 4, pp. 417–428, 2008.
- [10] European Committee for Standardization (CEN), *Eurocode 8: Design of Structures for Earthquake Resistance Part 1: General Rules, Seismic Actions and Rules for Buildings (EN 1998-1: 2004)*, European Committee for Standardization (CEN), Brussel, Belgium, 2004.
- [11] FEMA-356, *NEHRP Guidelines for the Seismic Rehabilitation of Buildings*, Building Seismic Safety Council, FEMA, Washington, DC, USA, 2000.
- [12] H. G. Park, T. Eom, and H. Lee, "Factored modal combination for evaluation of earthquake load profiles," *Journal of Structural Engineering*, vol. 133, no. 7, pp. 956–968, 2007.
- [13] S. K. Kunnath, "Identification of modal combinations for nonlinear static analysis of building structures," *Computer-Aided Civil and Infrastructure Engineering*, vol. 19, no. 4, pp. 246–259, 2004.
- [14] R. K. Goel and A. K. Chopra, "Extension of modal pushover analysis to compute member forces," *Earthquake Spectra*, vol. 21, no. 1, pp. 125–139, 2005.
- [15] J. C. Reyes and A. K. Chopra, "Three dimensional modal pushover analysis of buildings subjected to two components of ground motion, including its evaluation for tall buildings," *Earthquake Engineering and Structural Dynamics*, vol. 40, no. 7, pp. 789–806, 2011.
- [16] A. K. Chopra and R. K. Goel, "A modal pushover analysis procedure for estimating seismic demands for buildings," *Earthquake Engineering and Structural Dynamics*, vol. 31, no. 3, pp. 561–582, 2002.
- [17] G. Gupta and S. K. Kunnath, "Adaptive spectra-based pushover procedure for seismic evaluation of structures," *Earthquake Spectra*, vol. 16, no. 2, pp. 367–392, 2000.
- [18] C. Casarotti and R. Pinho, "An adaptive capacity spectrum method for assessment of bridges subjected to earthquake action," *Bulletin of Earthquake Engineering*, vol. 5, no. 3, pp. 377–390, 2007.

## Research Article

# An Investigation of Damage Mechanism Induced by Earthquake in a Plate Girder Bridge Based on Seismic Response Analysis: Case Study of Tawarayama Bridge under the 2016 Kumamoto Earthquake

Mya Nan Aye,<sup>1</sup> Akira Kasai,<sup>2</sup> and Mitsuhiro Shigeishi <sup>2</sup>

<sup>1</sup>Graduate School of Science and Technology, Kumamoto University, Kumamoto 860-8555, Japan

<sup>2</sup>Faculty of Advanced Science and Technology, Kumamoto University, Kumamoto 860-8555, Japan

Correspondence should be addressed to Mitsuhiro Shigeishi; [shigeishi@civil.kumamoto-u.ac.jp](mailto:shigeishi@civil.kumamoto-u.ac.jp)

Received 28 February 2018; Revised 15 April 2018; Accepted 11 June 2018; Published 12 August 2018

Academic Editor: Mikayel G. Melkumyan

Copyright © 2018 Mya Nan Aye et al. This is an open access article distributed under the Creative Commons Attribution License, which permits unrestricted use, distribution, and reproduction in any medium, provided the original work is properly cited.

This paper reports a damage survey and seismic analysis of a bridge. In the first part, the damage survey of some bridges that were affected by the 2016 Kumamoto Earthquake was discussed. Among these bridges, the Tawarayama Bridge, which is a plate girder bridge located very close to an active fault line, was particularly considered. This bridge incurred severe damage because of the earthquakes' epicenters very close to the bridge. The damage mechanism that can occur in this type of bridge was elucidated. During the damage survey, parts of Tawarayama Bridge were examined to determine the damage in order to examine the factors of occurrence and damage mechanism. In the second part, the seismic responses of Tawarayama Bridge were analyzed using ABAQUS software, and beam elements were applied for the structural members. Firstly, the time-history responses were analyzed using both longitudinal and transverse direction earthquake ground motions separately and simultaneously to investigate the dynamic response of the bridge. Both undamped and damped conditions were considered. For the dynamic response analysis, the recorded earthquake acceleration data of Ozu Station were applied for both undamped and damped conditions considering both east-west (EW) and north-south (NS) directions simultaneously and the damped condition for these directions separately. In addition, a damped model was analyzed by applying design earthquake input data obtained from the Japanese Seismic Design Specifications for Highway Bridges. Consequently, five cases were established for seismic response analysis. Subsequently, the seismic responses of Tawarayama Bridge were investigated, and the behavior of the lower lateral members was examined considering the observed buckling of these members during the damage survey. The field survey and dynamic response analysis indicate that the buckling design of the lower lateral members should be considered in the future design of bridges.

## 1. Introduction

A series of earthquakes occurred in Kumamoto, Japan, in April 2016. The first earthquake with a magnitude of 6.5 (Japan Meteorological Agency (JMA) seismic intensity of 7) occurred on April 14. This earthquake was a foreshock, and it was followed by a mainshock with a magnitude of 7.3 (JMA seismic intensity of 7) on April 16. Within two days after the mainshock, more than 140 aftershocks, including at least 11 with a magnitude of 4.5 and one with a magnitude of 6, occurred in this region [1]. Mashiki town and Higashi Ward of Kumamoto were severely affected as the epicenters

were located there. Many buildings and transportation infrastructures were damaged by these earthquakes. According to the records, the total fatality after the mainshock was 69 individuals, 364 individuals were seriously injured, and 1,456 suffered minor injuries, as of June 30, 2016. Overall, 8,044 buildings totally collapsed, 24,274 were half or partially destroyed, and 118,222 suffered moderate damage. Many bridges too were damaged [2, 3].

This study focuses on the damage incurred by bridges, especially plate girder bridges, during this series of earthquakes. Usually, buckling design is rarely considered in the design of lower lateral members of bridges. However, after the 2016

Kumamoto Earthquake, considering the observed buckling of the lower lateral members during the damage survey, concerns arose about the need for a buckling design for these members. It is essential to confirm the buckling of lower lateral members in a bridge by analytical methods to decide whether the buckling design of these members should be incorporated in future bridge designs. Therefore, a seismic response analysis of a plate girder bridge, whose lower lateral members underwent buckling, was carried out using the recorded earthquake motion data of the 2016 Kumamoto Earthquake.

The first section of this paper presented the introduction. The second one details the damage survey of bridges. The third one presents an overview of a plate girder bridge, namely, Tawarayama Bridge. The next two sections present the damage survey and seismic response analysis of Tawarayama Bridge. The response of the bridge subjected to the recorded motion of the 2016 Kumamoto Earthquake is then presented. Finally, some important findings and conclusions of the site survey and numerical analysis are presented.

## 2. Damage Survey of Bridges

*2.1. Summary of Earthquake Data.* According to the JMA, seven earthquakes with a high intensity (four with a magnitude of 5.4–5.9, two with a magnitude of 6.4–6.5, and one with a magnitude of 7.3) occurred in the same area between April 14 and 16. The epicenter was at Mashiki town in Kumamoto Prefecture [1].

Table 1 lists the time of occurrence, magnitude, and maximum seismic intensity of the largest earthquakes that occurred on April 14–16. Figure 1 shows a map presenting the locations of Kumamoto, Mashiki, and Mount Aso.

*2.2. Overview of Bridge Damage.* Among the 3,000 bridges in Kumamoto Prefecture, about 40 bridges, including Aso Bridge and Minami-Aso Bridge, were affected severely by the earthquake. Furthermore, 70 bridges under the Kumamoto Prefecture administration were damaged. In addition, the JR Kyushu Shinkansen (bullet train) was suspended because of the damage to the bridge on Kyushu Expressway. Although most bridge piers were not damaged after the foreshock, many bridges were severely damaged after the mainshock. In the Kumamoto region, pier settlement was the characteristic damage observed [2, 3]. Observation of the locations of damaged bridges on the map shows that most of these bridges were concentrated near faults, as shown in Figure 2 [4].

Bridges on Tawarayama Bypass, which is an important route connecting Kumamoto and Miyazaki Prefectures, were also damaged. Figure 2(a) is derived from an active fault database compiled by the National Institute of Advanced Industrial Science and Technology [4]. The thin red line at the center of the figure and the thick blue line show the Futagawa active fault and Prefectural Road No. 28, respectively. There are six bridges on Tawarayama Bypass; most of these bridges are curved bridges as the route passes through mountains. They were constructed in compliance with the 1996 version of specifications for highway bridges.

TABLE 1: Time of occurrence, magnitude, and maximum seismic intensity [1].

Time of occurrence	Magnitude	Maximum seismic intensity
4/14 21:26	6.5	7
4/14 22:07	5.8	6 (lower)
4/15 00:03	6.4	6 (upper)
4/16 01:25	7.3	7
4/16 01:45	5.9	6 (lower)
4/16 03:55	5.8	6 (upper)
4/16 09:48	5.4	6 (lower)

*2.3. Overview of Damage to Ookirihata Bridge.* Ookirihata Bridge is a five-span continuous curved bridge with a total length of 265.4 m. Girders supported by laminated rubber bearings and rubber joint load bearings are used as end supports. During this large-scale earthquake, the laminated rubber bearings underwent shear destruction, and the girder experienced a relative displacement of about 70 cm in the transverse direction. The main girder section prevented direct contact (collision) in the abutment parapet, preventing damage to the superstructure. This can be clearly seen in Figure 3(a). Figure 3(b) shows that a large step occurred at the expansion joint of Ookirihata Bridge [2, 3]. The bridge collapse-prevention cable was also deformed in a direction perpendicular to the bridge's axis. This led to rupture, and the girder fell down from its rubber bearing. This situation is depicted in Figure 3(c).

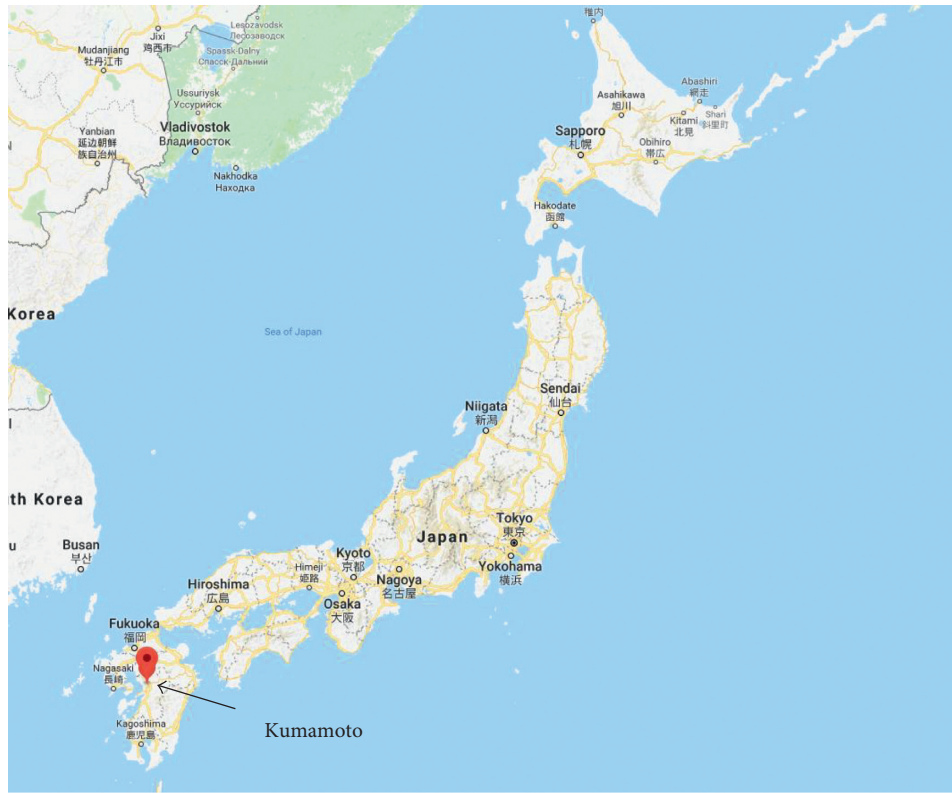
*2.4. Overview of Damage in Other Bridges.* Among the damaged bridges, Aso Bridge and Furo First Bridge, situated on the prefectural road across the Kyushu Expressway, collapsed totally. Aso Bridge collapsed because of a huge landslide, about 710 m high, with a dip angle of 33°. Figures 4(a) and 4(b) show the collapse of Aso Bridge and Furo First Bridge, respectively.

Some bridges, such as Hatanaka Dai-ichi Bridge, had to be urgently demolished. In Hatanaka Dai-ichi Bridge, the tops of piers completely collapsed, as shown in Figure 5. Figure 6 shows the damaged condition of Yokoe Bridge in Yatsushiro. In this bridge, the intermediate pier settled by about 2.3 m, causing the detachment of the bridge and sidewalk stairs [2, 3].

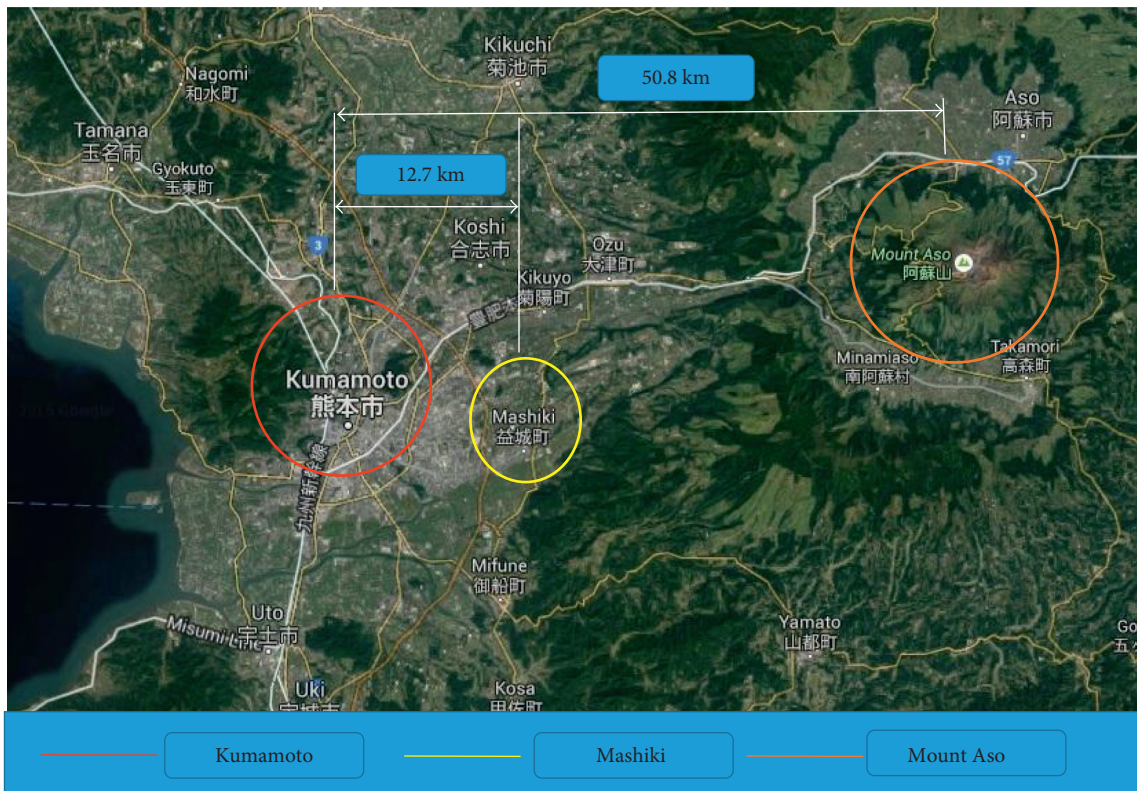
## 3. Overview of Tawarayama Bridge

Tawarayama Bridge is located on Prefectural Road No. 28, which is a route connecting Takamori with the vicinity of the downtown area of Kumamoto city center. It is a three-span girder bridge with a total length of 140 m, a maximum span length of 61.5 m, and an effective width of 8.5 m. The substructure consists of inverted T-type abutments (A1 and A2) and overhung piers (P1 and P2), and the foundation consists of caisson piles. The location of Tawarayama Bridge is shown in Figure 7. Figure 8 shows the longitudinal profile of the bridge. Figure 9 shows the plan view of the bridge; here, A1 represents the abutment on the Kumamoto side and A2 represents that on the Takamori side.

Furthermore, in the plan view, piers P1 and P2 represent the piers on the Kumamoto side and Takamori side,

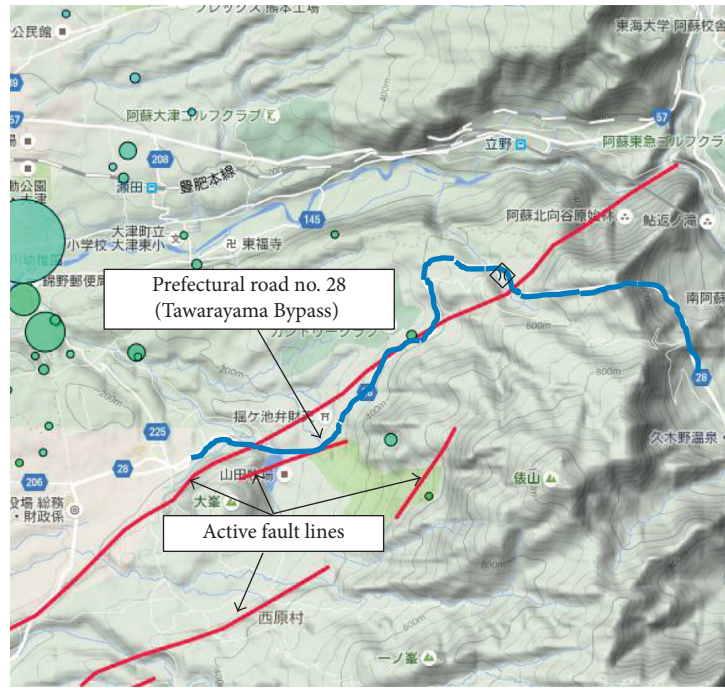


(a)

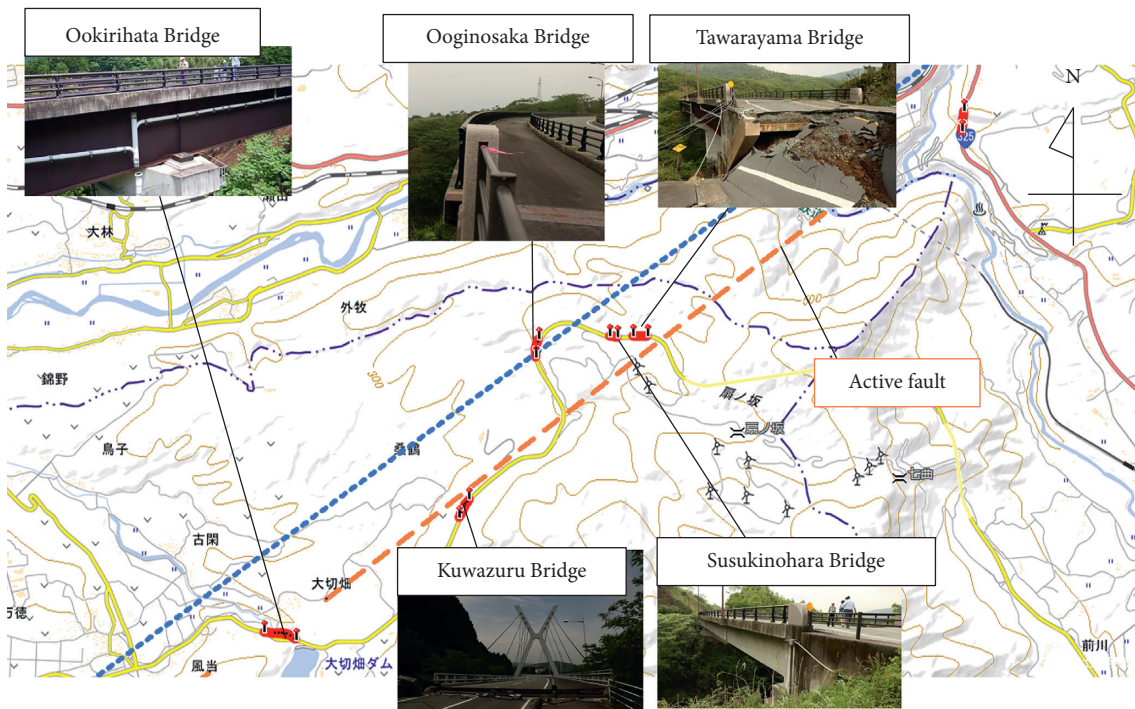


(b)

FIGURE 1: (a) The location of Kumamoto. (b) Distances between Kumamoto and Mashiki and Mount Aso. Source: <https://www.google.co.jp>.



(a)



(b)

FIGURE 2: (a) Futagawa fault [4]. (b) Tawarayama Bypass and locations of bridges.

respectively. Figure 10 shows a cross section of the superstructure. Abutments A1 and A2 are constructed as single columns with a deep foundation. The bridge is nearly straight and has a cable-type girder collapse-prevention structure, which connects the girder and the bridge abutment parapet. Rubber bearings are used, and side blocks are provided at the girder ends only.

#### 4. Site Survey of Tawarayama Bridge after the Earthquake

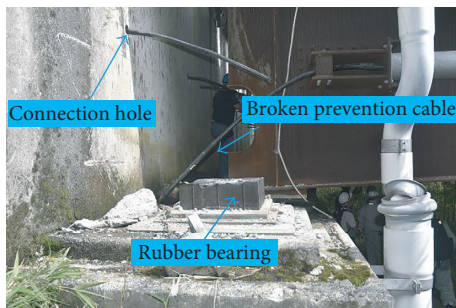
A site survey of Tawarayama Bridge was carried out. The damage was investigated by the Structural Mechanics Laboratory of Kumamoto University, led by Professor Toshitaka Yamao and Professor Akira Kasai, as the bridge was seriously



(a)



(b)



(c)

FIGURE 3: (a) Relative displacement of the girder, (b) damage to the expansion joint, and (c) damage to the bearing in Ookirihata Bridge.

damaged owing to its proximity to the active fault line. The deformation of the whole bridge can be seen in Figure 11, which was generated using a three-dimensional (3D) scanning technique that was developed by Yuta Ushitsuka.

According to the site survey data, all piers and abutments moved in the NE direction, and the movement and settlement of each abutment and pier were as follows:

- (i) Abutment 1 moved 1,759 mm toward Takamori and 1,924 mm toward the valley and underwent a settlement of 410 mm.
- (ii) Pier 1 moved 1,369 mm toward Takamori and 1,201 mm toward the valley.
- (iii) Pier 2 moved 680 mm toward Takamori and 1,006 mm toward the valley.



(a)



(b)

FIGURE 4: The collapse of (a) Aso Bridge and (b) Furyo First Bridge.



FIGURE 5: Damage to the tops of the piers of Hatanaka Dai-ichi Bridge.



FIGURE 6: Damage and detachment of the bridge and sidewalk stairs of Yokoe Bridge.

- (iv) Abutment 2 moved 501 mm toward Takamori and 769 mm toward the valley.

The settlements of each bridge's abutments and piers are shown in Figure 11(c).



FIGURE 7: Location of Tawarayama Bridge.

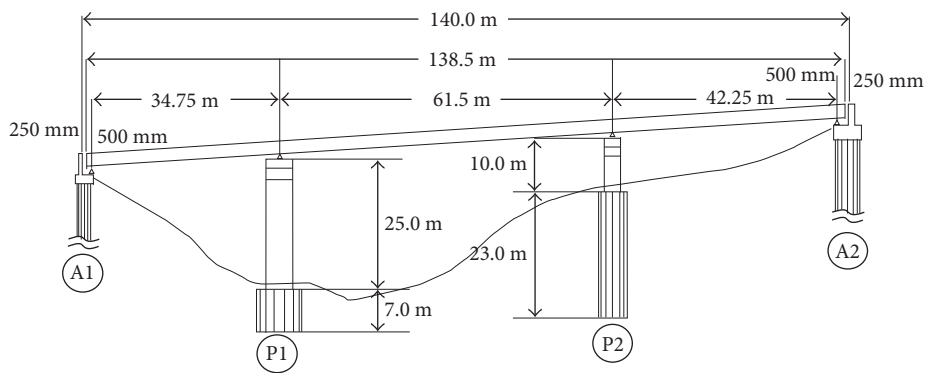


FIGURE 8: Longitudinal profile.

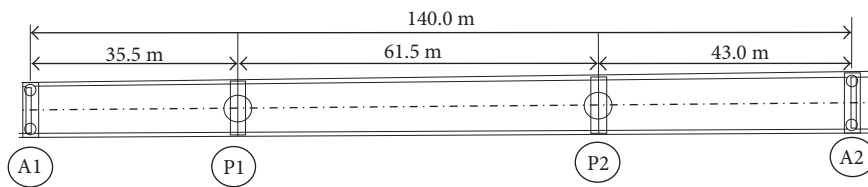


FIGURE 9: Plan view.

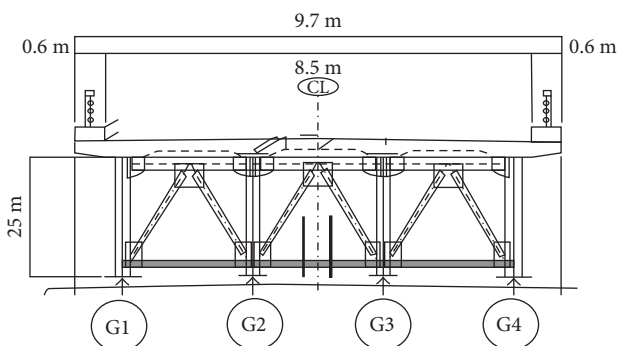


FIGURE 10: Cross section of the superstructure.

4.1. *Damage at Abutments.* The settlement of the deck slab occurred at the east side (A2 side) of the bridge because of the girders falling off from the rubber bearings and tilting of the abutment. A deck slab settlement of 53 cm was observed (Figure 12). The movement of the abutment by about 80 cm toward Takamori and the falling of the girder from the rubber bearing at abutment A2 are shown in Figure 13.

At the west side (A1 side, Figure 14), the road embankment collapsed because of the soil movement, exposing the pile foundation under the abutment. The base of abutment A1 was severely damaged, as shown in Figure 15. The shear deformation of the rubber bearing at abutment A1 is clearly seen in Figure 16.

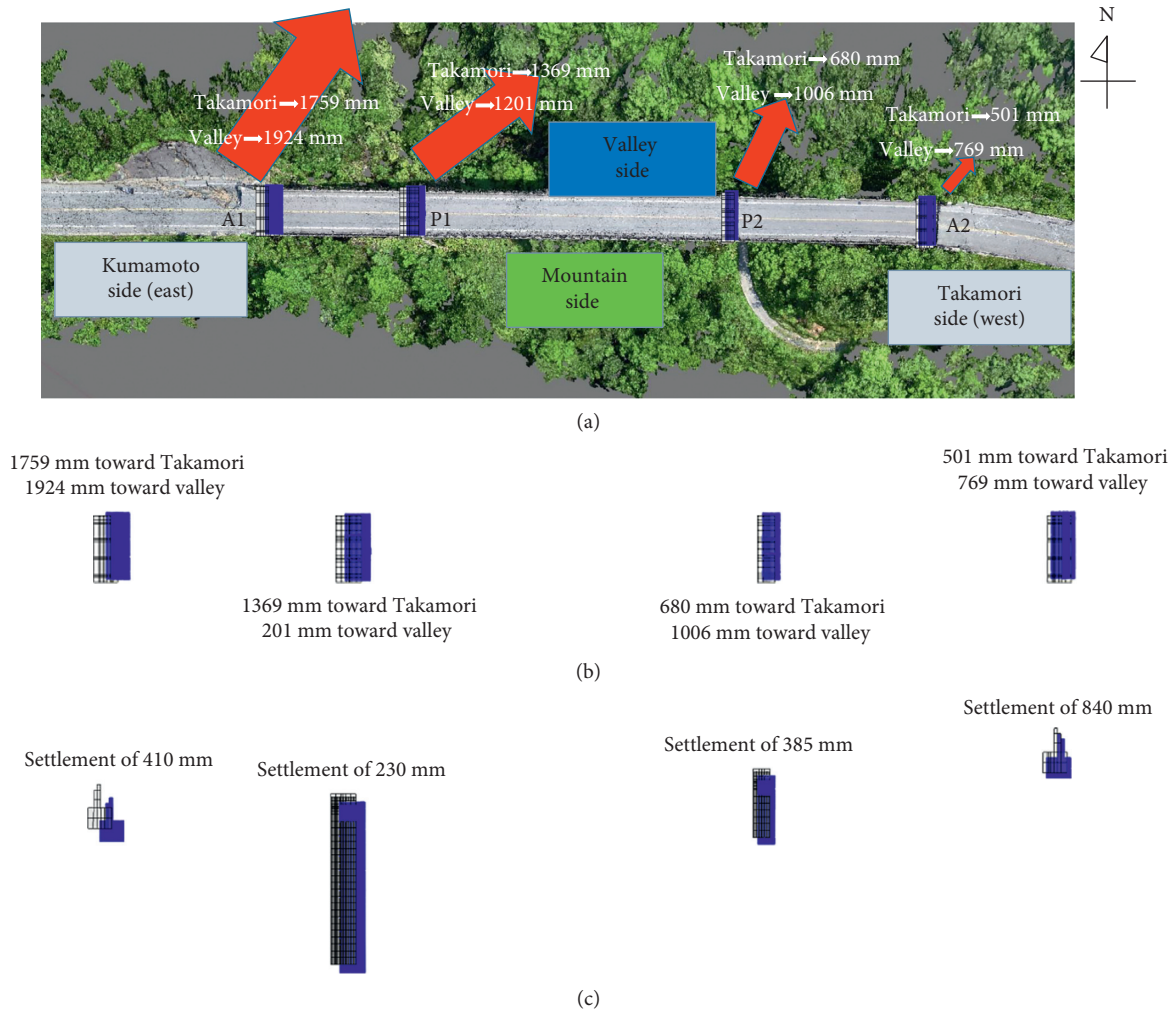


FIGURE 11: (a) Overall deformation of Tawarayama Bridge, (b) horizontal displacement of abutments and piers, and (c) settlement of abutments and piers.



FIGURE 12: Damage to abutment A2 (exterior).



(a)



(b)

FIGURE 13: Damage to abutment A2 (interior).



FIGURE 14: Damage to abutment A1 (exterior).



FIGURE 15: Damage to abutment A1 (interior).

4.2. *Damage to the Piers.* The rubber bearings at P2 were seriously damaged. One of the four rubber bearings under girder 1 completely collapsed. Many cracks that formed at the base of the pier were investigated. The following figures show the damage to the rubber bearing and the cracks that formed at the base (Figures 17–19).



(a)



(b)

FIGURE 16: Damage to the dampers at abutment A1 (interior).



(a)



(b)

FIGURE 17: Damage to the piers.

4.3. *Damage to Girders.* Figure 20 shows the deformation of the main girder and pier P1 as seen from the A1 side. The main girder bent and underwent inward deformation about 20 m from the A1 side while moving toward P1. Buckling in the vicinity of the lower lateral structure was confirmed near P1 and P2. The deformation of girder G3 is shown in Figure 21.



(a)



(b)

FIGURE 18: (a) Deformed rubber bearing under girder 1 at pier 2. (b) A rubber bearing that fell on the ground.



FIGURE 19: Cracks at the base of the pier.

**4.4. Damage Mechanism.** Figure 22 shows the original and deformed shapes of Tawarayama Bridge. The dotted line shows the original shape, and the solid line shows the deformed shape.

According to the damage survey presented in Sections 5.1–5.3, the impinging of the lower horizontal members buckling may be attributed to the compressive force acting on the bridge deck from both abutments A1 and A2 or to the displacement of the abutments toward the bridge girder. Figure 23 illustrates the deformation mechanism of the main girder and lower lateral members.

In this study, this event is considered the most important destructive mechanism. The extent of the compressive force that should be assumed for the seismic design of the bridge girder has not been verified yet. In addition, the actual ground motion was larger than what was assumed. Therefore, there is a need to identify the ground motion at the sites. According to this survey, in the future, the seismic design of bridge girders should be considered on the basis of

the buckling phenomenon of these girders in response to ground motion corresponding to a seismic intensity of 7.

## 5. Seismic Response Analysis

There were many papers concerning the seismic response analysis, seismic design specification of the bridges, and damages of bridges published by many researchers. Aso et al. [5] carried out nonlinear earthquake response analysis of PC cable-stayed bridge. Nazmy [6] presented seismic analysis and design evaluation of continuous plate-girder bridges with the help of a case study. Itani et al. [7] emphasized on seismic behavior of steel girder bridge superstructures to know the behavior of steel plate girder bridges during the earthquakes. Park et al. [8] simulated the seismic performance subjected to near-fault ground motion. Usami et al. [9] performed dynamic analysis to evaluate the seismic performance of steel arch bridges against major earthquakes. Kawashima and Unjoh [10] summarize the seismic design specifications for highway bridges after the 1995 Kobe Earthquake. Altun et al. [11] carried out dynamic analysis of suspension bridges and full-scale testing in which the effects of large deflections are taken into account. Takahashi and Hoshikuma [12] explored the damages of road bridges induced by the ground motion in the 2011 Great East Japan Earthquake and summarized the characteristics of damage to road bridges induced by the ground motion. Cahya et al. [13] also investigated seismic response behavior using static pushover analysis and dynamic analysis of half-through steel arch bridge under strong earthquake. The 2016 Kumamoto Earthquake survey report published by the Asia-Pacific Economic Cooperation [14] and an overview of damage to roads and bridges in Nishihara area by Narazaki and Kong [15] presented the damage conditions of bridges during the 2016 Kumamoto Earthquake. There was a research on the collapse process of cable-stayed bridges under strong seismic excitations by Wang et al. [16]. According to all these research works, it is obvious that the seismic response analyses and seismic design specifications of bridges as well as damage survey of bridges are essential. So, in the present study, a seismic response analysis of a plate-girder bridge, whose lower lateral members underwent buckling, was carried out using the recorded earthquake motion data of the 2016 Kumamoto Earthquake. ABAQUS (Simulia, 2017) software [17] was used to create a finite element (FE) model of Tawarayama Bridge. In this model, beam elements were used to study the buckling behavior. According to the design drawing sheets, L-, T-, I-beams were used for cross-bracing, top and bottom chords, and cross-beams, respectively. For rubber bearings, spring elements were applied in the FE model. The material properties of the model used in the numerical analysis were SM490 with a yield stress ( $\sigma_y$ ) of 315 MPa and a Young's modulus ( $E$ ) of 205 GPa for the main girder steel beams, SMA400w with a yield stress ( $\sigma_y$ ) of 245 MPa and a Young's modulus ( $E$ ) of 205 GPa for all bracing members, and concrete with a Young's modulus ( $E$ ) of 30.35 GPa.

The nonlinearity of the material was considered for the steel elements, which are the main elements of the



(a)



(b)

FIGURE 20: Deformation of the main girders and buckling of the lower lateral members.



FIGURE 21: Deformation of girder 3.

plate girder and lower lateral members. Beam elements were used for concrete piers. The equivalent Young's modulus was used to account for steel reinforcements too. The equivalent Young modulus used for P1 and P2 is 36.18 GPa and 38.14 GPa, respectively. In the present study, the elastic linear hardening model was used to consider the elastoplastic behavior of steel. The elastic linear hardening models of SM490 and SMA400w grade steels are shown in Figure 24 [18, 19]. The FE model created using ABAQUS CAE software is shown in Figure 25.

Beam type B31 (two-node linear beam) was used in the FE model. Spring elements were installed between piers and girders in all six directions to represent the rubber bearings in the real bridge. Dashpot coefficients were also applied, and the equation used and values are shown in the next section. A detailed calculation of the spring stiffness is presented in

the next section. Multipoint constraint (MPC) beam type was used between the girders and connections of the bracing members.

*5.1. Calculation of Spring Stiffness from the Properties of Rubber Bearings.* In the FE model of Tawarayama Bridge, spring elements were used for rubber bearings between girders and piers and abutments. The following formulae were used to calculate the spring stiffness in the model [20].

For the horizontal direction,

$$K_{so} = \frac{G_0 A}{\sum t_e},$$

$$K_{st} = \frac{G_0 A}{\sum t_e}. \quad (1)$$

For the vertical direction,

$$K_v = \frac{EA}{\sum t_e},$$

$$E = \begin{cases} (3 + 6.58S^2) & \text{for } \left(0.5 \leq \frac{b}{a} \leq 2\right), \\ (4 + 3.29S^2) & \text{for } \left(\frac{b}{a} < 0.5 \text{ and } \frac{b}{a} > 2\right), \end{cases} \quad (2)$$

$$S = \begin{cases} \frac{ab}{(2(a+b)t_e)} & \text{for } \left(0.5 \leq \frac{b}{a} \leq 2\right), \\ \frac{a}{2t_e} & \text{for } \left(\frac{b}{a} < 0.5 \text{ and } \frac{b}{a} > 2\right), \end{cases}$$

where  $K_{so}$ ,  $K_{st}$ , and  $K_y$  are the spring stiffnesses in the horizontal and vertical directions,  $G_0$  is the shear modulus,  $A$  is the area of the rubber bearing,  $t_e$  is the thickness of the laminated rubber,  $E$  is Young's modulus,  $S$  is the shape factor,  $a$  is the width of the rubber bearing, and  $b$  is the length of the rubber bearing.

The springs were installed at A1, P1, P2, and A2 between abutments or piers and girders. At each abutment and pier, four springs are installed under each girder. The values of each parameter used and the calculated spring stiffnesses are listed in Table 2.

*5.2. Seismic Input Data.* The recorded earthquake data from Ozu Station were used as seismic input data. The earthquake acceleration waves for the north-south (NS) and east-west (EW) directions are shown in Figures 26 and 27 [21]. The maximum acceleration occurred around 26 s in both directions. The values and times of occurrence are also shown in the figures. For Tawarayama Bridge, EW is the longitudinal direction and NS is the transverse direction. Both directions were considered to investigate the seismic

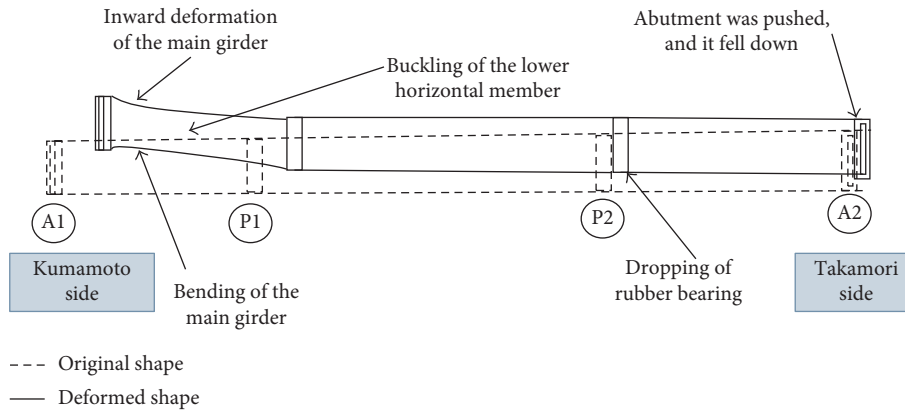


FIGURE 22: Deformation mechanism of the whole bridge.

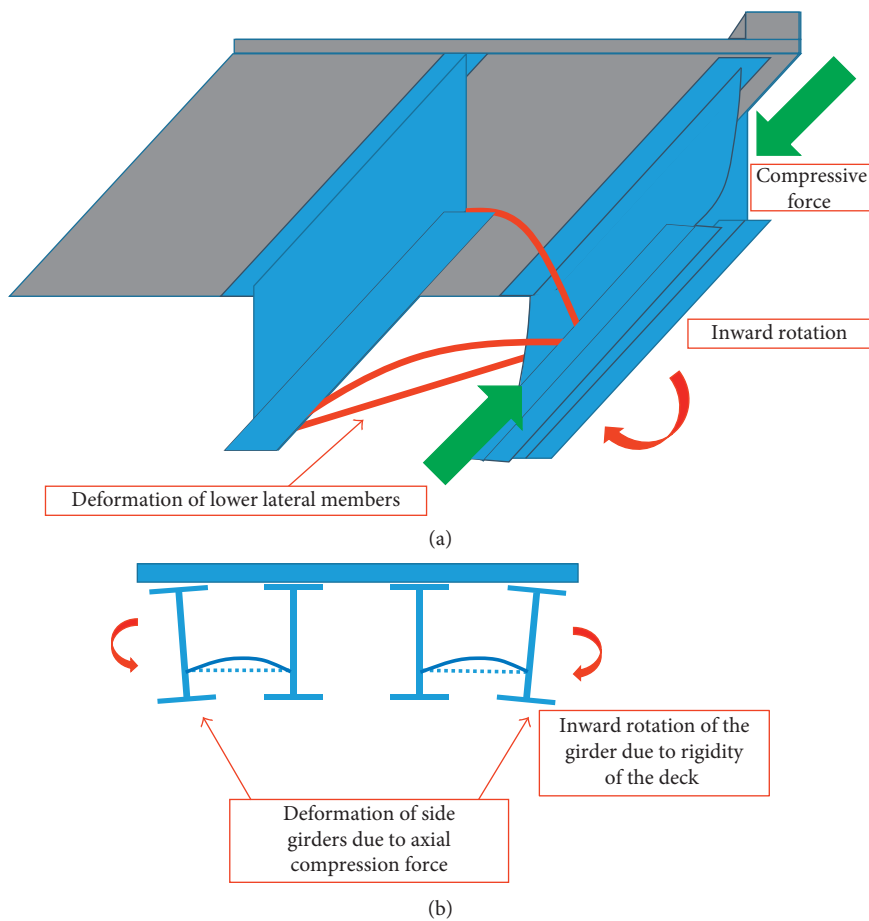


FIGURE 23: Deformation mechanism of the main girder and lower lateral members.

response of the bridge. In addition to the recorded earthquake data, analyses using the design earthquake data, considering level II, type II ground, ground motion type I, were also carried out [1, 20].

**5.3. Numerical Analysis.** For the numerical analysis, a constant time step of 0.01 s was utilized. MPC beam constraints were applied for the contacts between the members. The model

was assumed to have no residual stresses and no initial crookedness modes. The elastoplastic behavior of the steel material was considered during the analysis. First, an eigenvalue analysis was carried out in order to understand the vibration characteristics of the bridge. The values of the Rayleigh damping coefficients,  $\alpha$  and  $\beta$ , as determined from this analysis, are 0.6 and 0.002, respectively, for concrete and 0.11 and 0.0005, respectively, for steel materials. The seismic response analysis with a ground acceleration input and a constant dead load was

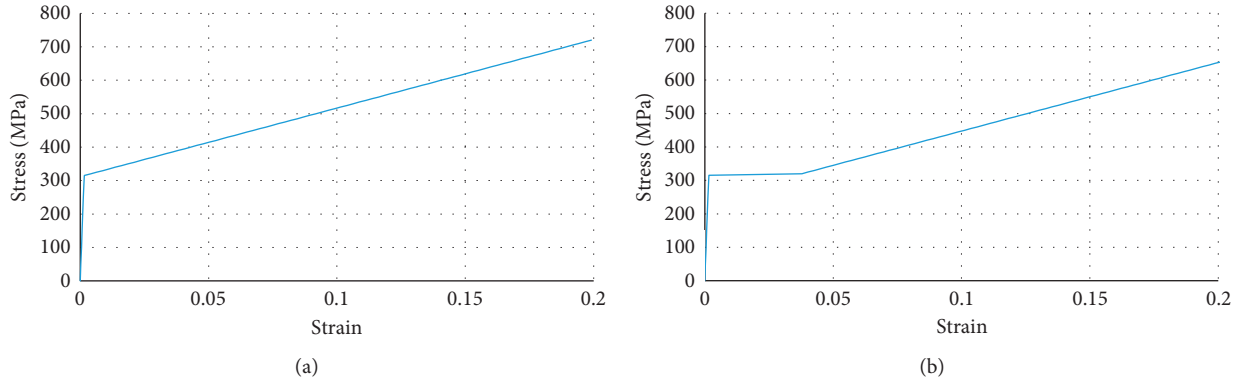


FIGURE 24: Stress-strain relationship for (a) SM490 and (b) SMA400w grade steels.

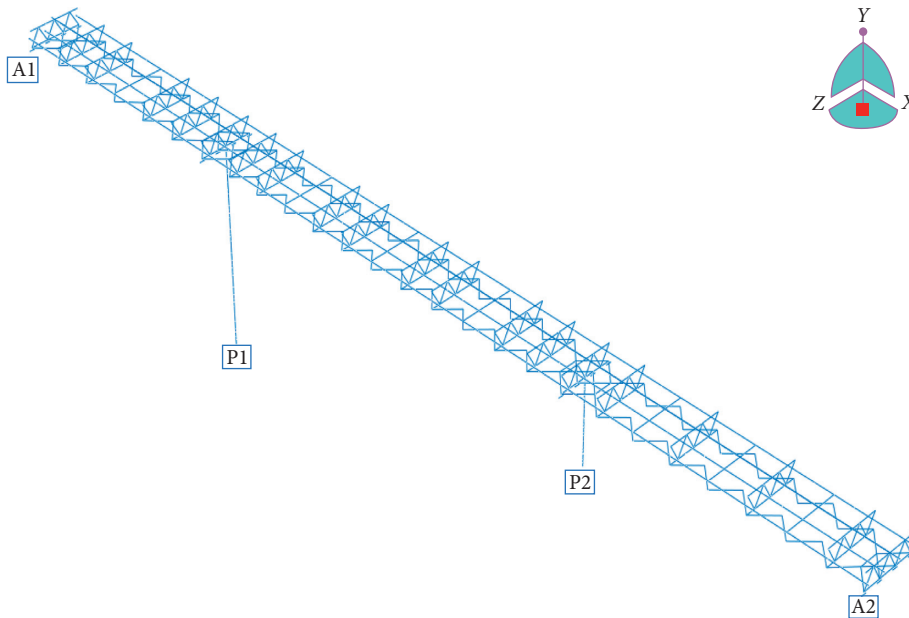


FIGURE 25: FE model of Tawarayama Bridge.

performed using the FEM ABAQUS program, which can account for geometric and material nonlinearities. In the analysis, both undamped and damped conditions were applied. For the undamped model, both transverse and longitudinal earthquake waves were applied simultaneously. For the damped model, three cases were examined. In the first case, the earthquake wave was applied only in the EW direction. In the second one, the wave was applied only in the NS direction. Finally, in the last one, the wave was applied in both longitudinal and transverse directions. In addition to Ozu Station data, level II, type II ground, ground motion type I, and earthquake data were also applied under the damped condition, and both EW and NS directions were considered in the analysis. The dashpot coefficients,  $c$ , that were used in the analysis are listed in the following Table 3. The dashpot coefficient equation used is as follows [17]:

$$c = \frac{2k\xi}{\omega}, \quad (3)$$

where  $c$  is the dashpot coefficient,  $k$  represents stiffness,  $\xi$  is the damping ratio, and  $\omega$  is the natural frequency.

## 6. Seismic Response Behavior of the Plate Girder Bridge

The seismic response behaviors of the plate girder bridge will be discussed in this session for four different parts. First, the stress states in the lateral bracing members are presented, and then, the behavior of the spring is discussed. Thereafter, the trajectory curves of the piers are illustrated. Finally, the behavior of the lower lateral bracings is examined.

**6.1. Stress States in the Lateral Bracing Members.** The stress states of all lateral bracing members for all five cases are presented in this section. The locations of all bracings are shown in Figure 28, and the stress states and maximum stress locations are shown in Figure 29.

TABLE 2: Properties of the rubber bearings and spring stiffnesses.

Part	$G_0$ (N/mm <sup>2</sup> )	$a$ (mm)	$b$ (mm)	$A$ (mm <sup>2</sup> )	$t_e$ (mm)	$n$	$\sum t_e$ (mm)	$S$	$E$ (N/mm <sup>2</sup> )	$K_{so}$ (Nm/mm)	$K_{st}$ (tf/cm)	$K_v$ (tf/cm)
A1	0.785	450	450	202500	12	17	204	9.375	456.064	794.117	794.117	461637
P1	1.177	600	650	390000	22	5	110	7.091	392.883	4252.54	4252.54	1420410
P2	1.177	750	750	562500	36	3	108	5.208	213.555	6250	6250	1134190
A2	0.785	450	450	202500	13	11	143	8.654	388.961	1132.87	1132.87	561661

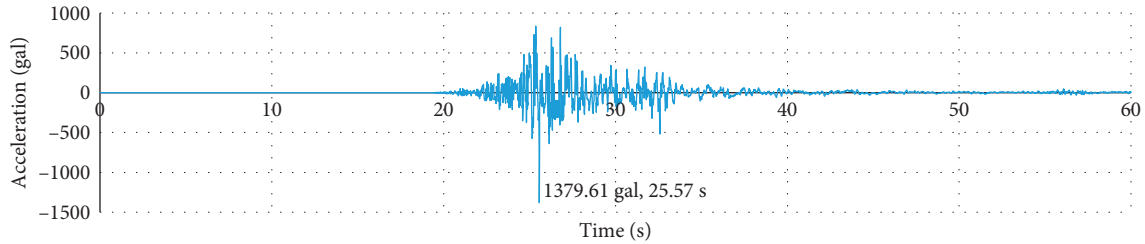


FIGURE 26: Earthquake input acceleration wave in the NS direction.

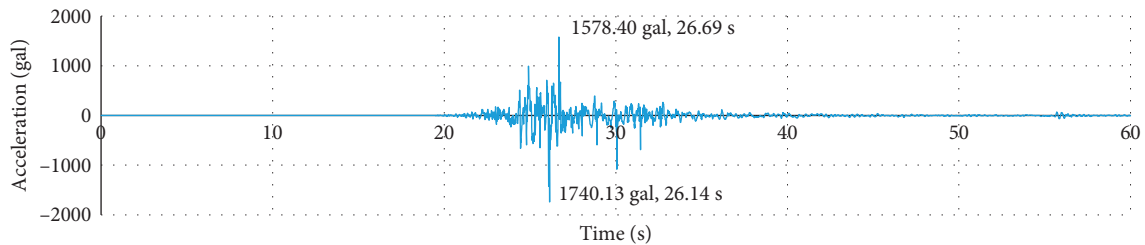


FIGURE 27: Earthquake input acceleration wave in the EW direction.

TABLE 3: Dashpot coefficients,  $c$ , for each abutment and pier.

	(A1, dir 1,3)	(A1, dir 2)	(A2, dir 1,3)	(A2, dir 2)	(P1, dir 1,3)	(P1, dir 2)	(P2, dir 1,3)	(P2, dir 2)
$k$	794.117	461637	1132.87	561661	4254.54	1.43E+06	6250	1.13E+06
$c$	15.88234	9232.74	22.6574	11233.22	85.0908	28528.2	125	22683.8

The present bridge has a total of 394 lateral bracing members. Among them, 66 members in the undamped case, 16 members in the design earthquake (EQ) case, and six members in the EW and NS case exceed the  $\sigma/\sigma_y$  value of 1, and for the EW case and NS case, the  $\sigma/\sigma_y$  value of no members exceeds 1. For each of the abovementioned cases, the number of members whose  $\sigma/\sigma_y$  values are between 0.8 and 1 is 100, 13, 2, 5, and 10, respectively. The  $\sigma/\sigma_y$  values of other members are less than 0.8. The maximum  $\sigma/\sigma_y$  value is 1.59 in the undamped case. Detailed data are listed in Table 4. The member with the maximum  $\sigma/\sigma_y$  value is an inclined member of P-bracing (bracing at piers) between G1 and G2. Most of the members with  $\sigma/\sigma_y$  values close to 1.5 are found near P1 and P2 (P-bracing and bottom bracing). The  $\sigma/\sigma_y$  values of most of the bracings and A-bracing members are less than 0.8. The minimum  $\sigma/\sigma_y$  value of 0.02 was found at A-bracing (bracing at abutments).

**6.2. Deformation of the Spring Element.** This section discusses the deformation of the spring elements, which were

used as rubber bearings in the bridge. Springs were installed at 16 locations (four for each pier and abutment) between the girder and piers/abutments, which are shown in Figure 30. Figure 31 presents the load-displacement relationship curves of a spring at P2 under the undamped condition in both longitudinal and transverse directions. The dotted lines in the figure show the theoretical displacement criteria of spring elements.

The theoretical displacement criteria of spring elements for each pier and abutment are listed in Table 5.

The displacement of all springs in all cases except in the undamped case was within their displacement criteria. In the undamped case, the displacement of springs at A2, P1, and P2 in the longitudinal direction and that of P2 in the transverse direction exceed the displacement criteria. The maximum displacement of springs occurred between 25.5 s and 26.8 s, which is close to the time when the maximum acceleration occurred.

At A1 and P1, displacements of the springs in the transverse direction are greater than those in the longitudinal direction for the design EQ case and NS case, whereas

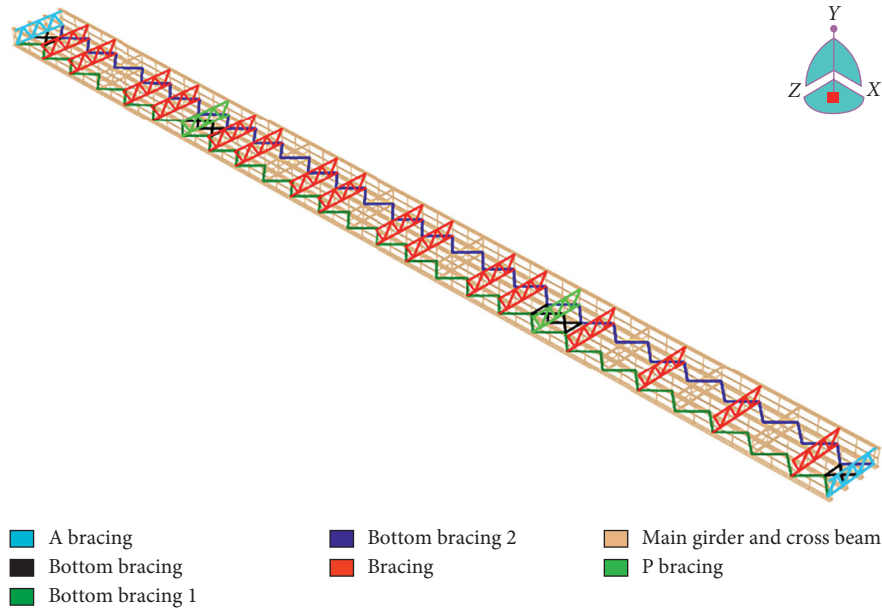


FIGURE 28: Locations of bracings.

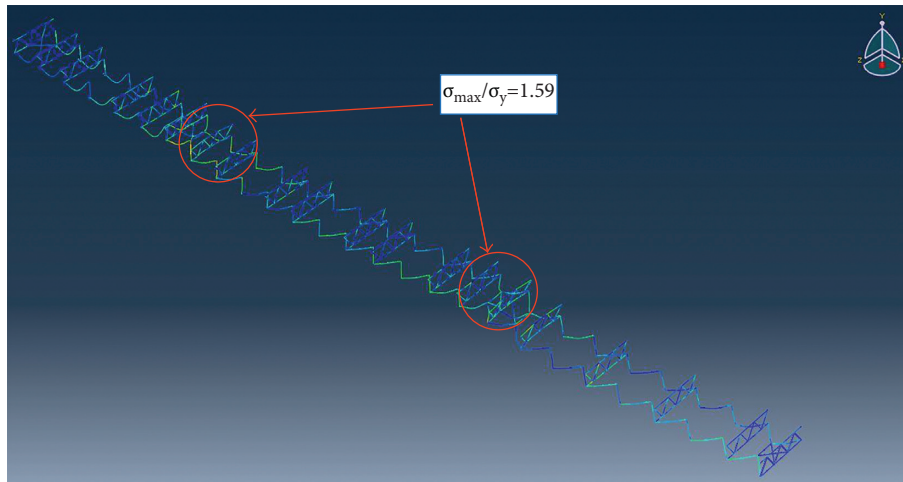


FIGURE 29: Members with the maximum  $\sigma/\sigma_y$  value.

TABLE 4: Number of members according to  $\sigma/\sigma_y$  values.

$\sigma/\sigma_y$ value	Undamped	Design EQ	EW	NS	EW and NS
$\sigma > 1$	66	16	0	6	0
$0.8 < \sigma \leq 1$	100	13	2	5	10
$\sigma < 0.8$	228	365	392	383	384
Max. $\sigma$	1.59	1.2	0.85	1.2	0.97

the longitudinal displacements of the springs are more dominant in the other cases. For A2 and P2, the maximum spring displacements in the longitudinal direction are greater than those in the transverse direction in all other cases, except for the NS case. The ratio of longitudinal to transverse displacements of P2 for EW and NS cases is 1.9, which is larger than the values of others (around 1). This fact and the fact that the spring displacement of P2 exceeds the

displacement criteria in both longitudinal and transverse directions may be the reason why one of the rubber bearings at the P2 pier fell down. The displacements of springs in the longitudinal and transverse directions for all cases are shown in Figure 32.

6.3. *Trajectory Curve of Piers.* The trajectory curves of piers were established in order to determine their response during the earthquake. These curves are shown in Figure 33. Among the five cases, the undamped case is more dominant, followed by the design earthquake one. It is clear that the displacements in the EW (longitudinal) and NS (transverse) directions are only dominant in their respective direction for both P1 and P2. The undamped displacements of both piers are more dominant in the

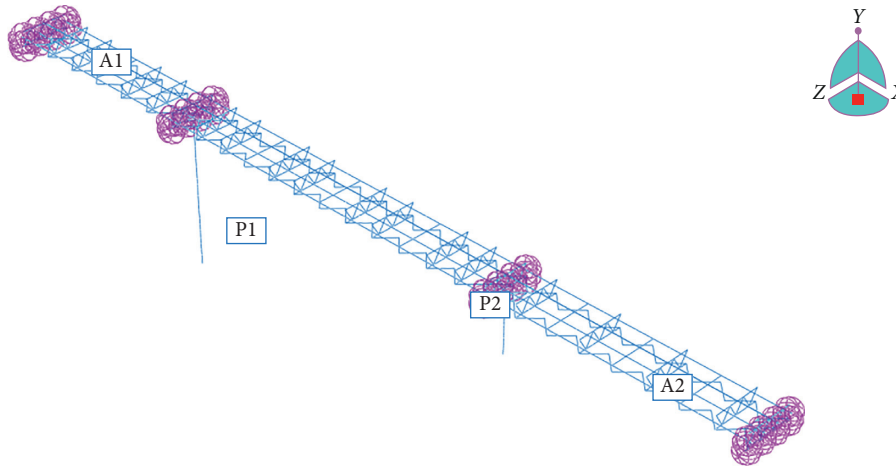


FIGURE 30: Location of springs.

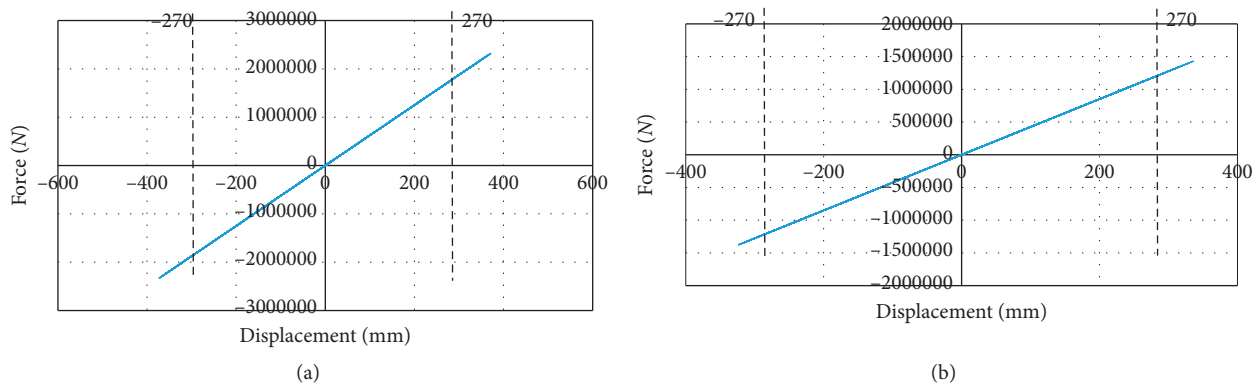


FIGURE 31: Force-displacement curves for the spring at pier 2.

TABLE 5: Displacement criteria of spring elements.

Pier/abutment	Displacement criteria (mm)
Pier 1	275
Pier 2	270
Abutment 1	510
Abutment 2	375

transverse direction. The design EQ displacements are also dominant in the transverse direction, although they are not very different from the undamped displacement, whereas the EW and NS displacements are nearly identical in both directions.

6.4. Behavior of Lower Lateral Bracings. The time history displacement response curves and force-displacement curves of some lower lateral bracing members were plotted in order to understand the behavior of lower lateral bracing members. The stresses of some of these members exceeded the maximum stresses, leading to hardening. Hence, some members exhibited an elastoplastic behavior, whereas some exhibited an elastic behavior only. Among the ten selected members shown in Figure 34, eight members buckled in the undamped case, five buckled in

the design EQ, and two each buckled in the EW and the EW and NS cases. In the NS case, no member buckled. Figure 35 shows that the members around P2 have a greater tendency to buckle, especially under the damped condition.

The lengths of the members, maximum forces, Euler’s buckling load, and buckling conditions for the undamped case are listed in Table 6. The buckling conditions for all bracing members for each case are presented in Table 7. No member buckled only in the EW case. In all the other cases, members exhibited a buckling behavior under earthquake motion. These data imply that the damper plays an important role in the buckling of members.

## 7. Discussion and Conclusion

In this study, field surveys of Tawarayama Bridge were conducted in order to review the actual conditions and damage mechanism that could have caused the deformation observed in the first part of this study. According to this damage survey, the following conclusions can be drawn.

- (1) A large ground motion occurred near Tawarayama Bridge. This led to the movement of the entire

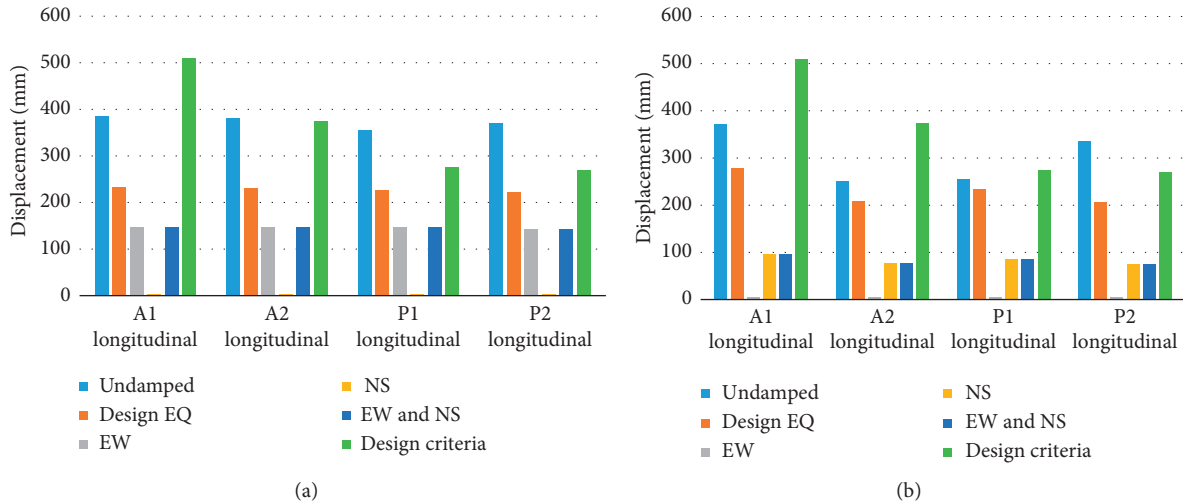


FIGURE 32: Spring displacement of the spring in each abutment and pier for all cases: (a) longitudinal direction and (b) transverse direction.

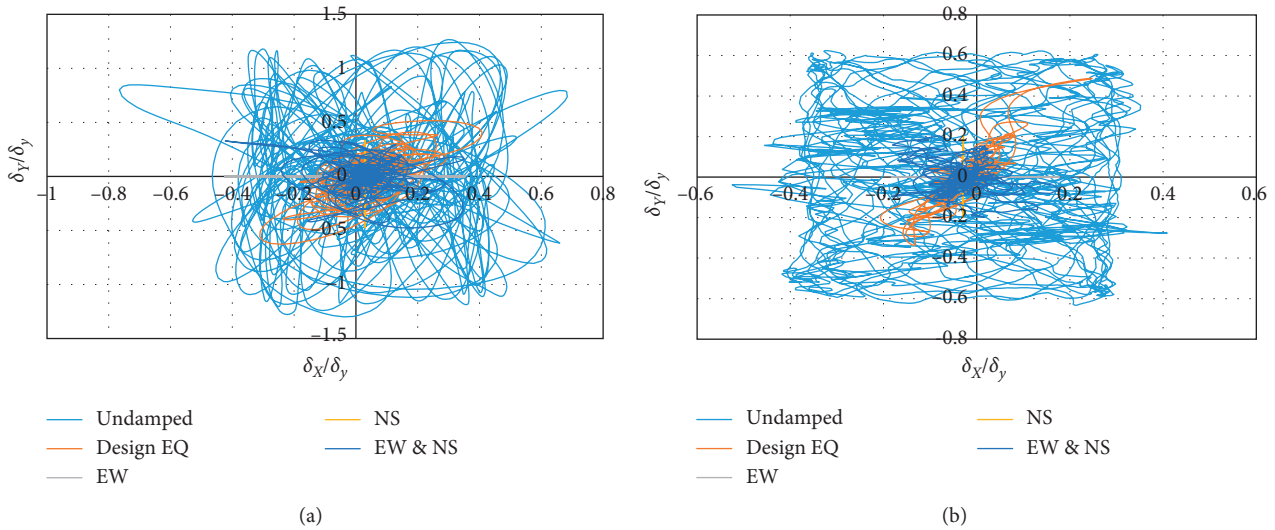


FIGURE 33: Trajectory curve for (a) pier 1 and (b) pier 2.

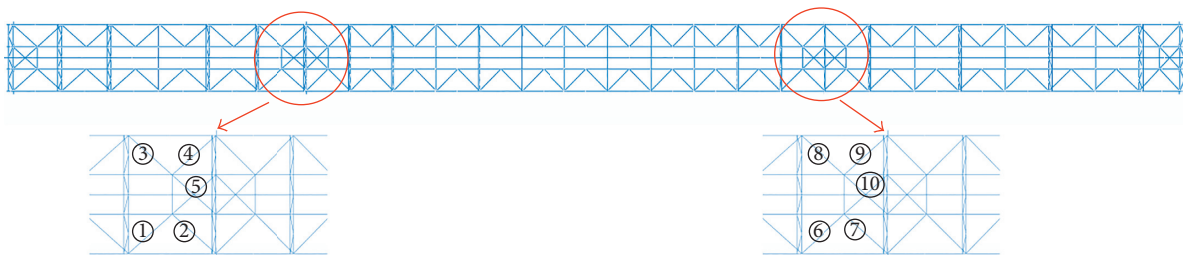


FIGURE 34: Locations of the buckled lower bracing members.

bridge in the NE direction (toward Takamori side in the longitudinal direction and toward the valley in the transverse direction). As a result, a large compressive and rotational force acted on the bridge girder.

(2) The lower lateral members buckled, and the rubber bearings underwent shear deformation. The movements were much larger in A1 and P1, and so the deformations of the bridge girder in both the flange and the web could be clearly seen.

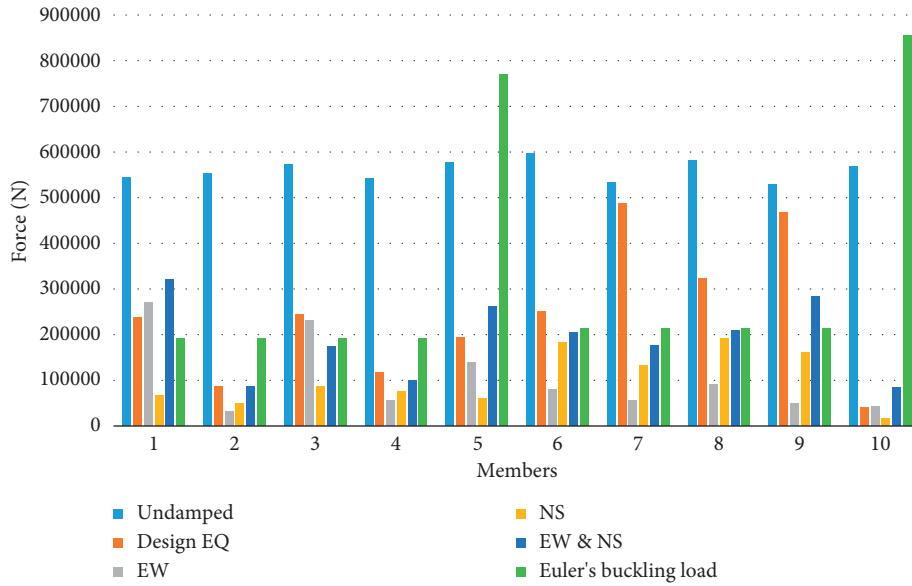


FIGURE 35: Maximum forces and Euler's buckling forces for each case.

TABLE 6: Buckling conditions of ten selected members under the undamped condition.

Member	1	2	3	4	5	6	7	8	9	10
Length (mm)	3895	3895	3895	3895	1947	3695	3695	3695	3695	1847
Max. force (N)	543107	552285	571835	541638	577698	597243	532315	581386	528864	567483
Euler's buckling load (N)	192618	192618	192618	192618	770471	214057	214057	214057	214057	856228
Buckle or not	Buckle	Buckle	Buckle	Buckle	Not buckle	Buckle	Buckle	Buckle	Buckle	Not buckle

TABLE 7: Buckling conditions of all members in different earthquakes.

	Undamped	Design EQ	EW	NS	EW and NS
Number of buckled members	66	16	0	6	39
Number of unbuckled members	100	378	394	388	355

- (3) Extensive damage occurred in every abutment and pier. The most serious damage included the exposure of the pile foundation and shear deformation of rubber bearings at abutment A1, the tendency of overturning of abutment A2, buckling at P1, and the falling off of one of the four rubber bearings at P2.
- (4) The possible damage mechanism may be attributed to the compressive force acting on the bridge deck from both abutments A1 and A2 or to the approaching of the abutments toward the bridge girder.

The second part of the study was a numerical analysis of Tawarayama Bridge. The numerical analysis is subdivided into eigenvalue analysis and seismic response analysis subject to the ground motion. The seismic analysis was carried out with the earthquake acceleration input data for longitudinal and transverse directions separately and simultaneously in order to investigate the seismic behavior of the bridge. The current findings and conclusions of these analyses are summarized as follows:

- (1) According to the eigenvalue analysis, the displacement in the transverse direction is dominant in mode

1, whereas that in the longitudinal direction is clear in mode 3. The movements of the bridge in both directions occurred in the real situation too. In mode 2, a vertical rotation is noticeable. This behavior is similar to the rotation of the bridge girder toward the valley side during the 2016 Kumamoto Earthquake.

- (2) The relative stresses in most bracing members are lower than 0.8 when considering the earthquake input data in only one direction. For the recorded bilateral earthquake input data of Ozu Station, the relative stresses of ten members exceeded 0.8 and those of the other members were below 0.8. For design earthquake data, the  $\sigma/\sigma_y$  values of 16 members exceeded 1, those of 13 members exceeded 0.8, and those of the rest were less than 0.8. For the undamped model, the numbers of the members with  $\sigma/\sigma_y$  exceeding 1 and 0.8 were 66 and 100, respectively.
- (3) While observing the displacement of springs, which represent the rubber dampers in the actual condition, spring displacements beyond the displacement criteria can be found only in the undamped case, especially for the springs at P2.

- (4) The performance of piers differs according to the cases. For the undamped and design earthquake cases, displacement in the transverse direction is dominant, and for the EW and NS case, displacements in both directions are quite similar. The displacements in the EW and NS case are dominant in their respective directions. Among the five cases, the undamped cases are dominant.
- (5) No buckling behavior is observed in the EW case, whereas six members buckled in the NS case. It is observed that some members exhibit a buckling behavior even in the design earthquake case. Overall, 39 members buckled under the recorded earthquake motion in the EW and NS directions. Here, 66 members buckled during the analysis under the undamped condition. In the real situation, it was confirmed that the rubber bearings underwent shear deformation, and one rubber bearing from P2 fell off. The buckling of lower lateral members was also clearly observed.
- (6) Thus, it can be concluded that the buckling of the lower lateral members should be given due importance in further bridge designs, especially for bridges with lower damping.

In the present work, only the recorded acceleration was considered as the input data for dynamic analysis, and large geometric deformations and bridge collapse-prevention cables were not considered. So, further studies should include these facts as analysis input data to obtain more accurate results.

### Data Availability

The data used to support the findings of this study are available from the corresponding author upon request.

### Disclosure

This paper is an extension of the work reported in the paper titled "Damage survey of bridges during 2016 Kumamoto Earthquake and seismic response analysis of plate girder bridge subjected to the Kumamoto Earthquake," presented at the International Workshop on the 2016 Kumamoto Earthquake–Japan-US Joint Workshop on March 6, 2017, at Fukuoka, Japan. The previous paper emphasized on the damage survey and eigenvalue analysis, and the present paper also includes the nonlinear dynamic analysis responses.

### Conflicts of Interest

The authors declare that they have no conflicts of interest.

### Acknowledgments

The authors would like to express their sincere gratitude to Professor Toshitaka Yamao for his leadership and guidance during the site survey of Tawarayama Bridge. Special thanks are due to Yuta Ushitsuka for helping to obtain the 3D image

for the deformation of Tawarayama Bridge by 3D scanner technique.

### References

- [1] *Data from JMA (Japan Meteorological Agency)*, 2016, <http://www.data.jma.go.jp>.
- [2] A. K. Tang and J. M. Eidiner, *Kumamoto, Kyushu, Japan, Earthquake of Mw 6.0 April 14, 2016, Mw 7.0 April 16, 2016, Lifetime Performance*, The Council of Lifeline Earthquake Engineering TCLEE No. 2 and Yokohama National University, Yokohama, Japan, 2017.
- [3] <http://www.eqclearinghouse.org>.
- [4] [https://gbank.gsj.jp/activefault/index\\_gmap.html](https://gbank.gsj.jp/activefault/index_gmap.html).
- [5] T. Aso, K. Mizutori, M. Shuto, A. Arikado, K. Momota, and H. Otsuka, "Non-linear earthquake response analysis of PC cable stayed bridge considering the fluctuant axial force," in *Proceedings of the 12WCCE (12th World Conference on Earthquake Engineering)*, Auckland, New Zealand, February, 2000.
- [6] A. S. Nazmy, "Seismic analysis and design evaluation of continuous plate-girder bridges: a case study," *International Journal of Structural Stability and Dynamics*, vol. 3, no. 1, pp. 91–106, 2003.
- [7] A. M. Itani, M. Bruneau, L. Carden, and I. G. Buckle, "Seismic behavior of steel girder bridge superstructures," *Journal of Bridge Engineering*, vol. 9, no. 3, pp. 243–249, 2004.
- [8] S. W. Park, H. Ghasemi, J. Shen, P. G. Somerville, W. P. Yen, and M. Yashinsky, "Simulation of the seismic performance of the Bolu Viaduct subjected to near-fault ground motions," *Earthquake Engineering and Structural Dynamics*, vol. 33, no. 13, pp. 1249–1270, 2004.
- [9] T. Usami, Z. Lu, H. Ge, and T. Kono, "Seismic performance evaluation of steel arch bridges against major earthquakes, Part 1: dynamic analysis approach," *Earthquake Engineering and Structural Dynamics*, vol. 33, no. 14, pp. 1337–1354, 2004.
- [10] K. Kawashima and S. Unjoh, "Seismic design of highway bridges," *Journal of Japan Association for Earthquake Engineering*, vol. 4, no. 3, pp. 174–189, 2004.
- [11] S. Altin, K. Kaptan, and S. S. Tezcan, "Dynamic analysis of suspension bridges and full scale testing," *Open Journal of Civil Engineering*, vol. 2, no. 2, pp. 58–67, 2012.
- [12] Y. Takahashi and J. Hoshikuma, "Damage to road bridges induced by ground motion in the 2011 Great East Japan Earthquake," *Journal of JSCE*, vol. 1, no. 1, pp. 398–410, 2013.
- [13] E. Cahya, T. Yamao, and A. Kasai, "Seismic response behavior using static pushover analysis and dynamic analysis of half-through steel arch bridge under strong earthquake," *International Journal of Civil Engineering and Technology (IJCIET)*, vol. 5, no. 1, pp. 73–88, 2014.
- [14] Asia-Pacific Economic Cooperation, "2016 Kumamoto earthquake survey report," in *Proceedings of the 10th Emergency Preparedness Working Group Meeting*, pp. 15–16, Lima, Peru, August, 2016.
- [15] Y. Narazaki and C. Kong, *Overview of Damage to Roads and Bridges in Nishihara Area*, 2016, <http://www.eqclearinghouse.org/2016-04-15-kumamoto/2016/05/19/overview-of-damage-to-roads-and-bridges-in-nishihara-area/>.
- [16] X. Wang, B. Zhu, and S. Cui, "Research on collapse process of cable-stayed bridges under strong seismic excitations," *Shock and Vibration*, vol. 2017, Article ID 7185281, 18 pages, 2017.
- [17] Dassault Systèmes Simulia Corp., *ABAQUS 6.14 Documentation*, Dassault Systèmes Simulia Corp., Providence, RI, USA, 2014.

- [18] W. F. Chen, *Plasticity for Structural Engineers*, Springer, Berlin, Germany, 2012.
- [19] Japan Road Association, *Handbook of Road Bridge Bearing*, Japan Road Association, Tokyo, Japan, 2004.
- [20] Japan Road Association, *Specifications for Highway Bridges, Part I-General, Part II-Steel Bridges, Part V-Seismic Design*, Japan Road Association, Tokyo, Japan, 2012.
- [21] <http://www.kyoshin.bosai.go.jp/>, 2016.

## Research Article

# Experimental Study of the Low-Cycle Fatigue in Double-Walled Hollow Pipe Members

Lu Zhaohong <sup>1</sup>, Zunce Wang <sup>1</sup>, Yan Xu <sup>1</sup>, Gao Shanshan,<sup>2</sup> and Han Lianfu<sup>1</sup>

<sup>1</sup>Northeast Petroleum University, Daqing, China

<sup>2</sup>Heilongjiang Key Laboratory of Disaster Prevention, Mitigation and Protection Engineering, Daqing, China

Correspondence should be addressed to Zunce Wang; wangzc@nepu.edu.cn

Received 27 December 2017; Revised 13 March 2018; Accepted 3 July 2018; Published 2 August 2018

Academic Editor: Tadeh Zirakian

Copyright © 2018 Lu Zhaohong et al. This is an open access article distributed under the Creative Commons Attribution License, which permits unrestricted use, distribution, and reproduction in any medium, provided the original work is properly cited.

This paper introduces a double-walled hollow pipe (DWHP) that demonstrates good corrosion resistance and mechanical properties and that can be used in pipeline transportation and structural stress components in marine, freshwater, and corrosive environments. We designed and machined the specimens to meet the bending bearing capacity using a cross section method. We conducted low-cycle loading tests of the specimens to investigate the energy dissipation capacity of the DWHP, the effects of different geometrical parameters, and the concrete-filled strength of the DWHP on energy dissipation capacity. The results show that the failure forms of the specimens are similar. The geometrical characteristics of the specimens, the cohesive function between the concrete and the steel plate, and the strength of the concrete-filled pipe showed a significant influence on the mechanical properties of the specimens. Hysteretic curves are plump and possess a high capacity for energy dissipation. The energy dissipation capacity of the specimen decreases with an increase in the slenderness ratio. The slope of strength degradation decreases with any increase in the strength of the concrete-filled pipe. We optimized the section design of the component by improving the constraint effect coefficient, and we effectively improved its stability by adding stiffeners to the inner side of the outer wall of steel.

## 1. Introduction

Stainless steel-concrete steel double-walled hollow pipe (DWHP) is a new type of structural component that can be used in engineering for suspended crossover pipes, building structural members, bridges, and offshore platform piles [1]. Because of the high cost of stainless steel materials, they should not be used in engineering applications in large quantities. The outer wall of steel can have a thin stainless steel form. The DWHP section pattern is shown in Figure 1. Steel pipe (e.g., oil and gas pipelines) and the formation of a sandwich component can be used as a new type of combined pipe for pipeline transportation. The cross section of a pipe is a composite structure.

In this study, double-walled hollow-walled concrete-filled steel tubular (CFST) members are considered to have low-cycle fatigue properties.

Scholars have conducted significant research on the mechanical properties of double-walled hollow tube components. Wang et al. [2] and Zhao et al. [3] have studied the

bearing capacity of CFSTs under axial compressive stress and proposed that the confining force between steel pipe and concrete significantly improves the bearing capacity of members. Zhao et al. conducted an axial compression load test on six double-walled hollow-walled CFSTs [4]. The effect of slenderness ratio on the bearing capacity was studied. The bearing capacity of the pipe was found to decrease as the slenderness ratio increased. Elchalakani et al. studied the ductility and failure modes of eight circular concrete-filled double-walled hollow-walled CFST columns under axial compressive load [5]. The experimental results are in close agreement with the standard Load and Resistance Factor Design (LRFD) specification for structural steel buildings [6]. Uy [7] conducted an experimental study on 30 squares of CFST and analyzed the effect of concrete grade and slenderness on the mechanical properties of concrete-filled steel tubes. The results showed that the bearing capacity of CFST columns decreased along with the slenderness ratio and increased along with an increase in concrete grade. Zhao and Grzebieta [8] conducted an experimental study on eight

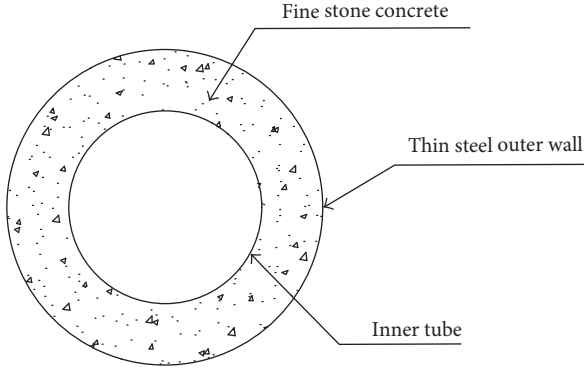


FIGURE 1: DWHP section pattern.

square concrete hollow stub columns with short columns and five long columns and showed the ratio of outer diameter to thickness to have a significant influence on the performance of hollow-walled CFST columns. Test results have shown that the failure mode of an outer steel wall is similar to that of solid CFST, and the failure mode of an inner steel tube is similar to that of an empty steel tube. Han conducted experiments on a new type of external stainless steel hollow steel tube concrete columns and proposed bearing capacity formula [9]. Huang and Li [10, 11] studied the mechanical properties of hollow-walled CFST under torsional load and steel tube initial stress, respectively, and proposed formulas to guide the engineering design. Lu [12] conducted an experimental study on the fire resistance of six hollow-walled CFST columns. This study examined the combined effect of two layers of steel pipe and a concrete sandwich between composite column specimens, which could be fully exerted under the fire load. Liu [13] conducted a double-walled hollow-tube seismic performance test and finite element analysis. Wang assessed the load-displacement relationship of three kinds of CFSTs and one square concrete-filled double-skin steel tube under reciprocating load [14]. Hong et al. studied the mechanical properties and failure modes of five double-walled hollow CFST short columns that were subjected to compressive, flexural, and shear stresses. The initial stiffness and ultimate load of the double-walled hollow-tube columns decreased as the shear span ratio increased [15].

This research mainly considered the influence of section type, slenderness ratio, and other factors on the bearing capacity and seismic performance of tubes. It did not fully consider the influence of sandwich concrete strength, size effect, or the thin-walled outer layer on the mechanical properties of DWHP components.

On the basis of these research studies, we studied the energy dissipation and antiseismic performance of double-walled hollow CFST members. Through low-cycle loading tests of three specimens, we conducted an analysis of the effects of the geometrical characteristics and filled concrete strength of stainless steel (thin steel outer wall)-concrete steel double-walled hollow-tube specimens on the mechanical properties, including hysteretic capacity, bearing capacity, and stiffness degradation. In conducting this research, we have provided the basis for the research and application of new composite tube members.

## 2. Test Specimen Design

**2.1. Test Specimen Size.** To analyze the influence of the thickness of the outer pipe and the strength of the interlayer concrete on the mechanical properties of that pipe, we conducted a comparative analysis in which we kept the inner pipe consistent and changed the parameters of the outer pipe and the strength of the concrete. We selected the wall thickness of the outer pipe according to the sectional stratification method proposed in [1]. We calculated the outer wall thickness  $t_1$ , the inner wall thickness  $t_2$ , the thickness of the concrete interlayer  $h$ , the inner diameter ( $d$ ), the outer diameter ( $D$ ), and the bending bearing capacity ( $M$ ) as follows [1]:

$$h = \frac{D-d}{2} - t_1,$$

$$M = \sum M_k,$$

$$= 2 \sum_{k=0}^n (\sigma_{s1,k} \gamma_{s1,k} d A_{s1,k} + \sigma_{s2,k} \gamma_{s2,k} d A_{s2,k} + \sigma_{c,k} \gamma_{c,k} a A_{c,k}), \quad (1)$$

where

$$\gamma_{s1,k} = \frac{D}{2} \sin(\theta_k - 0.5 d \theta),$$

$$\gamma_{s2,k} = \frac{d}{2} \sin(\theta_k - 0.5 d \theta), \quad (2)$$

$$\gamma_{c,k} = \left(\frac{D}{2} - t_1\right) \sin(\theta_k - 0.5 d \theta),$$

where  $\sigma_{s1,k}$  is the outer steel pipe  $k$  stratified zone with compressive stress,  $\sigma_{s2,k}$  is the inner steel pipe  $k$  stratified zone with compressive stress, and  $\sigma_{c,k}$  is the  $k$  stratified zone concrete compressive stress.

We used the inner tube parameter as the set value to determine the diameter of the outer tube, concrete strength, and maximum bending moment ( $M$ ). We used a cross section method to calculate the required outer-wall thickness.

According to the requirements of test equipment and the mechanical analysis of test components, we designed a total of three double-walled hollow-walled concrete specimens. The total specimen height was 1520 mm, and the net height was 1200 mm. We used Q235 steel. We filled the specimens with two types of concrete with different degrees of strength: C60 and C40.

The materials and geometrical dimensions of each specimen are given in Table 1.

**2.2. Specimen Material Strength.** We used the MTS electro hydraulic servo universal testing machine with inner and outer tube steel with unilateral tensile state yield strength of  $f_{yi}$  and  $f_{yo}$ , ultimate tensile strength of  $f_{ui}$  and  $f_{uo}$ , elastic modulus  $E_i$ ,  $E_o$ , and other mechanical properties; we determined the cubical compressive strength of the C60 and C40 concrete. We used (3) to calculate the nominal steel

TABLE 1: Geometric parameters of specimens.

Number	Concrete grade	$D_0 \times t_0$ (mm)	$D_i \times t_i$ (mm)	$A_{S0}$ (mm <sup>2</sup> )	$A_{CE}$ (mm <sup>2</sup> )
DWHP-1	C60	140 × 2	76 × 3	867.1	14527
DWHP-2	C60	140 × 2	76 × 3	867.1	14527
DWHP-3	C40	110 × 2	76 × 3	678.6	8825

TABLE 2: Material performance parameters of specimens.

Number	$\alpha_n$ (%)	$\xi$	$f_{yi}$ (MPa)	$f_{yo}$ (MPa)	$f_{ui}$ (MPa)	$f_{uo}$ (MPa)	$E_i$ (MPa)	$E_o$ (MPa)	$f_{cu}$ (MPa)
DWHP-1	5.969	0.42	301	288	442	407	1.56E5	1.77E5	63.43
DWHP-2	5.969	0.64	301	288	442	407	1.56E5	1.77E5	42.07
DWHP-3	7.690	1.65	301	288	442	407	1.56E5	1.77E5	42.07

content ( $\alpha_n$ ) of the pipe and (4) to calculate the steel pipe confinement effect coefficient ( $\xi$ ).

The material properties and other parameters are given in Table 2.

In Table 2,

$$\alpha_n = \frac{A_{s0}}{A_{CE}}, \quad (3)$$

$$\xi = \alpha_n \frac{f_{y0}}{f_{ck}}, \quad (4)$$

where  $A_{s0}$  is the outer tube cross section area and  $A_{CE}$  is the outer area surrounded by steel pipe.

### 3. Test Equipment and Loading System

Considering the second-order ( $P-\Delta$ ) effect of the component, we used a column loading mode. The test device was composed of a concrete floor, a frame to support the vertical load, a beam, and a rolling support. The specimen loading device is shown in Figure 2. We used a DGS-4 computer-controlled electro hydraulic servo-loading system to reciprocate specimen loading. The bottom of the specimen was connected using a fixed steel base, and the top was connected with a crossbeam. The beam was connected to the distribution beam and the horizontal actuator, as shown in Figure 2(a). A vertical load exerted by the hydraulic jack (100 t) above the distribution beam was transmitted to the test piece through the distribution beam and the crossbeam so that the test piece was axially compressed. We used a horizontal actuator (maximum test force of 250 kN, stroke of  $\pm 75$  mm) on the specimen's horizontal reciprocating load. The rolling support moved freely along the horizontal direction of the track. The rolling support and the crossbeam ensured that the top of the test specimen moved horizontally without twisting or bending.

We applied a vertical hydraulic jack to the specimen to test constant axial force and used the symmetrical displacement method to load the specimen's horizontal reciprocating load.

In the test, we preloaded the vertical load first, and then preloaded the horizontal load step by step. The loading scheme is shown in Figure 3. When the displacement amplitude was less than 6 mm, we loaded it in increments of

1.5 mm. When the amplitude was larger than 6 mm, we loaded it in steps of 6 mm. The load cycle for each stage was completed three times. Damage to the outer wall of the steel tube was the failure criterion for the test. [16].

### 4. Test Phenomenon and Analysis of Results

**4.1. Failure Mode.** Figure 4 shows the failure modes of the three test specimens under the action of fatigue load with the same axial compression ratio. The failure occurred toward the end of the specimen, and the damage property was caused by the bending failure. We subjected the specimens to repeated low-cycle loading. When we subjected the test specimen to low cyclic loading, the drum area at the end of the outer steel pipe appeared first, forming a plastic hinge area. Finally, fatigue damage formed in the plastic hinge area at the end of the outer steel pipe, which eventually caused the final damage. During the test, we observed that the outer steel pipe had an obvious tearing failure, which was accompanied by the sound of concrete fracturing. We observed that the concrete fractured after the outer wall was damaged. The bearing capacity of the specimen did not drop abruptly at any point from the loading to the final destruction of the outer wall, and the specimen did not sustain any overall damage, which showed its good ductility and low-cycle fatigue resistance.

**4.2. Hysteretic Curve.** Figure 5 shows the specimen's moment-curvature ( $M-\varphi$ ) hysteretic curve. At the initial stage of test loading, the area covered by the hysteretic curve of the test piece was small. We observed very little residual deformation of the test piece, and rigidity degeneration was not readily visible. The test piece was in an elastic working state. After the initial stage of the test loading, the area of the package gradually increased along with an increase in the number of loading cycles and the control displacement. The hysteretic curve tilted toward the displacement axis. The rigidity of the specimen began to decrease and entered the plastic working state. When we applied the maximum load, the specimen-bearing capacity and energy consumption began to decline gently.

Comparing the  $M-\varphi$  hysteretic curves of the specimens, we found the following: (1) The hysteresis curve of DWHP-1 was fuller, and the peak load capacity was greater than

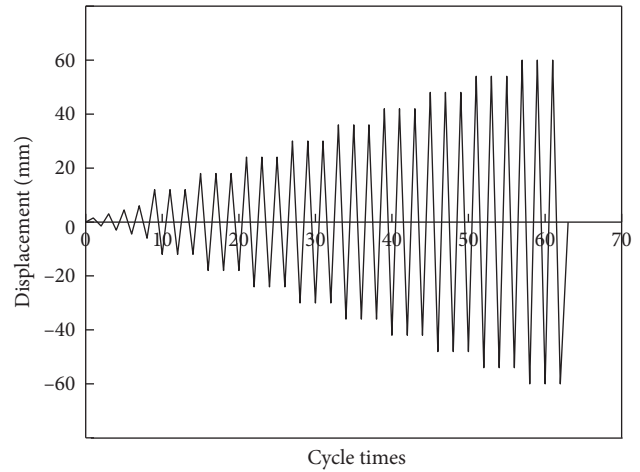
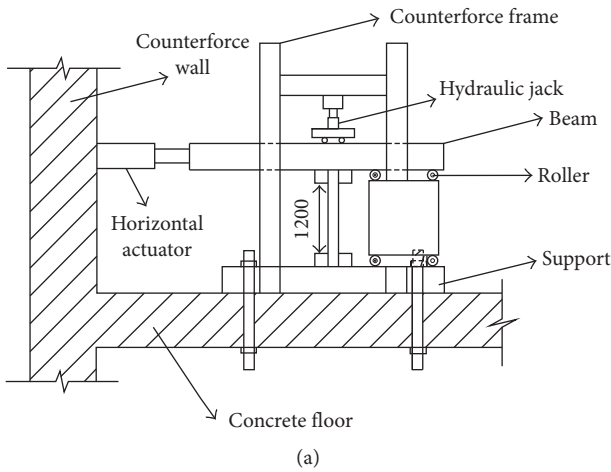


FIGURE 3: Sketch of loading scheme.



FIGURE 2: Loading device for specimen. (a) Sketch of sample loading device and (b) sample loading device spot map.

DWHP-2 and DWHP-3 specimens for the same geometric size, steel strength, and axial compression ratio. In this way, ductility and energy dissipation capacity of the specimens can be improved by appropriately increasing the strength of the concrete. (2) The specimen of DWHP-3 had a smaller section size and a lower strength level of concrete. The hysteretic curve was full, without a significant pinch phenomenon and showed good hysteretic performance. The analysis showed that although the cross section dimension of the DWHP-3 specimen was the smallest, the restraining effect coefficient  $\xi$  of this specimen was the largest, which

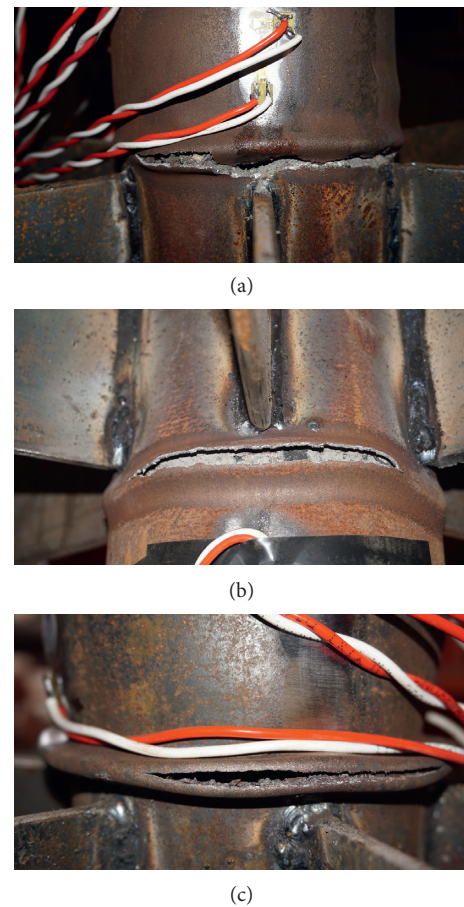


FIGURE 4: Failure modes of specimens. (a) Lower-end tearing of DWHP-1, (b) upper-end tearing of DWHP-2, and (c) lower-end tearing of DWHP-3.

was 2.5 times that of specimen DWHP-2 and 3.9 times that of specimen DWHP-1. Improving the component confinement factor can reduce the section size or the strength grade of the concrete, which is the purpose of optimizing the design of the structure.

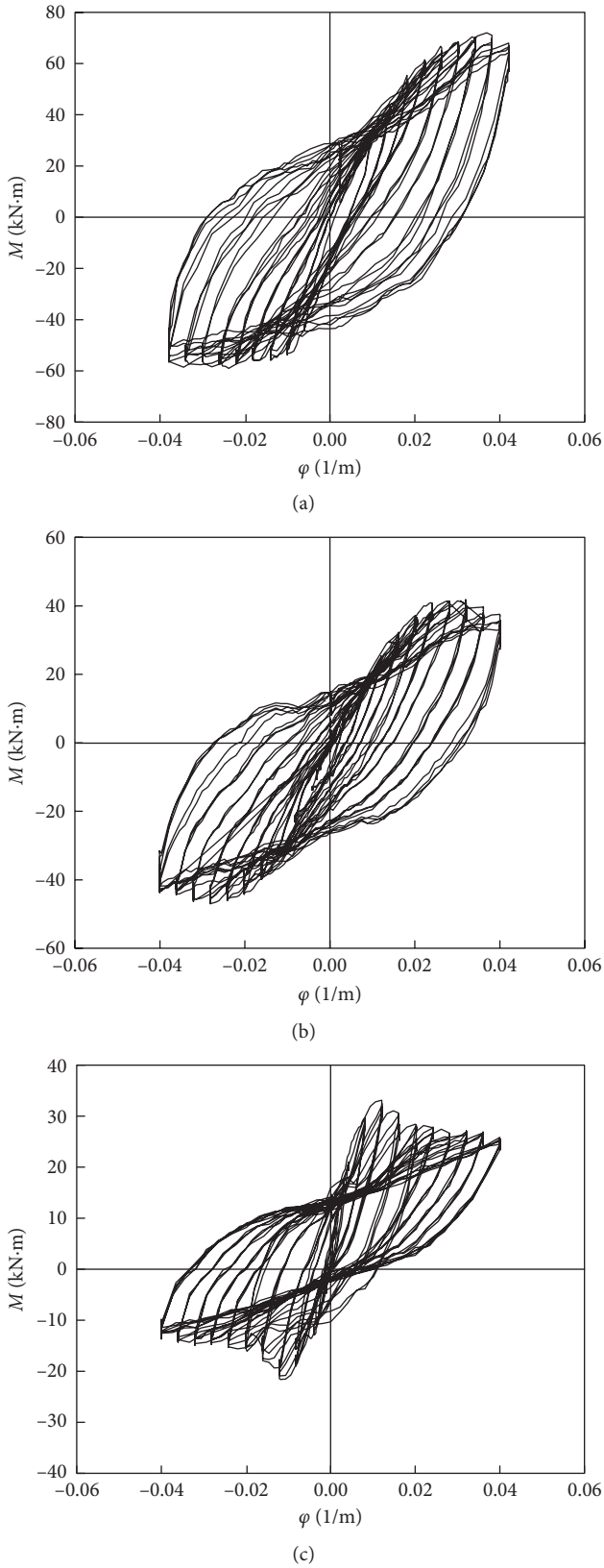


FIGURE 5:  $M$ - $\phi$  hysteretic loops of specimens. (a) Specimen DWHP-1, (b) specimen DWHP-2, and (c) specimen DWHP-3.

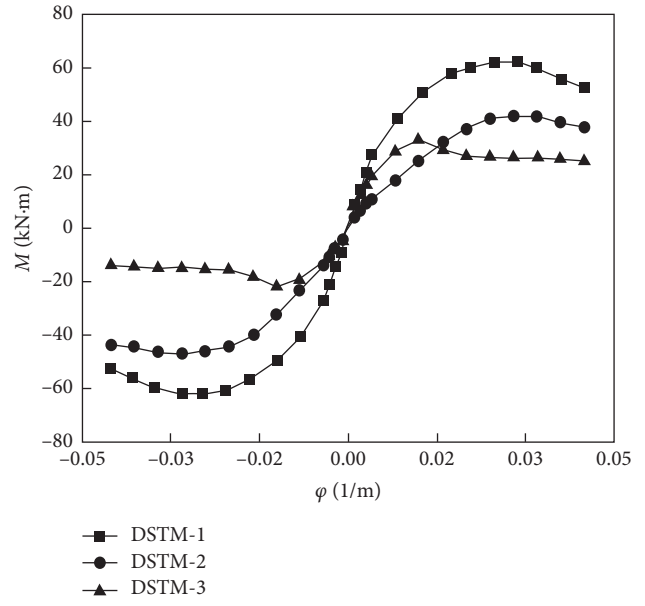


FIGURE 6:  $M$ - $\phi$  skeleton loops of specimens.

4.3. *Skeleton Curve.* We obtained the  $P$ - $\Delta$  skeleton curve of the specimen by first connecting the peak load points of the tested  $M$ - $\phi$  hysteretic curve to each target displacement [17]. The results are shown in Figure 6. Under low-cycle loading, the specimens underwent four working stages: elasticity, yield, peak, and damage. At the initial stage of specimen loading, the skeleton curve developed linearly. When the curve was loaded with an obvious inflection point, the specimen began to yield, and the stiffness began to degrade. As the control displacement increased, the stiffness of the specimen degenerated further. When the peak point of the skeleton curve was reached, the degradation of the bearing capacity of the specimen changed more smoothly. The results showed that the degradation rate of DWHP-2 was greater than that of DWHP-1 and smaller than that of DWHP-3. DWHP-3 showed significant degradation at the target displacement of  $\pm 20$ .

We analyzed the phenomenon by which the double-wall sandwich-filled concrete under the constraint of the double steel pipe in a three-dimensional compression could improve the strength of filled concrete, allow the concrete to be filled with steel to provide lateral support, and protect the thin steel wall from local instability. Under these working conditions, the specimen showed good overall plasticity and ductility. The outer side of the steel pipe had a thin steel layer, however, and its stability was greatly influenced by the bond between the concrete and the steel plate, and the strength of the concrete had a great influence on the ductility of the components. Within a certain range, the strength of the concrete could effectively increase the specimen ductility and improve fatigue resistance. The analysis showed that the reinforcement of the steel plate and the concrete could be strengthened by adding reinforcing ribs inside the outer wall, which effectively improved the local stability of the

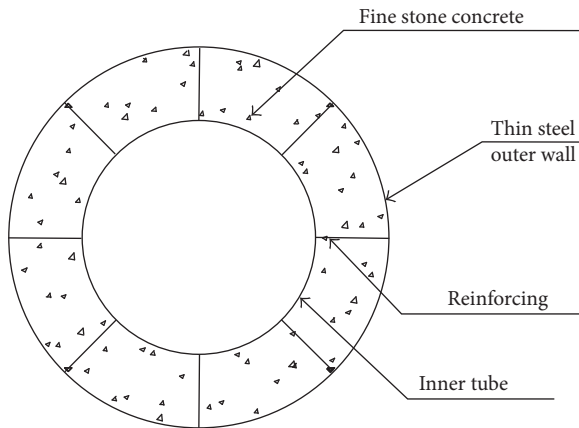


FIGURE 7: Section type of the stiffener pipe.

component. The addition of an outer-wall stiffener is shown in Figure 7.

**4.4. Hysteretic Energy Consumption.** We used the plastic hysteretic energy of the component to evaluate the seismic behavior of the structure. The numerical value was proportional to the seismic performance of the structure. The better the seismic performance of the buildings, the greater the plastic hysteretic energy value would be. In this experiment, the sum of the energy absorbed by the specimen was expressed as the area of the closed hysteretic loop formed after one week of the test specimen's circulation [17, 18]. We calculated the total hysteretic energy of the specimen according to the following equation:

$$W_p = \sum_{i=1}^n W_i, \quad (5)$$

where  $n$  is the  $i$ th cycle load times and  $W_i$  is  $i$ -hysteretic loop energy value.

The size of the area enclosed by the hysteretic ring reflects the pros and cons of the seismic performance of the structure to a certain extent. The energy dissipation values of the top of the member at each stage of the displacement cycle are given in Table 3.

To facilitate a comparative analysis, we assessed the axial loading-displacement curve fitted to each ring hysteretic loop, using the size of that area to indicate the hysteretic energy value. The sum of the energy dissipation values of the specimen in the displacement cycle at various stages is shown in Figure 8.

The hysteretic energy dissipation diagrams of DWHP-2 and DWHP-1 show that the other conditions are the same. When the concrete strength changed from 42.07 MPa to 63.43 MPa, the hysteretic energy of the specimen was controlled and changed from 2659.4 kN-mm to 4426.5 kN-mm, an increase of 1.66 times.

Compared with DWHP-3 and DWHP-2, the hysteretic energy loss of DWHP-3 was greater than that of DWHP-2 before the initial displacement and before the displacement of the 30 mm hysteretic energy value. When the control displacement was greater than 30 mm, the DWHP-3

TABLE 3: Energy dissipation of each cycle of specimen displacement.

Displacement	Hysteretic energy consumption (kN-mm)		
	DWHP-1	DWHP-2	DWHP-3
±6	48.49	45.29	32.96
±12	244.19	131.69	197.74
±18	444.58	201.09	332.2
±24	792.99	407.09	559.95
±30	1160.9	649.53	833.49
±36	1723.7	992.97	788.83
±42	2249.4	1279.5	754.16
±48	2921.8	1817.2	929.64
±54	3613.1	2305.3	1102.5
±60	4426.5	2659.4	1258.5

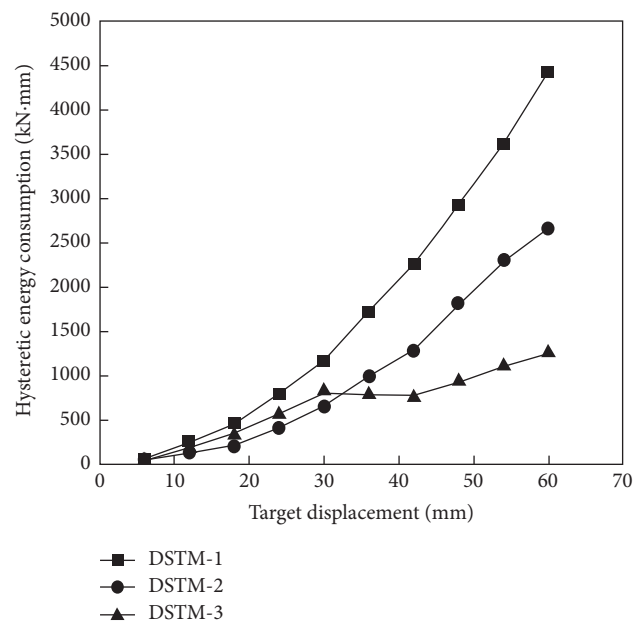


FIGURE 8: Hysteretic energy of specimens.

hysteretic energy value had a sudden downward trend and gradually fell below the DWHP-2 hysteretic energy value. When the control displacement reached ±42 mm, the bearing capacity of DWHP-3 decreased to about 80% of the peak load. The energy dissipation value of DWHP-3 began to increase as the target displacement increased, but the range of increase was obviously smaller than that of DWHP-2. An analysis of these test results suggested that the high-strength concrete made up for the brittleness defects of the material under the restraint of the double-layer steel pipe inside and outside greatly improved the energy-absorbing and damping capacity of the component. Because of the thin-walled steel pipe, under the condition of the same concrete strength, the size of the component had a greater impact on energy dissipation capacity. When the strength of the member reached about 80% of the yield load, the energy dissipation capacity of the ASTM-3 small section member had a downward trend when the displacement of the target was 30 mm.

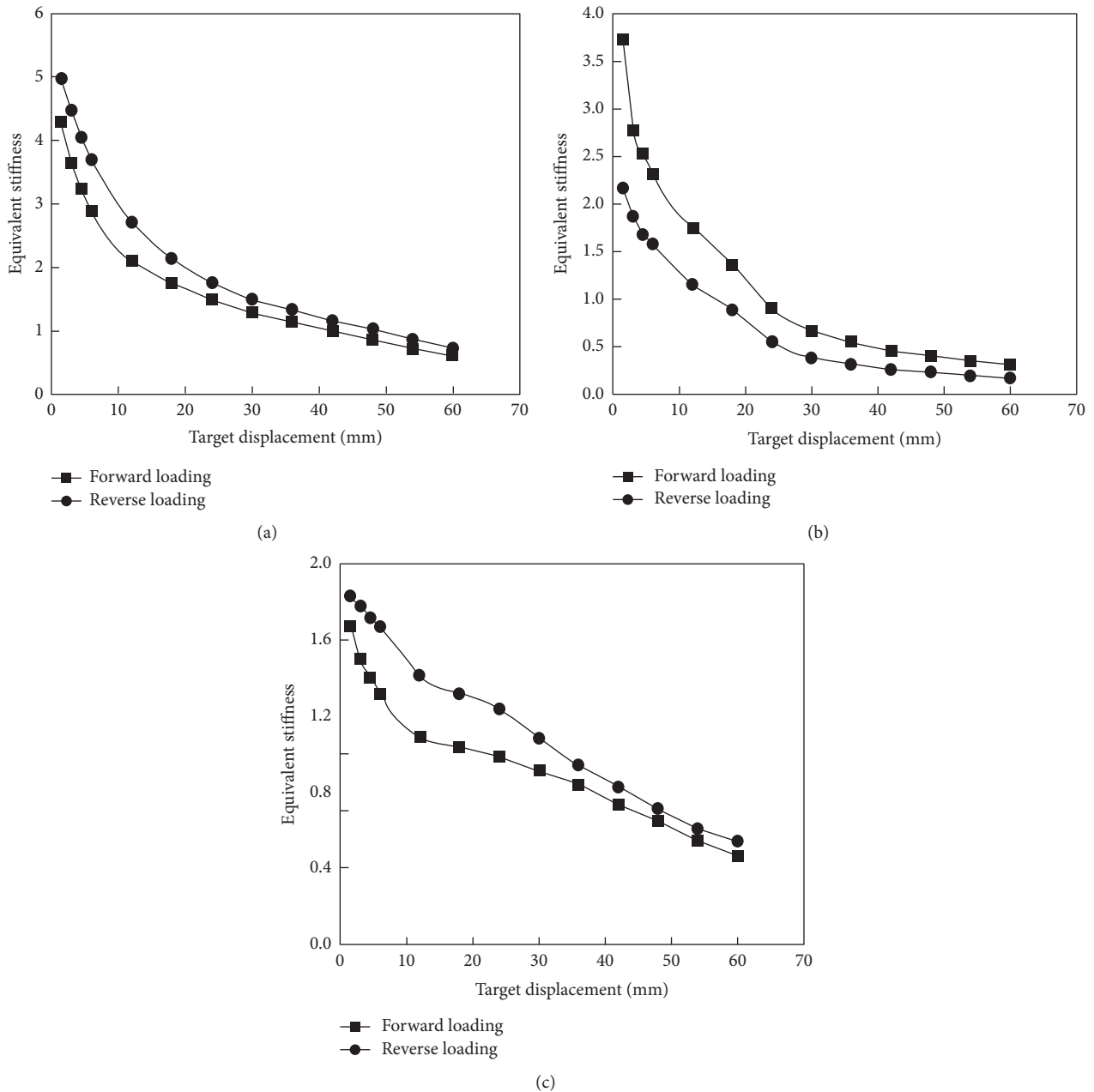


FIGURE 9: Degeneration rigidity loops of specimens. (a) Specimen DWHP-1, (b) specimen DWHP-2, and (c) specimen DWHP-3.

**4.5. Stiffness Degradation.** We used the equivalent stiffness to show the stiffness decay of the specimen under low-cycle loading. The stiffness of each specimen was the ratio of the corresponding load value to the target displacement value when the target displacement was reached for the first time. Equivalent stiffness of the specimen expression [19] is shown in the following:

$$K = \frac{P}{\Delta}. \quad (6)$$

Equivalent stiffness decay curve when the specimen is loaded is shown in Figure 9.

As shown in Figure 10, the stiffness degeneration trend of each specimen was similar; all specimens experienced

a degeneration process that changed from fast to slow. In the initial stage of loading, the specimen was in a flexible working condition and had the most rigidity. With the gradual increase of displacement of the experimental target, concrete cracks and continuous development of specimens increased until plastic deformation gradually occurred. When the relative slip between the inner and outer steel pipes and the filled concrete occurred, the restraint effect of the steel pipe on the core concrete began to weaken. The initial stiffness of specimens DWHP-1 and DWHP-2 with the same cross section size and different concrete strength was about 4.5 and 3.0, respectively. However, the degeneracy curves were basically the same and their stiffness degenerated similarly. The initial stiffness of DWHP-2 and

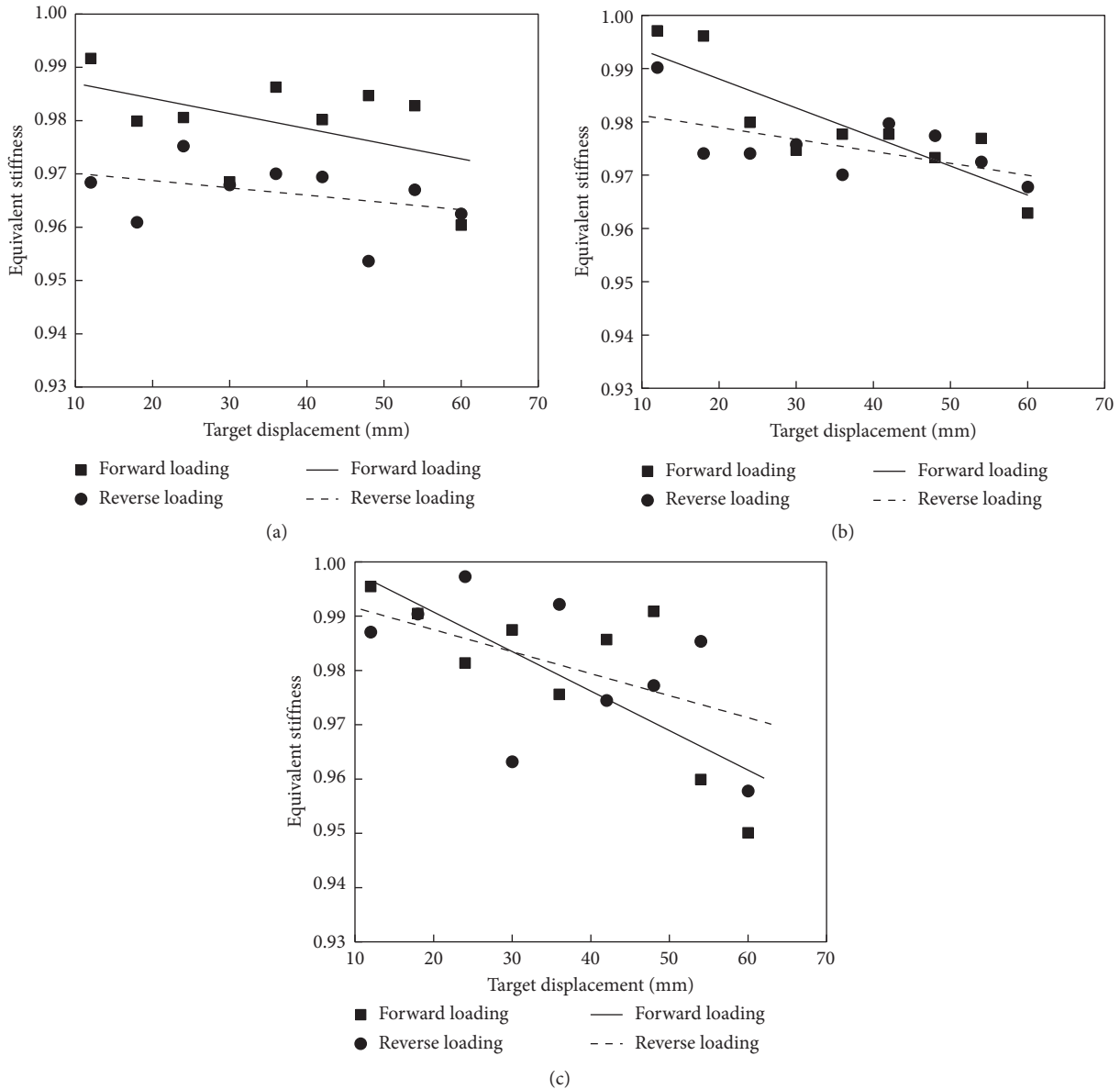


FIGURE 10: Degeneration loading loops of specimens. (a) Specimen DWHP-1, (b) specimen DWHP-2, and (c) specimen DWHP-3.

DWHP-3 with the same concrete strength and different cross section dimensions was about 3.0 and 1.7, respectively. The linear regression curves showed that the degeneracy rate of DWHP-3 was larger than that of DWHP-2.

According to the analysis of the test phenomenon, the initial elastic stiffness of the specimen was closely related to the concrete strength, whereas the stiffness degradation rate was less affected by the concrete strength under the reciprocating loading. The cross section dimension had a significant effect on the initial elastic stiffness and the rate of stiffness degradation. The larger the initial cross section stiffness, the lower the rate of stiffness degradation would be.

**4.6. Intensity Degradation.** The specimen’s bearing capacity was largest when the specimen reached the target displacement for the first time. The calculated value of the

degradation of bearing capacity was the load value  $P_i$  when the specimen reached the displacement at the  $i$ th time and was divided by the load value  $P_1$  when the specimen reached displacement the first time. We compared the second load value under each control displacement with the first load ratio of  $P_2/P_1$  to analyze the bearing capacity of the specimen decay. The bearing capacity degradation curve for each specimen is shown in Figure 10.

The results show that under the action of repeated low-cycle loading, the internal damage of the specimen developed, and the bearing capacity gradually decayed. The bearing capacity decay rule of each specimen was similar to the decay of bearing capacity of three specimens, and there was no significant attenuation of bearing capacity during the entire experiment. The loading rate of specimen DWHP-1 decayed slowly, and the slope of strength degradation was the smallest. The slope of bearing capacity degradation of

specimen DWHP-2 was similar to that of specimen DWHP-3. As shown, under cyclic loading, the slope of degradation was greatly affected by the strength of concrete. The higher the strength was, the smaller the slope of degradation was and the smaller the effect of size effect was.

## 5. Conclusion

According to the quasistatic test method, we conducted a low-cycle fatigue test of three double-walled hollow CFST specimens with different geometrical characteristics and different filled concrete strengths. The main conclusions are as follows:

- (1) We calculated the bending design of DWHP using the cross section method. Through a low-cycle loading test, the results showed that the strength grade of the C60 sandwich concrete, under the same geometrical size, steel strength, and axial compression ratio, had better ductility and energy dissipation capacity than that of the C40 concrete specimen. The ductility and energy dissipation capacity of the specimens could be improved by strengthening the concrete. Analysis showed that although the cross section dimension of DWHP-3 specimen was the smallest, the restraining effect coefficient  $\xi$  of this specimen was the largest, which was 2.5 times that of specimen DWHP-2 and 3.9 times that of specimen DWHP-1. The DWHP-3 specimen still had good ductility and energy dissipation capacity by improving the confinement factor to appropriately reduce the section size or strength grade of the concrete to optimize the design of the structural section.
- (2) The combination of DWHP concrete sandwich members, concrete, and steel worked together to ensure that the mechanical properties provided the specimens with higher strength and ductility. But the outer side of the steel pipe was a thin steel layer, and the bond between the concrete and the steel plate had a significant influence on the stability of the concrete. Because of the cohesive force, the strength of the concrete did not have an obvious influence on the local instability of the components. The analysis showed that addition of reinforcing ribs on the inner side of the outer wall of the steel pipe could improve the adhesion of the thin steel plate to the concrete, which could effectively improve the local stability of the specimens.
- (3) The composite cross section of the outer steel pipe for the thin steel layer, under the conditions of the same concrete strength, showed that the size of the component had a greater impact on energy dissipation capacity. When the strength of the specimens reached about 80% of the yield load, the energy dissipation capacity of the small section specimens had a downward trend when the displacement of the target was 30 mm. The main cause of the smaller yield displacement was the smaller geometrical dimension of the specimen.

- (4) Under cyclic loading of DWHP, the strength degradation slope of the C60 sandwich concrete was obviously lower than that of the C40 concrete specimen. The slope of the strength degradation of the specimens decreased with an increase in the strength of the filled concrete within a certain range, but the strength degradation slope was less affected by geometric characteristics.

## Conflicts of Interest

The authors declare that they have no conflicts of interest.

## Acknowledgments

This work was supported by the National Natural Science Foundation of China (51578120) and the National Youth Science Foundation (11402051).

## References

- [1] L. Zhaohong, Y. Liang, G. M. Zhang et al., "Calculation of the flexural capacity of double-skin-tubular members by section stratification method," *Journal of Hebei University of Engineering*, vol. 4, pp. 11–14, 2015.
- [2] Z. Wang, W. Zhang, S. Chi et al., "Flexural behavior of composite concrete-filled square thin-walled steel tubular specimens," *Journal of Building Structures*, vol. 38, no. 7, pp. 78–84, 2017.
- [3] J. Zhao, H. Guo, and X. Wei, "Research on bearing capacity of concrete filled double skin steel tubes column," *Journal of Architecture and Civil Engineering*, vol. 22, no. 1, pp. 50–54, 2005.
- [4] X. L. Zhao, R. H. Grzebieta, and M. Elchalakani, "Tests of concrete-filled double skin circular hollow sections," in *Proceedings of the First International Conference on Steel and Composite Structures*, pp. 283–290, Pusan, Korea, June 2001.
- [5] M. Elchalakani, X. L. Zhao, and R. Grzebieta, "Tests on concrete filled double-skin (CHS outer and SHS inner) composite short columns under axial compression," *Thin-Walled Structures*, vol. 40, no. 5, pp. 1–28, 2002.
- [6] Z. Raochun and Z. Xuhong, *The Principle of Steel Structure Design*, Higher Education Press, Beijing, China, 2013.
- [7] B. Uy, "Strength of concrete filled steel box columns incorporating local buckling," *Journal of Structural Engineering*, vol. 126, no. 3, pp. 341–352, 2000.
- [8] X. L. Zhao and R. Grzebieta, "Strength and ductility of concrete filled double-skin (SHS inner and SHS outer) tubes," *Thin-Walled Structures*, vol. 40, no. 2, pp. 199–213, 2002.
- [9] L. H. Han, Q. X. Ren, and W. Li, "Tests on stub stainless steel-concrete-carbon steel double-skin tubular (DST) columns," *Journal of Constructional Steel Research*, vol. 67, no. 3, pp. 437–452, 2011.
- [10] H. Huang, L. H. Han, and X. L. Zhao, "Investigation on concrete filled double skin steel tubes columns under pure torsion," *Journal of Constructional Steel Research*, vol. 90, no. 1, pp. 221–234, 2013.
- [11] W. Li, L. H. Han, and X. L. Zhao, "Axial strength of concrete-filled double skin steel tubular columns with preload on steel tubes," *Thin-Walled Structures*, vol. 56, no. 1, pp. 9–20, 2012.
- [12] H. Lu, L. H. Han, and X. L. Zhao, "Fire performance of self-consolidating concrete filled double skin steel tubular

- columns experiments,” *Fire Safety Journal*, vol. 45, no. 2, pp. 106–115, 2010.
- [13] Y. Liu, *Finite Element Analysis on Axial Compression and Seismic Behaviors of Multibarrel Tube-Confined Concrete*, Chang’an University, Xi’an, China, 2015.
- [14] N. Wang, *Experimental Research and Numerical Simulation of Concrete-Filled Double Skin Steel Tubes-Columns*, Hebei University of Engineering, Hebei, China, 2013.
- [15] H. Hong, S. Wei, C. Meng Cheng et al., “Experimental study on concrete-filled double-skin circular steel tubes under combined loadings,” *Journal of Building Structures*, vol. 9, pp. 53–59, 2015.
- [16] T. Zirakian and J. Zhang, “Buckling and yielding behavior of unstiffened slender, moderate, and stocky low yield point steel plates,” *Thin-Walled Structures*, vol. 88, pp. 105–118, 2015.
- [17] B. Zhu, *Structural Seismic Test*, Seismological Press, Beijing, China, 1989.
- [18] W. Zhang and W. Zhao, “On the issues of life cycle fatigue damage for the columns of concrete-filled steel tubular,” in *Proceedings of the 17th National Conference on Structure Engineering*, pp. 684–687, Huazhong University of Science and Technology, Wuhan, Hubei, China, 2008.
- [19] J. Zhou and S. Chen, *Experimental Study and Evaluation Method of Mechanical behavior of High Strength Reinforced-Concrete Structure*, Science Press, Beijing, China, 2015.

## Research Article

# Comparative Study of CFRP-Confined CFST Stub Columns under Axial Compression

Ying Guo<sup>1</sup> and Yufen Zhang<sup>2</sup> 

<sup>1</sup>School of Civil Engineering, Tianjin University, Tianjin 300072, China

<sup>2</sup>School of Civil and Transportation Engineering, Hebei University of Technology, Tianjin 300401, China

Correspondence should be addressed to Yufen Zhang; yufenzh@gmail.com

Received 25 May 2018; Revised 24 June 2018; Accepted 3 July 2018; Published 18 July 2018

Academic Editor: David M. Boyajian

Copyright © 2018 Ying Guo and Yufen Zhang. This is an open access article distributed under the Creative Commons Attribution License, which permits unrestricted use, distribution, and reproduction in any medium, provided the original work is properly cited.

This paper presented a comparative study of concrete-filled steel tubular (CFST) stub columns with three different confinement types from carbon fiber reinforced polymer (CFRP): outer circular CFRP, inner circular CFRP, and outer square CFRP. The compressive mechanism and physical properties of the composite column were analyzed firstly aiming at investigating the confinement effect of CFRP. Ultimate axial bearing capacity of these three CFRP-confined CFST columns was calculated based on Unified Theory of CFST and elastoplastic limit equilibrium theory, respectively. Meanwhile, the corresponding tests are adopted to validate the feasibility of the two calculation models. Through data analysis, the study confirmed the ultimate strength calculation results of the limit equilibrium method were found to be more reliable and approximate to the test results than those of Unified Theory of CFST. Then axial bearing capacity of the pure CFST column was predicted to evaluate the bearing capacity enhancement ratio of the three types of composite columns. It was demonstrated that the averaged enhancement ratio is 16.4 percent, showing that CFRP-confined CFST columns had a broad engineering applicability. Through a comparative analysis, this study also confirmed that outer circular CFRP had the best confinement effect and outer square CFRP did better than inner circular CFRP. The confinement effect of CFRP increased with the decrease of concrete strength, and it was proportional with relative proportions of CFRP and steel under the same concrete strength.

## 1. Introduction

Carbon fiber reinforced polymers (CFRPs) have been widely used in repair and retrofit of deficient structures in recent decades, because externally bonded CFRP material in the form of sheets or plates is particularly well suited for flexure and shear [1, 2]. In many engineering fields, the CFRP-metal composite tanks or tubes have been used widely, such as gas tank used in motor vehicle and pipeline system for transporting high pressure gas or liquid used in municipal engineering or chemical engineering. CFRP materials, as external jackets for the confinement of reinforced concrete columns, can enhance strength and ductility [3–6]. The superior mechanical and physical properties of CFRP make them excellent candidates to repair and retrofit steel structures as well. Concrete-filled

steel tubular (CFST) structures have been studied and used in civil engineering widely for many years [7]. However, steel tubes are susceptible to degradation due to corrosion and its thin-walled section before concrete hardening [8], which results in the decrease of axial strength of the CFST column [9]. Therefore, the CFRP-metal tube can also be used in civil engineering, for example, the CFRP-steel composite tube infilled with concrete has been used as the column [10], and CFRP has also been used to reinforce damaged CFST column [11]. As discussed by Gu [12], Li et al. [13], and Wang et al. [14], most of the research conducted has focused on the use of CFRP for CFST structure. Carbon fiber sheets or plates are attached to a steel tube or concrete in a CFST member to increase its bearing capacity and ductility. It was concluded that the ultimate lateral strength and flexural stiffness of CFRP-repaired CFST beam-columns increased with the

increasing number of CFRP layers. Meanwhile, the ductility of specimens increased slightly with the number of CFRP layers. And, as discussed by Tao et al. [15], the CFRP cylinder can also impede buckling of the stub column leading to dramatic improvements in buckling and postbuckling behavior of the entire system. Wang et al. [16, 17] conducted axial compression experiments for thirty-two circular CFRP-confined CFST columns and twenty-four square CFRP-confined CFST columns. Analyses of the tested results show that the steel tube and its outer CFRP material can cooperate both longitudinally and transversely. Therefore, all these studies draw upon the concepts that complementary action between steel tube and concrete was strengthened through the higher confinement of CFRP.

Upon the abovementioned research, other types of composite columns have also been proposed. Karimi et al. [18] proposed a type of FRP-encased steel-concrete composite columns in which a circular FRP was placed around the steel I-section and had the concrete filled between the steel I-section and the FRP tube. Feng et al. [19] proposed a steel-concrete-FRP-concrete column which had a square steel tube as the outer layer and a circular filament-wound FRP tube as the inner layer, with concrete filled both between these two layers and within the FRP tube. The results of these studies showed that the strength of concrete, FRP, and steel could be effectively utilized in the composite columns.

All those research achievements confirmed that the composite column has its feasibility in theoretical research and engineering practice, showing a great potential for more development. Compressive strength is an important parameter for structural members, and most of those researches listed above were concentrated on the superposition method to calculate the ultimate compressive strength, so different formulas were deduced for every cross section of the CFRP-confined CFST columns. Therefore, the purpose of this paper is to build unified methods applicative to different sections of the composite column by the idea of Unified Theory of CFST and limit equilibrium theory. The focus of this study is to investigate three different technology CFRPs to strengthen CFST stub columns through a comparative study of three different confinement types: outer circular CFRP, inner circular CFRP, and outer square CFRP. Compressive mechanism and physical properties of these three CFRP-confined CFST columns were analyzed firstly aiming at investigating the confinement effect of CFRP on CFST columns. Two theoretical calculation models are presented to obtain the axial compressive capacity of CFRP-confined CFST columns. One is the Unified Theory of CFST [20]: the equivalent confinement coefficient is proposed with consideration of different sections of steel tubes and CFRP cylinders, and then formulas are derived from Unified Theory of CFST to predict the bearing capacity of the composite column under compression. The other is elastoplastic limit equilibrium method: twin-shear unified strength theory (TDUST) [21] is applied to analyze the ultimate state of steel tube and concrete, respectively, and then the ultimate bearing capacities of the composite column are obtained by the limit equilibrium method. The theoretical predictions were compared with the

experimental results to validate the feasibility of the two calculation models. Lastly, the CFRP confinement effects on the axial bearing capacity were analyzed by comparison of these three CFRP-confined CFST columns.

## 2. Working Mechanism

Based on the summary of existing researches, three types of CFRP-confined CFST columns are considered with different CFRP confinements including outer circular CFRP, inner circular CFRP, and outer square CFRP, as shown in Figure 1. The CFRP cylinder is wrapped outside the circular CFST column in Type a; CFRP cylinder is placed inside the square CFST in Type b, and CFRP cylinder is wrapped outside the square CFST column in Type c. As can be seen in Figure 1, steel tubes together with the confined concrete can resist the axial compression remarkably, while the CFRP cylinders can provide the lateral confinement to the steel tube or concrete directly and make the composite column behave better indirectly.

As we all know, during the process of compression of the composite columns, there exists horizontal deformation when the vertical load acts on the whole section. Take the example of Type a in Figure 1, concrete is filled in the circular tube wrapped by the CFRP sheet, so its simplified model of stress can be plotted in Figure 2.

Concrete's horizontal deformation coefficient was small at the beginning of the axial load, so the lateral stress  $p$  from steel tubes and CFRP sheet is not evident. With the increasing axial compression, concrete's horizontal deformation starts to gradually increase especially after the column yielding. There would be many microcracks happened in concrete after the column entered into plastic stage [22], but both the CFRP cylinder and steel tube can confine the concrete to postpone its expansion. The concrete can be regarded as three-dimensional compressed, the steel tubes can be regarded as thin-walled cylinders, and CFRP is only tensile in the circumferential direction as shown in Figure 2. The ultimate state considers the following failure modes of the CFRP-confined CFST column: steel tube buckling and CFRP sheet rupturing [23, 24]. Although the CFRP cylinder has no direct contribution to the axial bearing capacity, the transverse fiber sheets contribute to the strength enhancement by confining the CFST column in whole (see Type a, c in Figure 1) or in part (see Type b in Figure 1), leading to a higher compressive strength of the column. Therefore, the wrapping CFRP can lead to a significant improvement in the inelastic axial deformation capacity prior to buckling and an improved load carrying capacity after buckling.

## 3. Calculations by Unified Theory of CFST

Unified Theory of CFST was presented by Professor Zhong Shan-tong in 1993 [25]. It considered CFST as a unified body, and a new composite material was used to study its behaviors. It was a new method to design and simplify the design work. Unified Theory of CFST has been extended to calculate the compressive strength of the composite CFST

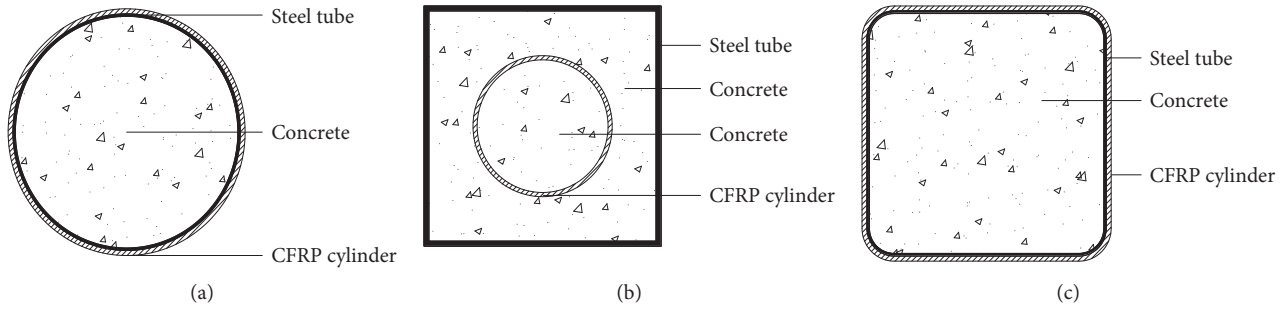


FIGURE 1: Cross section types of CFRP-confined CFST columns. (a) Outer circular CFRP. (b) Inner circular CFRP. (c) Outer square CFRP.

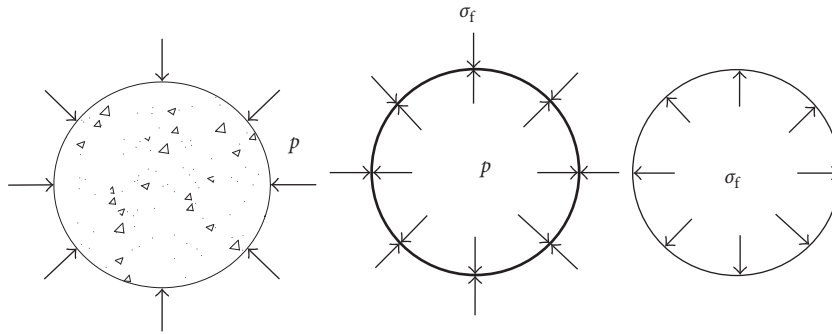


FIGURE 2: Stress model in the composite column under compression. (a) Concrete. (b) Steel tube. (c) CFRP cylinder.

columns with various confining materials and various cross sections under various loadings [26]. For CFRP-confined CFST columns, the concrete is still confined by the steel tube directly, and this confining effect is absolutely strengthened by the CFRP cylinder. One composite material can also be considered to assess its behaviors, but the confining effect should be reevaluated deriving from the steel tube and CFRP cylinder. We can extend deeper research works into CFRP-confined CFST columns, so one equivalent confinement coefficient  $\xi_{ssc}$  is presented, which can be expressed as

$$\xi_{ssc} = \frac{k_s A_s f_s + k_{cf} A_{cf} f_{cf}}{A_c f_{ck}}, \quad (1)$$

where  $A_s$ ,  $A_c$ , and  $A_{cf}$  are the cross section areas of the steel tube, concrete, and CFRP cylinder, respectively;  $f_s$  and  $f_{cf}$  are the yield strengths of steel and CFRP, respectively;  $f_{ck}$  is the standard compressive strength of the concrete;  $k_s$  and  $k_{cf}$  are the coefficients with consideration of section form of the confining material. Because in the composite column, there are two different materials to confine concrete, the effect of restraint is different from circular section to square section. Generally, the coefficient of circular section is taken as the basic parameter 1, and for square section, it is 0.74 [27].

Then the composite strength  $f_{ssc}$  of the stub column can be calculated by the formula derived from Unified Theory of CFST, and the equation can be expressed as

$$f_{ssc} = (1.212 + a\xi_{ssc} + b\xi_{ssc}^2) f_{ck}, \quad (2)$$

where  $a$  and  $b$  reflect the contributions of confining materials and concrete, respectively. They can be calculated by the following formula:

$$a = \frac{0.1759 f_{ss}}{235 + 0.974}, \quad (3)$$

$$b = \frac{-0.1038 f_{ck}}{20 + 0.0309},$$

where  $f_{ss}$  is the weighted average of the confining materials including both the steel tube and CFRP cylinder, which is calculated by

$$f_{ss} = \frac{A_s f_s + A_{cf} f_{cf}}{A_s + A_{cf}}, \quad (4)$$

Therefore, it is recommended to use the following formula to calculate the bearing capacity of the CFRP-confined CFST stub column.

$$N_y^1 = A f_{ssc}, \quad (5)$$

where  $A$  is the cross section area of the whole column and  $N_y^1$  is the bearing capacity calculated by Unified Theory of CFST.

## 4. Calculations by Limit Equilibrium Theory

**4.1. Basic Assumptions.** In this theoretical model for obtaining the axial compressive capacity, we can quantitatively analyze how much the confinement is influenced by the steel tube and CFRP. The interface between the steel tube and the CFRP sheet is constrained; the radial stress in the steel tube is ignored, and the steel tube is under biaxial stress; the CFRP material is linear elastic, and only the lateral stress is considered, so the stress along the fiber direction is

considered; the radial stress and the longitudinal stress are ignored.

Based on the above assumptions, the ultimate axial bearing capacity of CFRP-confined CFST columns can be calculated by

$$N_y^2 = N_s + N_c, \quad (6)$$

where  $N$ ,  $N_s$ , and  $N_c$  are vertical bearing capacities of the steel tube and concrete, respectively.  $N_y^2$  is the bearing capacity calculated by limit equilibrium theory. In the state of limit equilibrium, every part of the composite column can be analyzed using TSUST [21].

**4.2. Twin-Shear Unified Strength Theory (TSUST).** The TSUST considers the two larger principal shear stresses and the corresponding normal stresses and their different effects on the failure of materials. When the relationship function between them reaches one ultimate value, the material can be defined as failure at this state which is formulated as follows:

$$F = \tau_{13} + b\tau_{12} + \beta(\sigma_{13} + b\sigma_{12}) = C, \quad (7a)$$

$$\text{when } \tau_{12} + \beta\sigma_{12} \geq \tau_{23} + \beta\sigma_{23},$$

$$F' = \tau_{13} + b\tau_{23} + \beta(\sigma_{13} + b\sigma_{23}) = C, \quad (7b)$$

$$\text{when } \tau_{12} + \beta\sigma_{12} \leq \tau_{23} + \beta\sigma_{23},$$

where  $\tau_{12}$ ,  $\tau_{23}$ , and  $\tau_{13}$  are the principal shear stresses,  $\tau_{13} = (\sigma_1 - \sigma_3)/2$ ,  $\tau_{12} = (\sigma_1 - \sigma_2)/2$ , and  $\tau_{23} = (\sigma_2 - \sigma_3)/2$ ;  $\sigma_{12}$ ,  $\sigma_{23}$  and  $\sigma_{13}$  are the corresponding normal stresses on the principal shear stress element;  $\sigma_1$ ,  $\sigma_2$ , and  $\sigma_3$  are the principal stresses,  $\sigma_1 \geq \sigma_2 \geq \sigma_3$ ;  $b$  is a weighting coefficient, reflecting the relative effect of the intermediate principal shear stress  $\tau_{12}$  or  $\tau_{23}$  on the strength of materials;  $C$  equals to the material strength;  $\beta$  is the influence coefficient of positive stress on material damage. Denoting the tension-compression strength ratio as  $\alpha = \sigma_t/\sigma_c$ , we rewrite (7a) and (7b) in terms of principal stresses as follows:

$$F = \sigma_1 - \frac{\alpha}{1+b}(b\sigma_2 + \sigma_3) = \sigma_t, \quad \text{when } \sigma_2 \leq \frac{\sigma_1 + \alpha\sigma_3}{1+\alpha}, \quad (8a)$$

$$F' = \frac{1}{1+b}(\sigma_1 + b\sigma_2) - \alpha\sigma_3 = \sigma_t, \quad \text{when } \sigma_2 \geq \frac{\sigma_1 + \alpha\sigma_3}{1+\alpha}. \quad (8b)$$

**4.3. Formula of Ultimate Capacity.** By the principle of same area, the square cross section of the steel tube can be transformed into a circular one.  $B$  and  $t_s$  are the side length and thickness of the square steel tube, and  $r_o$  and  $t_o$  are the radius and thickness of the equivalent circular steel tube, respectively. The formulas are shown as follows:

$$r_o = \frac{B}{\sqrt{\pi}} = 0.5642B, \quad (9)$$

$$t_o = \frac{r_o - (B - 2t_s)}{\sqrt{\pi}} = r_o - 0.5642(B - 2t_s).$$

Meanwhile, because the confinement of the square steel is uneven along its side, the equivalent reduction factor should be considered to reduce the same confinement of the equivalent circular steel tube. Denoting thickness-side length ratio  $v = t/B$ , the expression of the equivalent reduction factor  $\xi = 66.4741v^2 + 0.9919v + 0.41618$  [28]. Meanwhile, there are effective and noneffective confining zones of the concrete inside the square steel tube. In this paper, the concrete strength reduction factor is considered to ignore these two influences. The concrete strength reduction factor is taken as  $\gamma_\mu = 1.67D_o^{-0.112}$  [28], where  $D_o$  is the inside diameter of the equivalent circular steel tube.

The simplified stress model of confined concrete is shown in Figure 2(a). The stresses can be explicated by  $0 > \sigma_1 = \sigma_2 > \sigma_3$ ,  $\sigma_1 = \sigma_2 = p$ . For  $\sigma_2 \geq ((\sigma_1 + \alpha\sigma_3)/(1 + \alpha))$ . Substituting them into the stress expression of TSUST, the following expression can be obtained as

$$\sigma_3 = \sigma_c = f_{ck} + k_c p, \quad (10)$$

where  $k_c$  is the lateral stress coefficient. In TSUST,  $k_c$  can be calculated by cohesion and friction angle at material failure state. According to the test of Richart [22],  $k_c$  has been taken as 4.1 simply here;  $p$  is the lateral stress on the concrete, and the lateral stress on concrete is from both the steel tube and CFRP cylinder for Type a and c as shown in Figure 1, so it can be expressed by

$$p = \sigma_f + \sigma_{rs}, \quad (11)$$

where  $\sigma_f = t_{cf}f_{cf}/r_{cf}$  and  $\sigma_{rs} = t_s f_s/r_s$ ;  $t_{cf}$  and  $r_{cf}$  are the thickness and radius of the CFRP cylinder, respectively;  $t_s$  and  $r_s$  are the thickness and radius of the steel tube, respectively. While for Type b in Figure 1, the concrete should be divided into exterior concrete and internal concrete under different lateral stresses. Exterior concrete is only confined by the steel tube, but internal concrete is considered both the steel tube and CFRP cylinder. Then the axial bearing capacity of the concrete can be expressed as

$$N_c = (f_{ck} + k_c p)A_c. \quad (12)$$

As can be seen in Figure 2(b), the steel tube is constrained by inside concrete so it can bear some vertical load under the ultimate state of the whole column,  $\eta$  is assumed as the strength reduction factor of the steel tube, and then the stress state of steel tubes can be explicated by  $\sigma_3 = \sigma_z = \eta f_s$ ,  $\sigma_2 = \sigma_r = 0$ ,  $\sigma_1 = \sigma_\theta = pr_o/t_s$ . For  $|\sigma_3| > \sigma_1$  and  $\sigma_2 \geq ((\sigma_1 + \alpha\sigma_3)/(1 + \alpha))$ , substitute them into the stress expression of TSUST, the following expression can be obtained:

$$\frac{pr_o}{t_s(1+b)} - \eta f_s = f_s. \quad (13)$$

TABLE 1: Comparison of calculations and test results.

Types Specimens	$t_{ef}$ (mm)	$f_{ef}$ (MPa)	$t_s$ (mm)	$A_s$ (mm <sup>2</sup> )	$f_s$ (MPa)	$f_{ek}$ (MPa)	$N_t$ (kN)	$N_0$ (kN)	$N_v^1$ (kN)	$N_v^2$ (kN)	$N_v^1/N_t$	$N_v^2/N_t$	$N_{CFST}$ (kN)	$N_t - N_{CFST}/N_{CFST}$ (%)	Sources
1-2.5	0.17	1260	2.5	1013.2	350	40.15	1294	859.2	1176.5	1293.7	0.92	1.00	1060.5	22.0	[30]
1-3.5	0.17	1260	3.5	1440.4	310	40.15	1348	959.1	1285.4	1408.0	0.95	1.04	1175.5	14.7	
1-4.5	0.17	1260	4.5	1880.2	310	40.15	1698	1103.6	1446.2	1575.6	0.85	0.93	1341.7	26.0	
2-2.5	0.34	1260	2.5	1013.2	350	40.15	1506	859.2	1293.3	1430.9	0.86	0.95	1060.5	42.0	
2-3.5	0.34	1260	3.5	1440.4	310	40.15	1593	959.1	1395.0	1540.1	0.86	0.97	1175.5	35.5	
2-4.5	0.34	1260	4.5	1880.2	310	40.15	1846	1103.6	1505.4	1702.0	0.82	0.92	1341.7	37.6	
SC41	0.167	1500	4	2400	295	53.6	2215	1850.5	2175.8	2341.1	0.98	1.06	2090.1	5.9	[13]
SC42	0.334	1500	4	2400	295	53.6	2275	1850.5	2261.3	2443.7	0.99	1.07	2090.1	8.8	
SC51	0.167	1500	5	3000	295	53.6	2485	2011.9	2326.4	2477.8	0.94	0.99	2244.0	10.7	
SC52	0.334	1500	5	3000	295	53.6	2585	2011.9	2407.9	2356.7	0.93	0.91	2244.0	15.2	
SC61	0.167	1500	6	3600	295	53.6	2710	2173.4	2472.8	2801.1	0.91	1.03	2394.3	13.2	
SC62	0.334	1500	6	3600	295	53.6	2775	2173.4	2550.0	2677.3	0.92	0.96	2394.3	15.9	
A-1	0.111	4900	3.5	1960	300	22.3	1107	982.5	1166.3	1110.7	1.05	1.00	1015.9	9.0	[31]
A-2	0.222	4900	3.5	1960	300	22.3	1129	982.5	1272.3	1192.6	1.13	1.06	1015.9	11.1	
A-3	0.333	4900	3.5	1960	300	22.3	1222	982.5	1380.2	1285.4	1.13	1.06	1015.9	20.3	
B-1	0.111	4900	3.5	1960	300	26.4	1200	1055.0	1260.5	1228.5	1.05	1.02	1111.3	8.0	
B-2	0.222	4900	3.5	1960	300	26.4	1237	1055.0	1365.7	1266.3	1.10	1.02	1111.3	11.3	
B-3	0.333	4900	3.5	1960	300	26.4	1294	1055.0	1472.6	1305.6	1.14	1.01	1111.3	16.4	
C-1	0.111	4900	3.5	1960	300	32.8	1204	1168.2	1409.3	1297.1	1.17	1.08	1261.1	-4.5	
C-2	0.222	4900	3.5	1960	300	32.8	1300	1168.2	1513.8	1352.5	1.16	1.04	1261.1	3.1	
C-3	0.333	4900	3.5	1960	300	32.8	1400	1168.2	1619.8	1405.9	1.16	1.00	1261.1	11.0	
D-1	0.111	4900	3.5	1960	300	40	1601	1295.6	1578.0	1502.1	0.99	0.94	1430.5	11.9	
D-2	0.222	4900	3.5	1960	300	40	1742	1295.6	1682.2	1655.4	0.97	0.95	1430.5	21.8	
D-3	0.333	4900	3.5	1960	300	40	1815	1295.6	1787.8	1797.6	0.99	0.99	1430.5	26.9	

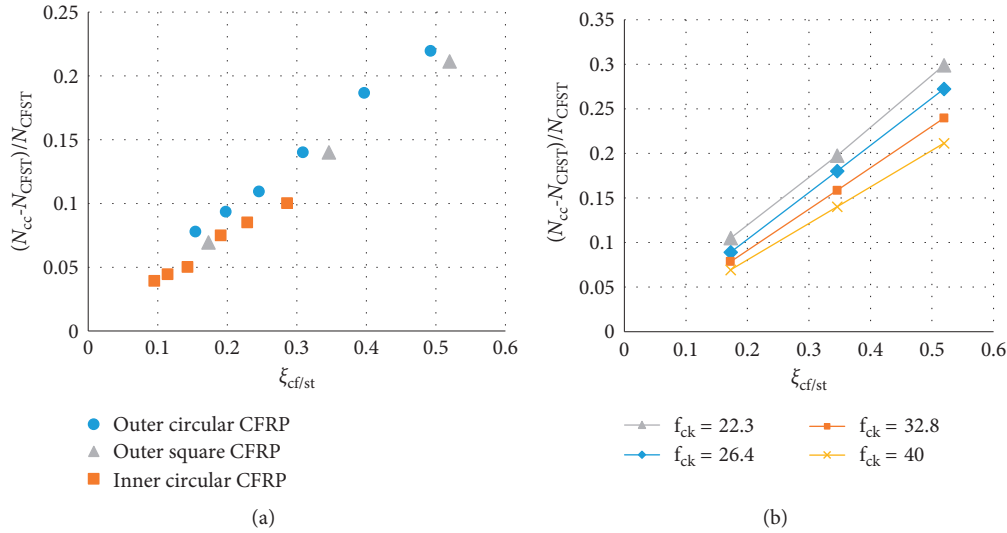


FIGURE 3: Relationship between  $(N_{cc} - N_{CFST})/N_{CFST}$  and  $\xi_{cf/st}$ . (a)  $f_{ck} = 40.15$ . (b) Different  $f_{ck}$ .

Then  $\eta$  was obtained as 0.65 by experimentation and statistical data [29], so the ultimate capacity of the steel tube can be calculated by

$$N_s = n f_s A_s. \quad (14)$$

Lastly, the ultimate capacity of CFRP-confined CFST column can be expressed as follows:

$$N_y^2 = \eta f_s A_s + (f_{ck} + k_c p) A_c. \quad (15)$$

## 5. Comparison and Analysis

The three types of CFRP-confined CFST stub columns shown in Figure 1 have been tested under axial compression [13, 30, 31]. Calculations  $N_y^1$  and  $N_y^2$ , obtained by Unified Theory of CFST and limit equilibrium theory, respectively, are listed in Table 1 together with the test results  $N_t$ . The calculated results both have good agreement with the test results within small errors less than 20%. Comparing the value of  $N_y^2/N_t$  and  $N_y^1/N_t$  shown in Table 1, we can find that  $N_y^2$  obtained by the limit equilibrium method is more accurate and reliable than  $N_y^1$  obtained by the method of Unified Theory of CFST. On the other hand, the method of Unified Theory of CFST is simple and easy to realize since it just considers the column as one composite material, while the method of limit equilibrium method sound complicated since it applies TSUST to analyze every component of the composite column. Therefore, these two methods can both be applied to investigate the axial bearing capacity of CFRP-confined CFST stub columns, and they can provide reference for engineering design. Then axial bearing capacity of pure CFST columns can be predicted by the limit equilibrium method in order to evaluate the bearing capacity improvement due to the CFRP confinement. By reviewing test results, the bearing capacity enhancement rate is described as the expression of  $(N_t - N_{CFST})/N_{CFST}$  as shown in Table 1. It was found that the averaged bearing capacity enhancement

rate of CFRP-confined CFST stub columns is 16.4 percent in comparison with the pure CFST columns. Because the CFRP sheet is very thin, it is demonstrated that the bearing capacity of the composite columns improves more than the corresponding pure CFST columns with the nearly same cross section area. Therefore, it is very applicable to use CFRP to strengthen the CFST column, and the composite columns can result in significant savings in column size, which ultimately realize the material potency and bring economic benefits.

Through data analysis of the calculated and experimental results, it can be found that concrete strength and the relative proportions of CFRP and steel are the main parameters to influence the axial bearing capacity of the composite column. The confining mechanism of CFRP and axial bearing capacity improvement needs to be validated, so the relative proportions of CFRP and steel is proposed according to the concept of equivalent confinement coefficient  $\xi_{ssc}$  (1). The relative proportions of CFRP and steel  $\xi_{cf/st}$  considers strength, content, and confining effect of section form, that is,

$$\xi_{cf/st} = \frac{k_{cf} A_{cf} f_{cf}}{k_s A_s f_s}. \quad (16)$$

Since the test results of the bearing capacity of the stub columns have a certain degree of dispersion and some parameters need to be taken as the same value, the calculated axial bearing capacity  $N_{cc}$  is used to describe the bearing capacity enhancement ratio with the expression of  $(N_{cc} - N_{CFST})/N_{CFST}$ , which reflects the function of the CFRP cylinder to confine the CFST column, where  $N_{CFST}$  is the calculated value for the corresponding pure CFST column.  $N_{cc}$  is obtained by limit equilibrium theory.

The relationship between  $(N_{cc} - N_{CFST})/N_{CFST}$  and  $\xi_{cf/st}$  for the three types of composite columns is shown in Figure 3. In reference to the experimental data in Table 1,  $f_{ck}$  of Type b and Type c is taken as 40.15 MPa similar to Type a, and Figure 3(a) shows the relationship between

$(N_{cc} - N_{CFST})/N_{CFST}$  and  $\xi_{cf/st}$  under the same concrete strength. The relationship is linear and directly proportional to the CFRP-wrapped composite columns with the outer circular CFRP or outer square CFRP because the outer CFRP cylinder strengthens the whole CFST column. But for the inner circular CFRP-confined columns, there is no linear proportion because inner CFRP only strengthens its inside concrete directly. It can also be found that outer circular CFRP has the best confinement effect to provide the highest bearing capacity enhancement ratio at the same relative proportions of CFRP and steel. Meanwhile, outer square CFRP does better than inner circular CFRP as shown in Figure 3(a), that is, CFRP as external jackets can provide the better confinement than the internal one. On the other hand, we choose the basic parameters of outer square CFRP-confined CFST columns in Table 1 to get the relationship between  $(N_{cc} - N_{CFST})/N_{CFST}$  and  $\xi_{cf/st}$  under different concrete strength as shown in Figure 3(b). For every group, the steel tube and the concrete are the same, so the bearing capacity enhancement ratio is linear and direct proportional to the content of the CFRP cylinder. Among the four groups, with the decrease of concrete strength, the bearing capacity enhancement ratio increases with the improvement of relative proportions of CFRP and steel. It indicates that the confinement effect of CFRP increases with the decrease of concrete strength. The reason is mainly that the contributions of the CFRP cylinder are the displacement resistance of the CFST column, and low-strength concrete has the better deformation capacity to make the CFRP play better especially during the postbuckling process.

## 6. Conclusions

This paper presented a comparative study of concrete-filled steel tubular (CFST) stub columns with three different confinement types from carbon fiber reinforced polymer (CFRP): outer circular CFRP, inner circular CFRP, and outer square CFRP. CFRP-confined CFST column takes the advantage of not only the good performance of CFST but also a substantial improvement in higher confinement of CFRP. The compressive mechanism and physical properties of the composite column were analyzed firstly aiming at investigating the confinement effects of the different CFRP on CFST Columns.

Two methods based on Unified Theory of CFST and elastoplastic limit equilibrium method have been applied to investigate the axial bearing capacity of CFRP-confined CFST stub columns. The calculated results have good agreement with the test results. Through data analysis, the study confirmed the ultimate strength calculation results of limit equilibrium method were found to be more accurate and reliable than that of Unified Theory of CFST. Then axial bearing capacity of pure CFST columns was predicted to evaluate the bearing capacity improvement factor coming from the CFRP confinement. It was demonstrated that the averaged enhancement ratio is 16.4 percent, showing that the three kinds of CFRP-confined CFST columns had a broad applicability.

CFRP can increase CFST members' bearing capacities significantly because complementary action between the steel tube and concrete is strengthened through CFRP. The relationship between the bearing capacity enhancement ratio and relative proportions of CFRP and steel is nearly linear, especially for the CFRP-wrapped columns with the outer circular CFRP or outer square CFRP. Through a comparative analysis, this study confirmed that outer circular CFRP had the best confinement effect and outer square CFRP did better than inner circular CFRP. The confinement effect of CFRP increased with the decrease of concrete strength, and it was proportional with relative proportions of CFRP and CFST under the same concrete strength.

## Data Availability

All data used for this paper are publicly available and accessible online. We have annotated the entire data building process and empirical techniques presented in the paper. We have given formal citations in article references. While we did not directly draw upon these sources for the empirical analysis, these efforts confirmed our understanding of the scope, scale, and accuracy of the CFRP-confined CFST columns.

## Conflicts of Interest

The authors declare that they have no conflicts of interest.

## Acknowledgments

The authors would like to acknowledge the support provided by the Chinese National Science Foundation (Grant no. 51478004). Meanwhile, the financial support from Hebei University of Technology is also appreciated.

## References

- [1] O. Chaalal and M. Shahawy, "Performance of fiber-reinforced polymer: wrapped reinforced concrete column under combined axial flexural loading," *ACI Structure Journal*, vol. 97, no. 4, pp. 659–668, 2000.
- [2] Y. Xiao, "Applications of FRP composites in concrete columns," *Advances in Structural Engineering*, vol. 7, no. 4, pp. 335–343, 2004.
- [3] J. G. Teng, Y. L. Huang, L. Lam, and L. P. Ye, "Theoretical model for fiber reinforced polymer-confined concrete," *Journal of Composites for Construction*, vol. 11, no. 2, pp. 201–210, 2007.
- [4] J. G. Teng, T. Jiang, L. Lam, and Y. Z. Luo, "Refinement of a design-oriented stress-strain model for FRP-confined concrete," *Journal of Composites for Construction*, vol. 13, no. 4, pp. 269–278, 2009.
- [5] Y. Zheng, L. F. Zhang, and L. P. Xia, "Investigation of the behaviour of flexible and ductile ECC link slab reinforced with FRP," *Construction and Building Materials*, vol. 166, pp. 694–711, 2018.
- [6] Y. Zheng and L. P. Xia, "Investigation of the ultimate capacity of NSM FRP-strengthened concrete bridge deck slabs," *Arabian Journal of Science and Engineering*, vol. 43, pp. 1597–1615, 2018.

- [7] Z. F. Amir and H. R. Sami, "Confinement model for axially loaded concrete confined by circular FRP tubes," *ACI Structure Journal*, vol. 98, no. 4, pp. 451–461, 2001.
- [8] L. H. Han, *Concrete-Filled Steel Tube Structures-Theory and Design*, Science Press, Beijing, China, 2nd edition, 2007.
- [9] B. C. Chen and T. L. Wang, "Overview of concrete filled steel tube arch bridges in China," *Practice Periodical on Structural Design and Construction*, vol. 14, no. 2, pp. 70–80, 2009.
- [10] Y. Che, Q. L. Wang, and Y. B. Shao, "Compressive performances of the concrete filled circular CFRP-steel tube (C-CFRP-CFST)," *International Journal of Advanced Steel Construction*, vol. 8, no. 4, pp. 311–338, 2012.
- [11] Z. Tao, L. H. Han, and L. L. Wang, "Compressive and flexural behaviour of CFRP repaired concrete-filled steel tubes after exposure to fire," *Journal of Constructional Steel Research*, vol. 63, no. 8, pp. 1116–1126, 2007.
- [12] W. Gu, "Study on mechanics of concrete-filled CFRP-steel tube column," Thesis for doctor degree, DaLian Maritime University, Dalian, China, 2007.
- [13] G. C. Li, L. Ma, and J. L. Yang, "Bearing capacity of short columns of high-strength concrete filled square steel tubular with inner CFRP circular tubular under axially compressive load," *Journal of Shenyang Jianzhu University*, vol. 24, no. 1, pp. 62–66, 2008.
- [14] Q. L. Wang, G. Y. Wang, and F. Han, "Experimental study on concentrically compressed stub columns reinforced by concrete filled CFRP-steel tube," in *4th International Conference on Advances in Steel Structures*, Elsevier Science Ltd., pp. 671–676, London, UK, 2005.
- [15] Z. Tao, L. H. Han, and J. P. Zhuang, "Using CFRP to strengthen concrete-filled steel tubular columns: stub column tests," in *4th International Conference on Advances in Steel Structures*, Elsevier Science Ltd., pp. 701–706, London, UK, 2005.
- [16] Q. L. Wang, S. E. Qu, Y. B. Shao, and L. M. Feng, "Static behavior of axially compressed circular concrete filled cfrp-steel tubular (c-cf-cfrp-st) columns with moderate slenderness ratio," *Advanced Steel Construction*, vol. 12, no. 3, pp. 263–295, 2016.
- [17] Q. L. Wang, Z. Zhao, Y. B. Shao, and Q. L. Li, "Static behavior of axially compressed square concrete filled CFRP-steel tubular (S-CF-CFRP-ST) columns with moderate slenderness," *Thin-Walled Structures*, vol. 110, pp. 106–122, 2017.
- [18] K. Karimi, M. J. Tait, and W. W. El-Dakhkhni, "Testing and modeling of a novel FRP-encased steel-concrete composite column," *Composite Structures*, vol. 93, no. 5, pp. 1463–1473, 2011.
- [19] P. Feng, S. Cheng, Y. Bai et al., "Mechanical behavior of concrete-filled square steel tube with FRP-confined concrete core subjected to axial compression," *Composite Structures*, vol. 123, no. 5, pp. 312–324, 2015.
- [20] S. T. Zhong, *Unified Theory of Concrete Filled Steel Tubular Structure*, Tsinghua University Press, Beijing, China, 2006.
- [21] M. H. Yu, *Unified Strength Theory and Its Applications*, Springer Press, Berlin, Heidelberg, Germany, 2004.
- [22] F. E. Richart, A. Brandtzaeg, and R. L. Brown, "A study of the failure of concrete under combined compressive stresses," Bulletin No. 185, Engineering Experimental Station, University of Illinois, Urbana, IL, USA, 1928.
- [23] Q. L. Wang, W. Gu, and Y. H. Zhao, "Experimental study on concentrically compressed concrete filled circular CFRP-steel composite tubular stub columns," *China Civil Engineering Journal*, vol. 38, no. 10, pp. 44–48, 2005.
- [24] A. H. Varma, R. Sause, and J. M. Ricles, "Development and validation of fiber model for high strength square concrete filled steel tube beam-column," *ACI Structural Journal*, vol. 102, no. 1, pp. 73–84, 2005.
- [25] S. T. Zhong, "New concept and development of research on concrete-filled steel tube (CFST)," in *Proceeding of 2nd International Symposium on Civil Infrastructure Systems*, pp. 9–12, Hong Kong, December 1996.
- [26] Y. F. Zhang and Z. Q. Zhang, "Study on equivalent confinement coefficient of composite CFST column based on unified theory," *Mechanics of Advanced Materials and Structures*, vol. 23, no. 1, pp. 22–27, 2016.
- [27] H. T. Chen, "Theoretical study on continuity of basic behavior of every-sectioned CFT stub columns under axial loads," Thesis for doctor degree, Harbin Institute of Technology, Harbin, China, 2001.
- [28] X. W. Li and J. H. Zhao, "Mechanics behavior of axial loaded short columns with concrete-filled square steel tube," *Chinese Journal of Highway and Transport*, vol. 19, no. 4, pp. 77–81, 2006.
- [29] Y. F. Zhang, J. H. Zhao, and W. F. Yuan, "Study on compressive bearing capacity of concrete filled square steel tube column reinforced by circular steel tube inside," *Journal of Civil Engineering and Management*, vol. 19, no. 6, pp. 787–795, 2013.
- [30] W. Gu and H. N. Li, "Research in the properties of the concrete filled steel tube columns with CFRP composite materials," *Advanced Materials Research*, vol. 163–167, pp. 3555–3559, 2011.
- [31] Q. L. Wang and Y. B. Shao, "Compressive performances of concrete filled square CFRP-steel tubes (S-CFRP-CFST)," *Steel and Composite Structures*, vol. 16, no. 5, pp. 455–480, 2014.